

HYBRID MODELING OF FLOATING WIND TURBINES

By

Matthew T. J. Hall

Dipl. Eng. University of Prince Edward Island, 2008

BSc, University of New Brunswick, 2010

MASc, University of Victoria, 2013

A DISSERTATION

Submitted in Partial Fulfillment of the

Requirements for the Degree of

Doctor of Philosophy

(in Mechanical Engineering)

The Graduate School

The University of Maine

August 2016

Advisory Committee:

Andrew J. Goupee, Libra Assistant Professor of Mechanical Engineering,
Advisor

Krish P. Thiagarajan, Alston D. and Ada Lee Correll Presidential Chair in
Energy and Professor of Mechanical Engineering

Senthil S. Vel, Arthur O. Willey Professor of Mechanical Engineering

Habib J. Dagher, Bath Iron Works Professor of Structural Engineering and
Director, Advanced Structures and Composites Center

Jason M. Jonkman, Senior Engineer, National Renewable Energy Laboratory

DISSERTATION ACCEPTANCE STATEMENT

On behalf of the Graduate Committee for Matthew T. J. Hall, I affirm that this manuscript is the final and accepted dissertation. Signatures of all committee members are on file with the Graduate School at the University of Maine, 42 Stodder Hall, Orono, Maine.

Andrew J. Goupee, Libra Assistant Professor of Mechanical Engineering (Date)

© Matthew Hall 2016
All Rights Reserved

LIBRARY RIGHTS STATEMENT

In presenting this dissertation in partial fulfillment of the requirements for an advanced degree at The University of Maine, I agree that the Library shall make it freely available for inspection. I further agree that permission for “fair use” copying of this dissertation for scholarly purposes may be granted by the Librarian. It is understood that any copying or publication of this dissertation for financial gain shall not be allowed without my written permission.

Matthew T. J. Hall

(Date)

HYBRID MODELING OF FLOATING WIND TURBINES

By Matthew T. J. Hall

Dissertation Advisor: Dr. Andrew Goupee

An Abstract of the Dissertation Presented
in Partial Fulfillment of the Requirements for the
Degree of Doctor of Philosophy
(in Mechanical Engineering)
August 2016

Hybrid modeling combining physical tests and numerical simulations in real time opens new opportunities in floating wind turbine research. Wave basin testing is an important validation step for floating support structure design, but current methods are limited by scaling problems in the aerodynamic loadings. Actuating wind turbine loads from a simulation that responds to the basin test in real time offers a way to avoid scaling problems and make floating wind turbine design validation in realistic coupled conditions more accessible to researchers. This thesis describes the development, realization, and demonstration of an approach for hybrid modeling of floating wind turbines.

Possible coupling arrangements for hybrid modeling were considered and simulated numerically to determine performance requirements for the mechatronic system needed to connect the physical and numerical sub-models. The sensitivity of floating wind turbine response to errors in the coupling system was quantified, leading to actuation accuracy specifications. The results suggest that achieving accurate hybrid modeling is feasible.

To provide the numerical sub-model, modifications were made to a widely-used floating wind turbine simulator to allow coupling with external dynamics models. Also, a new dynamic mooring line model was developed and validated which provides important accuracy improvements over previously-standard approaches with minimal computational cost. It has been integrated into a variety of simulation tools and is also well-suited for use in hybrid modeling involving simulated moorings.

An approach for the hybrid coupling system using cable-based actuation was developed. Feedforward and feedback control elements take input from motion tracking equipment and cable tension measurements to provide responsive actuation of forces on a moving floating platform. A prototype two-cable system was built and bench tested to refine the control approach and measure performance.

Finally, the system was applied to 1:50-scale testing of a floating wind turbine in a wind-wave basin. Results using the hybrid model agree closely with conventional wind-wave tests, experimentally validating the hybrid approach. Additional tests with the hybrid system incorporating true-to-scale aerodynamics and also the presence of wind turbulence in the numerical sub-model demonstrate significant changes in response, indicating the value of a hybrid model approach in floating wind turbine basin testing.

DEDICATION

To the many people in the renewable energy research community who have, professionally or personally, generously lent me a helping hand during the journey of graduate research. The spirit of sharing is inspiring, and the generosity is something one can only hope to pay forward.

ACKNOWLEDGEMENTS

I have to thank many colleagues, collaborators, mentors, and friends over the past years at University of Maine. Thanks to Andrew Goupee, my advisor, for his deep expertise, calm perspective, and dedication in keeping me focused on the priorities. Thanks to Marco Masciola, my mooring modeling mentor, whose generous advice was tremendously helpful in the development of MoorDyn. Thanks to Jason Jonkman for the input and assistance on so many occasions, the encouragement on MoorDyn, and writing the dissertation that served as my primary textbook during graduate studies. Thanks to Krish Thiagarajan for the experienced perspective and inclusive approach during my time at UMaine, as well as for providing my first formal instruction on ocean engineering and fluid-structure interaction. Thanks to Prof. Vel for the course that challenged me in mathematical areas that turned out to be very useful. Thanks to Habib Dagher, whose energy, vision, and leadership have made so much at UMaine possible.

I'm grateful to Matt Cameron for kindly looking out for my project and for all the help with putting rubber to the road, especially the immense effort setting up for basin testing. Thanks to Raul Urbina for all the advice over the years and the generous assistance during basin testing. Thanks to Senu Sirnivas for the collaborations and the kind support as I considered my next steps. Thanks to Valentin Chabaud for enjoyable discussions, expert advice on control approaches, and generous hospitality. I'm tremendously grateful to the International Network on Offshore Renewable Energy (INORE) and its sponsors for collaboration travel support and the many great symposia. There are too many INORE members to thank for their advice and friendship. Thanks to Giacomo Vissio, along with his

colleagues at Politecnico di Torino, for the hospitality, the exciting collaborations, and the expert advice on hardware-in-the-loop testing. Thank you to Adam Brown for never being afraid to clearly state the mission.

Thank you to Sebastien Gueydon for his input whenever we crossed paths and for providing second-order wave excitation files for DeepCwind semi and TLP platforms. Thanks to Line Roald for providing the same for the OC3 Hywind platform. Thanks to Tiago Duarte for kindly sharing second-order wave excitation algorithms. Thanks to Matt Fowler for preparing the 1:50-scale DeepCwind semisubmersible for basin testing that I used at the end of my work. As mentioned in the dedication, I have been frequently awed by the spirit of helpfulness and generosity among colleagues in the field, and I cannot thank those people enough for the positivity light it casts everything in. Thanks to Phil McGillivray for all the advice and news feeds. Thanks to Andy Trivett for inspiring me down this path years ago and always being there when I faced tough decisions. Thanks to Haley for being a truly wonderful friend, and to Javi for the unfailing positive energy. Thanks to all my friends – fish people, jockeys, others – for the adventures and good times. Thanks to Ildara, for everything; I don't think I'd have made it otherwise. Thanks to my family for the steadfast support and for putting up with me during these busy years.

The 2011 test data used in this work were provided by the DeepCwind Consortium through DOE grants DE-EE0002981 and DE-EE0003728, NSF grant IIP-0917974, and the University of Maine. I am grateful to the Natural Sciences and Engineering Research Council of Canada for supporting my graduate studies.

TABLE OF CONTENTS

DEDICATION	iv
ACKNOWLEDGEMENTS	v
LIST OF TABLES	xii
LIST OF FIGURES	xiv
Chapter	
1. INTRODUCTION	1
1.1 Background on Hybrid Modeling	4
1.1.1 Applications in Other Fields	5
1.1.2 Floating Wind Turbine Applications	6
1.2 Objectives and Scope	10
1.3 Contributions.....	11
1.4 Outline.....	13
2. NUMERICAL MODELING	14
2.1 Wind Turbine Model Modification	15
2.2 Mooring Dynamics (MoorDyn) Model Development	19
2.2.1 Mooring Modeling Background	19
2.2.2 Lumped-Mass Model Formulation	23
2.2.2.1 Internal Forces.....	25
2.2.2.2 External Forces.....	27
2.2.2.3 Mass and Integration	28

2.2.3	Coupling with Other Codes	30
2.2.4	Validation with DeepCwind Semisubmersible Test Data	32
2.2.4.1	The DeepCwind Semisubmersible Tests	33
2.2.4.2	1:50-Scale Wind Turbine Model.....	35
2.2.4.3	Semisubmersible Platform Model	36
2.2.4.4	Mooring System Static Properties	37
2.2.4.5	Mooring System Hydrodynamic Properties	40
2.2.4.6	Uncoupled Mooring Model Validation	43
2.2.4.7	Coupled Floating Wind Turbine Model Validation.....	50
2.2.5	Multi-Segment Mooring Model Validation	57
2.2.6	Conclusions on Mooring Modeling.....	60
3.	DEVELOPMENT OF PERFORMANCE SPECIFICATIONS	62
3.1	Methodology	62
3.1.1	Coupling Location	63
3.1.2	Specifications Considered	64
3.1.3	Simulation Approach	65
3.1.4	Wind Turbine and Support Structure Designs	68
3.1.5	Environmental Conditions	69
3.2	Validation of Numerical Modeling	70
3.3	Actuation Performance Envelope Requirements	74
3.3.1	Motions.....	75
3.3.2	Forces.....	79
3.3.3	Summary	80

3.4	Hybrid Coupling Quality Requirements	82
3.4.1	Summary	86
3.4.2	Discussion	88
3.4.2.1	Replacing Latency with Motion Tracking Noise	89
3.4.2.2	Sensitivity to Coupling Bandwidth	90
3.4.3	Demonstration of Finding Specifications	91
3.5	Conclusions on Performance Specifications	95
4.	THEORETICAL DEVELOPMENT OF HYBRID MODELING	97
4.1	Physical and Numerical Sub-Models	97
4.2	Actuation System	98
4.2.1	Actuator Type	99
4.2.2	Background on Cable Robots	100
4.2.3	Actuator Modularity and Reconfigurability	101
4.2.4	Measurements and Feedback	107
4.2.4.1	Winch Instrumentation	107
4.2.4.2	Centralized Instrumentation	108
4.2.5	Cable Robot Mechanics and Control	108
4.3	Hybrid Coupling Control	111
4.3.1	Admittance Control Approach	114
4.3.1.1	Motion Constraints	116
4.3.1.2	Practical Limitations on Admittance-Control Coupling	117
4.3.2	Impedance Control Approach	119
4.3.2.1	Tension Feedback	120
4.3.2.2	Motion Accommodation	123
4.3.2.3	Motion Observer, Delay Compensation, and Stability	125
4.3.2.4	Feedforward Control and Tension Observer	130
4.3.2.5	Integrated Controller	132

5.	HYBRID MODEL REALIZATION AND TESTING	135
5.1	Hybrid Coupling System Setup	136
5.1.1	Winch Units.....	136
5.1.1.1	Sizing.....	137
5.1.2	Data Acquisition and Control.....	140
5.1.2.1	Load Cell Measurements.....	142
5.2	Bench Testing	143
5.2.1	Pendulum Test Rig	144
5.2.2	Motor Motion Verification	146
5.2.3	Spring Calibration	148
5.2.4	Tension Control Testing.....	151
5.2.4.1	Tension Filtering	153
5.2.4.2	Effect of Gain and Stiffness on Response	156
5.2.4.3	Use of Feedforward Control	158
5.2.5	Motion Accommodation Testing.....	160
5.2.6	Hybrid Coupling Testing	163
5.2.7	Pendulum-FAST Coupling Testing	165
5.2.8	Conclusions on Bench Testing	167
5.3	Basin Testing.....	169
5.3.1	Experimental Setup.....	170
5.3.1.1	Hybrid Coupling Setup	172
5.3.2	Validation of Hybrid Approach	175
5.3.3	Results with New Hybrid Model Features	183
5.3.4	Conclusions on Basin Testing	192
6.	CONCLUSIONS	194
6.1	Limitations of a Hybrid Approach.....	196
6.2	The Advantage of Accessibility	199
6.3	Future Work.....	201

REFERENCES	203
APPENDIX – PERFORMANCE SPECIFICATIONS FOR MOORING-PLATFORM HYBRID COUPLING	214
BIOGRAPHY OF THE AUTHOR	220

LIST OF TABLES

2.1	Sea states considered	34
2.2	Properties of the DeepCwind wind turbine	35
2.3	DeepCwind semisubmersible platform properties	36
2.4	DeepCwind semisubmersible platform quadratic drag coefficients.....	37
2.5	DeepCwind mooring chain properties	38
2.6	Pretension and tuning of line lengths	39
2.7	Fairlead tension RAO comparison	47
2.8	Uncoupled fatigue and extreme mooring loads for design sea state and dynamic wind.	50
2.9	Coupled fatigue and extreme mooring loads for design sea state and dynamic wind.	56
3.1	Environmental conditions simulated	70
3.2	Surge and pitch offsets under steady 16.1 m/s wind	72
3.3	First tower-bending natural frequency of each design (Hz).....	72
3.4	Range, velocity, and force requirements for tower-base coupling, all designs	81
3.5	Range, velocity, and force requirements for aero-elastic coupling, all designs	81
3.6	Individual tolerances for 10% RMS discrepancy in tower-base bending moment	88
3.7	Example 1:50-scale specifications for tower-base coupling	94
3.8	Example 1:50-scale specifications for aero-elastic coupling	94
5.1	Stiffness and linear range of springs used in testing.....	149

5.2	Pendulum properties used in hybrid coupling tests including hub-height linearized values.....	164
5.3	Results of free decay tests with hybrid model	164
5.4	Summary of test cases used in wind-wave basin.....	170
5.5	Comparison of hybrid and conventional approaches with and without wind.....	178
5.6	Standard deviations of measured quantities in hybrid model testing	185
5.7	Standard deviations of simulated quantities in hybrid model testing	185
6.1	Limitations of conventional and hybrid approaches for basin testing	197
A.1	Maximum forces and motions in mooring-platform coupling for each design	217

LIST OF FIGURES

1.1	Floating wind turbine motions	2
1.2	1:50-scale DeepCwind semisubmersible during testing in 2011	4
2.1	Coordinate system and Euler angles	18
2.2	Mooring line discretization and indexing.....	24
2.3	Internal and external cable forces.....	25
2.4	Overview of lumped-mass mooring model coupling with FAST v7.....	31
2.5	Equilibrium fairlead tensions and angles normalized by quasi-static result	39
2.6	Fairlead 1 tensions for regular wave 5 with $\pm 50\%$ variation of hydrodynamic coefficients	42
2.7	Fairlead 1 tensions for regular wave 5 with different numbers of cable segments	42
2.8	Sample of original and filtered platform motions from regular wave 5	43
2.9	Fairlead tensions in regular wave 5.....	45
2.10	Fairlead tension PSDs in regular wave 5	45
2.11	Comparison of fairlead tension RAO magnitudes from test data, lumped-mass model, and quasi-static model	46
2.12	Slack line conditions apparent in fairlead 1 tension for regular wave 7	47
2.13	Fairlead tensions for design wave and dynamic wind	48
2.14	Fairlead tension PSDs for design wave and dynamic wind	49
2.15	Platform motions and fairlead tensions for regular wave 5	52

2.16	Comparison of platform motion RAO magnitudes from test data, lumped-mass model, and quasi-static model.	53
2.17	Comparison of fairlead tension RAO magnitudes from test data, lumped-mass model, and quasi-static model.	53
2.18	Surge motion in operational 2 sea state with different drift contributions	54
2.19	Platform motion and fairlead tension time series for design sea state with dynamic wind.	55
2.20	Mooring system used in 1:20-scale ISWEC tests (image courtesy of Giacomo Vissio)	58
2.21	Fairlead tensions on the ISWEC device in regular waves.	59
3.1	Tower-base and aero-elastic hybrid coupling types	64
3.2	Surge RAO magnitude from white noise sea state	73
3.3	Heave RAO magnitude from white noise sea state	74
3.4	Pitch RAO magnitude from white noise sea state.....	74
3.5	Maximum surge displacements at coupling point	76
3.6	Maximum pitch angles at coupling point	76
3.7	Maximum surge velocities at coupling point.....	77
3.8	Maximum pitch rates at coupling point.....	77
3.9	Motion bandwidth in surge	79
3.10	Motion bandwidth in pitch	79
3.11	Maximum surge forces at coupling point	80
3.12	Maximum pitch moments at coupling point	80
3.13	Sensitivity to translational motion tracking noise	84
3.14	Sensitivity to rotational motion tracking noise	84
3.15	Sensitivity to noise in actuated force.....	85

3.16	Sensitivity to noise in actuated moment	85
3.17	Sensitivity to latency in coupling.....	86
3.18	Tower-base bending moment time series comparison for a case with 11.3% RMS relative discrepancy	87
3.19	Sensitivity to force noise cutoff frequency in aero-elastic coupling (vertical lines indicate first tower bending natural frequency)	90
3.20	Effect of noise in actuated force at 1:50 scale.....	93
4.1	Single DOF (fore-aft) actuation configurations	103
4.2	Two-DOF (fore-aft and side-side) actuation configurations.....	104
4.3	Two-DOF (surge and pitch) actuation configuration.....	105
4.4	Tentative layout for a 6-DOF actuation system with a 1:50-scale floating platform	105
4.5	Configuration for airborne wind energy converter on floating platform	106
4.6	Hybrid model coupling schemes	112
4.7	Resonances in a two-cable admittance-controlled hybrid coupling	118
4.8	Tension control block diagram	121
4.9	Tension control disturbance rejection block diagram.....	121
4.10	Disturbance accommodation and tension control block diagram.....	124
4.11	Final actuator control system including feedback, feedforward, and motion accommodation elements.....	133
5.1	Winch unit design	137
5.2	System electronics arrangement as used in basin testing	141

5.3	Overview of hybrid coupling data acquisition and control process.....	142
5.4	Experimental setup for tension tests with fixed endpoint	143
5.5	Test rig with opposing winch units and 1:100-scale pendulum	146
5.6	Motion repeatability test.....	148
5.7	Cable length and tension in spring calibration test	150
5.8	Force-displacement relationship in spring calibration test	150
5.9	Tension setpoint sequence for tension-control tests	151
5.10	Sample of processed tension step response data.....	152
5.11	Sample of processed tension harmonic response data	153
5.12	Tension step response metrics for different gains and filter types.....	154
5.13	Tension magnitude response for different controller gains and filter types.....	155
5.14	Tension phase lag for different controller gains and filter types.....	155
5.15	Tension step response metrics versus controller gain for feedback control.....	156
5.16	Tension magnitude frequency response with feedback control.....	158
5.17	Tension phase frequency response with feedback control	158
5.18	Tension step response metrics versus controller gain for feedforward control	159
5.19	Tension magnitude frequency response with feedforward control	160
5.20	Tension phase frequency response with feedforward control	160
5.21	Free decay tests with motion accommodation	162
5.22	Effect of delay compensation in free decay tests	163

5.23	Raw (gray) and filtered (black) time series of free decay tests with pendulum-FAST hybrid model.....	166
5.24	Layout of basin testing	171
5.25	1:50-scale DeepCwind semisubmersible in basin with hybrid coupling attached	172
5.26	Arrangement of cable system in basin	173
5.27	Turbine nacelle with cable system attached for hybrid model basin testing	174
5.28	Applied force time series in zero-thrust test	175
5.29	Applied force PSD in zero-thrust test.....	176
5.30	Comparison of hybrid (solid line) and conventional (dashed line) wave-only and wind-wave tests	181
5.31	PSD comparison of hybrid (solid line) and conventional (dashed line) wave-only and wind-wave tests	182
5.32	Sample time series of different hybrid model test cases	188
5.33	PSD comparison of different hybrid model test cases	189
5.34	Sample FAST time series of different hybrid model test cases	190
5.35	FAST PSD comparison of different hybrid model test cases.....	191
6.1	Hybrid coupling system used at basin.....	200
A.1	Mooring-platform hybrid coupling.....	215
A.2	Maximum surge forces in mooring coupling	216
A.3	Maximum heave forces in mooring coupling	216
A.4	Maximum pitch moments in mooring coupling.....	217
A.5	Sensitivity to translational tracking errors in mooring coupling.....	217
A.6	Sensitivity to rotational tracking errors in mooring coupling.....	218
A.7	Sensitivity to latency in mooring coupling.....	218

Chapter 1

INTRODUCTION

Floating offshore wind turbines are a nascent technology that offers a means of harvesting wind energy over deep-water regions. The deep-water wind resource is vast [1, 2], and being able to convert that resource into usable energy is in many respects the next frontier for the wind energy industry. This opportunity comes with a unique set of technical challenges. Floating wind turbines have to withstand a harsh offshore environment for a typical service life on the order of 20 years. They face larger wind loads than traditional offshore structures yet much tighter cost constraints. The design process is made difficult by the complexity of modeling a flexible structure under the influence of combined wind and wave loadings. The quality of the modeling determines the safety margins needed in the design process, which in turn affect the cost of the technology. The overall aim of the research described in this thesis is to develop a hybrid numerical-physical modeling approach that could improve the small-scale testing step in floating wind turbine design.

Modeling floating wind turbines is particularly challenging because of the aero-hydro-elastic coupling involved (Figure 1.1). A model needs to adequately represent three different sub-systems: the wind turbine interacting with the air, the floating platform interacting with the waves, and the mooring system interacting with the water and seabed. Furthermore, in most cases the model needs to capture the *dynamic coupling* between these three sub-systems in order to be fully useful.

Models can typically be classified as either numerical (i.e. simulations) or physical (i.e. experiments). While simulations are used throughout the floating wind turbine design process, small-scale experiments are used at key points in the process to (1) validate numerical models being used and (2) validate the design itself. Validating numerical models is usually the first goal, because if these tools can be validated using just a handful of experimental scenarios, then they can be relied on to simulate numerous other scenarios. However, validating the design itself is also often an important goal of testing. Experimentally characterizing the coupled response of the entire design not only provides a comparison with numerical model predictions but also can reveal complex phenomena that may only emerge outside the idealized framework of computer simulation. As well, experiments provide a physical "proof of concept" that can be valuable in providing a convincing performance demonstration to developers, investors, and other stakeholders.

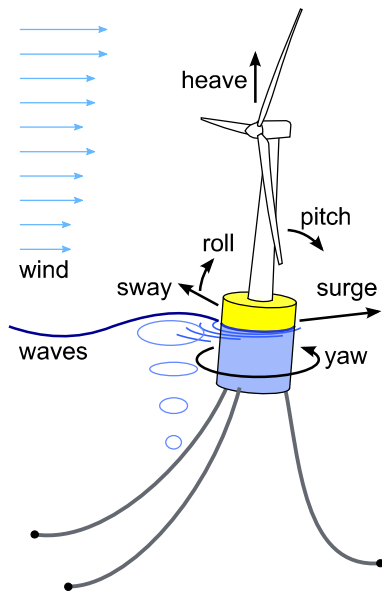


Figure 1.1: Floating wind turbine motions

For floating wind turbines, both numerical and physical modeling techniques face different specific challenges. Numerical models – especially the computationally-efficient ones used in the course of floating platform design – rely on simplifying assumptions and empirical coefficients that warrant experimental validation and tuning. From a floating system design perspective, experimentally checking the platform portion of the model is particularly important. As well, a variety of limitations in the models (see e.g. [3, 4]) limit their accuracy in certain situations.

Laboratory-scale physical models, meanwhile, face challenges reproducing the coupled dynamics at small scale. Typically, the entire floating wind turbine system is scaled by Froude number to reproduce realistic platform-wave interactions.

Figure 1.2 shows an example of a Froude-scaled test. Because Reynolds number cannot also be preserved, this scaling can introduce changes in the hydrodynamics and aerodynamics. The effect on the wind turbine is particularly severe: even with special low-Reynolds number rotor geometries, true-to-scale thrust and torque characteristics have not yet been demonstrated simultaneously, although research is ongoing [5, 6]. This, along with difficulties creating elastic characteristics and control actuation at small scale, makes it challenging to represent details like independent blade pitch control, turbine faults, and unsteady wind conditions. Under the water, the mooring system often has to be truncated to fit within the wave basin.

The focus of this thesis concerns a way to bypass some of these challenges by combining physical and numerical models together. In basin tests, the most scalable and important part of the experiment, the floating platform, will be retained. The turbine, however, will be removed and replaced with an actuation system. This actuation system will be controlled by a computer simulation to

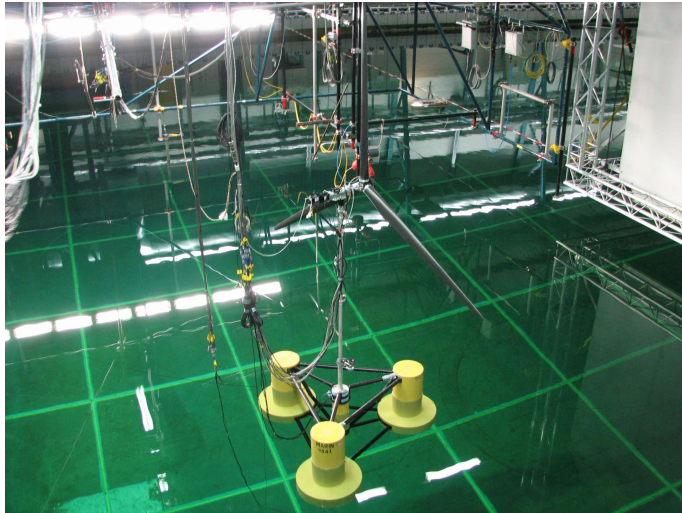


Figure 1.2: 1:50-scale DeepCwind semisubmersible during testing in 2011

provide the same forces on the platform as would be provided by a wind turbine. The wind turbine simulation reacts to the experiment by accepting as inputs the measured platform motions. In this way, the simulation and experiment are dynamically coupled in real time. Since the wind turbine is simulated, performance and control characteristics can be chosen at will, subject to the limitations of the numerical model. If the mooring lines are also simulated using this approach, then the problem of mooring system truncation can be avoided as well. Since this approach constitutes a combination of physical and numerical sub-models, it can be labeled a hybrid model. The aim of my research is to develop such a model and demonstrate how this approach can be of value to floating wind turbine development.

1.1 Background on Hybrid Modeling

Coupling physical and numerical models together in real time is not a new idea – it has been applied in other fields under a variety of names: “real-time hybrid testing” for seismic engineering, “hardware-in-the-loop simulation” for controls

design, and “PTO emulation” for wave energy converter testing, for example. However, few connections have been made between these different applications and there are differences in terminology and techniques. I use the general label “hybrid modeling” in the spirit of recognizing the commonalities and drawing on experience from across fields.

1.1.1 Applications in Other Fields

In seismic engineering, hybrid testing is used to describe any coupling of simulations and experiments. Traditionally, this meant “pseudodynamic” couplings in which a simulation of structural dynamics would interact with a quasi-static experiment (providing experimental force-displacement relations) at a speed slower than real time [7]. With improvements in computers, controllers, and actuators, truly dynamic couplings were developed to better represent structures with high natural frequencies [8]. Termed “real-time hybrid testing,” this application saw the development of compensation methods for coupling imperfections like latency and actuator dynamics [9, 10].

In automotive applications, especially relating to controls development, hybrid modeling is often used under the name hardware-in-the-loop (HIL) simulation. Typically, the control hardware under development (sensors, embedded controllers, etc.) is tested in conjunction with a simulation of the plant (e.g. the vehicle) [11]. This can save time and money by allowing testing of the embedded control hardware before prototypes of the entire vehicle are ready.

In small-scale testing of wave energy converters (WECs), hybrid modeling is commonly used to avoid using a physical small-scale power take-off (PTO). The challenge of recreating small-scale hydraulic devices and the need for experimenting with many different PTO tunings and control strategies makes

putting the PTO on the simulation side very attractive. The single degree of freedom typically required makes the coupling relatively easy. This has been done successfully with linear servomotors [12, 13].

The inverse arrangement has also been used. Developers of a WEC with an elaborate gyroscope-based PTO have done hardware-in-the-loop experiments with the PTO, providing hull motions using an actuator controlled by a real-time simulation of the WEC hydrodynamics [14].

Hybrid modeling has also been used in scale model tests of more conventional offshore platforms for some time. One application is using a ducted fan to provide an approximation of wind loads on vessels [15]. Another idea is active truncated mooring systems, in which actuation of the mooring lines is used to compensate for a basin depth being too shallow for deep water mooring systems [16].

1.1.2 Floating Wind Turbine Applications

Hybrid modeling is especially applicable to floating wind turbines because of the challenges in scale-model tests. Like other offshore structures, floating wind turbine designs are best validated through scale-model wave-basin testing. However, aerodynamic loads are vastly more important to floating wind turbines than to other offshore structures. This brings about a particularly challenging scaling problem. The dimensionless number key to scaling aerodynamics is Reynolds number, which represents the ratio of inertial to viscous forces and is defined as

$$Re = \frac{VL}{\nu}, \quad (1.1)$$

where V is a characteristic speed, L is a characteristic length, and ν is the fluid's kinematic viscosity.

Reynolds number plays a role in the hydrodynamics of the floating platform, but an even more important dimensionless quantity for free-surface hydrodynamics is Froude number, which represents the ratio of inertial to gravitational forces and is defined as

$$Fr = \frac{V}{\sqrt{gL}}, \quad (1.2)$$

where g is acceleration due to gravity.

Since the hydrodynamics of the floating platform are affected more by gravity wave forces than by viscous forces, wave tank testing usually employs Froude scaling. For floating wind turbines, scaling by Froude number is necessary to obtain reasonable free surface hydrodynamics. As apparent from (1.2) and (1.1), Froude scaling invariably lowers the Reynolds number. This may be acceptable for the hydrodynamics, as the Reynolds dependence is often small. However, viscous effects are important to wind turbine aerodynamics and Froude-scaled wind turbines can experience severe performance reductions due to the lowered Reynolds number [17]. The necessity of adhering to a consistent scaling scheme, combined with the incompatibility of Reynolds and Froude scaling, means that experiments with unaltered Froude-scaled floating wind turbine models do not give a true-to-scale representation of the coupling between aerodynamic and hydrodynamic forces. Müller et al. [18] provide a review of various approaches for overcoming this scaling problem.

The conventional approach is to modify the wind turbine rotor geometry with low-Reynolds number airfoils and enlarged chord lengths [19, 20, 5]. This approach has given good results at matching full scale thrust curves with the correct wind speeds and tip speed ratios, a significant improvement over geometrically-scaled rotors. However, torque curves have yet to be matched at the same time, meaning there is still a discrepancy from full scale. The fidelity lost in this compromise may

be important for more detailed investigations considering, for example, loads on the rotor blades, platform pitch damping at different wind speeds, or advanced blade-pitch control strategies.

Avoiding the scaling incompatibilities by handling the aerodynamics in a computer simulation (in which the Reynolds number can be arbitrarily modified) is one of the main motivations behind developing hybrid modeling for floating wind turbines. Additional advantages include the possibility of greater fidelity in the wind turbine modeling – such as the inclusion of turbine elasticity, independent blade pitch control, and precise wind turbulence – which are hard to produce at model scale. There is also the benefit of enabling floating wind turbine basin testing without a physical wind-generation capability, something that makes this sort of research more accessible to institutions with less advanced wave basin facilities.

It is also worth mentioning that the inverse hybrid model is also being explored to aid research in the unsteady aerodynamics that can be encountered by floating wind turbines undergoing large wave-induced motions. Bayati et al. explored a system in which a numerical model of the floating platform is used to drive the dynamics of a wind turbine in a wind tunnel [21]. Their design uses a rigid parallel manipulator specially designed to fit the narrow confines of a wind tunnel [22].

Returning to the original problem, several forms of hybrid modeling have already been attempted in floating wind turbine basin tests. The most well-established approach, elegant in its simplicity, is using a small ducted fan mounted atop the turbine tower in place of the rotor. The fan is controlled to provide the thrust force calculated by a computer simulation running in parallel with the test and responding to the platform motions. Because of its high flow speed and small swept area, the fan's speed-to-thrust ratio is negligibly affected by the change in relative wind speed due to the platform motion, simplifying the control problem.

Also, because the fan is fixed to the tower, it always provides the out-of-plane force component of the simulated rotor, which is the largest and most important component. Azcona et al. [23] describe a system used in 1:40-scale tests at École Centrale de Nantes. Comparisons between experiments and simulations show that the system performed well, generally matching dynamic thrust loads closely in free decay tests. However, some limitations in thrust rate of change imposed by the fan inertia were apparent. The fan took more than half a second to match a step speed command, suggesting that the performance at wave frequencies, where aerodynamic damping plays a role, could match less well.

The other approach is to use an actuator attached to a fixed structure, which offers better response times and a more plausible means of coupling multiple degrees of freedom. Chabaud et al. at the Norwegian University of Science and Technology (NTNU) and Marintek provide an introduction to this idea and the accompanying control challenges [24]. With colleagues at the University of Maine (UMaine), I studied the performance requirements for such a system [25]. More recently, researchers at NTNU and Marintek conducted a study on the effect of limited actuation [26].

The actuation approach I and the group at NTNU/Marintek each selected, independently from each other, is a redundant (pulling in opposing directions) cable-based actuation system. Using cables allows application of wind turbine loads in one or more degrees of freedom and offers higher bandwidth and more complex loading capabilities than a ducted-fan approach. However, the equipment and controls requirements are more demanding. Using a six-cable actuation system developed by Valentin Chabaud, Sauder et al. describe the experimental setup used at Marintek to couple a floating platform basin test with numerically-modeled wind loads applied in five degrees of freedom [27]. Bachynski

et al. describe the results of applying this approach in 1:30-scale wave basin testing of a semisubmersible floating wind turbine, showing very good measures of performance [28].

The work described in this thesis occurred concurrently with that at NTNU and Marintek, but without technical exchange save for published literature and face-to-face conversations in January 2016. This speaks to the merit of the cable-based coupling approach, that it was selected by two independent parties who approached the same problem from different backgrounds and using different techniques. The design work and implementation details are of course different. While the project at NTNU/Marintek targeted a more advanced system at a larger scale, my work covered different background material and used UMaine's unique above-basin wind generation capability to provide a direct comparison between hybrid and conventional scale-model testing, enabling a first fully-experimental validation of the method.

1.2 Objectives and Scope

My overarching goal in this PhD research was to develop a hybrid modeling approach and demonstrate that hybrid modeling of floating wind turbines is achievable and worthwhile. Out of that come three objectives:

1. Assemble the numerical modeling and theoretical control elements to create a complete hybrid modeling approach.
2. Design and build a hybrid coupling system prototype.
3. Demonstrate the hybrid model approach by applying the prototype system to an industry-standard basin-testing scenario.

A hybrid model integrates many elements – relating to numerical models, physical models, actuation, instrumentation, control, etc. – and these all need to be present for a complete functional system. I tried to focus not on the physical or numerical sub-models, but rather on the process of coupling them together since that is where the novelty of the approach lies. However, some work was needed in adapting the numerical models for use in a hybrid-coupled situation. Working with simulation tools also led into development of a new numerical mooring model which, though not yet applied to a hybrid model testing application, would be well suited for it. This work falls under the first objective.

In the main task of developing, realizing, and testing the hybrid coupling system (pertaining to all three objectives), my approach was to draw on existing techniques and tools wherever possible, in order to avoid redundant work and focus on proper selection and integration of the many elements required.

Modifications had to be made for the specific application, but I strove to keep developments in any given system element as simplistic as possible in order to maintain a reasonable overall scope. For example, more advanced control schemes could offer the possibility of performance improvements or reduce instrumentation requirements, but this would have detracted from the larger goal. Ultimately, the novelty lies not in any of the individual elements but in the adaptation and integration of diverse techniques toward the realization and demonstration of a new approach for modeling floating wind turbines.

1.3 Contributions

My work presented here contains four main contributions.

- I developed a dynamic mooring line model that targets a balance of performance and efficiency while facilitating ease of coupling. I validated the model and after collaborating with various parties, it has become an important component of widely used floating wind turbine and wave energy converter simulators. The model is also uniquely suited to use in hybrid modeling. The model formulation and validation has been published in Ocean Engineering [29] and the coupling efforts have lead to several conference papers thus far.
- I created a methodology for studying the effect of hybrid coupling inaccuracies and used it to determine performance guidelines for developing hybrid coupling systems. These results inform coupling system design and provide insight in understanding the quality of hybrid model results. Preliminary work was published in a conference paper and a journal manuscript is in review.
- I developed a practical and versatile approach for achieving a hybrid model of a floating wind turbine using cable-based actuation. I refined the technique through creation and bench testing of a fully functional prototype system.
- I conducted experiments with the prototype side-by-side with conventional wind-wave testing, providing the first one-to-one experimental validation of the hybrid modeling approach for floating wind turbines. Other results of the tests demonstrate the ability to use true-to-scale wind loads including wind turbulence, and the important differences those make. A journal manuscript is in preparation.

At a higher level, the contribution lies in showing that the cable-based hybrid model approach is feasible and effective – that it can give more true-to-scale wind

loads than conventional approaches using a system that, while challenging to develop, is not prohibitively complex nor expensive. This could be an encouraging step toward higher fidelity and broader accessibility in basin testing of floating wind turbines.

1.4 Outline

The following chapters present the work that went into meeting the goal of developing and demonstrating a hybrid modeling system for floating wind turbines.

Chapter 2 introduces the associated numerical modeling tools, including modifications to an existing wind turbine simulator and the development of a new mooring line model.

Chapter 3 describes a study of performance requirements for the hybrid coupling system across various coupling arrangements, environmental conditions, and platform types.

Chapter 4 presents the theoretical development of approaches to a hybrid coupling system and details the final configuration that I settled on.

Chapter 5 describes the prototype hybrid coupling system, its testing in simplified laboratory conditions, and its demonstration in a complete 1:50-scale floating wind turbine wave-basin experiment.

Chapter 6 presents conclusions from the work as a whole and describes possible future extensions.

Chapter 2

NUMERICAL MODELING

Numerical modeling is important to this work both for providing one half of a hybrid model and for simulating the system as a whole in the process of developing the hybrid coupling. Simulating the entire floating wind turbine provides a benchmark to compare the hybrid model results against, while another is provided by experiments. Simulating the entire system including the effect of a hybrid coupling informs design of the coupling system and aids understanding of its influence on the results.

For use in a hybrid model, the choice of numerical models is limited by the requirement for real-time performance. In this case, “real time” is with reference to model scale, which is faster than full-scale time. Using a common scaling ratio for floating wind turbines of 1:50, which is suitable for testing in the UMaine W² wind-wave basin facility, the time ratio as determined by Froude scaling would be:

$$t_2/t_1 = \sqrt{(L_2/L_1)} = \sqrt{50} \approx 7. \quad (2.1)$$

This means any numerical model would have to be able to operate at least seven times faster than real time.

I relied on FAST (Fatigue, Aerodynamics, Structures, and Turbulence), a widely-used coupled floating wind turbine simulation tool developed at the National Renewable Energy Laboratory (NREL) [30, 31], for all of the numerical wind turbine modeling in this thesis, including the numerical aero-elastic component of the hybrid model. Its code is open source, allowing for adaptability

to meet different needs. An overview of FAST v7 and the customizations I made to it is given in Section 2.1.

At the time this research began, there was a gap in coupled simulation tools with regards to mooring models; computationally-efficient mooring models that accounted for dynamics were not freely available. In previous work I had found the existing quasi-static models to have significant shortcomings in predicting mooring line loads [32]. Accordingly, I sought to developing a mooring model that could provide the missing capability. A second goal was to be able to model mooring dynamics in a code computationally efficient enough for use in a hybrid modeling situation. Details of the model are presented in Section 2.2.

2.1 Wind Turbine Model Modification

FAST is a nonlinear time-domain simulator for wind turbines, including floating offshore wind turbines. The version used for all the work in this thesis, FAST v7, includes limited structural degrees of freedom (DOFs), blade-element-momentum theory aerodynamics, linear hydrodynamics, and quasi-static mooring modeling [31]. Although a new version of FAST was released part-way through my work, I continued using FAST v7 in order to build on customizations and enhancements already made in this version.

FAST v7 models structural deflections of the turbine using a linear approach based on pre-calculated mode shapes. Each mode adds a degree of freedom to the model. Each blade has two flapwise bending modes and one edgewise bending mode. The tower has two fore-aft and two lateral bending DOFs. Additional DOFs include the generator rotation, nacelle rotation, a spring-damper model of the low speed drive shaft torsion, and six DOFs for the base of the turbine to account for movement of

a floating platform as were shown in Figure 1.1. The formulation of the tower and turbine dynamics assumes small tilt angles of the support platform [31]. More information about the modeled turbine DOFs can be found in the FAST User’s Guide [30].

The aerodynamic sub-model, AeroDyn, uses a blade element momentum model or a generalized dynamic wake model for the rotor aerodynamics [33]. It includes tip and hub loss corrections and a Beddoes-Leishman dynamic stall model [34]. The aerodynamics are fully coupled to the motion of the blades. There are known limits to this modeling approach when the turbine undergoes large motions [4]. However, because floating wind turbines are designed to minimize motion, it is unclear at what point more advanced aerodynamic modeling methods become necessary. As well, such models are not yet available in easily-coupled and computationally-efficient implementations.

FAST’s hydrodynamic sub-model, HydroDyn, treats the platform as a rigid body and models fluid-structure interaction with a combination of linear hydrodynamics (i.e. the Cummins equation [35]) and viscous drag coefficients. FAST v7 features a quasi-static mooring line model; the mooring line profiles are solved for at each time step assuming that each cable is in static equilibrium in still water, thereby neglecting cable inertia and hydrodynamic damping [31].

In terms of real-time performance for use in hybrid modeling, the aero-elastic portion of FAST that would be required can be computationally-efficient enough to meet 1:50-scale time depending on computer capabilities. The computation time is constrained by the need for a small time step size (typically 12.5 ms) to represent the rotor and tower elasticity without instability. However, for cases where the turbine is assumed rigid (as discussed in the following chapter), having the structural degrees of freedom disabled allows a larger time step size (e.g. 30

ms) which ensures the simulation can meet even 1:100-scale time requirements on older computers. This assumes a coupling interval longer than the mentioned time step sizes. For use with control systems requiring a significantly higher communication rate, even faster models could be needed. In that case, reduced models such as the turbine portion of the OC3-Hywind model developed by Sandner et al. [36], which runs at 100 times real-time when simulating the entire floating turbine, could be used.

I made a number of modifications to the FAST program for use in this work. I integrated additions written by Andrew Goupee that allow custom damping and drag forces on the platform and higher-order blade- and tower-bending mode shapes to better capture model test dynamics. I also created modifications that allow interfacing with separate mooring line models, inclusion of externally-calculated wave excitation loads, inclusion of additional forces acting on the turbine, and arbitrary control of the platform motions during simulation. This last capability is important because it allows for simulation of the effects of an imperfect coupling between different parts of the simulation, such as might exist in a real hybrid model. This is described more in Chapter 3. The same capability also provides the mechanism for the wind turbine simulation to be driven in response to measured physical platform motions, as is required in a hybrid model.

Figure 2.1 shows the coordinate system I used when interfacing with the FAST wind turbine model. The platform position is specified relative to a reference point defined as the intersection of the tower centerline with the mean water line. The x, y, and z axes describe the displacements of the reference point in surge, sway, and heave, respectively, from its equilibrium position (point O_p). I describe the orientation of the platform using three Euler angles acting about the platform

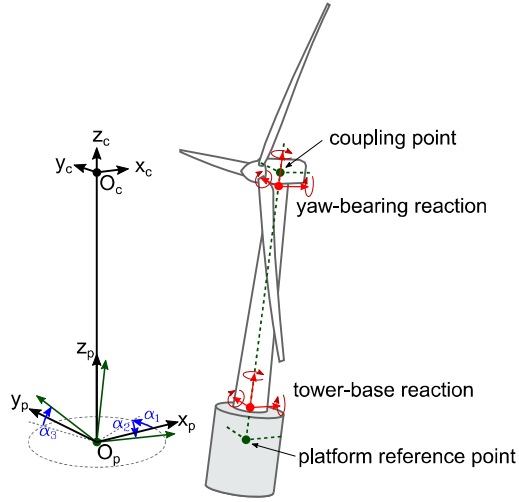


Figure 2.1: Coordinate system and Euler angles

reference point. These are illustrated about the origin as angles $\alpha_1, \alpha_2, \alpha_3$. The order is yaw-pitch-roll, as indicated by the subscript numbering.

Figure 2.1 also shows the two locations from which forces calculated by FAST are accessed in coupled model work described in later chapters. Tower-base reaction forces account for the aero-elastic loads transmitted from the entire turbine to the platform. Yaw-bearing reaction forces account for the aerodynamic and structural loads from the rotor and nacelle transmitted to the top of the tower. Importantly, if structural deflections are disabled and the mass of the turbine is set to zero, the yaw-bearing reaction forces represent only the aerodynamic loading on the turbine. In the work of the following chapters, I rely on these two sets of reaction forces and the motions of the platform reference point when interfacing with FAST. I use coordinate transformations to translate forces and motions between these points and the desired coupling point on the turbine, taking care that structural DOFs and masses are disabled when appropriate.

To verify the approach of coupling with the wind turbine portion of FAST, I made a comparison of normal- and hybrid-coupled FAST simulations. First, I ran a

normal FAST simulation of the DeepCwind semisubmersible in irregular waves and turbulent winds. Then, I took the platform motions from those results and used them as inputs to a simulation using the hybrid-coupling modified version of FAST operating under the same wind conditions. The deflections and loads in the turbine were identical between simulations, indicating that the hybrid coupling approach with FAST was correct under these conditions.

2.2 Mooring Dynamics (MoorDyn) Model Development

This section describes the creation and validation of a new lumped-mass mooring line dynamics model that is now released under the name MoorDyn and used by others. I designed the model with three goals in mind: (1) capturing the dynamic effects that are important to floating wind turbine moorings, (2) prioritizing simplicity to achieve run times suitable for typical medium-fidelity loads analysis (e.g. FAST), and (3) facilitating easy and flexible coupling with floating structure models. Although I began the project for the sake of my own simulation interests and the requirements of a course project, it became apparent that the mooring model could grow into a tool useful to others as well as a component of mooring-focused hybrid modeling.

2.2.1 Mooring Modeling Background

Mooring modeling plays an important role in predicting the global response (or platform motion) and mooring line loads of floating wind turbines and other offshore structures. Since mooring systems are sized based on the extreme and fatigue loadings expected over their lifetime, accurate prediction of these loads is important. This is especially true for offshore renewable energy devices, where

cost-of-energy goals encourage low safety factors and dynamic loadings are large due to the harvesting of kinetic energy.

Quasi-static mooring models, which solve for the continuous mooring line profile and tension using a set of analytical equations based on the assumption that the line is in static equilibrium, have long been used for mooring analysis [37]. This type of model is computationally efficient, easy to work with, and available in open-source implementations (e.g. [38]). However, quasi-static models neglect hydrodynamic and inertial forces on the line. For structures that move significantly in the water, as renewable energy devices tend to do, these neglected factors can be important.

To accurately predict the loads on the mooring lines, a model that incorporates mooring line *dynamics* is usually required. Most dynamic mooring models use a lumped-mass approach to discretize the cable behavior. These discretize the governing equations in space, leaving continuous time derivatives to be solved by an external integration routine to move the model forward through time. However, some models use a finite-difference method, which discretizes the governing equations in both space and time, making the time-stepping approach inherent to the formulation. Walton and Polacheck lay the groundwork for discretized mooring line modeling with a two-dimensional finite-difference model assuming rigid cable segments connected by joints without bending stiffness [39]. The model accounted for hydrodynamic drag and added mass forces applied uniformly over each segment. Results suggested that dynamics were important to the mooring loads. Khan and Ansari demonstrated a lumped-mass approach in three dimensions [40]. As in the previous case, the cable segments were assumed rigid and massless and subject to hydrodynamic forces while the masses are concentrated at the node points. Huang developed a three-dimensional finite-difference model that

incorporated axial elasticity of the cable, and demonstrated its capability by simulating a subsea unit being towed by a maneuvering vessel [41]. More recently, Palm et al. developed and validated a lumped-mass model using a discontinuous Galerkin method with the aim of better modeling snap loadings than conventional discretization approaches [42]. Some lumped-mass models also incorporate discrete handling of bending stiffness at the node points.

Lumped-mass mooring models have also been extended to incorporate bending and torsional elasticity of the cable segments themselves, using the finite-element method (e.g. [43, 44, 45]). Buckham developed an improved finite-element model that approximates the cable profile using a cubic spline fit through the node points, giving the model sufficient fidelity to predict the dynamics of low-tension cables undergoing intricate deformations [46]. These high-fidelity features make finite-element models good at accurately predicting mooring line behavior over a wide range of conditions. This can incur a computational cost, however, making such models less suited for some applications such as modeling inside of an optimization process (e.g. [47]).

A number of recent studies have shown the importance of using dynamic models for accurately predicting floating wind turbine mooring line loads. This accuracy is important for designing a mooring system to withstand extreme and fatigue loads over its service life, which is crucial to a floating offshore wind turbine's safety. Kallesoe and Hansen compared coupled simulation results of a spar floating wind turbine with two different mooring models [48], finding that a dynamic finite-element mooring model predicted lower tower loads but similar blade loads compared to a quasi-static model in normal operating conditions. Matha et al. made a similar comparison using the OC3-Hywind design and a multi-body mooring line model, but with more focus on the platform and mooring response

[49]. They observed that the dynamic model predicted reduced platform motions and much larger mooring line fatigue loads than a quasi-static model. Masciola et al. compared the response of the OC4-DeepCwind semisubmersible design in coupled simulations using FAST and the lumped-mass mooring model OrcaFlex, as well as the default quasi-static mooring model, against 1:50-scale test data [50]. They found platform motions were influenced by mooring dynamics only in extreme sea states but that mooring dynamics are important to prediction of mooring line tensions in all load cases.

In earlier work, I compared the quasi-static mooring line model built into FAST with the finite-element mooring simulator ProteusDS after coupling it with FAST [32]. Comparing coupled simulation results across three designs and a variety of load cases, I came to conclusions consistent with the aforementioned studies.

Mooring dynamics have an influence on platform motions when those motions are large, and mooring dynamics are always important to the prediction of mooring line loads. As such, mooring dynamics can be accurately analyzed separately for platforms with small responses in mild conditions. For platforms with large responses or any platform in severe conditions, the mooring dynamics should be included in the coupled analysis. This speaks to the importance of making a mooring line model easy to couple with other simulation tools.

A number of dynamic mooring line models beyond those already mentioned have also been applied to floating wind turbine simulation (e.g. [51, 52, 53]). One reason that the use of dynamic mooring models is a recent development for floating wind turbine analysis is that, unlike quasi-static models, implementations of dynamic mooring models have in the past only been available commercially; this closed-source nature has meant they are not always easily integrable into coupled floating wind turbine simulations. A computationally-efficient dynamic mooring

model implementation that is open source and designed to link with existing floating offshore wind turbine simulation tools would make dynamic mooring modeling more accessible to the floating wind turbine research community.

In my earlier work with ProteusDS, a sensitivity study indicated that bending and torsional elasticity were of negligible importance to the mooring line tension responses for the barge, spar, and TLP platforms that I simulated, regardless of load case. The results were the same whether the model used the significant bending stiffness of a wire rope or the non-existent bending stiffness of a chain. This suggested that if a dynamic mooring line model were to be implemented without accounting for bending and torsional elasticity, it could produce adequate results for these types of designs at less computational cost than typical mooring models which account for these factors. Such a model would have application to offshore renewable energy devices and provide a more computationally-efficient means of accounting for mooring line dynamics in the design process.

2.2.2 Lumped-Mass Model Formulation

I adopted a lumped-mass approach to discretize the cable dynamics over the length of the mooring line. In this approach, illustrated in Figure 2.2, the cable is divided into N evenly-sized line segments connecting $N + 1$ node points. The indexing starts at the anchor, with the anchor node given a value of 0 and the cable segment between nodes 0 and 1 given an index of 1/2.

The right-handed inertial reference frame is defined with the z axis being measured positive up from the water plane. The location of each node point i is defined by the vector \mathbf{r}_i which contains the x , y , and z coordinates of the node position. Each segment $i + \frac{1}{2}$ of a cable has identical properties of unstretched

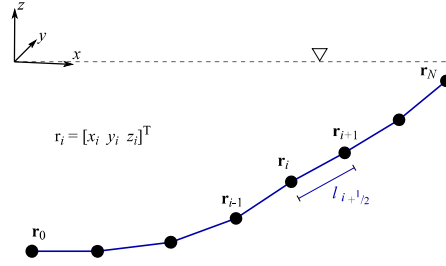


Figure 2.2: Mooring line discretization and indexing.

length (l), volume-equivalent diameter (d), density (ρ), Young's modulus (E), and internal damping coefficient (C_{int}).

The cable model combines internal axial stiffness and damping forces with weight and buoyancy forces, hydrodynamic forces from Morison's equation, and forces from contact with the seabed. These forces are illustrated as vectors in Figure 2.3. The internal stiffness and damping forces in cable segment $i + \frac{1}{2}$ are represented by $\mathbf{T}_{i+\frac{1}{2}}$ and $\mathbf{C}_{i+\frac{1}{2}}$, respectively. The cable weight lumped at each node i is represented by \mathbf{W}_i .

I chose to calculate hydrodynamic loads directly at the node points rather than the more common approach of calculating them at the segment midpoints and then distributing to the node points [39, 40]. In theory, calculating the drag at the nodes provides damping of line motions in all cases, whereas calculating drag at the segment centers cannot provide damping for motions in which the segment centers do not translate (eg. cable vibrations having a wavelength of twice the segment length). I approximate the cable tangent direction at each node point (illustrated by the dotted lines in Figure 2.3) as the average of the tangent directions of the two adjacent cable elements. This tangent direction is necessary for calculating the hydrodynamic forces. Transverse drag and added mass are calculated using Morison's equation [54]. Axial drag and added mass, particularly relevant for

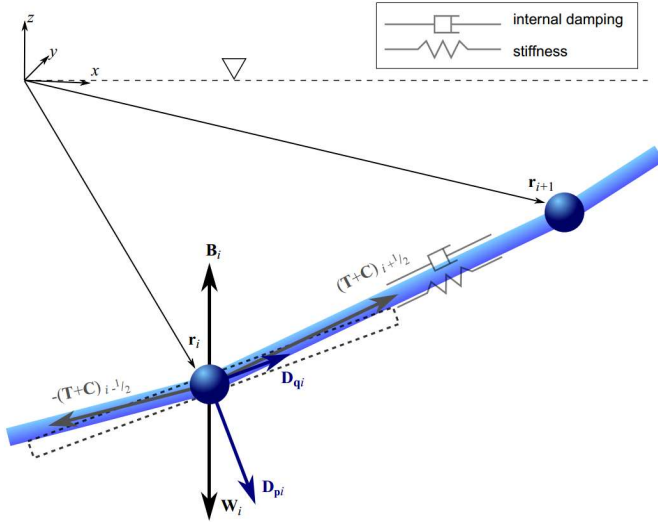


Figure 2.3: Internal and external cable forces.

chain moorings, are calculated in a similar way. The following subsections describe how I included the internal and external forces in the discretization.

2.2.2.1 Internal Forces

The internal forces in the model are axial stiffness, axial damping, and weight. Buoyancy is applied together with weight for convenience.

The net buoyancy of each segment $i + \frac{1}{2}$ is

$$W_{i+\frac{1}{2}} = \frac{\pi}{4} d^2 l (\rho_w - \rho) g, \quad (2.2)$$

where ρ_w is the water density and g is the magnitude of acceleration due to gravity. This force is divided evenly among the two connecting nodes, giving the net buoyancy or weight at node i in vector form as

$$\mathbf{W}_i = \frac{1}{2} (W_{i+\frac{1}{2}} + W_{i-\frac{1}{2}}) \hat{\mathbf{e}}_z \quad (2.3)$$

where $\hat{\mathbf{e}}_z$ is a unit vector in the positive z direction.

The tension in cable segment $i + \frac{1}{2}$ is

$$T_{i+\frac{1}{2}} = E \frac{\pi}{4} d^2 \epsilon_{i+\frac{1}{2}} = E \frac{\pi}{4} d^2 \left(\frac{\|\mathbf{r}_{i+1} - \mathbf{r}_i\|}{l} - 1 \right), \quad (2.4)$$

where $\epsilon_{i+\frac{1}{2}}$ is the axial strain and the double vertical lines ($\|\cdot\|$) denote the L^2 norm or magnitude of the vector they contain. Multiplying (2.4) by a unit vector pointing along the line segment gives a vector representation of the tension force:

$$\begin{aligned} \mathbf{T}_{i+\frac{1}{2}} &= E \frac{\pi}{4} d^2 \left(\frac{\|\mathbf{r}_{i+1} - \mathbf{r}_i\|}{l} - 1 \right) \left(\frac{\mathbf{r}_{i+1} - \mathbf{r}_i}{\|\mathbf{r}_{i+1} - \mathbf{r}_i\|} \right) \\ &= E \frac{\pi}{4} d^2 \left(\frac{1}{l} - \frac{1}{\|\mathbf{r}_{i+1} - \mathbf{r}_i\|} \right) (\mathbf{r}_{i+1} - \mathbf{r}_i). \end{aligned} \quad (2.5)$$

I define this tension force's direction as pointing from node i to node $i + 1$, indicating the force on node i . The negative of this force vector is the force on node $i + 1$. A tension force is applied only if there is positive tension in the line (i.e. if $\|\mathbf{r}_{i+1} - \mathbf{r}_i\| > l$). Otherwise, the tension force is set to zero; no compression force is modeled.

To provide necessary numerical damping, I also apply an internal damping force:

$$\mathbf{C}_{i+\frac{1}{2}} = C_{int} \frac{\pi}{4} d^2 \dot{\epsilon}_{i+\frac{1}{2}} \left(\frac{\mathbf{r}_{i+1} - \mathbf{r}_i}{\|\mathbf{r}_{i+1} - \mathbf{r}_i\|} \right), \quad (2.6)$$

where the internal damping coefficient, C_{int} , has units of stress per strain rate (Pa-s) and the strain rate of the segment, $\dot{\epsilon}_{i+\frac{1}{2}}$, is calculated as

$$\begin{aligned} \dot{\epsilon}_{i+\frac{1}{2}} &= \frac{\partial \epsilon}{\partial t} = \frac{\partial}{\partial t} \left(\frac{\|\mathbf{r}_{i+1} - \mathbf{r}_i\|}{l} \right) \\ &= \frac{1}{2l} \frac{1}{\|\mathbf{r}_{i+1} - \mathbf{r}_i\|} \frac{\partial}{\partial t} [(x_{i+1} - x_i)^2 + (y_{i+1} - y_i)^2 + (z_{i+1} - z_i)^2] \\ &= \frac{1}{l} \frac{1}{\|\mathbf{r}_{i+1} - \mathbf{r}_i\|} [(x_{i+1} - x_i)(\dot{x}_{i+1} - \dot{x}_i) + (y_{i+1} - y_i)(\dot{y}_{i+1} - \dot{y}_i) + (z_{i+1} - z_i)(\dot{z}_{i+1} - \dot{z}_i)]. \end{aligned} \quad (2.7)$$

2.2.2.2 External Forces

To avoid the complexities of tracking wave kinematics, I neglect the effect of waves in the hydrodynamic analysis. Section 2.2.4.5 provides a justification for this approximation. The first step in applying hydrodynamic drag and added mass models is to resolve the relative fluid velocities and accelerations over the node points into transverse and tangential components. I approximate the tangent direction, $\hat{\mathbf{q}}_i$, at each node as the direction of a line passing between the two adjacent node points:

$$\hat{\mathbf{q}}_i = \frac{\mathbf{r}_{i+1} - \mathbf{r}_{i-1}}{\|\mathbf{r}_{i+1} - \mathbf{r}_{i-1}\|}. \quad (2.8)$$

The transverse direction, denoted by the subscript \mathbf{p} in later equations, is defined as perpendicular to $\hat{\mathbf{q}}_i$ and aligned with the direction of the relative water velocity over the cable. In still water, the relative water velocity over the cable node is equal to $-\dot{\mathbf{r}}_i$. The tangential component of this flow is given by the projection vector of $-\dot{\mathbf{r}}_i$ onto $\hat{\mathbf{q}}_i$, which is $(-\dot{\mathbf{r}}_i \cdot \hat{\mathbf{q}}_i)\hat{\mathbf{q}}_i$. The transverse component of the flow is then $(\dot{\mathbf{r}}_i \cdot \hat{\mathbf{q}}_i)\hat{\mathbf{q}}_i - \dot{\mathbf{r}}_i$.

I calculate the transverse hydrodynamic loads on the cable using Morison's equation [54], treating the cable as a slender cylindrical structure. Using the velocity components just described, the transverse drag force applied to node i is

$$\mathbf{D}_{\mathbf{p}_i} = \frac{1}{2}\rho_w C_{dn} d l \|(\dot{\mathbf{r}}_i \cdot \hat{\mathbf{q}}_i)\hat{\mathbf{q}}_i - \dot{\mathbf{r}}_i\|[(\dot{\mathbf{r}}_i \cdot \hat{\mathbf{q}}_i)\hat{\mathbf{q}}_i - \dot{\mathbf{r}}_i], \quad (2.9)$$

where C_{dn} is the transverse drag coefficient. Similarly, a tangential drag force to account for skin friction and form drag (eg. for chains) can be calculated as

$$\mathbf{D}_{\mathbf{q}_i} = \frac{1}{2}\rho_w C_{dt} \pi d l \|(-\dot{\mathbf{r}}_i \cdot \hat{\mathbf{q}}_i)\hat{\mathbf{q}}_i\|(-\dot{\mathbf{r}}_i \cdot \hat{\mathbf{q}}_i)\hat{\mathbf{q}}_i, \quad (2.10)$$

where C_{dt} is the tangential drag coefficient.

The added mass force in the transverse direction is

$$\mathbf{a}_{\mathbf{p}_i} \ddot{\mathbf{r}}_i = \rho_w C_{an} \frac{\pi}{4} d^2 l [(\ddot{\mathbf{r}}_i \cdot \hat{\mathbf{q}}_i) \hat{\mathbf{q}}_i - \ddot{\mathbf{r}}_i], \quad (2.11)$$

where C_{an} is the added mass coefficient in the transverse direction and $\mathbf{a}_{\mathbf{p}_i}$ is the corresponding transverse added mass matrix. Similarly, a tangential added mass force, applicable for chains or other moorings that have surface area facing the tangent direction, can be calculated as

$$\mathbf{a}_{\mathbf{q}_i} \ddot{\mathbf{r}}_i = \rho_w C_{at} \frac{\pi}{4} d^2 l (-\ddot{\mathbf{r}}_i \cdot \hat{\mathbf{q}}_i) \hat{\mathbf{q}}_i, \quad (2.12)$$

where C_{at} is the tangential added mass coefficient and $\mathbf{a}_{\mathbf{q}_i}$ is the added mass matrix for this tangential component. Since I neglect wave kinematics, Froude-Krylov forces are not modeled.

To handle interactions with the seabed, I added a linear spring-damper model to represent the vertical reaction forces whenever a cable node touches the seabed. A stiffness coefficient, k_b , represents the stiffness per unit area of the seabed. A damping coefficient, c_b , represents the viscous damping per unit area. The model is only active when a node contacts the seabed (i.e. when $z_i \leq z_{bot}$). When that condition is true, the force due to the interaction is modeled as

$$\mathbf{B}_i = dl[(z_{bot} - z_i)k_b - \dot{z}_i c_b] \hat{\mathbf{e}}_z. \quad (2.13)$$

I did not account for horizontal friction from contact with the seabed in the model. This, along with modeling of bathymetry details, could be added if representation of more realistic seabed interaction was needed.

2.2.2.3 Mass and Integration

I discretize the mass of the cable into point masses at each node by assigning each node half the mass of the two adjacent cable segments. The 3×3 mass matrix for

node i can be expressed as

$$\mathbf{m}_i = \frac{\pi}{4} d^2 l \rho \mathbf{I}, \quad (2.14)$$

where \mathbf{I} is the identity matrix.

The added mass, which is proportional to $\ddot{\mathbf{r}}_i$, also needs to be included in the mass matrix. Rearranging (2.11) and (2.12) to factor out $\ddot{\mathbf{r}}_i$ and reversing signs to move the terms to the left-hand side of an equation $ma = f$ gives the added mass matrix for node i :

$$\mathbf{a}_i = \mathbf{a}_{\mathbf{p}_i} + \mathbf{a}_{\mathbf{q}_i} = \rho_w \frac{\pi}{4} d^2 l [C_{an}(\mathbf{I} - \hat{\mathbf{q}}_i \hat{\mathbf{q}}_i^\top) + C_{at}(\hat{\mathbf{q}}_i \hat{\mathbf{q}}_i^\top)]. \quad (2.15)$$

The complete equation of motion for each node i along the length of a line is:

$$\underbrace{[\mathbf{m}_i + \mathbf{a}_i]}_{\text{mass and added mass}} \ddot{\mathbf{r}}_i = \underbrace{\mathbf{T}_{i+\frac{1}{2}} - \mathbf{T}_{i-\frac{1}{2}} + \mathbf{C}_{i+\frac{1}{2}} - \mathbf{C}_{i-\frac{1}{2}}}_{\text{internal stiffness and damping}} + \underbrace{\mathbf{W}_i + \mathbf{B}_i}_{\text{weight and contact}} + \underbrace{\mathbf{D}_{\mathbf{p}_i} + \mathbf{D}_{\mathbf{q}_i}}_{\text{drag}} \quad (2.16)$$

This equation can also be adapted for “connection” nodes – nodes at the ends of lines. These nodes support connections to multiple lines of similar or dissimilar properties, as well as kinematic constraints corresponding to a fixed anchor endpoint or a moving fairlead endpoint. Additional mass, buoyancy, and hydrodynamic terms can be added to represent point properties as appropriate for clump weights and floats. In this way, the formulation of the mooring model is adaptable to mooring systems with different sets of line properties, arbitrary line interconnections, and clump weights or floats. The second-order system of ordinary differential equations represented in (2.16) can be easily reduced to a system of first-order differential equations. These are then solved using a constant-time-step second-order Runge-Kutta (RK2) integration algorithm.

A detailed validation of this modeling approach for single mooring lines is given in Section 2.2.4 and some preliminary validation for a more complicated multi-segmented mooring system is given in Section 2.2.5.

2.2.3 Coupling with Other Codes

Being able to couple easily with other modeling tools was one of my goals when developing the mooring model. Being written in C++, it can be compiled on Windows, Mac OS, or Linux into a dynamically-linked library. This library (termed a DLL on Windows) can then be called using standard methods by many types of software.

I equipped the model with straightforward, externally-callable functions that perform simulation initialization, time stepping in reaction to motions passed by an external program (e.g. a floating platform simulator), and simulation termination. With these functions, the model can be tested by simple “driver” programs in C++, Python, and Matlab that prescribed fairlead motions to the mooring system. The next step, to allow the model to contribute to coupled floating wind turbine simulations, was to create a coupling with FAST.

The coupling with FAST v7, which I used in the first validation efforts, serves as a good example of how coupling with the model works in general. In keeping with the module naming style used in FAST, I named the lumped-mass mooring model MoorDyn. I created a loose-coupling arrangement, as defined in [55]. For a typical floating wind turbine simulation, FAST runs with the widely-used time step of 12.5 ms and MoorDyn with a shorter time step of 1.25 ms to ensure stability of the RK2 integrator. At the start of each FAST time step, FAST transmits the platform position and velocity to MoorDyn. MoorDyn then calculates the fairlead kinematics and solves for the line dynamics over the duration of the FAST time

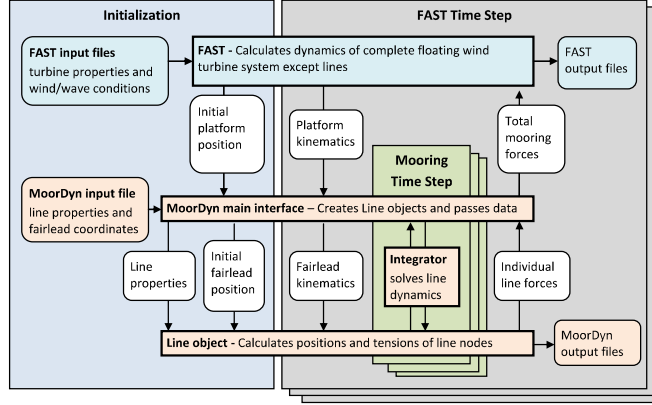


Figure 2.4: Overview of lumped-mass mooring model coupling with FAST v7

step (entailing ten mooring time steps). Finally, the resulting mooring forces are transmitted back to FAST to be used in FAST’s dynamics solver. This process is diagrammed in Figure 2.4.

I created a number of changes in the FAST v7 source code to accommodate a new subroutine to interact with the MoorDyn DLL in place of the default quasi-static mooring subroutine. With these changes, FAST can be run with MoorDyn by simply switching the mooring line options flag in the platform input file and adding a new input file describing the mooring line properties. The initial conditions for the mooring system, in terms of node positions, are set using the quasi-static mooring line model of FAST. This coupling with FAST v7 is validated in the comparison presented in Section 2.2.4.7.

A collaboration with researchers at Politecnico di Torino in Italy lead to a method for coupling MoorDyn in Simulink simulations. We developed this method to provide mooring modeling of a wave energy converter device under development there. A brief overview of validation efforts with test data from this device is given in Section 2.2.5. This Simulink coupling provided the starting point for making a

coupling between MoorDyn and WEC-Sim, an open-source Simulink-based wave energy converter simulator developed by NREL and Sandia National Labs. This collaboration included a validation of MoorDyn with experimental data of a floating buoy and verification against Orca-Flex simulations [56].

To contribute to the current version of FAST, I rewrote MoorDyn in FORTRAN and restructured it to follow the FAST Modularization Framework [55]. While the underlying mooring model is the same, increased compartmentalization in the time-integration parts of this version allow for it to be used in tight coupling schemes, where the dynamics of MoorDyn and any models it is coupled to are solved and integrated forward in time together. MoorDyn as coupled in FAST v8 has been verified against Orca-Flex and validated against UMaine’s 2013 DeepCwind semisubmersible model tests [57] and UMaine’s 2011 spar model tests [58] (both conducted at MARIN).

2.2.4 Validation with DeepCwind Semisubmersible Test Data

To validate MoorDyn, I conducted a comparison study with test data from UMaine’s 2011 tests of the DeepCwind semisubmersible floating wind turbine at MARIN. This is the same design that is featured in the basin testing at the end of this thesis. The complete published version of this validation study is available in [29]. The following subsections describe the tests being modeled, characterization of the mooring system in these tests, and the simulation results produced by MoorDyn in comparison to the experimental data. All quantities describing these experiments and the comparison with simulation results are at full scale.

2.2.4.1 The DeepCwind Semisubmersible Tests

The DeepCwind semisubmersible is a buoyancy-stabilized floating wind turbine design developed at UMaine with input from Technip that has been widely studied through both experiments and simulations. The design features a 5 MW horizontal-axis wind turbine atop a three-column semisubmersible platform with a smaller fourth central column. The outer columns feature heave plates, and station keeping is provided by three slack catenary chain moorings.

The DeepCwind semisubmersible design has had several incarnations, including a 1:50-scale model tested in 2011 [59], a refined 1:50-scale model tested in 2013 [60], and a set of full-scale specifications used for numerical modeling in the Offshore Code Comparison Collaboration Continuation (OC4) project [61]. This last version is referred to as the OC4-DeepCwind semisubmersible and has been analyzed widely [62]. The version I considered in all my work is the original 1:50-scale model that was tested in 2011. This incarnation has many similarities to the OC4-DeepCwind specifications; the main difference is that the scale model features a turbine that is modeled after, but slightly different from, the NREL 5 MW reference turbine used in the OC4 project. The 2011 DeepCwind semisubmersible model is shown in Figure 1.2.

Table 2.1 lists the sea states from that test campaign that I used in the comparison study, characterized by wave height (H) and period (T) for regular waves and significant wave height (H_s) and peak spectral period (T_p) for irregular waves. The table also provides the calculated mean viscous drift force ($F_{visc.}$) described later in Section 2.2.4.3.

A number of earlier studies looked at developing and validating numerical models from the test results, including the wind turbine performance [19] and the platform

Table 2.1: Sea states considered

Sea state	H or H_s (m)	T or T_p (s)	$F_{visc.}$ (N)
regular wave 1	1.92	7.5	6,884
regular wave 2	7.578	12.1	162,790
regular wave 3	7.136	14.3	97,378
regular wave 4	7.574	20	61,467
regular wave 5	10.304	12.1	409,244
regular wave 6	10.74	14.3	331,979
regular wave 7	11.122	20	194,632
operational 1	1.916	7.5	6,841
operational 2	7.006	12.1	128,640
design	10.39	14.3	300,569

hydrodynamics [63]. More details about those aspects of the design and their modeling is available in those references.

2.2.4.2 1:50-Scale Wind Turbine Model

I used a FAST wind turbine model created by Andrew Goupee to match the physical and aerodynamic characteristics from the 2011 test campaign, as detailed in [63]. The upwind, three-bladed wind turbine is similar to the NREL 5 MW reference turbine [64] used in the OC4-DeepCwind design, having an identical rotor diameter (126 m) and hub height (90 m), but the 1:50-scale model has an increased nacelle mass due to instrumentation requirements. Table 2.2 summarizes the gross properties of the wind turbine and further details are available in [17]. Additional deviations from the NREL reference design are that the blade pitch angle was set to 6.4 degrees in the operational wind cases and increased wind speeds and slightly elevated rotor RPMs were used. As described by [17], these changes were necessary in order to reproduce full-scale thrust characteristics in the low-Reynolds number conditions of the Froude-scaled test environment.

In terms of structural properties, the rotor blades used in the tests were very rigid compared to the full scale design; accordingly, rotor blade bending degrees of freedom are disabled in the simulations. Deflections of the tower were not negligible and finite-element analysis of the tower suggested the use of 9th-order mode shapes for the tower bending modes. Accordingly, I used these higher-order modal characteristics, described in [63], in the modified version of FAST.

Table 2.2: Properties of the DeepCwind wind turbine

rotor diameter	126 m
hub height above SWL	90 m
overhang	10.58 m
shaft tilt	0 deg
precone	0 deg
total tower-top mass	397,160 kg

2.2.4.3 Semisubmersible Platform Model

The DeepCwind semisubmersible platform consists of four cylinders with a draft of 20 m. The central cylinder has a diameter of 6.5 m and supports the wind turbine. The outer three cylinders have a diameter of 12 m except for the bottom 6 m portion, which has an enlarged diameter of 24 m, serving as a heave plate. The outer cylinders are spaced at a distance of 40.87 m from the platform centerline. The cylinders are connected by 1.6 m diameter cross bracing. The mass characteristics of the platform, described about its center of mass (CM), are provided in Table 2.3. Further details about the platform are available in [61].

In previous model validation work, Coulling et al. [65, 63] modeled the platform hydrodynamics by supplementing FAST's default linear hydrodynamics approach with quadratic damping coefficients in each of the six platform degrees of freedom and later included the effects of second-order difference-frequency forces using Newman's approximation. I built on that work, using the same quadratic damping coefficients (given in Table 2.4) but extending the hydrodynamics to include full second-order wave excitation forces and a viscous mean drift force in surge.

I calculated sum-frequency and difference-frequency second-order wave excitation loads following the method of [66]. An additional source of mean drift is noticeable in the test results, which I sought to capture in the coupled mooring validation

Table 2.3: DeepCwind semisubmersible platform properties

draft	20 m
airgap	10 m
ballasted mass	13,444,000 kg
displacement	13,987 m ³
depth of CM	14.4 m
roll inertia about CM	8.011E9 kg-m ²
pitch inertia about CM	8.011E9 kg-m ²
yaw inertia about CM	1.391E10 kg-m ²

Table 2.4: DeepCwind semisubmersible platform quadratic drag coefficients

DOF	Coefficient
surge	1.25E6 N·s ² /m ²
sway	9.50E5 N·s ² /m ²
heave	3.88E6 N·s ² /m ²
roll	3.35E10 N·s ² ·m
pitch	3.35E10 N·s ² ·m
yaw	1.15E10 N·s ² ·m

simulations by calculating the viscous mean drift forces. I calculated the viscous contribution to mean drift force in surge following DNV-RP-C205 [67]. For cylinders in regular waves, the force is proportional to wavenumber (k), diameter (D), and the cube of wave amplitude (A):

$$F_{visc.} = \frac{2}{3\pi} \rho g k C_d D A^3. \quad (2.17)$$

I applied the equation for each of the four columns of the platform. To be comparable with the experimental results, I set the drag coefficient to 1.2 according to the coefficients given in [67] for the model-scale Reynolds number. For irregular waves, to obtain a crude mean drift force, I used (2.17) with half the significant wave height substituted for A and the peak period used to calculate k . Table 2.1 shows the viscous drift force calculated for each sea state.

2.2.4.4 Mooring System Static Properties

In the 1:50-scale tests in 2011, the semisubmersible was moored by three chains of approximately 835 m length (full scale) to anchor points at a radius of 837.6 m from the platform centerline. The water depth was 200 m. I measured a 100-link length of chain from the tests, including displaced volume, making some adjustments from the properties previously reported in [63]. Table 2.5 gives the resulting properties after scaling to full scale. The properties of the studless chain

Table 2.5: DeepCwind mooring chain properties

Quantity	Symbol	Value
nominal diameter	D	77.9 mm
link straight length	L	286 mm
link curve radius	R	106 mm
links per m		2.38 m^{-1}
linear density	$\rho\pi d^2/4$	116.6 kg/m
displacement per m	$\pi d^2/4$	0.01405 m ²
equivalent diameter	d	133.76 mm

used for testing do not match a commercially-available chain size. The cable diameter, d , discussed in Section 2.2.2 should be considered a volume-equivalent diameter for the mooring chain – the diameter of a cylindrical cable having the same displacement per unit length as the chain.

I used the quasi-static mooring line model from FAST [31] as a baseline for verifying the steady-state performance of MoorDyn. Figure 2.5 shows the fairlead tension and line angle predicted by MoorDyn for different levels of discretization, normalized by the value predicted by the quasi-static model. The unevenness of the tension curve is likely due to the discrete handling of seabed contact, in which the number and position of the touchdown node changes irregularly between different discretization levels.

As the number of segments is increased, the convergence of fairlead tensions and angles predicted by MoorDyn toward the analytical quasi-static values serves as a quasi-static verification of the model. Accordingly, for catenary moorings modeled with sufficient levels of discretization, any significant differences seen between MoorDyn and a quasi-static model can be attributed to dynamic effects. At a discretization level of 20 elements along the line, both the tension and the angle are well within 1% of the quasi-static value. Accordingly, I used 20 elements for each mooring line in the following analyses. At this level of discretization, use of

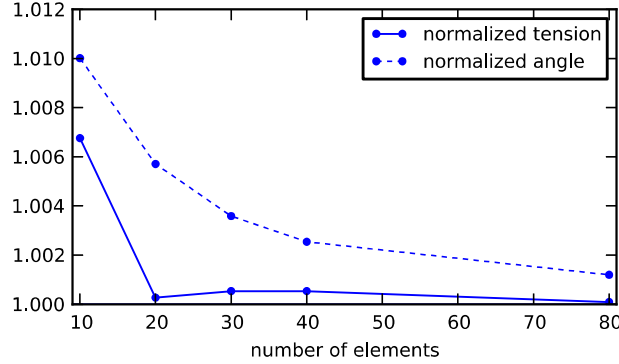


Figure 2.5: Equilibrium fairlead tensions and angles normalized by quasi-static result

Table 2.6: Pretension and tuning of line lengths

Line number	1	2	3
target fairlead tension (kN)	1124	1067	1065
original lengths			
unstretched length (m)	835.35	835.35	835.35
QS fairlead tension (kN)	1043	1043	1043
LM fairlead tension (kN)	1036	1037	1037
Tuned lengths			
unstretched length (m)	833.6	834.8	834.85
QS fairlead tension (kN)	1124	1067	1065
LM fairlead tension (kN)	1124	1070	1068

MoorDyn increased the simulation time by 10-15% compared to a normal FAST v7 simulation with the quasi-static mooring model.

In simulations, I slightly adjusted the unstretched line lengths reported in previous work [63] in order to better match the line pretensions measured in the experiments. These pretensions are not quite equal, hence each line has a different unstretched length, as indicated in Table 2.6. Tension results are shown from both the lumped-mass MoorDyn (LM) and quasi-static (QS) models.

2.2.4.5 Mooring System Hydrodynamic Properties

Since I formulated the mooring model based on cylindrical elements, the drag and added mass coefficients need to be adjusted to account for the use of a chain mooring. To begin with, I selected a transverse drag coefficient of 2.0 in accordance with the recommendations for scale-model chains in DNV-RP-F205 [68]. This value is based on the chain's nominal diameter (the diameter of the bar that composes each chain link). Scaling by the ratio of the nominal diameter to the volume-equivalent diameter ($0.0779/0.13376$) gives the equivalent drag coefficient required by the model. In addition, the chain used in the tests is of a more slender proportion than the standard dimensions the recommended drag coefficients are meant to reflect. Therefore, I scaled the drag coefficient to account for the reduced frontal area per unit length (A_L). The final transverse drag coefficient I provided to the model is

$$C_{dn} = C_d \frac{A_{L,test}}{A_{L,typical}} \frac{D}{d} = 2.0 \left(\frac{0.2296}{0.2470} \right) \left(\frac{0.0779}{0.13376} \right) = 1.08, \quad (2.18)$$

where, for the sake of determining the scaling ratio, I approximated A_L using the frontal area of a chain link oriented normal to the flow:

$$A_L \approx \frac{(2L + 2\pi R)D}{L + 2R - D}. \quad (2.19)$$

The tangential drag coefficient is based on the value of 1.15 recommended for studless chain in DNV-OS-E301 [69]. Scaling for the equivalent diameter formulation of the model and dividing by π gives $C_{dt} = 0.213$. I did not make a correction for the chain shape in this coefficient since the overlap of links makes identifying the proper frontal area for axial drag calculations ambiguous and its bearing on the line tensions is relatively small. I calculated added mass coefficients in both transverse and tangential directions by applying the theoretical coefficient

of 1.0 for cylinders in transverse flow, as given in DNV-RP-C205 [67], to the chain link geometry. This gives $C_{an} = 0.865$ and $C_{at} = 0.269$.

The suitability of the four hydrodynamic coefficients can be seen by comparing the fairlead tensions measured in the model tests with those calculated by MoorDyn when the fairlead is moved according to the test data. Figure 2.6 shows this comparison for the tension of fairlead 1, the upwind fairlead, during a regular wave case. The shaded areas indicate the sensitivity of the fairlead tension to the four different hydrodynamic coefficients. The upper and lower bounds of the shaded regions correspond to $\pm 50\%$ variations of each of the four hydrodynamic coefficients. It can be seen that the simulation (labeled “LM”) closely matches the test data (labeled “test”) and that the fairlead tensions are most sensitive to the transverse drag coefficient.

Figure 2.6 also shows, between 300 s and 320 s, how the inclusion of wave kinematics in the drag calculations affects the fairlead tension. In this case, including wave kinematics increases the tensions on fairlead 1, which is aligned with the wave propagation direction, by just over 3%. The change in tensions on fairleads 2 and 3 is less than 1%. This is a conservative indication since regular wave case 5 can be expected to have the greatest wave particle velocities of all the regular wave cases. Accordingly, I concluded that wave kinematics can be neglected without having a large impact on the results for the mooring system and load cases in this study.

The effect of discretization on the line dynamic response is also worth considering. Figure 2.7 shows that using 20 segments per mooring line gives convergent results. For this level of discretization, I found that an internal damping coefficient of $C_{int} = 100 \text{ MPa}\cdot\text{s}$ reduces high-frequency tension vibrations not seen in the test data without affecting the gross tension amplitudes.

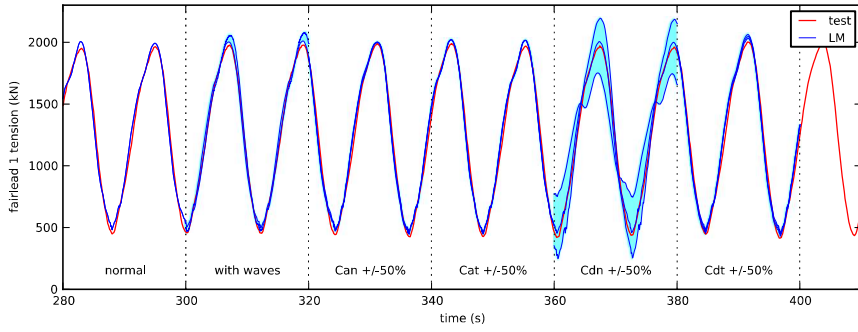


Figure 2.6: Fairlead 1 tensions for regular wave 5 with $\pm 50\%$ variation of hydrodynamic coefficients

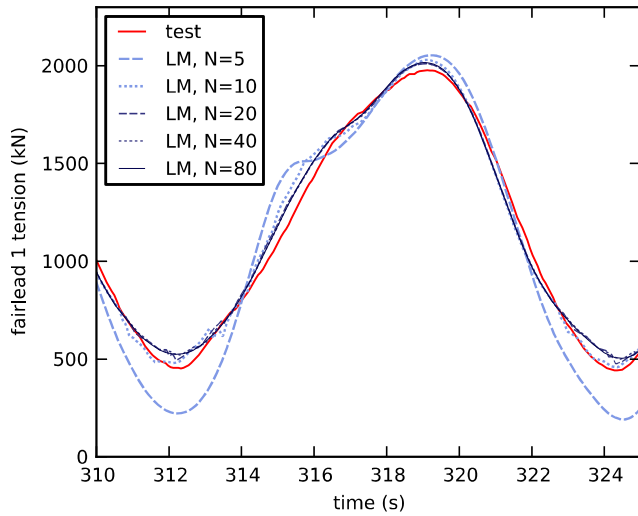


Figure 2.7: Fairlead 1 tensions for regular wave 5 with different numbers of cable segments

For bottom contact modeling, I used a stiffness coefficient of $k_b = 3 \text{ MPa/m}$ and damping coefficient of $c_b = 300 \text{ MPa}\cdot\text{s/m}$. These provided for negligible sinking and bouncing of nodes on the seabed.

2.2.4.6 Uncoupled Mooring Model Validation

The first set of validation results focuses on comparing only the mooring line behavior between the model predictions and the test data. I studied the mooring line behavior in isolation by using the platform motions from the test data to prescribe the fairlead motions in the mooring model. The platform motions in the 2011 tests were measured by an NDI Certus optical motion tracking system using three LEDs on the platform. Noise in the measurements made it necessary to filter the motions inputted to the mooring model to avoid severe and unrealistic line tension fluctuations. I used a fourth-order Butterworth low-pass filter with 0.5 Hz cutoff frequency to strike a balance between rejecting measurement noise and leaving intact the true platform motion signal. Figure 2.8 shows a sample of the platform motions before and after filtering.

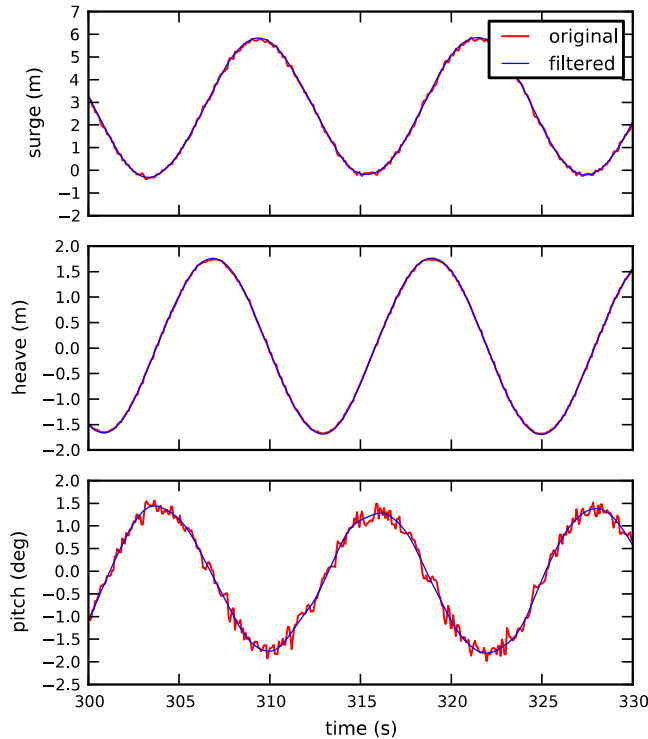


Figure 2.8: Sample of original and filtered platform motions from regular wave 5

For regular wave cases, the mooring line tensions predicted by MoorDyn match the experimental data quite well, in terms of both magnitudes and phases. Figure 2.9 shows a portion of the fairlead tension responses for regular wave 5, comparing those measured in the tests, those predicted by the lumped-mass mooring model, and those predicted by FAST v7's quasi-static mooring model. Good agreement in amplitudes between MoorDyn and the test data is evident, as is the large amplitude underprediction by the quasi-static model. Figure 2.10 shows the corresponding power spectral density (PSD) plots of these fairlead tensions. The large peaks at 0.083 Hz correspond to the wave excitation frequency, and peaks are also visible at multiples of this frequency. Good agreement at the first and second peaks can be observed between MoorDyn and the test data, although the model predicts higher levels of excitation between the peaks. Overprediction by MoorDyn of tensions at three times the wave frequency, also seen as fluctuations in the rising and falling of the tensions in Figure 2.9, is thought to be caused by the discrete handling of bottom contact. When nodes transition on or off the sea floor, the total suspended mooring line weight changes abruptly. This transient appears as a mild tension fluctuation at the fairlead as a result of attenuation from drag as it travels up the mooring line. The quasi-static model undepredicts the excitation across the spectrum.

I calculated response amplitude operators (RAOs) describing the magnitude and phase of the fairlead tension response using sine-wave fits to the tension time series results. Table 2.7 summarizes how the fairlead tension RAOs predicted by the lumped-mass and quasi-static mooring line models compare with the RAOs of the test data across all 7 regular wave cases. Figure 2.11 provides a visual comparison of the RAO magnitudes between the test data and the simulations. Agreement tends to improve with increasing wave amplitude. The level of disagreement ranges

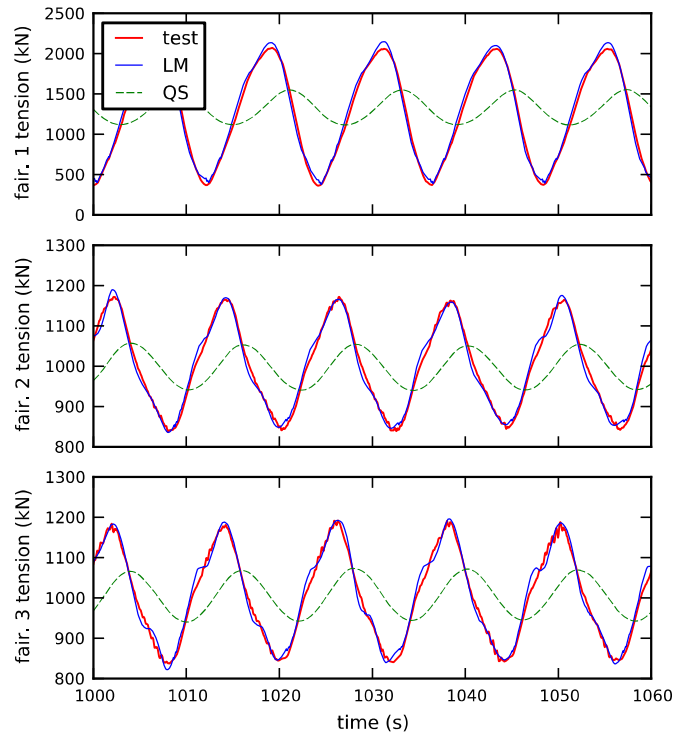


Figure 2.9: Fairlead tensions in regular wave 5

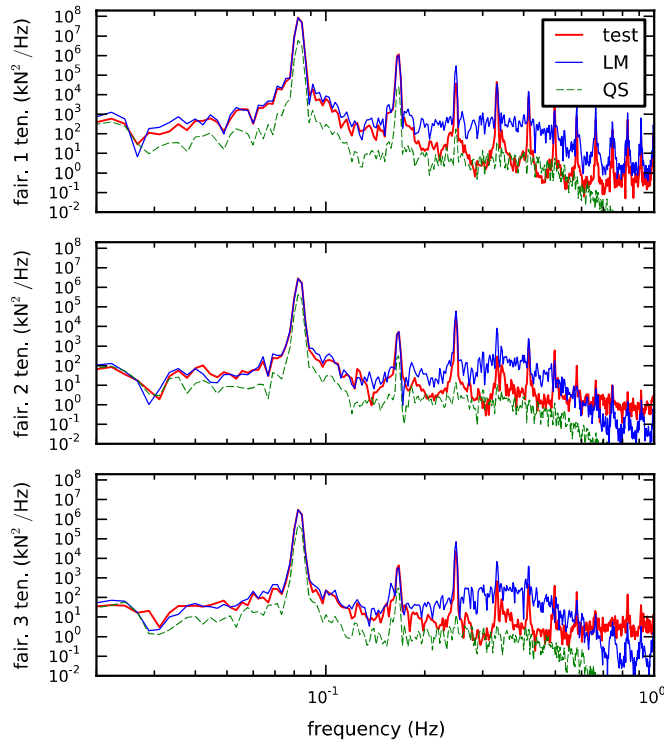


Figure 2.10: Fairlead tension PSDs in regular wave 5

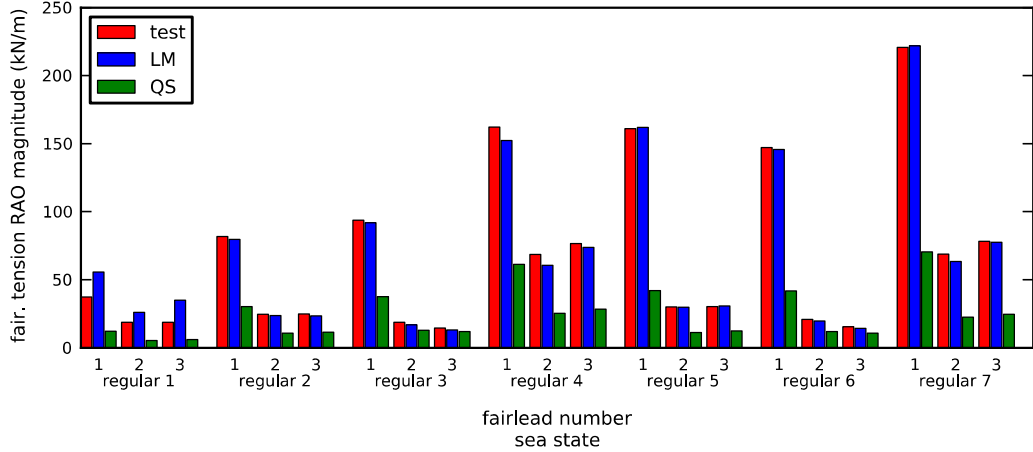


Figure 2.11: Comparison of fairlead tension RAO magnitudes from test data, lumped-mass model, and quasi-static model

from up to 90% tension overprediction and 15° phase error in regular wave 1 to less than 8% tension error and 7° phase error for regular waves 5, 6, and 7. It seems likely that at smaller wave amplitudes, the lower signal-to-noise ratio in the platform motion data causes the measurement noise to have a larger effect on the simulated mooring line tensions. The phase difference compared to the test data is below 10° for MoorDyn in most cases, while it is consistently over 45° for the quasi-static model.

Regular wave 7 provides a good case for studying snap loads since line 1, the upwind mooring, loses tension with every wave. Figure 2.12 shows the fairlead 1 tension time series for this case, comparing the quasi-static and lumped-mass model predictions with the test data. MoorDyn predicts the onset of the slack condition very well, although it lags a bit in the tension recovery. The quasi-static model on the other hand neither matches the tension cycle amplitude nor predicts the slack condition.

To look at the mooring model performance in irregular wave conditions, I prescribed fairlead motions from a test case with the design sea state and dynamic

Table 2.7: Fairlead tension RAO comparison

Wave	Model	Magnitude difference			Phase difference		
		fair. 1	fair. 2	fair. 3	fair. 1	fair. 2	fair. 3
1	LM	50%	39%	88%	-15°	-11°	-10°
1	QS	-67%	-72%	-68%	112°	100°	117°
2	LM	-3%	-4%	-6%	-3°	-5°	-8°
2	QS	-63%	-57%	-54%	90°	69°	72°
3	LM	-2%	-10%	-10%	3°	-15°	-8°
3	QS	-60%	-31%	-18%	81°	56°	55°
4	LM	-6%	-12%	-4%	2°	3°	5°
4	QS	-62%	-63%	-63%	85°	58°	66°
5	LM	1%	0%	1%	-4°	-1°	-3°
5	QS	-74%	-62%	-59%	75°	59°	65°
6	LM	-1%	-6%	-6%	0°	-4°	-6°
6	QS	-72%	-43%	-30%	74°	58°	46°
7	LM	0%	-8%	-1%	-2°	3°	6°
7	QS	-68%	-67%	-69%	76°	53°	60°

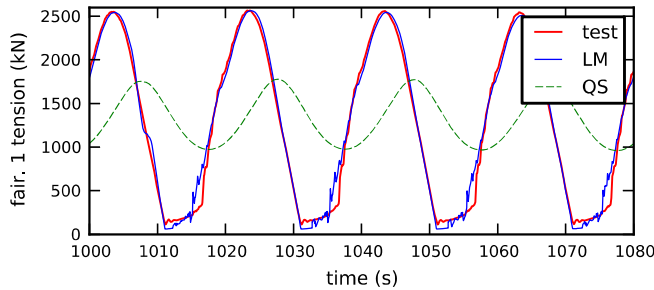


Figure 2.12: Slack line conditions apparent in fairlead 1 tension for regular wave 7

wind. As given in Table 2.1, the design sea state is defined by a 10.5 m, 14.3 s JONSWAP spectrum. The dynamic wind is based on a National Petroleum Directorate (NPD) spectrum [70] with a mean hub-height speed of 19.6 m/s, standard deviation of 2.04 m/s, and wind shear exponent of 0.0912. As explained by Coulling et al. [63], these simulation values were chosen to match the experimental wind field.

Figure 2.13 compares the predicted fairlead tensions with those in the recorded test data. MoorDyn matches the fairlead tensions very well in terms of phase and

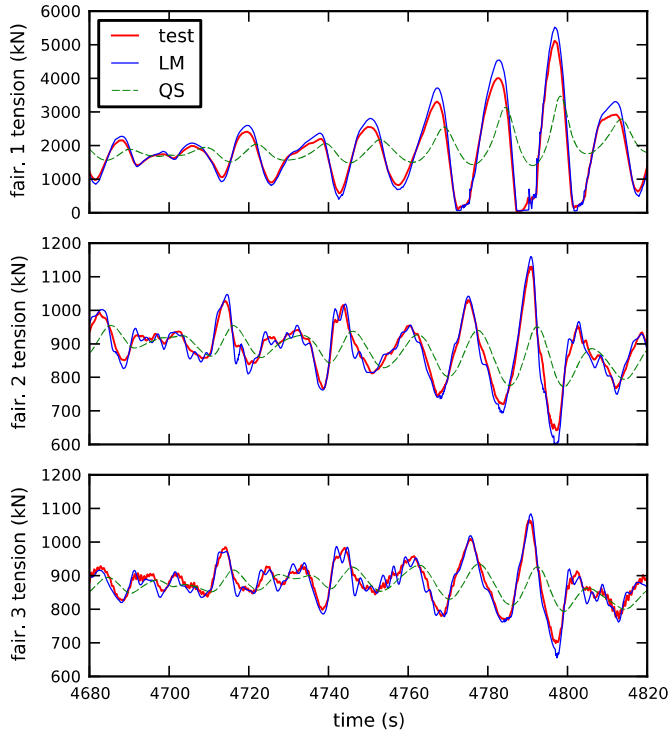


Figure 2.13: Fairlead tensions for design wave and dynamic wind

moderately well in terms of amplitude. The model captures the snap load events in line 1 occurring after 4770 s. In contrast, the quasi-static model has large disagreement from the test results in both amplitude and phase, and does not give any sign of the snap loads. Figure 2.14 shows the corresponding PSD plots. Agreement between simulation and test data is relatively good. There is a small overprediction of excitement visible in fairleads 2 and 3 around 0.4 Hz. This suggests the presence of motion measurement noise within the passband of the 0.5 Hz low-pass filter. A large peak in fairlead 3 around 1.2 Hz in the test data only is consistent with the higher-frequency oscillations visible in that channel in many of the test data time series; its presence only in fairlead 3 suggests it is an artifact of the experimental setup rather than a representation of the true mooring line dynamics.

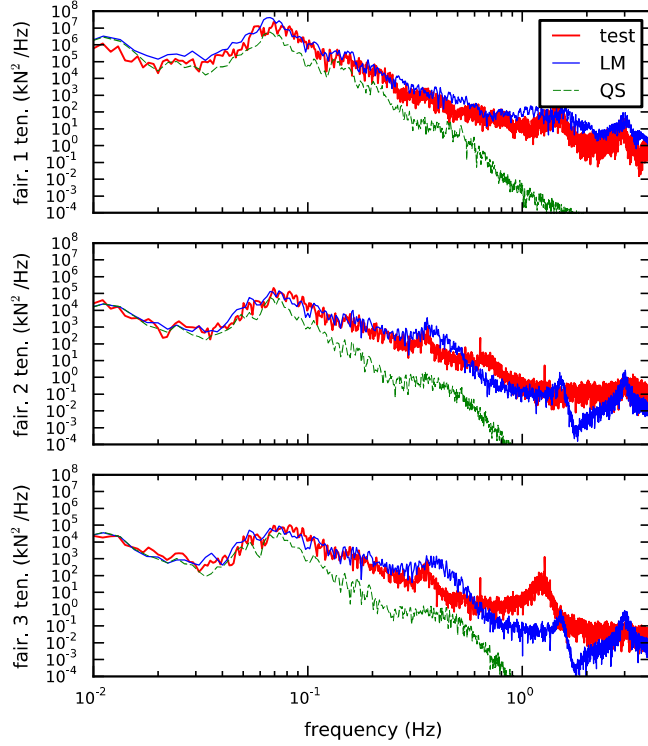


Figure 2.14: Fairlead tension PSDs for design wave and dynamic wind

The difference between the two models is also evident in the fairlead fatigue loads predicted for this same design wave and dynamic wind case. Table 2.8 gives the damage-equivalent and extreme loads calculated by NREL's MLife tool [71] for each fairlead connection using the two models. For these calculations, I assumed an S/N curve slope of $m = 3$ and essentially infinite ultimate strength, consistent with the methodology described by Matha [72]. The table shows that the values predicted by MoorDyn agree to within 10% of the test data, except for the fairlead 1 extreme load whose disagreement is slightly larger. Meanwhile, the quasi-static model underpredicts the extreme loads by 10-25% and the fatigue loads by 65-75%.

In summary, the above results of the lumped-mass mooring model in regular and irregular conditions show consistently close agreement with the fairlead tensions in the test data. Predicted fairlead tension RAOs, extreme loads, and fatigue loads

Table 2.8: Uncoupled fatigue and extreme mooring loads for design sea state and dynamic wind.

	Damage-equivalent load (kN)			Extreme load (kN)		
	fairlead 1	fairlead 2	fairlead 3	fairlead 1	fairlead 2	fairlead 3
test	1040	88.3	78.5	5120	1170	1090
LM	966	94.2	81.3	5680	1200	1130
QS	273	30.8	26.5	3800	1010	979

are in most cases within 10% of the experimental values. Furthermore, the model predicts snap loads reliably. This indicates that the dynamic phenomena affecting catenary chain mooring systems are represented well in MoorDyn.

2.2.4.7 Coupled Floating Wind Turbine Model Validation

I validated the coupling between MoorDyn and FAST (Section 2.2.3) by using it to simulate the full DeepCwind semisubmersible floating wind turbine in combined wind and wave conditions as were tested in 2011. I matched the environmental conditions in FAST to those used in the experiments by setting the time series of calibrated wave elevations and wind speed measurements from the MARIN tests as inputs. For wave loadings, I used fast Fourier transforms to produce a spectral representation of the sea state from the wave elevation time series, which is necessary for calculating the linear and second-order wave loadings in the simulation. Since my aim was comparison in the time domain, I took care to observe correct phasing and synchronization between (1) the processed wind and wave inputs to the simulation and (2) the conditions in the tests being compared against.

Applying the coupled simulation capability to regular wave cases provides an indication of which aspects of the numerical models match the test data well and which need further improvement. I analyzed regular wave cases 1 through 7 in the

absence of wind using FAST with both MoorDyn and the default quasi-static model. The wave loadings applied to the platform include second-order and viscous-drift components, as described in Section 2.2.4.3.

Figure 2.15 shows a sample of the platform motion and fairlead tension time series from the regular wave 5 case with no wind. The platform motions are based on a coordinate system located at the mean water line. It can be seen that the choice of mooring model has at most a small impact on the platform motions. The pitch response predicted by the simulations matches the test data well, but surge and heave motions are underpredicted. The heave motion has the greatest disagreement, with the simulations underpredicting the amplitude by 26% and leading in phase by 40° . This was visible in other regular wave cases as well. Not surprisingly, the fairlead tensions predicted by MoorDyn show similar disagreements with the data: namely, underpredicting the amplitude and having some phase lead. An additional observation about the MoorDyn results is the presence of tension pulses during the low-tension phase of the response in fairleads 2 and 3 which are not seen in the test data. Evidence of similar pulses, albeit at different phases, is observable in other cases as well, including in the uncoupled results shown in Figures 2.9 and 2.13.

Figure 2.16 compares the predicted platform motion RAO magnitudes in surge, heave, and pitch with those of the test data. Figure 2.17 compares the corresponding fairlead tension RAO magnitudes. The fairlead tension responses predicted by MoorDyn are in general somewhat less than those of the test data and also those predicted by the uncoupled simulations (shown in Figure 2.11). The heave RAO magnitudes are similarly underpredicted, regardless of the mooring model, suggesting that the fairlead tension underprediction is a result of the heave underprediction.

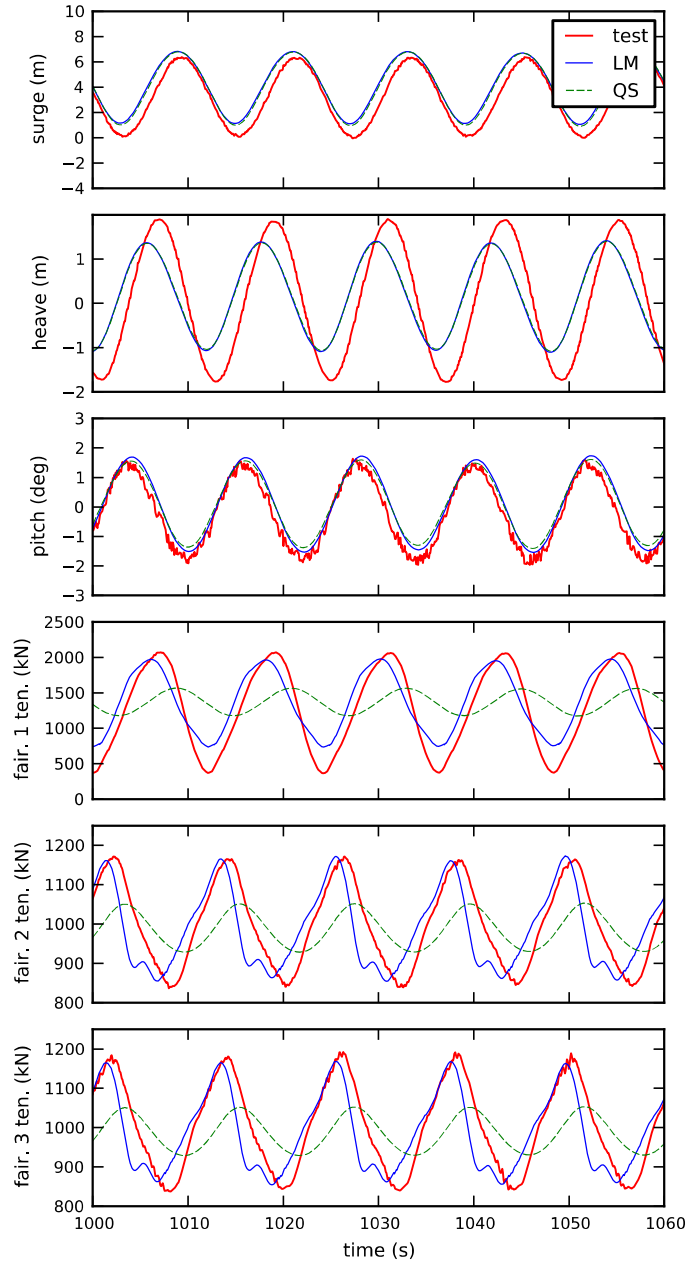


Figure 2.15: Platform motions and fairlead tensions for regular wave 5

Making the coupled simulations compare well with the test data required some attention to the platform hydrodynamics modeling. Since my focus is on the mooring model, I did not modify the platform hydrodynamic characteristics developed in previous work [65]. However, the mean drift of the platform in surge

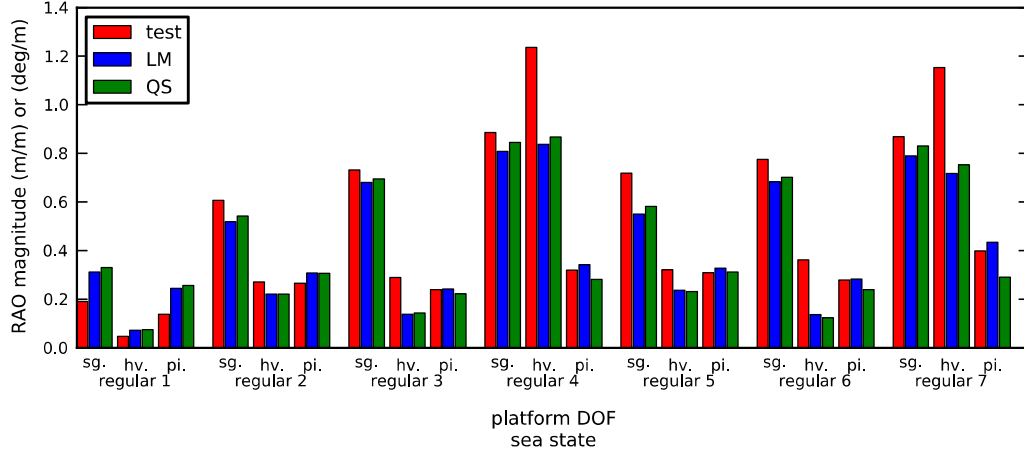


Figure 2.16: Comparison of platform motion RAO magnitudes from test data, lumped-mass model, and quasi-static model.

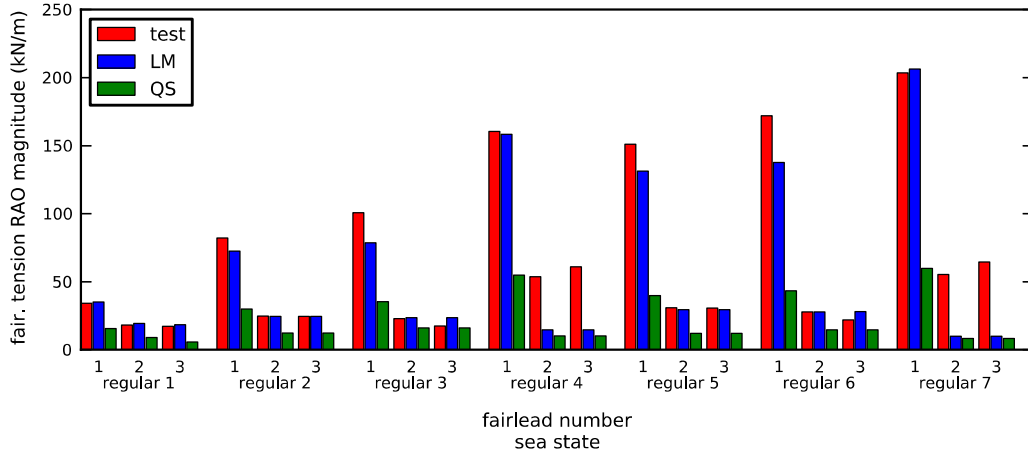


Figure 2.17: Comparison of fairlead tension RAO magnitudes from test data, lumped-mass model, and quasi-static model.

is very important to the mooring tensions, so I added full second-order wave excitation and viscous mean drift forces as described in Section 2.2.4.3. Figure 2.18 shows the effect of including these components on the surge motion of the platform in operational wave 2 without wind. As can be seen, there is a noticeable difference in mean surge between the test results and the simulation with only linear hydrodynamics. Inclusion of second-order hydrodynamics corrects for roughly half of this difference; the additional drift forcing provided by the viscous mean drift

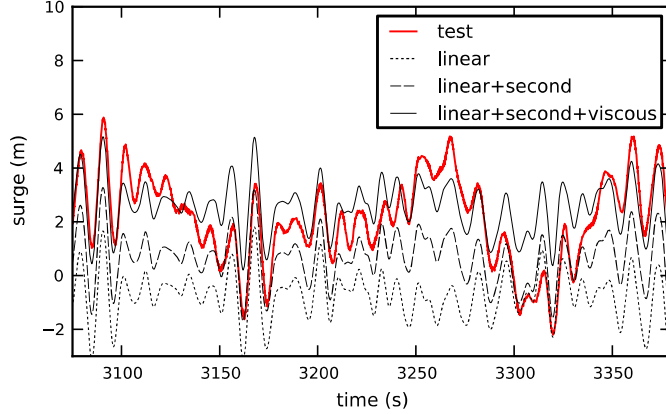


Figure 2.18: Surge motion in operational 2 sea state with different drift contributions

model of (2.17) is needed to make up the rest of the difference. The effect of second-order forces on the response in other degrees of freedom is relatively small.

To illustrate the performance of the coupled model in stochastic environmental conditions, Figure 2.19 shows platform motion and fairlead tension time series for the design sea state (10.5 m, 14.3 s JONSWAP spectrum) and NPD wind spectrum with mean hub-height speed of 19.6 m/s. In this case, the turbine operates with a constant speed of 12.73 RPM. For the most part, the platform motions show some agreement in the amplitudes and phases around the peak wave excitation frequency. However, the heave response shows consistent underprediction of the response amplitude and also some phase differences, regardless of the mooring model.

Looking at the corresponding fairlead tensions, MoorDyn generally underpredicts the tension response amplitudes compared to the test data. For fairleads 2 and 3, the tension fluctuations are relatively small and signs of agreement with the test data are only evident during times of larger tension amplitude. For fairlead 1, the tension amplitudes are larger and some agreement in phases can be seen. Several snap load events are visible in the test data beginning at $t = 4772$ s. MoorDyn predicts reduced tensions at these times but, unlike in the uncoupled results, it

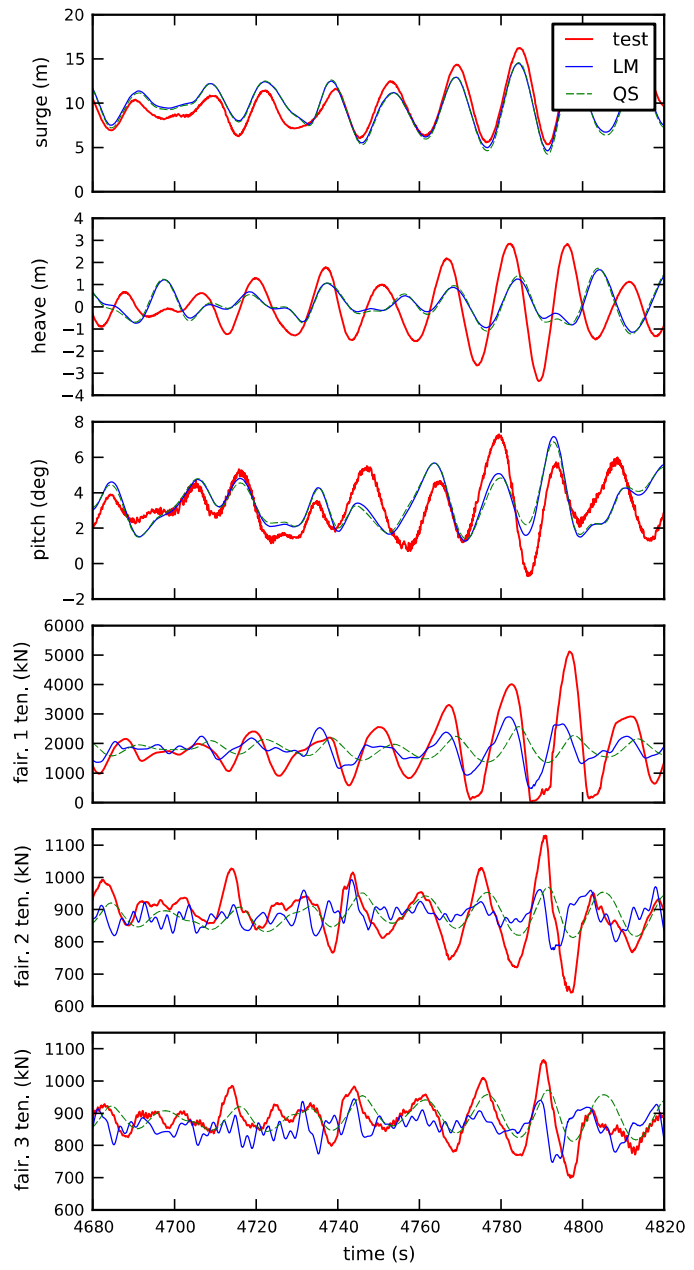


Figure 2.19: Platform motion and fairlead tension time series for design sea state with dynamic wind.

Table 2.9: Coupled fatigue and extreme mooring loads for design sea state and dynamic wind.

	Damage-equivalent load (kN)			Extreme load (kN)		
	fairlead 1	fairlead 2	fairlead 3	fairlead 1	fairlead 2	fairlead 3
Test	1040	88.3	78.5	5120	1170	1090
LM	522	56.7	57.2	3190	994	995
QS	293	35.0	35.2	2910	970	972

does not predict the fully slack condition. As with the regular wave results, the fairlead tension response underprediction seems to correspond with underpredicted platform heave response. In all cases, the quasi-static mooring line model underpredicts the mooring tension response amplitudes to a greater degree.

Table 2.9 gives the damage-equivalent and maximum fairlead loads calculated for the same test case, using the same fatigue parameters as in the previous section. The evident underprediction of both fatigue and extreme line loads matches the amplitude differences visible in the time series of Figure 2.19.

I attribute the underprediction of fairlead tension amplitudes in the coupled results to underprediction of heave response, since tension agreement was good in Section 2.2.4.6 where the fairlead motions were prescribed. The heave underprediction is similar to that observed by Koo et al. [53], which was attributed to the presence of a cancellation frequency phenomenon, where diffraction and Froude-Krylov wave excitation forces cancel, in a diffraction-based analysis. Using a linear hydrodynamics approach combined with global viscous damping coefficients based only on absolute platform motions neglects viscous wave forces on the heave plates and truss members. This results in significant underprediction of heave response at the cancellation frequency, where viscous forces are the dominant source of heave excitation. This explanation is corroborated by the findings of the OC4 project [62], which concluded that using only a global drag matrix to represent viscous

loads may be inadequate, especially in large waves. In fact, the OC4 findings suggest that a Morison-based approach to the platform hydrodynamics may in general provide a closer match to the experiments than an approach using only linear hydrodynamics. In summary, there are clear indications of how changes to the platform model could improve the coupled results. Many of these aspects are accounted for in the hydrodynamics module of FAST v8.

2.2.5 Multi-Segment Mooring Model Validation

The first validation of MoorDyn with a multi-segmented mooring system was a collaboration with Giacomo Vissio at Politecnico di Torino using a wave energy converter (WEC) design being developed there [73]. Inertial Sea Wave Energy Converter (ISWEC) features a unique gyroscopic power take-off (PTO) that allows the hull to be completely sealed. The WEC is designed to resonate in pitch under wave excitation. The PTO axis is aligned with the wave propagation direction and a flywheel system uses the gyroscopic effect to provide self-reaction for power take-off. The ISWEC design is a good subject for mooring analysis because of its large motions and the complex mooring system used to provide the needed compliance.

The portion of the mooring system we modeled in MoorDyn was the more active upper part, consisting of four lines. These are shown at 1:20-scale in Figure 2.20. Two lines extend from the ISWEC hull in a bridle arrangement to attach to a clump weight. A short chain attaches this clump weight to a float, then a fourth chain moors the float down to an anchor point. In the full-scale design, this anchor point is replaced with a four-point catenary mooring.

We compared model results with test data from 1:20-scale experiments conducted at the HMRC wave basin of University College Cork, Ireland. The hull motions

and fairlead tensions were measured in these tests, however the hull motions lacked an absolute reference with respect to the anchor points, adding uncertainty in the model comparison. All values for this work are at model scale.



Figure 2.20: Mooring system used in 1:20-scale ISWEC tests (image courtesy of Giacomo Vissio)

I set up the MoorDyn model with the measured lengths and chain properties of the experimental mooring system. The clump weight and float volume in the ISWEC mooring provided the first opportunity to check these modeling capabilities in MoorDyn. As in the uncoupled analysis of Section 2.2.4.6, MoorDyn was driven with the measured hull motions from the experiments, allowing comparison of the predicted and experimentally-measured tensions.

Figure 2.21 shows the simulated and measured fairlead tensions in the most successful comparison. The case was regular waves with 1 s period and 0.1 m amplitude (model scale). Many of the test cases did not provide this close of a comparison; we attribute this to the lack of absolute reference in the experimental position measurements and our limited ability to guess the correct offsets from intuition. However, that we were able to achieve this level of tension agreement in any tests is already an encouraging result toward the validity of the different modeling components considering the complexity of the mooring system.

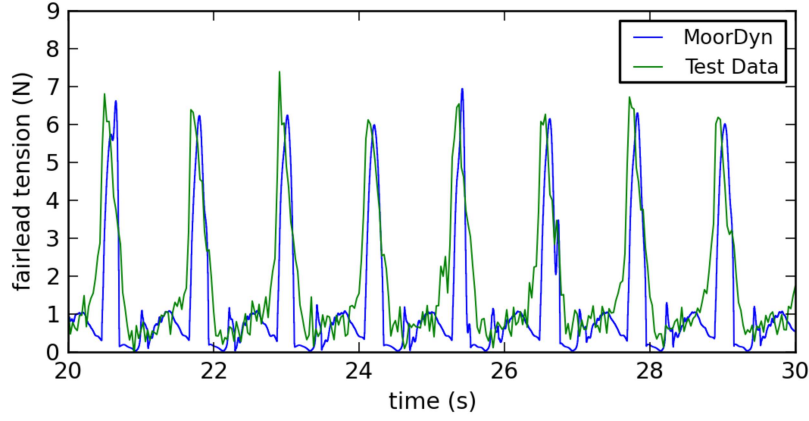


Figure 2.21: Fairlead tensions on the ISWEC device in regular waves.

Several complications arose in modeling the ISWEC device. Stiffness properties are not preserved in Froude scaling and experiments of the ISWEC mooring did not incorporate springs to compensate. Accordingly, the mooring line stiffnesses were greater than true-to-scale values. These elevated stiffnesses had to be retained in the model to capture snap loads accurately. A small time step (0.1 ms) was needed for stable modeling of these stiff mooring elements. This was also the first test of MoorDyn with clump weights and it raised the complication of how clump weights are attached. In the tests, the clump weight was suspended from the chains by a hook (as seen in Figure 2.20) which gives a radius between the chains and the clump weight center of mass. This had an important effect on lessening the magnitude of snap load tensions at the fairlead. Because MoorDyn models clump weights as point masses, I added an additional single-segment mooring line to represent this distance between the center of mass and the attachment point. This detail was essential for matching the snap loads measured in the experiments.

2.2.6 Conclusions on Mooring Modeling

The project to develop an efficient dynamic mooring model resulted in the tool now called MoorDyn. By neglecting bending and torsional stiffnesses, it captures the main dynamic behaviors affecting mooring lines of the type suitable for floating wind turbines at small computational cost.

Validation against 1:50-scale test results of the DeepCwind semisubmersible has shown very good agreement with experimental data in predicting fairlead tensions resulting from platform motion. The matching of tension amplitudes and fatigue load calculations are within 10% and prediction of slack conditions also matches well. These are significant improvements over quasi-static models that were the only open-source options at the time I began the project. Initial validation studies with more complex mooring systems have also shown promising results.

MoorDyn has been integrated into a number of comprehensive floating structure simulation tools, including FAST v8, WEC-Sim, and several others in progress. While reliably predicting mooring line loads, MoorDyn adds little computational cost to floating wind turbine simulations. In FAST simulations conducted in this work, using MoorDyn rather than the quasi-static model increased the computation time by only 10-15%. In the work presented in the next chapter, I used MoorDyn coupled with FAST v7 to provide improved representation of the mooring dynamics in the coupled floating system response.

The goals under which I developed MoorDyn – balancing fidelity and efficiency while making coupling with other models as easy as possible – make it well suited for use in hybrid modeling. It would require no modifications to serve as the numerical portion of a hybrid model in basin test cases where using physical mooring lines is undesired. It can simulate a typical floating wind turbine mooring

system at about 20 times faster than real time. This is more than adequate for use in a hybrid model running at 1:50 or even 1:200 Froude-scaled real time. Since the internal MoorDyn time step is typically 1 ms or less, much higher coupling control loop rates are possible with MoorDyn than with FAST, which may be necessary for work involving the fast response of taut moorings or snap loads.

In testing in small wave basins, even if the desired quasi-static response can be achieved with a truncated mooring system, it is unlikely that the mooring dynamics can be matched. Therefore, an efficient mooring model that has been shown to capture those dynamics could be hybrid-coupled with the floating structure experiment to, in space-constrained cases, give a more true-to-scale representation of the overall platform response. Appendix A contains further exploration of this idea.

Chapter 3

DEVELOPMENT OF PERFORMANCE SPECIFICATIONS

The main challenge of realizing a hybrid model of a floating wind turbine lies in creating a mechatronic system to couple the physical and numerical sub-models together. At its simplest, this system requires a means of measuring the floating platform motions to be passed to the wind turbine simulation, and a mechanism for applying the reaction forces calculated by the simulation back onto the floating platform. The key issue in a hybrid modeling approach, regardless of its type, is the quality of the dynamic coupling between experiment and simulation.

Addressing this challenge during the design process requires an understanding of the relationship between coupling quality and system performance. This chapter focuses on assessing that relationship and then showing how it can be used to produce performance specifications to use as targets when designing a hybrid coupling system.

3.1 Methodology

Simulations provide a way to determine performance requirements for a hybrid coupling system and study the relationship between system performance and coupling quality. I considered two different hybrid coupling approaches and three different floating wind turbine designs in order to provide a broad view of the range of possibilities.

3.1.1 Coupling Location

In a hybrid floating wind turbine model aimed at simulating the aerodynamics, there is a choice of where the transition occurs between physical and numerical sub-models. The most common choice is at the aero-elastic interface – where the inertia (and potentially elasticity) of the entire turbine is modeled experimentally, and only the aerodynamic loads are handled in the numerical sub-model. Another option is to include the rotor inertia in the numerical side, in order to capture details such as gyroscopic forces. In this study I consider two possible coupling points, which span the range of likely options:

- **Tower-base coupling** considers numerical modeling of the entire wind turbine, from the base of the tower upward. This provides a clear transition point between physical and numerical models but is a demanding approach since the hybrid transition occurs through the structure and inertial loads will be present on both sides of the coupling. True-to-scale rotor and tower elasticity can be modeled numerically, representing an improvement over current capabilities in wind-wave testing since Froude-scaled rotor blades are typically very rigid.
- **Aero-elastic coupling** considers numerical modeling of the aerodynamics only. The (non-spinning) inertia of the rotor is modeled on the physical side. A numerical model of the spinning rotor includes inertia only inasmuch as it effects the motions of the blades and hence the aerodynamic loads. The rotor is assumed to be inelastic and massless to avoid inertial contributions in the forces calculated by the numerical model. The rotor's inertia can be added to the physical structure by arranging masses at the tower top. Gyroscopic forces (such as could be achieved by using spinning masses) are not considered here.

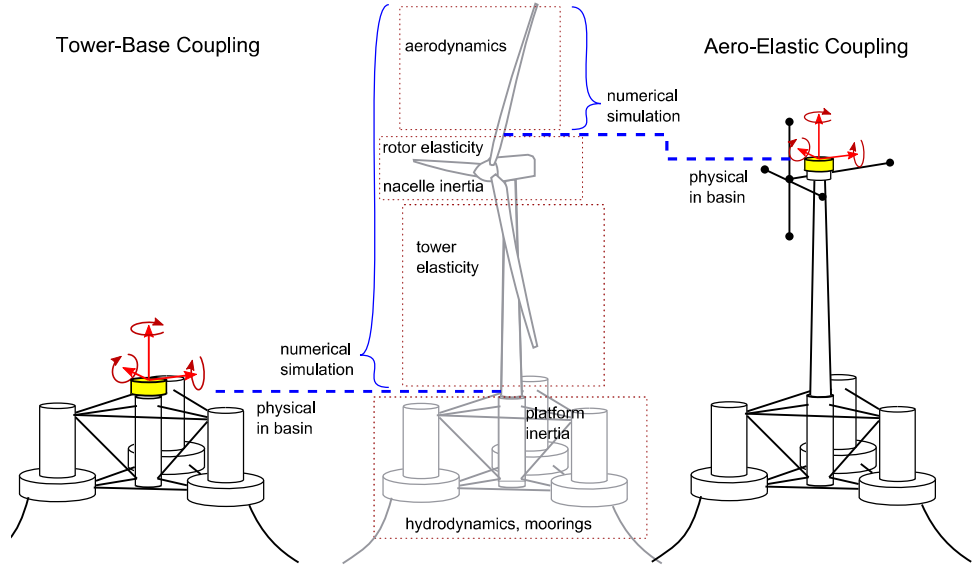


Figure 3.1: Tower-base and aero-elastic hybrid coupling types

These two coupling approaches are illustrated in Figure 3.1. The tower properties are assumed to be true-to-full-scale in both cases. For aero-elastic coupling I assume that, without the need for a physical wind turbine, it is feasible to recreate the true tower elastic behavior at model scale.

3.1.2 Specifications Considered

I divided the hybrid coupling requirements into specifications for the performance envelope or range of the coupling system and specifications for the quality or accuracy of the coupling system.

The following four specifications concern the performance envelope of the coupling system:

1. range of motion,
2. maximum velocities,
3. maximum forces and moments,

4. motion bandwidth.

These pertain to the actuation mechanics only and can be determined through simulations of cases typical to scale-model testing.

Three specifications concern the quality of the coupling:

1. error tolerances for motion tracking,
2. error tolerances for actuation force,
3. acceptable latency levels.

These pertain to the hybrid coupling system as a whole, and can be analyzed through a sensitivity study that introduces perturbations in the relevant quantities in a time-domain simulation. Item 1 reflects errors occurring in tracking the motion of the physical model platform being tested in a basin. Item 2 represents errors in the forces applied to the platform by the actuation system. Item 3 represents the time delay inherent in measuring the platform motion, simulating the wind turbine dynamics, and applying the resulting forces back onto the platform.

3.1.3 Simulation Approach

I used simulations to study the behavior of a hybrid model subject to errors in the hybrid coupling and to identify actuation performance envelope requirements. The simulations use FAST v7 and MoorDyn, coupled as described in Section 2.2.3. Since these tools have done well in validations against scale-model experiments and are computationally-efficient enough to run at Froude-scaled real time in hybrid modeling systems, they are well suited for the topic at hand. I used the

modifications to FAST that add viscous drag contributions and second-order wave excitation described in Section 2.2.4.3.

I ran simulations corresponding to typical basin testing scenarios but with true-to-scale wind turbine behavior to indicate the performance envelope needed for a hybrid coupling actuation system. The required forces, displacement ranges, speeds, and bandwidths can be found from the results, which are presented in Section 3.3.

I ran simulations incorporating coupling errors to determine requirements for the quality of the hybrid coupling system. Inserting various amounts of the three errors listed in the previous section and looking at the sensitivity of the results of interest reveals the acceptable error tolerances for any desired level of accuracy.

For the sake of clarity, I use the words “error” to describe the flaws introduced in the hybrid coupling and “discrepancy” to describe the resulting change in the output quantities of interest compared to the results with no coupling errors.

A modified version of FAST allows the introduction of the three types of coupling errors in the simulation:

1. I modeled inaccuracies in the motion tracking of the physical platform (or tower top) in the basin by inserting errors in the tower-base (or tower-top) kinematics in the portion of FAST that calculates the aero-elastic response of the wind turbine.
2. I modeled errors in the force provided by the actuation system on the floating platform (or tower top) by inserting additional forces occurring at the coupling point into the FAST simulation.

3. I modeled latency in the overall coupling system's response by adding a delay of a discrete number of time steps in the tower-base (or tower-top) kinematics that are provided to the aero-elastic portion of FAST. (The platform kinematics given to the aero-elastic simulation are from N time steps previous.)

Motion and force errors (items 1 and 2 above) are represented by band-limited white noise signals of varying amplitudes. I computed this noise using the Box-Muller method [74] with the same random-number seed for each run to provide simulation consistency, but different starting points for each directional component of each error type to ensure that there is no phase alignment between the different introduced errors. My goal in setting the frequency range of the white noise was to start at a frequency below the system's natural frequencies and the wave excitation frequencies (the results are insensitive to this value) and stop at a frequency greater than the cutoff frequency of the platform response (which is identified in Section 3.4.2.2). For the tower-base coupling approach, the white noise spans frequencies from 0.01 Hz to 0.5 Hz, which satisfies the aforementioned goal and also encompasses the first tower-bending natural frequency, allowing the effect of this simulated degree of freedom to be passed over the coupling. For the aero-elastic coupling approach, the noise added to the forces and motions passed through the coupling spans 0.01 Hz to 0.25 Hz. Unlike in the tower-base coupling, I kept the cutoff frequency below the first tower-bending frequency to avoid a tower-bending resonance susceptibility that I observed in this coupling approach. The results show that aerodynamic reaction forces at these higher frequencies, while perhaps contributing to damping of tower bending modes, have a negligible influence on the output quantities of interest in a test, as will be discussed in more detail in Section 3.4.2.2.

All simulations in the sensitivity analysis have a duration of 30 minutes, with the first 30 seconds discarded to avoid start-up transients associated with the introduced coupling errors.

3.1.4 Wind Turbine and Support Structure Designs

For producing specifications, I considered the three support structure designs that were tested experimentally by the University of Maine at MARIN in 2011 [75]. Using these designs allows for comparison with test data and provides results from each of the three floating support structure stability classes. The spar design is based on the OC3 Hywind design [76] but with a semi-taut mooring system and represents the ballast-stabilized stability class. The DeepCwind semisubmersible was described in Section 2.2.4.1 and is representative of buoyancy-stabilized designs. The tension-leg platform (TLP), based in part on a design by Glosten Associates [77], represents mooring-stabilized designs and has also been studied by others (e.g. [78, 79]). Specifications of the floating platforms and mooring systems of these designs are given in [80].

For the simulations in this work, I complemented FAST and MoorDyn models of the three floating wind turbine designs with second-order wave excitation coefficients supplied from other studies. Those for the semisubmersible come from Gueydon et al. [66]. Those for the spar come from Roald et al. [81]. Those for the TLP come from Gueydon et al. [82] and include tower bending in the estimation of first-order response. Together, these provide for simulated global response characteristics that agree well with experimental data.

The wind turbine itself deserves special attention because there are important differences between the characteristics at full-scale and those in the experiments. The full-scale wind turbine characteristics are those of the NREL 5 MW offshore

reference turbine [64], a widely-used reference design. I used the generator-torque and blade-pitch controllers developed for the Offshore Code Comparison Collaboration (OC3) project [76] in the simulations. The Froude-scaled turbine characteristics are those of the turbine used in the 2011 DeepCwind experiments described in Section 2.2.4.2.

For the following analyses, I used the Froude-scaled turbine properties for the purpose of checking the simulation setup against the experimental data (in Section 3.2) and the full-scale turbine properties for producing all the specification results (in Sections 3.3 and 3.4). This means that the simulations used for producing the specifications will not completely correspond with test data, since the simulations use turbine properties that cannot as of yet be reproduced in physical, Froude-scaled wind turbine testing. For consistency and generality, all values are in full-scale units unless otherwise noted.

3.1.5 Environmental Conditions

I used seven wind-wave environments in the numerical analyses, listed in Table 3.1. The first six cases feature wind and wave conditions corresponding to below-rated, at-rated, and above-rated operation in typical and 50-year wave environments. The wind and wave parameters correspond to conditions in the Gulf of Maine, as identified by Viselli et al. [83], that fit design load case (DLC) 1.2 and 1.6 requirements as defined in floating wind turbine guidelines of the American Bureau of Shipping [84]. The wave parameters describe the significant wave height, H_s , peak period, T_p , and peak shape parameter, γ , of a JONSWAP wave spectrum. The given mean wind speeds, U_m , are for Class B turbulent wind, as defined by the International Electrotechnical Commission's standard IEC 61400-1 [85]. The resulting characteristic turbulence intensity (TI) at hub height is also given in the

table. I produced the turbulent wind inputs for the simulations with TurbSim, a program that calculates realistic spatially- and temporally-varying wind flow fields using a variety of spectral turbulence models [86].

The seventh case features a “white noise” sea state without wind with a significant wave height of 7 m with component periods ranging from 3 s to 25 s. This broadband spectrum of wave excitation is a common way to test for a floating platform’s response amplitude operators across a wide frequency range in a single test (e.g. [63]).

All seven cases feature unidirectional and aligned wind-wave conditions. While many multidirectional and misaligned environmental conditions could be considered, the aligned situation is likely the most challenging operating condition for a hybrid coupling system since it entails the greatest interaction between aerodynamic and hydrodynamic loadings.

Table 3.1: Environmental conditions simulated

Case	H_s (m)	T_p (s)	γ	U_m (m/s)	TI (%)
1	0.96	7.04	1.5	8	20.3
2	1.21	7.3	1.6	12	17.0
3	2.45	8.48	1.7	20	14.4
4	8	12.7	2.75	8	20.3
5	8.5	13.1	2.75	12	17.0
6	9.8	14.1	2.75	20	14.4
7	7	3-25	-	0	0

3.2 Validation of Numerical Modeling

After preparing the simulation capability, I ran simulations of select load cases to check the modeling against experimental data. These simulations are of the “model of the model” type, matching the properties of the Froude-scaled turbine used in

the tests. The focus here is not to tune the models to match the test data but rather to check that the coupled FAST-MoorDyn simulations provide reasonable representations of the dynamics as seen in the experiments. The experimental data is from the 2011 DeepCwind tests, which considered the same three designs at 1:50-scale [75].

The first comparison looks at the platform surge and pitch offsets under steady wind in still water. This provides a combined check on the wind turbine model's thrust force and the support structure (platform and mooring) model's stationkeeping and hydrostatic restoring properties. The case shown here corresponds to a steady wind speed of 16.1 m/s and a fixed rotor speed of 9.19 rpm. This high wind speed is a result of the compensation that was used for the Froude-scaled aerodynamic performance in the experiments, as mentioned in Section 3.1.4. Table 3.2 gives the steady-state surge and pitch offsets predicted by simulations of the three designs alongside the values measured from the DeepCwind experiments.

The underprediction of the semisubmersible's surge offset is likely due to the significant frontal area exposed to the wind in this design since wind loading on the platform is not included in the simulation. Otherwise, the results agree fairly well. The absolute difference in the TLP steady-state pitch is only 0.2 degrees, a quantity that could be explained by a slight offset in the experimental measurements or setup.

The natural frequency of the first tower bending mode provides a useful modeling check because it is influenced by the tower properties as well as the inertia of the support structure and turbine. In the Froude-scaled models tested in 2011, these frequencies can be identified in hammer tests by looking at power spectral density (PSD) plots of tower-top acceleration. The values I found using this method

Table 3.2: Surge and pitch offsets under steady 16.1 m/s wind

	Semi.	Spar	TLP
sim. surge (m)	5.74	4.65	4.99
test surge (m)	4.13	5.10	4.76
sim. pitch (deg)	1.97	2.98	0.25
test pitch (deg)	2.02	3.23	0.061

match those reported in [87]. I also identified these natural frequencies in the simulation models by looking at PSD plots of the tower-top acceleration under white-noise wave excitation (case 7). These values are listed in Table 3.3 for the test data and for three different simulation arrangements. The first row of simulation results correspond to model-of-the-model conditions in which the experimental turbine and tower properties are used. These can be seen to agree quite closely with the experimental findings, as is expected. The next row corresponds to simulations using the full-scale NREL 5 MW reference turbine properties. The last row modifies these properties for the aero-elastic coupling scenario in which the rotor is simulated as massless and this inertia is instead provided by putting additional mass at the hub. The close agreement between this case and the former one suggests that the reallocation of mass in the aero-elastic coupling situation does not have an appreciable effect on the tower bending dynamics – an encouraging result for hybrid couplings of this type.

Table 3.3: First tower-bending natural frequency of each design (Hz)

Model type	Semi.	Spar	TLP
test data	0.34	0.42	0.27
sim. of test	0.34	0.39	0.26
sim. of full scale	0.41	0.47	0.31
sim. of full scale, lumped rotor mass	0.41	0.48	0.30

I compared the global responses of the simulated designs with those of the DeepCwind experimental models by looking at the response amplitude operators (RAOs) calculated from a white noise wave case. To provide the best comparison, I ran the simulations with the same wave elevation time series that was measured in the experimental wave case being compared against. As shown in Figures 3.2 to 3.4, the comparison indicates no unexpectedly-large discrepancies in the important motions for each platform, over the frequency range of the white noise wave spectrum. Some discrepancies are expected because the white noise RAO approach cannot address nonlinear parts of the response and the numerical model neglects some of these nonlinearities. For example, some noticeable disagreements of the semisubmersible are visible around 0.07 Hz, which is a known frequency where linear hydrodynamic forces cancel and viscous drag is the dominant excitation mechanism in heave (as described by Koo et al. [53] and also seen in the results of Section 2.2.4.7).

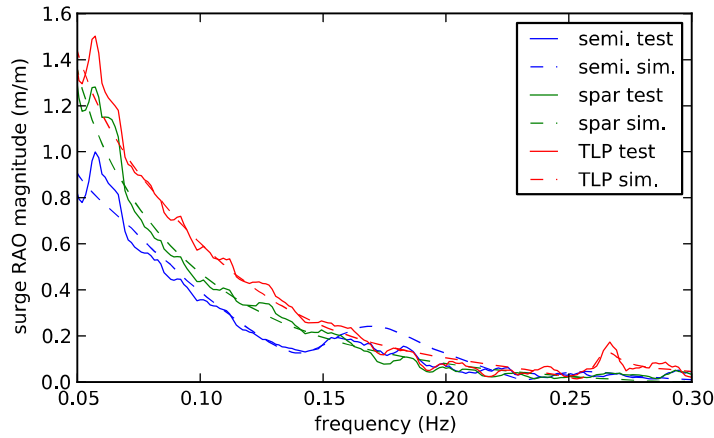


Figure 3.2: Surge RAO magnitude from white noise sea state

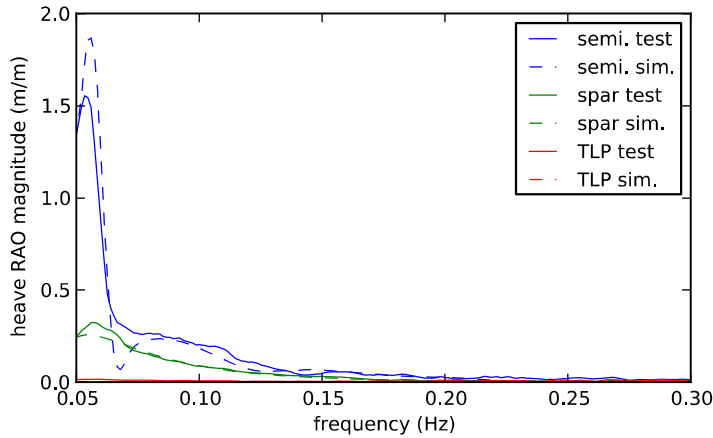


Figure 3.3: Heave RAO magnitude from white noise sea state

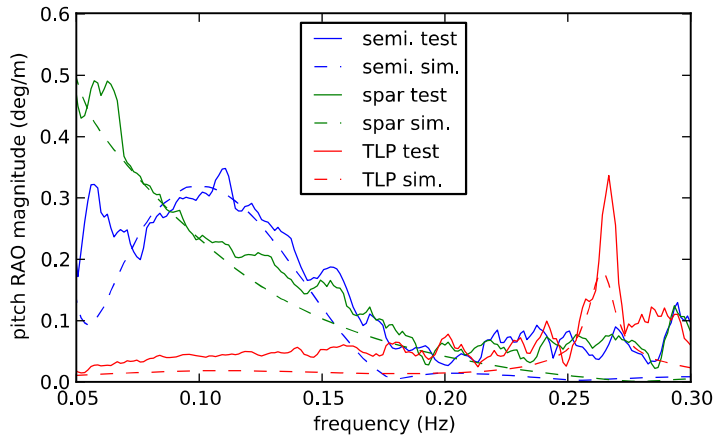


Figure 3.4: Pitch RAO magnitude from white noise sea state

3.3 Actuation Performance Envelope Requirements

I ran simulations of the load cases given in Table 3.1 for each of the three designs to identify the performance envelope needed from an actuation system. These simulations use the full-scale NREL 5MW reference turbine properties in order to reflect the true-to-scale turbine behavior that could be realized in a hybrid modeling basin test. Since the tower-base hybrid coupling arrangement would see actuation at the tower base while the aero-elastic hybrid coupling would see actuation at the tower-top (or hub height), I did the analysis about both of these

points on the turbine. I ran six simulations with different stochastic wind and wave realizations for each turbine design and load case, allowing presentation of the means and standard deviations of the quantities of interest. Each simulation was 10 minutes long after discarding the first 30 seconds.

3.3.1 Motions

I characterized the motion requirements as the maximum displacements, maximum velocities, and cutoff frequencies found in the simulations.

Figure 3.5 shows the maximum absolute values of surge displacement for the three platforms under each load case. Figure 3.5a shows the results for tower-base coupling and Figure 3.5b shows the results for aero-elastic coupling. The bar heights indicate the average maximum values found in each set of six simulations for a given case. The error bars indicate the standard deviation in these six maxima. Figure 3.6 shows the maximum pitch angle statistics following the same approach.

Comparing the magnitudes of different designs and the different coupling points confirms some expected behaviors. For example, the surge and pitch extremes found for the semisubmersible change relatively little between the two coupling types, consistent with this design’s tendency toward opposite-phase pitch and surge motions which reduce nacelle translation. The spar design, in contrast, has much larger extreme displacements at the tower top than at the tower base because it tends to pivot about the fairleads of its taut mooring system. The simulated tower-base pitch extremes of the TLP design are very low as would be expected given the stiff and taut vertical moorings. The slightly larger pitch at the TLP tower-top can be attributed to deflection of the tower. Another noteworthy difference is that the semisubmersible design has much greater standard deviations

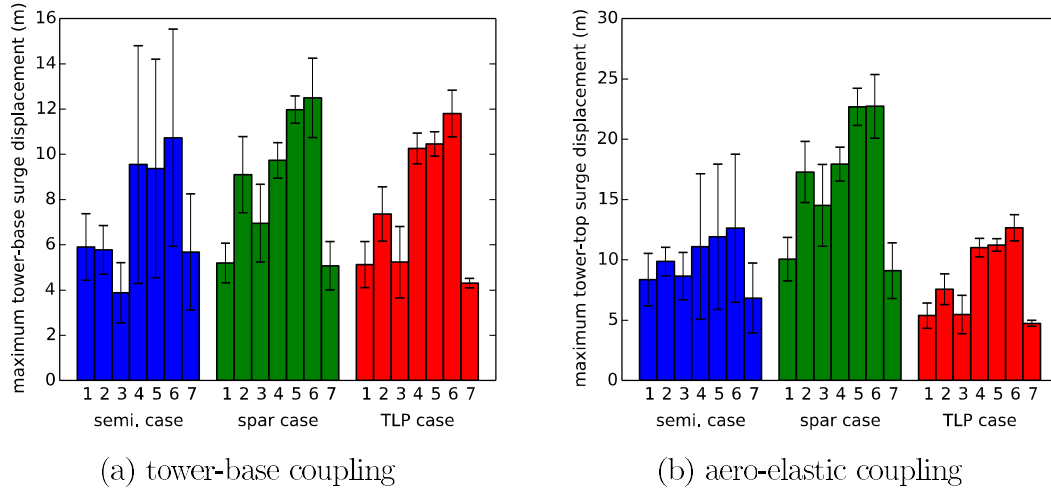


Figure 3.5: Maximum surge displacements at coupling point

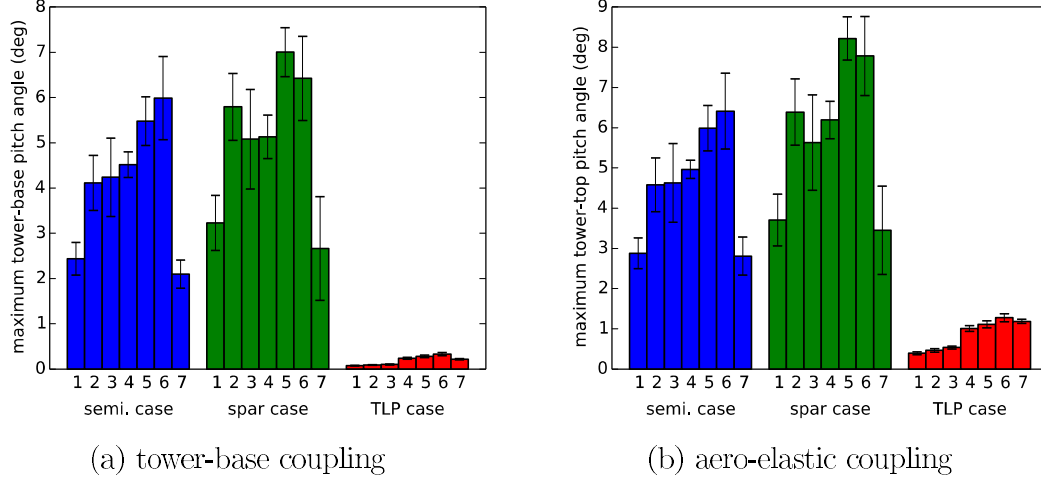


Figure 3.6: Maximum pitch angles at coupling point

in maximum surge displacement. This indicates its motions are more sensitive to chance occurrences of specific conditions, suggesting designs like this warrant a more careful statistical approach to ensure that extreme displacements in low-probability conditions are adequately accounted for.

I estimated velocity requirements using a similar approach as displacements, by aggregating the maximum linear and angular velocities found in the six simulations of each case. The velocity time series come from differentiating the

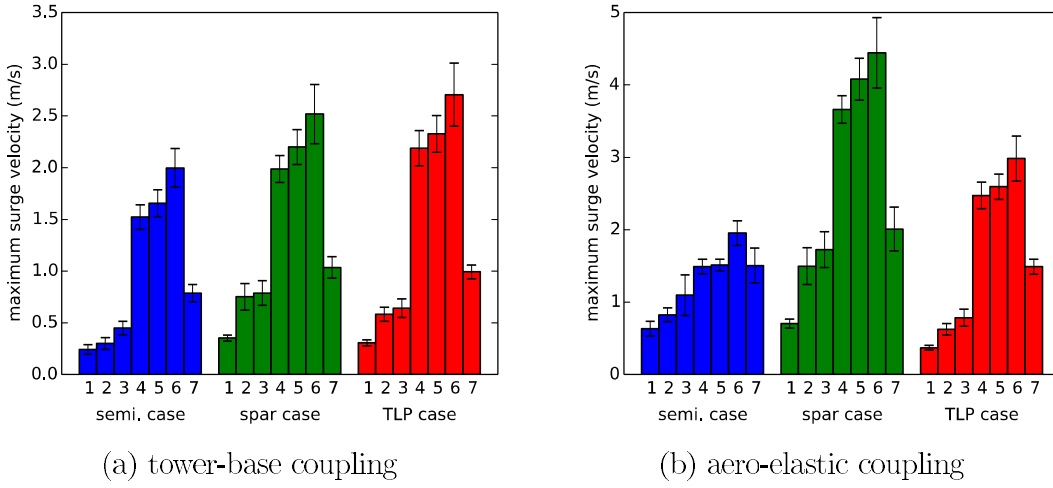


Figure 3.7: Maximum surge velocities at coupling point

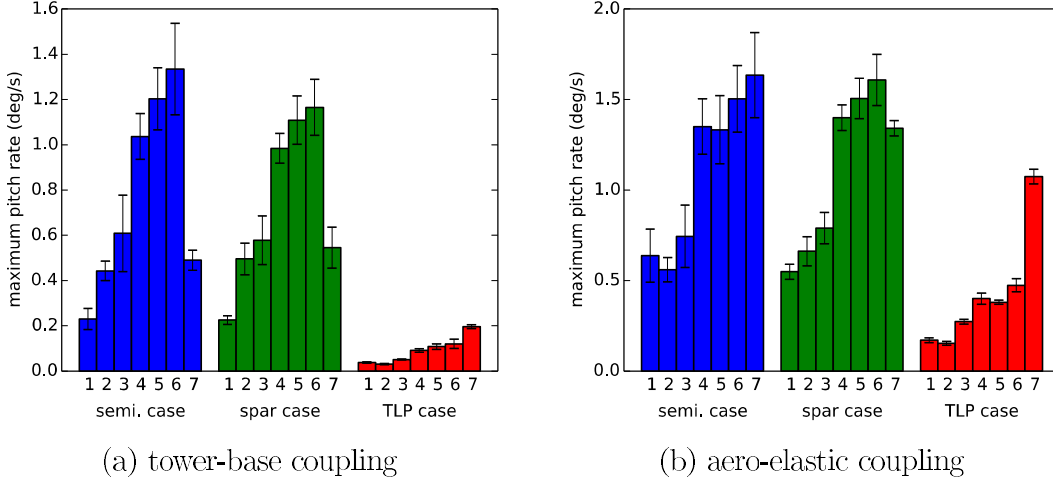


Figure 3.8: Maximum pitch rates at coupling point

position outputs/measurements and applying a sixth-order Butterworth low-pass filter with 0.5 Hz cutoff frequency to remove measurement noise. The results were not sensitive to this choice of cutoff frequency. The maximum surge velocities and pitch rates are shown in Figures 3.7 and 3.8, respectively. The magnitude trends in these maximum velocities between the different designs and coupling types are very similar to those found for the maximum displacements.

The frequency response required of the coupling system is also important. Figures 3.9 and 3.10 show the bandwidth, or cutoff frequency, calculated for the coupling point movements in surge and pitch, respectively. Motions, rather than forces, are more likely the limiting factor for this type of coupling application since the actuator could be force controlled and hence feedforward control could be used to apply forces at frequencies higher than the feedback bandwidth.

I estimated the motion bandwidth requirements from PSDs of the coupling point displacements and rotations. The bandwidth presented here is defined as the frequency below which 97% of the power exists. In the plots that follow, the consistently lower bandwidths seen in cases 4 to 6 are a result of their larger wave excitation. Since the dominant wave excitation frequencies of these sea states are low (well below 1 Hz), 97% of the power is contained within a lower frequency range. In Figure 3.9b, the outlying bandwidths for the semisubmersible in cases 1 and 7 are likely due to excitation at the 0.41 Hz tower bending natural frequency being at the edge of the bandwidth criterion in these lower-energy sea states. A similar phenomenon appears to be present for the TLP. The high bandwidth of the TLP in platform pitching (Figure 3.9) can be attributed to the TLP's very small pitching motions. As a whole, these results suggest the bandwidth needed of an actuator, which in turn informs how actuation errors should be simulated in the sensitivity study given in Section 3.4.

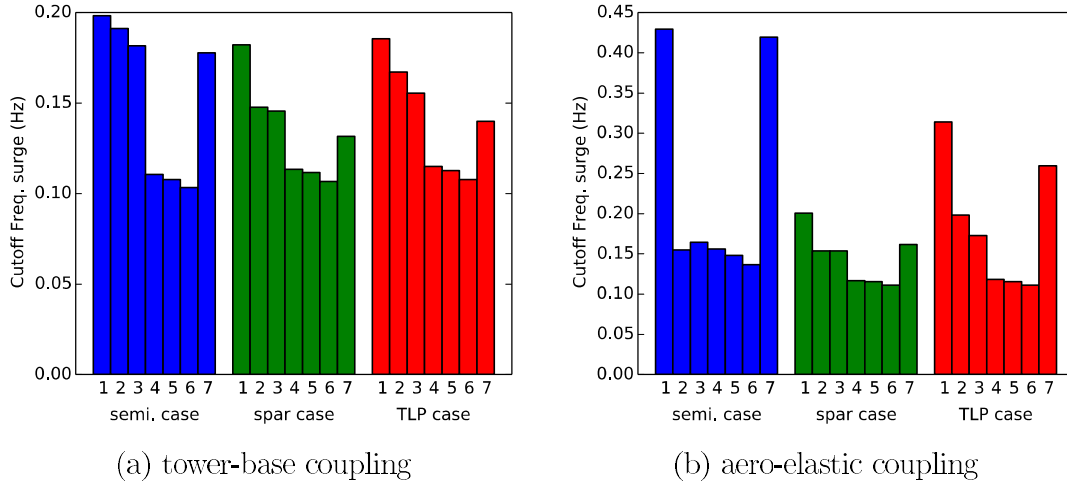


Figure 3.9: Motion bandwidth in surge

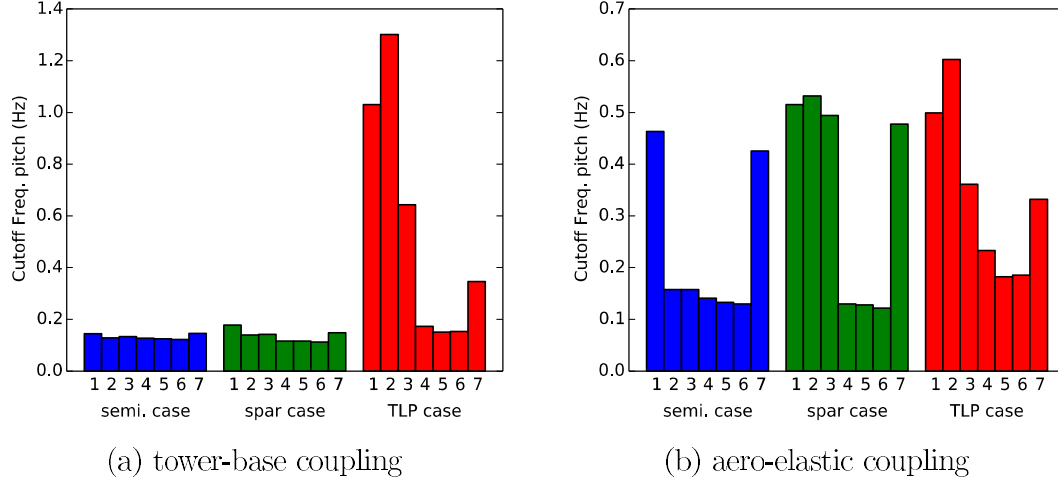


Figure 3.10: Motion bandwidth in pitch

3.3.2 Forces

The maximum forces and moments required of an actuation system for the two hybrid coupling types can be extracted from simulation results following a similar approach to the motion requirements. Figures 3.11 and 3.12 show the maximum surge forces and pitch moments, respectively, identified in the various simulation cases. Comparing the left and right subplots shows the significant difference between the maximum forces at the tower-base coupling point versus those at the

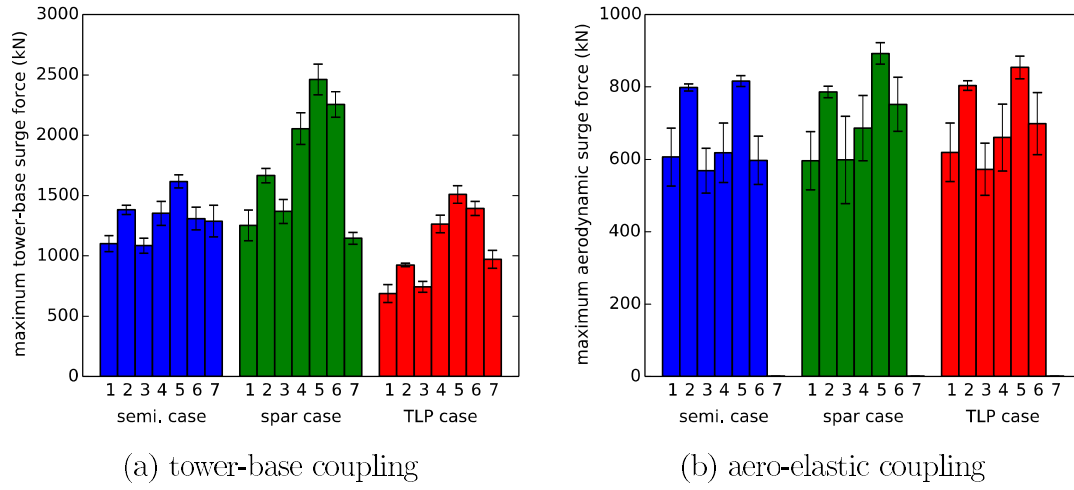


Figure 3.11: Maximum surge forces at coupling point

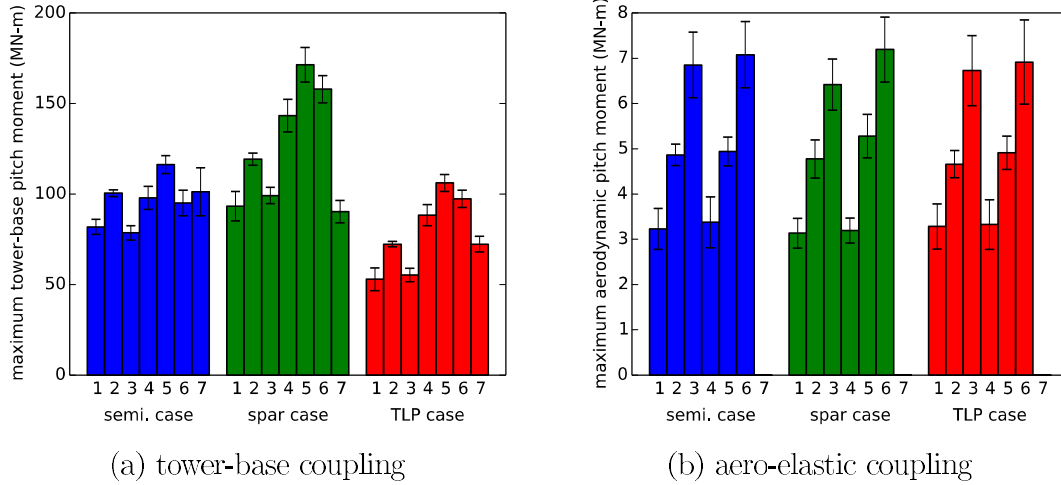


Figure 3.12: Maximum pitch moments at coupling point

tower-top in an aero-elastic hybrid coupling. As expected, the aero-elastic coupling approach is less demanding in terms of actuation.

3.3.3 Summary

From the means and standard deviations of the extreme displacements, velocities, and forces calculated in the simulations, estimates of the required coupling system performance envelope can be made. Tables 3.4 and 3.5 give a demonstration of

this, showing the minimum requirements for a coupling system to support the motions and forces of all three support structure designs in all seven load cases considered. Here the requirements are based on a “three-sigma” approach in which each value is set at three standard deviations above the mean extreme value. If the extremes values were normally distributed, this approach would imply a 99.7% probability of having the required performance for the most challenging of the cases considered in a test of 10 minutes duration. For the tower-base coupling case, the indicated force in the heave direction excludes the steady contribution of turbine weight.

Table 3.4: Range, velocity, and force requirements for tower-base coupling, all designs

	Surge	Sway	Heave	Roll	Pitch	Yaw
range (m, deg)	25.3	3.5	5.8	2.5	9.2	11.2
max. velocity (m/s, deg/s)	3.62	0.32	1.19	0.31	1.94	0.90
max. force (kN, MN-m)	2848	379	354	33.5	200	9.0

Table 3.5: Range, velocity, and force requirements for aero-elastic coupling, all designs

	Surge	Sway	Heave	Roll	Pitch	Yaw
range (m, deg)	31.1	6.5	5.7	2.8	10.7	11.2
max. velocity (m/s, deg/s)	5.90	0.70	1.09	0.39	2.34	0.91
max. force (kN, MN-m)	982	128	232	14.2	9.7	8.3

The use of six simulations with 10 minute durations for each case gives results that reflect general magnitudes and trends for the three floating wind turbine designs considered. Safety factors could be applied to these results in order to ensure that a hybrid coupling system is developed to specifications that exceed all requirements. For a greater level of precision in determining specifications, particularly when the exact designs and load cases of interest are known and the project size justifies use of extra computational resources, it would make sense to

use longer simulation durations and consider more stochastic wind-wave realizations per case.

3.4 Hybrid Coupling Quality Requirements

The second half of the performance specifications relates to the quality of the hybrid coupling. I represented the requirements in terms of limits on the noise in motion capture, noise in actuated forces, and latency between measuring motions and applying the calculated reaction forces. As described in Section 3.1.3, appropriate limits can be determined by inserting various amounts of each type of error into simulations and analyzing how the results change. Normal, unperturbed simulations serve as a baseline case for comparison. I quantified deviations in the results of perturbed simulations by taking the standard deviation of the residual between the time-series output of the perturbed simulation and that of the baseline. I normalize this standard deviation by the standard deviation of the baseline simulation’s time series to yield a relative error, expressed as a percentage in the plots that follow.

I considered three channels in this sensitivity study: platform surge, platform pitch and tower-base bending moment (abbreviated as “moment” in the plot legends”). Platform surge and pitch are the two global response parameters most affected by the turbine. Tower-base bending moment is useful here because it is a design-driving turbine load that is affected by the turbine and will be affected by both tower-base and aero-elastic hybrid coupling schemes. It is also the most relevant of the three channels since the greatest impact of the hybrid coupling system is expected to be in the simulated dynamics of the wind turbine rather than in the physical motions of the platform. Also, the importance of platform surge and pitch depend heavily on the support structure design. Therefore, I

focused on tower-base bending moment in the analysis; platform surge and pitch are shown only for comparison.

I used a single load case for the sensitivity analysis for the sake of computational manageability, case 6 of Table 3.1. This load case features the turbine's rated wind speed for DLC 1.6 wave conditions, which is a 50 year extreme case as specified in the ABS guide for floating wind turbines [84]. Comparison of the sensitivity to hybrid coupling errors across different load cases showed that the sensitivity tends to be inversely proportional to the severity of the load case, a result that makes intuitive sense in light of how the sensitivity is based on a value normalized to the standard deviation of the original time series. Ultimately, if this normalized metric is used, it should be applied to the load case that represents the most crucial conditions being evaluated in a wave-basin test requiring wind loads. For the purpose of demonstrating the method, I took that load case to be the 50-year storm condition of DLC 1.6 at rated wind speed where the influence of aerodynamics on the floating structure is greatest. While the sensitivity would be greater in the milder conditions of a DLC 1.2 scenario, basin test results in such a case would likely be less design-driving. Ultimately, the approach shown here should be applied to the load case(s) of greatest interest for a given application.

I examined the effects of noise in motion tracking of the coupling point in translational and rotational measurements separately since their relationship may depend on the motion tracking technology being used. I describe all noise magnitudes in terms of root-mean-square (RMS) values. I simulated noise levels in translational motion tracking at up to 0.4 m RMS for the tower-base coupling and 1.6 m RMS for the aero-elastic coupling. The resulting normalized RMS discrepancies in the platform surge, and platform pitch, and tower-base bending moment are shown for the three designs in Figure 3.13. In terms of change in

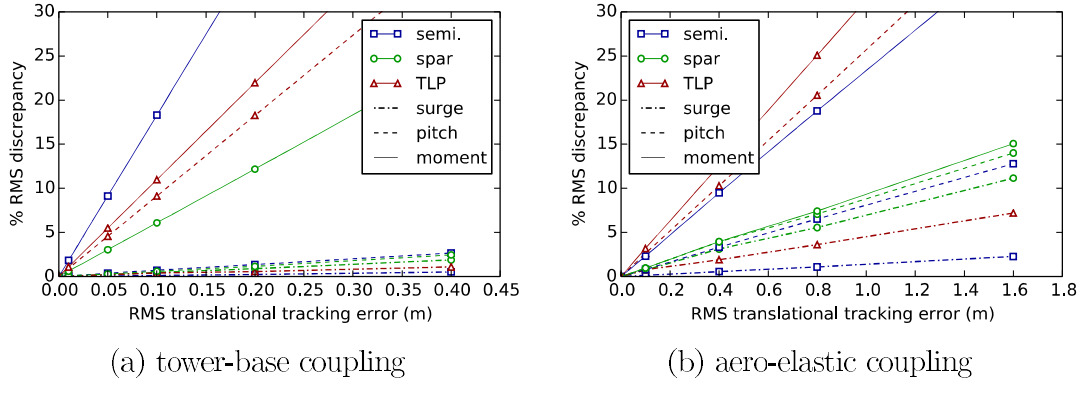


Figure 3.13: Sensitivity to translational motion tracking noise

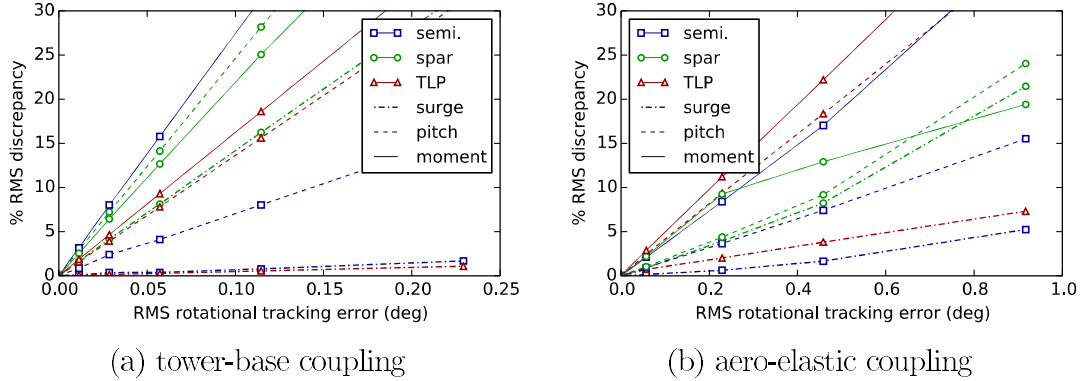


Figure 3.14: Sensitivity to rotational motion tracking noise

tower-base bending moment, the results show the tower-base coupling to be much more sensitive to measurement noise than the aero-elastic coupling.

Sensitivity to errors in tracking the coupling point orientation is shown in Figure 3.14. Here again the sensitivity of the tower-base coupling case is much greater than that of the aero-elastic coupling case. The spread of sensitivities between different designs, however, is narrower than for the translational motion tracking errors.

I analyzed sensitivity to noise in the forces and moments applied by the actuation system separately because their ratio would depend on the actuator design. The sensitivities to these force and moment perturbations are shown in Figures 3.15 and 3.16, respectively.

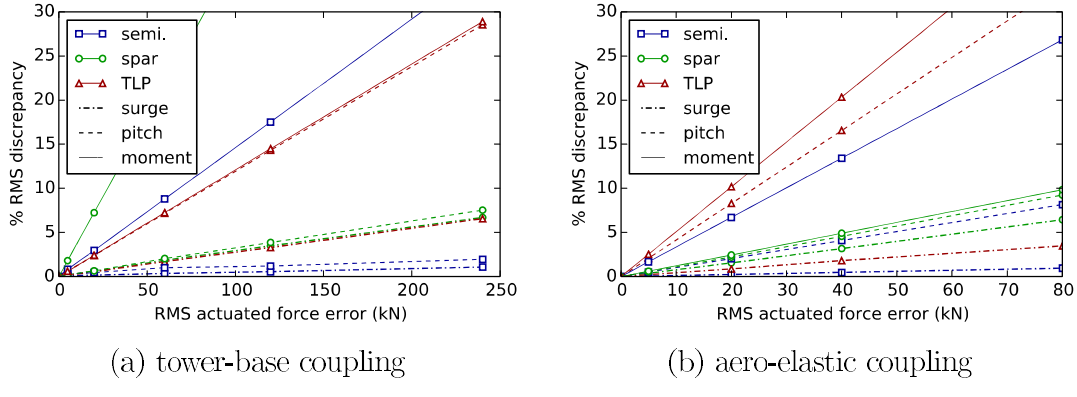


Figure 3.15: Sensitivity to noise in actuated force

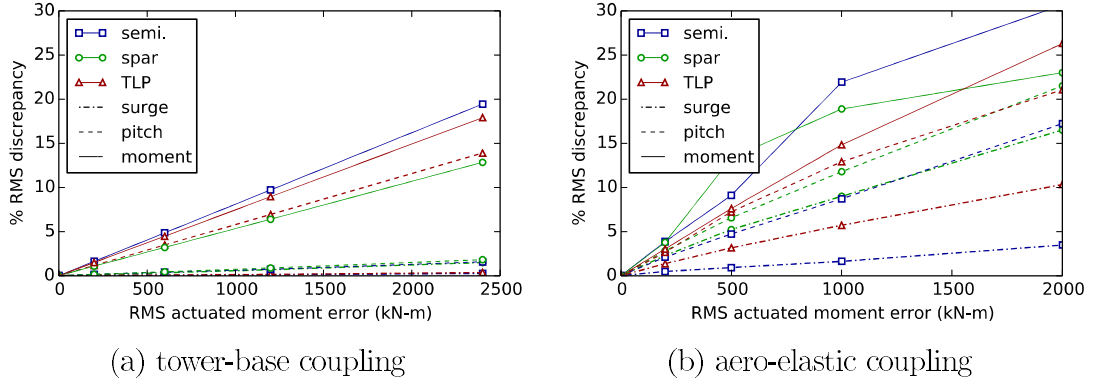


Figure 3.16: Sensitivity to noise in actuated moment

For the effect of force errors on tower-base bending moment, the spar design is the most sensitive in the tower-base coupling case and the least sensitive in the aero-elastic coupling case, likely a result of its low center of mass and large pitch inertias. The sensitivities of the semisubmersible and TLP designs are similar in both cases. For noise in moments, the sensitivities of all three designs are similar.

The effect of latency in the hybrid coupling is shown in Figure 3.17. As is apparent, the aero-elastic coupling case can tolerate latencies of more than one second without drastic changes in the results. The tower-base coupling case meanwhile suffers from large response changes and even simulation divergence or instability with just several tenths of a second of latency, presumably because of the significant high-frequency structural loads that are passed through the tower base.

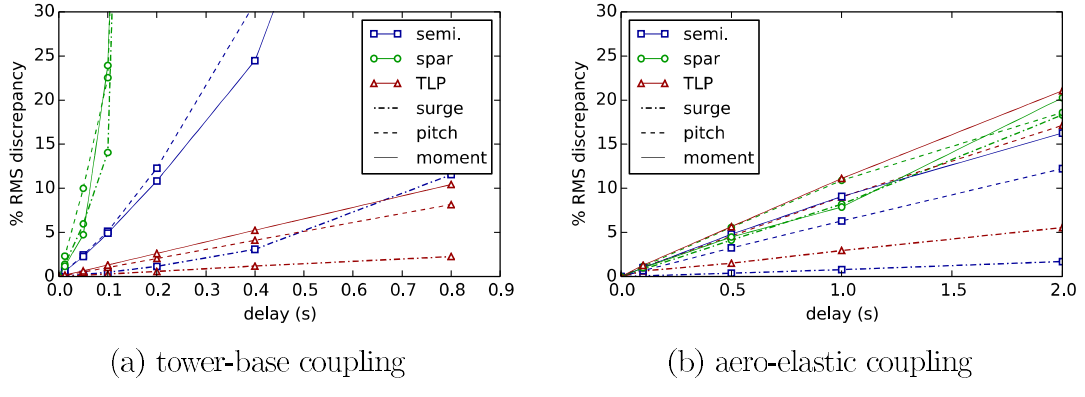


Figure 3.17: Sensitivity to latency in coupling

The low sensitivity to latency in the aero-elastic case reflects that much of the dynamic loading at the tower base comes from inertial rather than aerodynamic forces and is therefore less affected by delay in the aerodynamic loading.

3.4.1 Summary

The curves in Figures 3.13 to 3.17 show the sensitivity of simulated hybrid model accuracy to different types of errors that could be present in a hybrid coupling system. The sensitivities are for the most part linear but they vary in magnitude for the different support structure designs. These curves can be used to identify coupling error bounds necessary for keeping a given level of accuracy in a hybrid model.

The degree of accuracy desired in the model results is case specific. For the sake of demonstration, I used the criterion that tower-base bending moments in the hybrid model should stay within 10% of those in a perfectly-coupled model. In other words, discrepancies introduced by the hybrid coupling should be less than 10% in the relative RMS sense discussed earlier. Since this is based on a time series comparison in which phase differences can contribute significantly to the measured discrepancy, the difference in load metrics of interest is much less than 10%. This

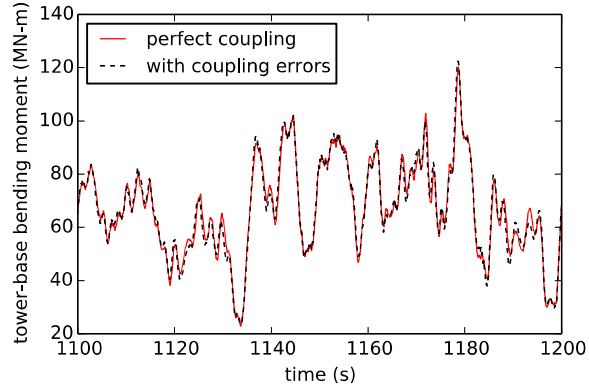


Figure 3.18: Tower-base bending moment time series comparison for a case with 11.3% RMS relative discrepancy

is illustrated in Figure 3.18, which shows time series of tower-base bending moment in an unperturbed case and in a case with 11.3% RMS discrepancy; the characteristics of the loads can be seen to be very similar.

Based on the sensitivity findings already presented, Table 3.6 lists the individual error tolerances required to keep discrepancies in the tower-base bending moment to less than 10% for all three of the support structure designs. I calculated these values by interpolating or extrapolating the 10% intercept in the sensitivity curves. As such, they satisfy the 10% discrepancy requirement only if a single one of the errors is present at a time. In a real case, however, the different types of coupling errors would be present in combination, in which case their impact on the model accuracy would compound. The bottom row of Table 3.6 shows the percent discrepancy in tower-base bending moment when these errors, at levels that individually give a 10% discrepancy, are combined; the result is approximately double the individual discrepancy level. Determining specifications for a hybrid coupling system therefore requires analysis of the effects of the various coupling imperfections in combination. A demonstration of this is given in Section 3.4.3.

Table 3.6: Individual tolerances for 10% RMS discrepancy in tower-base bending moment

	Tower-Base Coupling			Aero-Elastic Coupling		
	semi.	spar	TLP	semi.	spar	TLP
latency (s)	0.19	0.06	0.77	1.13	1.17	0.90
position error (m)	0.055	0.164	0.091	0.422	1.070	0.318
orientation error (deg)	0.036	0.045	0.062	0.272	0.276	0.204
force error (kN)	68.3	27.7	82.8	29.8	80.0	19.7
moment error (kN-m)	1234	1870	1341	472	530	673
combined discrepancy	23%	22%	24%	19%	23%	21%

3.4.2 Discussion

The sensitivity data yield some important observations about the effect of coupling errors on the modeling results.

First, as might be expected, a hybrid model that couples at the tower-base interface is much more sensitive to coupling quality than a hybrid model that is coupled at the aero-elastic interface. Coupling through a solid structural member such as the base of the tower is demanding because of the high-frequency loads that are present, whereas coupling at the aero-elastic interface is easier since the aerodynamic loads act predominantly at lower frequencies.

Second, results of different support structure designs are more sensitive to different types of coupling error. This can be attributed to the platforms having different magnitudes of reactions to coupling errors because of their different inertial properties and also to these magnitudes being of different levels of importance in light of the baseline load levels of each design.

Third, the different types of coupling errors act in combination with each other to produce discrepancies in the model results. A given amount of discrepancy can be produced by different combinations of coupling errors, whether only latency, only

force actuation noise, or a combination. This implies that different coupling error tolerances can be traded off against each other when trying to achieve a given discrepancy limit. This is important because it provides some flexibility in finding an optimal set of performance specifications, for example in satisfying requirements of different support structure types. Given this flexibility in error tolerances, coming up with a good set of specifications requires knowledge of the costs and constraints of the various coupling quality determinants. An example of how a specification set can be found, if some of these value are known beforehand, is given in Section 3.4.3.

3.4.2.1 Replacing Latency with Motion Tracking Noise

There is in general a practical trade-off between latency and motion-tracking error in a hybrid coupling application. Noise in motion tracking can be reduced by real-time filtering, but this inevitably adds delay in proportion to the level of filtering. Conversely, delay can be reduced by compensated techniques such as extrapolation [10], but this has the effect of increasing noise in the measurement. It should also be noted that delay compensation has implications for bandwidth: a low-pass frequency response needs to be enforced to ensure stability. Delay compensation could also be applied at the force actuation stage, but the likelihood of feedforward control in the actuation system makes this option less practical than compensating at the motion tracking stage. These issues are discussed in Chapter 4.

Given the ability to trade-off different error tolerances and the high sensitivity to latency found in the present results, it would seem generally advisable to compensate for latency (at the expense of motion tracking noise) in a hybrid modeling system for basin testing floating wind turbines. The feasibility of this is

of course subject to the equipment capabilities and modeling goals of the specific application.

3.4.2.2 Sensitivity to Coupling Bandwidth

An important issue that emerged in this work was that of coupling errors exciting structural resonances in the physical portion of the model. The introduction of band-limited white noise to simulate errors in motion tracking and force actuation adds energy to the system. This energy can result in increased excitation of modes whose natural frequencies are in the range of excitation.

This was particularly problematic for the aero-elastic coupling approach. As mentioned in Section 3.1.3, I reduced the cutoff frequency of the noise added to simulate errors in the aero-elastic coupling to 0.25 Hz in order to avoid exciting the first tower bending mode. To demonstrate the difference this makes, Figure 3.19 shows how the discrepancy induced by force noise changes when different cutoff frequencies are used. The coupling error in these tests was force noise at a level of 40 kN RMS. As can be seen, a dramatic increase in sensitivity occurs with increasing cutoff frequency in the proximity of the tower-bending natural frequency.

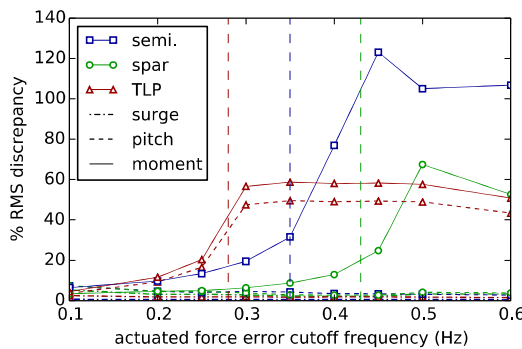


Figure 3.19: Sensitivity to force noise cutoff frequency in aero-elastic coupling (vertical lines indicate first tower bending natural frequency)

Although excluding the tower bending modes from the aero-elastic hybrid coupling may seem limiting, the results suggest that a good representation of the coupled response can still be achieved. The very low sensitivity to latency in the aero-elastic coupling case (Figure 3.17b) indicates that aero-elastic interactions at higher frequencies have little impact on the results being considered. If aerodynamic forces at 0.5 Hz were important to the coupled response, then a coupling latency of 0.5 s (a 90 degree phase lag) would yield much larger changes in the results than have been seen in this work. Accordingly, it seems in this case that a coupling system with a lower cutoff frequency can avoid the problem of exciting tower bending modes without having a large impact on the hybrid system's response.

3.4.3 Demonstration of Finding Specifications

To show how the coupling error simulation technique can be used in determining specifications for a hybrid coupling system, I created a case study based on estimated conditions at UMaine. I assumed a scale of 1:50 and all numbers are in model rather than full scale in order to base the analysis on real equipment capabilities. This case study seeks to find specifications for a hybrid coupling system suitable for all three designs studied and uses as a target that discrepancies introduced in the tower-base bending moment be limited to 10%. Like the preceding work, I carried out the analysis for both tower-base and aero-elastic coupling types.

An early 1:50-scale wind-wave test at the UMaine W² facility showed high-frequency noise or error in position measurements at a level of 0.25 mm RMS (12.5 mm full scale) and in orientation measurements at a level of 0.003 degrees RMS. As mentioned in Section 3.4.2.1, it may be advisable to compensate for

latency in the coupling system. Although delays are inherent in the measurements, the simulation process, and the actuation response, the use of delay compensation techniques makes it possible to remove latency in the coupling subject to limits imposed by measurement noise and required system bandwidth. Some noise amplification is inherent in the delay compensation. I multiplied the noise level by a factor of two to account for this, an estimate based on experience given an assumed 20 ms measurement-control-actuation latency and a capability of 3.5 Hz (0.5 Hz full scale) system bandwidth. This gives expected achievable motion tracking noise limits of 0.5 mm and 0.006 degrees.

What remain to be specified are the error levels in the forces and moments applied by the actuation system. Without confining the analysis to a certain type of actuation system, it is possible to estimate the ratio between errors in actuated forces and moments by choosing a reasonable characteristic spacing of the actuator's connection points on the floating system. I assume this spacing is 0.5 m (25 m full scale). This constitutes the ratio of force versus moment errors, leaving the magnitude of either of them as the one remaining independent variable. The magnitude of these actuation force/moment errors that gives the targeted amount of discrepancy in tower-base bending moment (or any output quantity of interest) can then be found, defining the actuation accuracy tolerance that needs to be met in realizing a hybrid coupling system.

I ran simulations in which these magnitudes were varied, while maintaining the 0.5 m ratio between force and moment noise levels. These simulations also included the estimated errors in motion tracking, thereby representing the entire set of expected coupling errors. Figure 3.20 shows the resulting normalized RMS error in tower-base bending moment for the different actuation error magnitudes.

Although both force and moment errors are present, the curves are with respect to

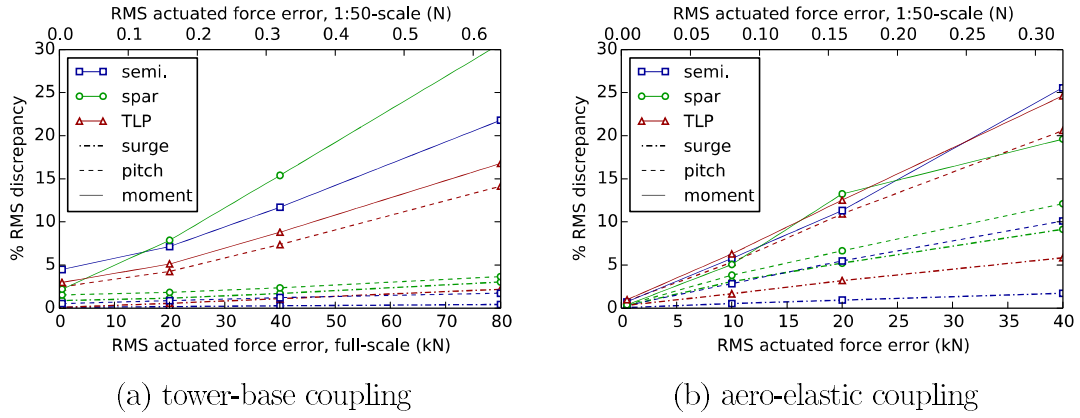


Figure 3.20: Effect of noise in actuated force at 1:50 scale

the force error level since the effect of moment errors is small at these magnitudes (as indicated by Table 3.6).

It can be seen that, as with the earlier sensitivity results, there are significant differences between designs and between the two coupling types. The tight tolerances for motion tracking required by the tower-base coupling mean that the discrepancy levels from the expected motion tracking errors are significant (the y-axis intercept in Figure 3.20a) while they are negligible for the aero-elastic coupling case. However, the similar force noise sensitivities make the actuated force error tolerances that satisfy all three designs have a similar order of magnitude for both coupling types: 0.21 N (26 kN full scale) RMS for tower-base coupling and 0.13 N (16 kN full scale) RMS for aero-elastic coupling. These values can be used to inform the design of the actuator and control system. To summarize the results of the case study, based on the assumed capabilities of the motion tracking and control/coupling systems, the specifications required for 10% accuracy in hybrid model test results are shown in Tables 3.7 and 3.8. As before, the maximum force in heave excludes the steady component from turbine weight. I assumed delays are fully compensated for so no latency tolerance is shown.

Table 3.7: Example 1:50-scale specifications for tower-base coupling

	Surge	Sway	Heave	Roll	Pitch	Yaw
max displacement (m, deg)	0.506	0.071	0.116	2.5	9.2	11.2
max velocity (m/s, deg/s)	0.51	0.05	0.17	2.2	13.7	6.4
max force (N, N-m)	22.8	3.0	2.8	5.4	32.0	1.4
motion error (mm, deg)		0.5			0.006	
force error (N, N-m)		0.21			0.10	

Table 3.8: Example 1:50-scale specifications for aero-elastic coupling

	Surge	Sway	Heave	Roll	Pitch	Yaw
max displacement (m, deg)	0.621	0.129	0.113	2.8	10.7	11.2
max velocity (m/s, deg/s)	0.83	0.10	0.15	2.8	16.6	6.4
max force (N, N-m)	7.9	1.0	1.9	2.3	1.6	1.3
motion error (mm, deg)		0.5			0.006	
force error (N, N-m)		0.13			0.06	

Looking at the specifications for 1:50-scale testing, the requirements appear to be achievable. The displacements, velocities, and forces required of the actuator in both coupling cases reflect the expected dynamics at 1:50 scale. The tower-base coupling has somewhat larger force and moment actuation requirements given the inertia and moment arm of the turbine. The force error tolerances do not seem unreasonably small compared to the force magnitudes required of the actuation system. I calculated the motion tracking accuracy limits based on observed noise levels in translational and rotational tracking from existing equipment and these can be seen to satisfy the 10% RMS discrepancy limits. It is also worth noting that this 10% discrepancy level is a time-series measure that responds strongly to small changes in phase (as shown in Figure 3.18); accordingly, more generous tolerances are likely suitable for many applications.

3.5 Conclusions on Performance Specifications

The main challenge of hybrid modeling lies in the coupling system that connects the physical and numerical sub-models. The work of this chapter sought to shed light on the requirements for, and implications of, the performance of that coupling.

I ran and analyzed simulations of three floating wind turbine designs under a variety of load cases to find the performance envelope requirements of a hybrid coupling system in terms of displacements, velocities, forces, and bandwidth. The results are full-scale values that can be scaled to inform actuation system design for hybrid modeling at any given scale.

I studied coupling quality requirements by running simulations of a typical load case and introducing errors that represent flaws in the hybrid coupling. By delineating relationships between these errors and the discrepancies they produce in key output channels like tower-base bending moment, I demonstrated how tolerances for motion tracking errors, force actuation errors, and latency of a hybrid coupling system can be chosen based on desired overall accuracy targets.

A case study demonstrated the application of these techniques. Using input parameters based on experience with the UMaine W2 facility, the method suggested that implementing a hybrid coupling system that keeps relative RMS errors in the tower-base bending moment below 10% is achievable. The conclusions for a different context with different equipment capabilities could be different.

Aside from the quantitative findings which can be used to create coupling system specifications, the sensitivity study produced some qualitative conclusions:

- Tower-base coupling has much tighter requirements on latency and motion tracking error than aero-elastic hybrid coupling because of the structural connection.
- The sensitivity to different types of coupling error changes depending on the support structure design.
- Different types of coupling error act in combination with each other and different error tolerances can be traded off against each other when trying to achieve a given discrepancy limit.
- Excitation of the first tower bending mode may be a problem, particularly in aero-elastic coupling, and can be avoided without significant detriment to the coupled response by setting the bandwidth of the coupling system below this natural frequency.

In addition to the two aerodynamics-focused hybrid modeling scenarios, I also applied the methods presented above to consider the requirements of a mooring-focused hybrid coupling. In this scenario, MoorDyn would be used to calculate mooring loads to apply on a floating wind turbine experiment. Those results are given in Appendix A.

The qualitative findings in this work shed light on how coupling errors will effect hybrid model results. The quantitative findings can be turned into performance specifications to use in developing a hybrid coupling system. These specifications can inform first the selection of an appropriate actuation method and then the sizing and equipment selection of the actuation system. These matters are part of the discussion of the next chapter, which addresses the design of a hybrid actuation system.

Chapter 4

THEORETICAL DEVELOPMENT OF HYBRID MODELING

This chapter discusses the theoretical development of a hybrid modeling approach for floating wind turbines in basin testing. In other words, it explains the development of a strategy for dynamically coupling a scaled physical model of a floating support structure in a wave basin with a numerical model of a wind turbine. The next chapter will then describe how I put this strategy into practice.

Many considerations go into devising a hybrid coupling approach, such as how simulation outputs will be actuated onto the physical sub-model, how measurements will be made in order to drive the numerical sub-model, and how inertia will be divided between both sub-models. The discussion is kept general where possible. When specifics are needed, the focus is on the aero-elastic hybrid modeling type as described in the last chapter since this is the least demanding approach and the one most easily applied to testing at the UMaine W² facility.

4.1 Physical and Numerical Sub-Models

The goal of this work is to develop a hybrid modeling system suitable for use at wave basin facilities such as the one at UMaine or MARIN. Scale-model floating wind turbines are usually tested at on the order of 1:50 scale at such places. The DeepCwind semisubmersible discussed in Section 2.2.4.1 is representative of a design that might be used in these tests, and considering it has already been widely studied and is being used for facility validation at UMaine at 1:50 scale, I

chose this as the target of the hybrid coupling system. Characteristics of the design are shown in Table 2.3.

While this design serves as the target, it is likely that the hybrid modeling system could work equally well for other floating wind turbine designs at similar scale.

The findings in the previous chapter suggest that the coupling system would not give significantly worse results for the DeepCwind Spar or TLP designs.

During the process of developing the system, I used “dry” proxies for the floating platform in the form of pendulums with large towers. The pendulum’s single rotational DOF can be tuned to mimic the pitch response of a floating wind turbine platform. I reduced the size to represent 1:100-scale dynamics for the sake of safety while developing the system. The pendulum used for the majority of testing is detailed in Section 5.2.1.

The numerical model used is the wind turbine portion of FAST v7. I set up the simulation to match the aero-elastic coupling case discussed in the previous chapter, in which only aerodynamic forces are passed from the simulation to the physical model (via the yaw-bearing forces in FAST) and the coupling point is at the nacelle of the turbine. To achieve this, I disabled all structural degrees of freedom and set the rotor and nacelle mass to zero to exclude inertial loads. The exchange of motions and aerodynamic reaction forces follows the approach described in Section 2.1.

4.2 Actuation System

A key challenge of developing the hybrid modeling system is designing an actuation system that can meet the force and motion requirements while also being practical in terms of controls, logistics, and cost.

4.2.1 Actuator Type

A number of established 6-DOF actuator types exist that could be appropriate as a basis for what is needed for the hybrid coupling. These include

- a serial manipulator, the stereotypical “robot arm”;
- a Stewart platform or ‘hexapod’, the common choice for high-load low-range 6-DOF actuation needs;
- a delta robot, a very fast, lightweight translational manipulator, with the addition of a “wrist” for rotations;
- a gantry robot, common in machining and 3D printing, with the addition of a wrist;
- a cable robot, a redundant parallel manipulator based on winches;
- a fan or system of fans mounted on the platform itself, as has been explored by others.

For the sake of time in a PhD scope, rather than quantitatively evaluating each actuation alternative, practicality required that a single strategy be chosen based on limited knowledge and then that strategy be explored and developed.

Considering the possibilities qualitatively, the serial manipulator is structurally simple and has good range but is problematic because of its high inertia, the expense of harmonic drives necessary for achieving good stiffness, and the control challenge of inverse kinematics and changing dynamics of a serial manipulator.

The Stewart platform, in contrast, has very high stiffness, affordable cost, and acceptable response time. However, for its size, its range of motion is quite limited. A Stewart platform is better suited to large-force small-motion applications, which is the opposite of scale-model floating wind turbine testing. A delta robot is light

and fast and has reasonable stiffness. Unfortunately, the addition of a wrist or other means of providing rotational DOFs adds inertia and complexity, reducing the advantage of the design. That said, approaches to expand the delta configuration to 6 DOFs could be worth exploring. A gantry robot, while simple in design and control, has very high inertia and slow response time. Cable robots offer a large and expandable workspace, very low inertia and fast response, and affordability. However, they are less stiff than some other options. Lastly, platform-mounted fans are attractive because they simplify the control problem significantly, and are affordable. However, work so far suggests bandwidth limitations may constrain their applicability to only the less challenging coupling situations.

Weighing the above qualitative characteristics, as well as published values related to the performance of various options, I selected a cable robot as the most promising approach to develop. Its low inertia makes this type highly responsive without attendant control challenges. The use of cables lends itself to large workspaces and reconfiguration to meet different trade-offs between range and precision.

4.2.2 Background on Cable Robots

Cable robots, also known as wire robots or cable-driven parallel manipulators, have been under study since the 1990s, primarily as a way to improve the response, range, and affordability of existing parallel manipulators having rigid links. Low inertia gives cable robots very fast response characteristics. As early as 1995, Kawamura et al. demonstrated accelerations of 43 Gs, speeds of 13 m/s, and effective control of vibrations all while using inexpensive 60 W direct-current (DC) motors [88]. As well, cable robots can work over large workspaces without

increased cost because the distance-spanning structure of the actuator is made from inexpensive cable.

Because cables only perform in tension, a distinguishing feature of high-performance cable robots compared to many other common actuator types is redundancy; a cable robot should have at least one more cable than the number of platform’s DOFs being controlled. A 6-DOF cable robot will have at least 7 cables. The term “redundant” is used here and in the literature to refer to the number of actuator axes exceeding the number of controlled platform DOFs and is not meant to imply any degree of excess or backup in the system.

The consequence of redundancy in a cable robot is that the force on the platform and the overall amount of tension in the cables can be controlled independently [89]. This ensures that the cables are under adequate tension at all times. It can also play a role in controlling vibrations because of the nonlinear relationship between cable tension and manipulator stiffness [88, 90]. The mechanics involved in redundant cable robots are discussed in Section 4.2.5.

4.2.3 Actuator Modularity and Reconfigurability

Cable robots allow a degree of modularity since each actuator axis consists of a separate winch unit and the only physical interconnection is in the attachment of the cable ends to the actuated platform. Each winch unit can be considered a separate module and, through different numbers and arrangements of winch units, a cable robot can be reconfigured for different applications

A given winch unit needs to hold a motor and drum for spooling the cable, and one or more sensors for feedback to the control system. The choice of feedback measurements is discussed in Section 4.2.4. The motor and spool mechanism can

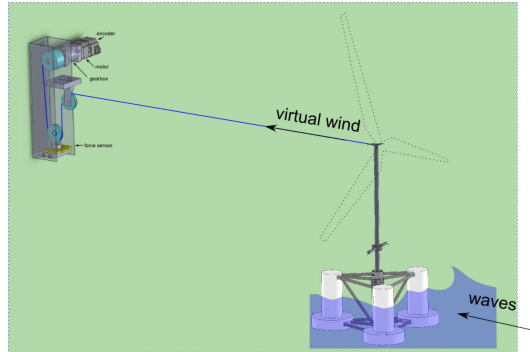
be as simple as a directly-driven drum although more sophisticated approaches exist. Details of the winch unit design I developed are given in Section 5.1.1.

Cable robots make it convenient to actuate a reduced numbers of DOFs, and this suits the floating wind turbine application well. With appropriate winch locations and platform connection points, six possible degree-of-freedom arrangements can be achieved, ranging from a single direction to all six [91].

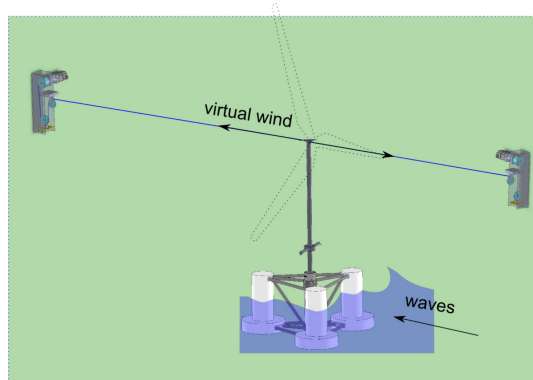
By developing a coupling system that acts in a single DOF, the approach can be refined and proven under simpler conditions and at less investment. This is the approach I followed in this work, focusing on the fore-aft DOF at hub height while leaving the other DOFs unaffected. The fore-aft DOF is the direction along which the main component of the aerodynamic forces acts. A single cable could be used if the force of the turbine can be assumed to always be in one direction (Figure 4.1a), or a redundant two-cable arrangement could be used for greater performance (Figure 4.1b). Early experiments showed that the redundant two-cable is much more practical from a control point of view.

From the initial one-DOF arrangement, whether redundant or not, another cable can be added to provide coupling in a second DOF, such as side-side translation (Figure 4.2) or pitch (Figure 4.3). Additional DOFs could be added in this same piecewise fashion. The end goal is full six-DOF control using 7 or 8 drive units, as drawn in Figure 4.4. In this case, there is greater flexibility in the coupling point location and the types of loads that can be actuated since all forces and moments can be controlled separately.

A cable-based hybrid coupling system could also be adapted to other applications, such as testing of airborne wind energy converters tethered to floating platforms offshore. Conventional wind-wave model testing of these devices would be nearly



(a) non-redundant

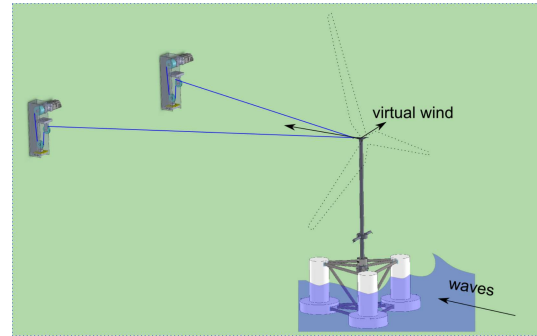


(b) redundant

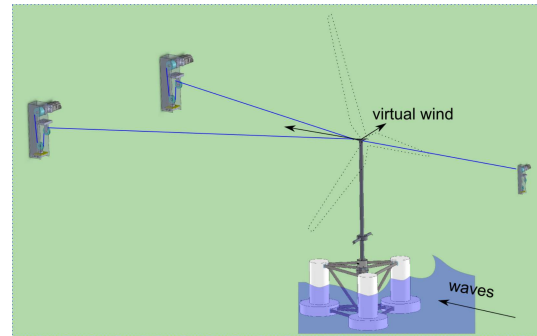
Figure 4.1: Single DOF (fore-aft) actuation configurations

impossible because of the high altitudes involved. Hybrid modeling, however, could be used to apply realistic loads on the floating platform based on a simulation of the airborne turbine. Since the turbine is tethered to the platform, a system of three winch units arranged as shown in Figure 4.5 could be used to provide the simulated turbine forces.

The use of a cable robot in comparison to other actuation approaches also has benefits in terms of adapting to different scales. Provided the motors and winch units are adequately sized, the same system could be set up for 1:100-scale tests with the winch units at a distance of 2 m or 1:50-scale tests with the winch units at a distance of 8 m with only minor adjustments.

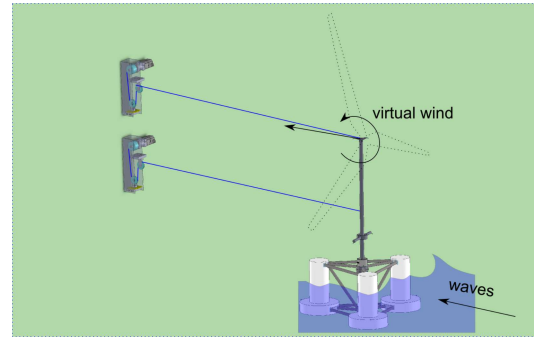


(a) non-redundant

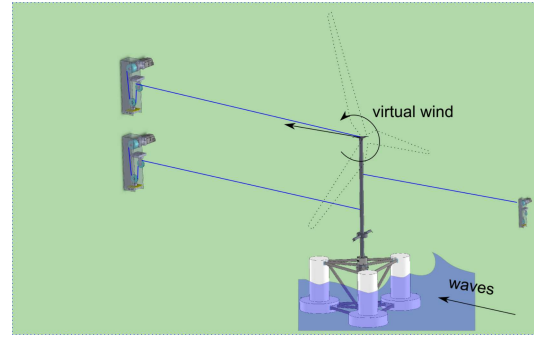


(b) redundant

Figure 4.2: Two-DOF (fore-aft and side-side) actuation configurations



(a) non-redundant



(b) redundant

Figure 4.3: Two-DOF (surge and pitch) actuation configuration

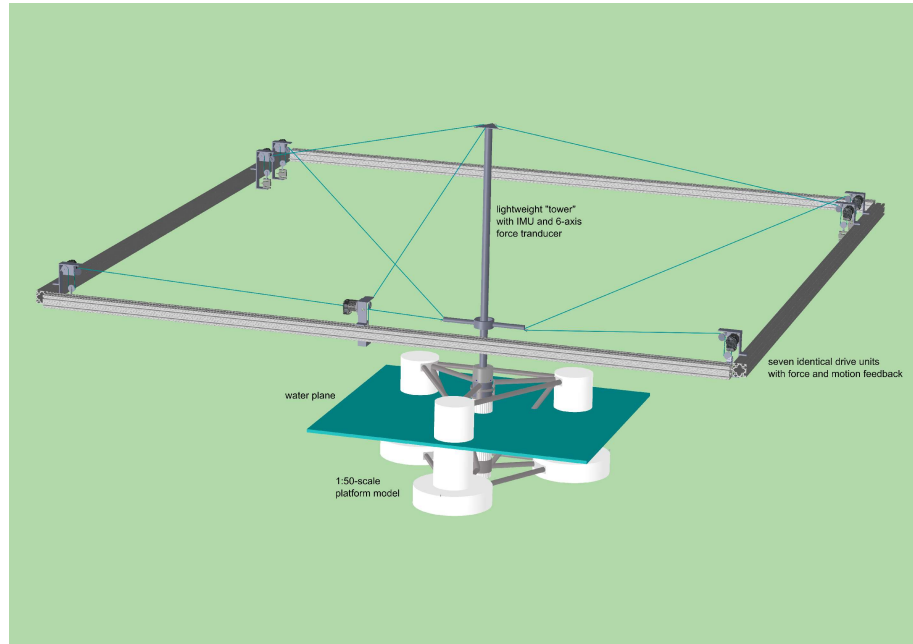


Figure 4.4: Tentative layout for a 6-DOF actuation system with a 1:50-scale floating platform

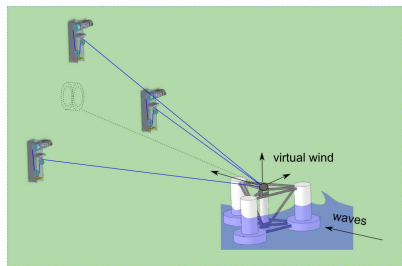


Figure 4.5: Configuration for airborne wind energy converter on floating platform

4.2.4 Measurements and Feedback

Measurements needed in the coupling system of a floating wind turbine hybrid model include measurements of the motions or forces at the coupling point, as well as separate measurement of motions or forces within the actuation system to provide feedback for actuator control. The proper allocation of force and motion sensing between the coupling point and the actuator depends on the application and the control approach.

4.2.4.1 Winch Instrumentation

There are many examples to draw from when it comes to winch design. Almost all designs incorporate encoder-based feedback to measure changes in line length (e.g. [88, 92, 93]). Not all incorporate direct tension measurement in the winch units; instead, some infer tension from motor current (e.g. [90]), some use load cells on the platform (e.g.[92]), and some avoid estimating cable tension completely (e.g. [93]). This is possible because accurate measurement of the tensions is only required in some applications. For the control approach I adopted, which is explained more in Section 4.3, measurement of each cable's tension is needed for tension-control feedback. I decided this would be most easily handled with a load cell in each winch unit.

Measurements of cable length and tension from the winch units could also be used to estimate the position of the platform and the forces acting across the coupling. However, it seems likely that more direct measurement of one of these quantities would be needed for good performance.

4.2.4.2 Centralized Instrumentation

Measurement of the force applied by the actuator could be done with a six-axis load cell at the connection point. This is expensive and adds mass in situations where such a load cell is not already in place. The alternative is to rely on individual cable tension measurements along with knowledge of cable directions to calculate the applied force. In the general case, knowing cable directions requires measurement of platform position.

Accordingly, I decided it would be best to measure the platform position directly using an optical tracking system. This is not a burdensome equipment requirement because most wave basin facilities already have high-quality optical tracking equipment in place for measuring prototype motions. In the UMaine W² facility, a Qualisys system provides this functionality. This system, like most of the options on the market, has a data streaming functionality that can allow the optical tracking to feed into a real-time control system.

As discussed further in Chapter 5, I used simpler position measurement solutions during the system development leading up to basin testing. Initially, I used an open-source optical tracking library, ARToolkit Plus, which uses a single camera and specially-patterned flat markers to track motion in six DOFs [94]. Later, for most of the work evaluating the control system, I used a string potentiometer to measure constrained motion in a single DOF.

4.2.5 Cable Robot Mechanics and Control

The theory for describing the mechanics of cable robots is well established and described in a number of papers (e.g. [95, 96, 97]). This section summarizes it briefly, assuming the general case of a cable system with m cables supporting a

platform free to move in n DOFs. For redundancy, $m > n$. The inverse kinematics, here meaning the mapping from platform position to cable lengths, can be expressed for a cable i as

$$l_i \mathbf{u}_i = \mathbf{a}_i - \mathbf{x} - \mathbf{R}\mathbf{b}_i, \quad (4.1)$$

where l_i is the cable length, \mathbf{u}_i is the cable tangent direction, \mathbf{a}_i is the winch location, \mathbf{b}_i is the cable's attachment point on the platform relative to the coupling point, \mathbf{x} is the position of the platform, and \mathbf{R} is a direction cosines matrix representing the orientation of the platform.

The Jacobian for the inverse kinematics of the entire cable robot is defined as

$$\mathbf{A} = \frac{\partial \mathbf{l}}{\partial \mathbf{x}}, \quad (4.2)$$

where \mathbf{l} is a vector of the m cable lengths. This Jacobian gives the instantaneous relationship between winch and platform velocities:

$$\dot{\mathbf{l}} = \mathbf{A}\dot{\mathbf{x}}. \quad (4.3)$$

Commonly used when considering the actuator forces is the transpose of the Jacobian, \mathbf{A}^\top , referred to as the structure matrix. For a platform free to move in all six DOFs ($n = 6$), the structure matrix can be calculated as

$$\mathbf{A}^\top = \begin{bmatrix} \mathbf{u}_1 & \dots & \mathbf{u}_m \\ \mathbf{b}_1 \times \mathbf{u}_1 & \dots & \mathbf{b}_m \times \mathbf{u}_m \end{bmatrix}. \quad (4.4)$$

The vector of forces and moments on the platform, \mathbf{w} , often called the wrench, is related to the cable tensions, \mathbf{f} , by

$$\mathbf{w} = -\mathbf{A}^\top \mathbf{f} \quad (4.5)$$

Accordingly, any vector of cable tensions within the null space of \mathbf{A}^\top will apply zero net force to the platform. This is essential to the control of cables robots and

means that the desired cable tensions can be represented as a summation of two components:

$$\mathbf{f} = \mathbf{f}_w + \mathbf{f}_0. \quad (4.6)$$

The first component applies the desired wrench force on the platform such that $\mathbf{A}^\top \mathbf{f}_w = -\mathbf{w}$. The second component, the so-called ‘internal force’, controls the overall cable tension levels provided that $\mathbf{A}^\top \mathbf{f}_0 = \mathbf{0}$. The choice of \mathbf{f}_0 is not trivial.

Once the desired wrench force, \mathbf{w} , is known, the cable tensions can be set as long as they satisfy the vector closure condition ($\mathbf{A}^\top \mathbf{f} = -\mathbf{w}$) for the given platform position [90]. The difference between number of cables and number of DOFs ($m - n$) decides the dimension of the solution space. The challenge is in how to choose the solution within this space, i.e., what algorithm will provide practical tensions in all cases without slowing down the control loop? In terms of equation (4.6), the question is how do we choose \mathbf{f}_0 .

A variety of internal force control approaches have been proposed and demonstrated, ranging from simple heuristics to analytically-derived algorithms. Fortin-Cote et al. [93] show that a simple heuristic approach using a tension threshold to stop motors has been effective in motion control applications. The approach of Kawamura et al. [90] chooses one cable’s tension and calculates the remaining ones from the vector closure condition. Pott et al. [97] provide a more careful way of choosing the tensions in closed form by setting

$$\mathbf{f}_0 = \mathbf{f}_m - \mathbf{A}^{+T} \mathbf{A}^\top \mathbf{f}_m, \quad (4.7)$$

where \mathbf{f}_m is a vector whose elements are identically the desired mean tension and \mathbf{A}^{+T} is the Moore-Penrose pseudo-inverse of the structure matrix, defined as $\mathbf{A}^{+T} = \mathbf{A}(\mathbf{A}^\top \mathbf{A})^{-1}$ if $m > n$ and $\mathbf{A}^{+T} = (\mathbf{A}\mathbf{A}^\top)^{-1}\mathbf{A}$ if $m < n$.

This pseudo-inverse can also be used to rearrange (4.5), giving a total cable tension target, expanded from (4.6) of

$$\mathbf{f} = -\mathbf{A}^{+\top}\mathbf{w} + \mathbf{f}_m - \mathbf{A}^{+\top}\mathbf{A}^{\top}\mathbf{f}_m. \quad (4.8)$$

Techniques such as this provide the necessary building blocks for creating a cable robot control scheme.

4.3 Hybrid Coupling Control

Control in the context of a hybrid model includes two parts: the controller commanding the actuator, and the mathematical rules governing the connection between numerical and physical models.

Coupling between physical and numerical dynamics models requires prescribing a relationship between the kinematics and the forces at the coupling point. For this, some of the best material comes from the field of haptic interfaces, the specialization of robotics that deals with the sense of touch. That field typically uses a human hand or a surgery subject as the “physical model”, but the concepts are the same if the physical model is a floating platform. Two opposite control schemes exist for relating the kinematics and forces of a robot manipulator: impedance control and admittance control [98]. Figure 4.6 illustrates these for the tower-base hybrid coupling case.

An impedance-control coupling takes the physical motions as inputs to the numerical model and applies the calculated forces back onto the physical system. The measurement requirements can vary with the order of the model; i.e. modeling stiffness requires only position measurements, modeling damping requires measuring velocities, and modeling inertial effects requires measuring accelerations.

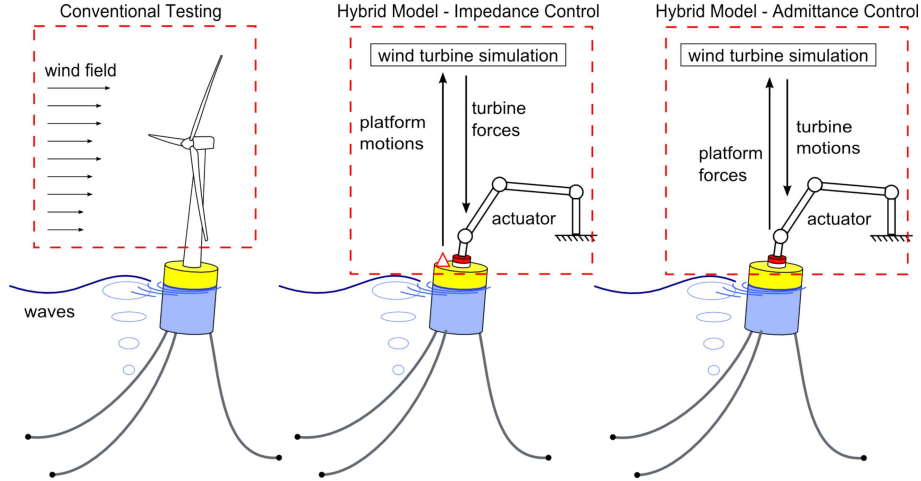


Figure 4.6: Hybrid model coupling schemes

One challenge is dealing with measurement noise if damping or inertia are to be modeled. Another is providing the output as a force – friction will affect torque-control approaches and force feedback adds a layer of control complexity.

Impedance coupling can be expressed as

$$\mathbf{w}_{sim} = \mathbf{F}_{sim}(\mathbf{x}, \dot{\mathbf{x}}, \ddot{\mathbf{x}}, t), \quad (4.9)$$

where \mathbf{w}_{sim} is the force to be applied onto the physical system, \mathbf{F}_{sim} is the functional form of the simulation, \mathbf{x} is the measured platform position, and t is time.

An admittance control coupling takes physical forces as inputs to the numerical model and applies the calculated motions back onto the physical system. Modeling the system inertia is required (otherwise the accelerations would be infinite). Because the input measurement is force, there is no additional noise caused by having to differentiate the inputs. The position/velocity/acceleration output is given as a command to each actuator axis and then standard servomotor controllers ensure these motions are achieved. This type of arrangement has the

advantage that friction in the actuator is not an issue, since it is easily compensated for by the servomotor motion controllers [93].

Admittance coupling can be expressed as

$$\ddot{\mathbf{x}}_{sim} = \mathbf{M}_{sim}^{-1}(\mathbf{w}_{sim}(\mathbf{x}, \dot{\mathbf{x}}, t) + \mathbf{w}), \quad (4.10)$$

where $\ddot{\mathbf{x}}_{sim}$ is the desired acceleration of the physical system as calculated by the simulation, \mathbf{M} is the mass matrix of the numerical portion of the system about the coupling point, \mathbf{w}_{sim} is the simulated force calculated inside the numerical sub-model, and \mathbf{w} is the force measured from the physical system that also acts on the numerical sub-model.

There are many nuances in how the two coupling schemes work, involving in particular how the output commands are implemented and how the inertia is divided between the physical and numerical parts of the model. Once the feedback loop(s) of the actuator controller are taken into account, an admittance coupling control can actually be considered a force control loop, with the modeled inertia being inversely proportional to the force controller's integral gain.

Separately from the coupling performance, the placement of the coupling point and the apportioning of system inertia need to be handled carefully in reduced-DOF applications if the system model is to remain valid. A one-DOF fore-aft actuation system with the coupling point at hub height raises a particular problem. If an impedance coupling is used and all the turbine mass is placed at the top of the physical tower, the system inertia will be reasonable (if the elasticity and mass distribution of the turbine can be neglected). If, however, an admittance controller is used with part of the turbine mass modeled numerically, the gravitational and vertical-acceleration forces from that mass will be excluded from the model because the actuator only operates in the fore-aft direction. This means

a $mgh \sin \theta$ term will be missing from the system's pitch response. To reduce this discrepancy, the numerical portion of the mass should be minimized – but this increases the potential for vibrations of the cable actuator. These are the sorts of challenges that exist in realizing a hybrid coupling.

The following subsections discuss the specific control approaches that could be used for hybrid coupling of a floating wind turbine system. Section 4.3.1 describes an approach I developed using admittance control that was ultimately unsuccessful. Section 4.3.2 describes the approach I developed using impedance control which, after the explained refinements, was successful in providing the required hybrid coupling.

4.3.1 Admittance Control Approach

For a multi-cable system, the admittance control approach initially seemed promising. It offers the benefits already mentioned of avoiding errors from friction and allowing inertia in the numerical model without acceleration measurements. Furthermore, work by others has shown that it can give high levels of performance; Ho et al. [92] achieved a bandwidth of 13.3 Hz in an admittance-controlled haptic interface. They used the internal force control method of Pott et al. [97].

The admittance control approach I developed combines elements from the approaches of Ho et al. [92] and of Fortin-Cote et al. [93]. As in [93], an admittance control scheme accepts the measured forces and calculates the resulting acceleration of the numerical portion. This is integrated to find the velocity at the next time step. Inverse kinematics is then used to find the appropriate speed commands to be sent to each motor:

$$\dot{\mathbf{i}}_{\mathbf{x}} = \mathbf{A} \left[\dot{\mathbf{x}}(t) + \int_t^{t+dt} \ddot{\mathbf{x}}_{sim}(\tau) d\tau \right] \quad (4.11)$$

where $\ddot{\mathbf{x}}_{\text{sim}}(\tau)$ is the acceleration at time τ calculated in the simulation.

Commanding motor speed rather than position allows the use of less expensive servo motors and has been suggested to reduce the likelihood of problems with jitter [93]. In this case, simulations of tension control on a spring with one end fixed showed that a proportional control approach is effective.

On top of the motor speed required for achieving the desired platform motion (4.11), an additional speed correction is needed to control the line tensions.

Whereas Ho et al. [92] used an unspecified LQR (linear quadratic regulator) controller to produce a *position* setpoint correction, I use a simple proportional controller to produce a *velocity* setpoint correction. The controller operates on feedback from the measured mean tension across all cables. In the simplest case, the controller for each cable's velocity correction would look like

$$\dot{t}_f = -K_p (f_{md} - f_m) \quad (4.12)$$

where, similarly to (4.7), f_{md} is the desired mean cable tension and f_m is the measured mean tension across all cables.

This equation is valid only in cases where equal cable tensions will result in zero wrench force (\mathbf{w}), such as in the case of two opposing cables controlling fore-aft motion at hub height. For the general case, the vector closure condition must be satisfied, ensuring that the wrench force contributed by this tension adjustment is zero. This can be done by adapting the form of (4.7). The resulting speed correction to ensure proper cable tensions is then

$$\dot{\mathbf{f}}_f = (\mathbf{I} - \mathbf{A}^{+\top} \mathbf{A}^\top) [-K_p (\mathbf{f}_{md} - \mathbf{f}_m)], \quad (4.13)$$

where the desired and measured mean tensions vectors, respectively, are

$$\mathbf{f}_{\text{md}} = \begin{Bmatrix} 1 \\ \vdots \\ 1 \end{Bmatrix} f_{md} \quad \text{and} \quad \mathbf{f}_m = \begin{Bmatrix} 1 \\ \vdots \\ 1 \end{Bmatrix} \sum_{i=1}^m f_i. \quad (4.14)$$

Since this approach seeks to control cable tension by adjusting cable length, it relies on the approximation of linear cable stiffness and the choice of K_p depends on the cable stiffness.

Adding the tension-management speed corrections (4.13) to the platform-motion speed setpoints calculated by the admittance controller (4.11) yields a controller that can achieve admittance coupling while maintaining desired mean cable tensions,

$$\dot{\mathbf{i}}_d = \dot{\mathbf{i}}_x + \dot{\mathbf{i}}_f. \quad (4.15)$$

If only velocity is controlled, and cable lengths are not being measured or cable elasticity is not well characterized, there is potential for the platform positions to deviate over time from the values calculated by the simulation. To correct for these small accumulating differences, absolute position measurements such as from an optical tracking system could be used as feedback in a low gain controller to gently correct for drift.

4.3.1.1 Motion Constraints

An advantage of admittance control is that it facilitates constrained motion experiments. Because the platform or coupling point position is controlled by the actuator, arbitrary constraints on the motion can be applied into the controller software without otherwise altering the physical or simulation setup.

Motion constraints can be integrated easily into the admittance control calculations (4.10) through the addition of “constraint forces”, \mathbf{w}_c . As described by Witkin et al. [99], for known forces acting on a rigid body with known mass properties, constraint forces can be calculated such that the body motion adheres to any desired constraints. Constraint forces calculated according to this method could be used to constrain the physical platform motion as desired, as long as the actuation system could provide the needed forces. The admittance control equation (4.10) would become

$$\ddot{\mathbf{x}}_{sim} = \mathbf{M}_{sim}^{-1}(\mathbf{w}_{phys} + \mathbf{w}_{sim} + \mathbf{w}_c). \quad (4.16)$$

As before, this acceleration would then determine the speed commands sent to the actuator according to (4.11).

4.3.1.2 Practical Limitations on Admittance-Control Coupling

In practice, I found that the viability of an admittance control approach for hybrid modeling depends heavily on the inertias in each sub-model. Because admittance control requires some amount of inertia to exist on the simulation side, and because some compliance and response limit is inevitable in the actuation, an admittance-coupled hybrid model is at minimum a two-body system.

Figure 4.7 depicts the simplest single-DOF two-cable case, where m_{phys} represents the mass of the physical part of the system, and m_{sim} represents the simulated mass. If the winches are set for some desired pretension and then held fixed, when the physical mass is perturbed it will free decay with frequency $\omega = \sqrt{\frac{2K_{EA}}{m_{phys}}}$, where K_{EA} is the cable stiffness. Conversely, if the physical mass is held fixed and the winches are operated by the admittance controller, a perturbation in the numerical sub-model will free decay with frequency $\omega = \sqrt{\frac{2K_{EA}}{m_{sim}}}$.

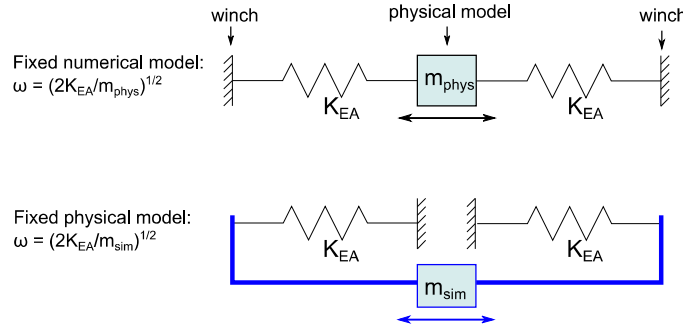


Figure 4.7: Resonances in a two-cable admittance-controlled hybrid coupling

The potential for resonance due to the elasticity of the actuator in admittance-control coupling became apparent during initial tests. When the numerical mass was greater than the physical mass, the system behaved stably since the higher-frequency resonance of the physical model was physically damped. However, when the numerical mass was less than the physical mass, a resonance would develop on the side of the numerical mass (which lacks physical damping). A control approach that damped this resonance would be needed for admittance control to work in this situation. The implementation would not be trivial since this damping should not be felt by the physical sub-model. I took this as evidence that impedance control is the more suitable approach for a floating wind turbine hybrid model.

Without more advanced control approaches, an admittance-control approach would only be appropriate if the majority of inertia was on the numerical side, such as in the inverse arrangement in which a floating platform simulation is coupled to a wind-tunnel test. For basin testing, an admittance control approach would likely be suitable only in the extreme case of a very lightweight scale-model platform moved by a powerful actuator – the majority of platform mass would be simulated and the platform would need to be very light and well-instrumented

with load cells at the actuator attachment point so that all wave loadings on the platform could be sensed and fed to the simulation.

4.3.2 Impedance Control Approach

Because an impedance coupling control approach is based on controlling the force applied by the actuator rather than the platform position, it can avoid the two-body resonance problem encountered in admittance coupling. Instead, the main challenge is ensuring that the applied force, through cable tensions, is what it should be. Despite the different focus, the approach presented here has many similarities with the admittance control scheme given in the previous section.

Impedance-control approaches for cable robots in haptic applications in the literature often use model-based computed-torque control techniques rather than relying on direct measurement of the applied forces (e.g [100]). These techniques work well when precise force actuation is not crucial or when using advanced control techniques and carefully-selected motors whose dynamics can be characterized and compensated for. To avoid this degree of control complexity and equipment dependence, I opted to implement a simpler force control scheme based on tension feedback from load cells in each winch unit.

The scheme incorporates three control components to provide responsive force actuation on the moving platform while maintaining the desired mean tension levels.

1. A proportional tension-feedback controller manages mean cable tensions and provides corrections to the applied force.
2. A disturbance-accommodating controller compensates for the platform motion.

3. A feedforward controller uses a model of cable elasticity to actuate dynamic forces on the platform.

Each of these components contributes a cable length rate of change command.

These are then summed to give the motor speed setpoint that is transmitted to the motor drive on each winch unit.

4.3.2.1 Tension Feedback

The foundation of the impedance control approach is a proportional controller that adjusts the cable length rate of change based on tension feedback. This allows management of mean cable tensions and adjusts the cable tensions to provide the desired wrench force on the platform and accommodate platform motion.

The feedback controller that sets the cable length rates is similar to that used for tension management in the admittance coupling approach (4.13):

$$\dot{\mathbf{f}} = -K_p(\mathbf{f}_d - \mathbf{f}). \quad (4.17)$$

This time, however, the desired cable tensions, \mathbf{f}_d , account for both the desired mean tensions, \mathbf{f}_{md} , and the desired wrench force to be applied on the platform, \mathbf{w}_d . From (4.8) and the discussion in Section 4.2.5:

$$\mathbf{f}_d = \mathbf{f}_0 + \mathbf{f}_w = \mathbf{f}_m - \mathbf{A}^{+\top} \mathbf{A}^\top \mathbf{f}_m - \mathbf{A}^{+\top} \mathbf{w}_d. \quad (4.18)$$

This approach works well at following a tension setpoint when the platform is not moving. Figure 4.8 shows the block diagram of the proportional tension controller for a single cable pulling in the x direction on the platform. Variables are shown in the time domain for the sake of consistent nomenclature with the equations and because much of the controls development used time-domain analysis. I simplified

the problem by assuming that the servomotor responds instantly to velocity setpoints and its response can therefore be omitted.

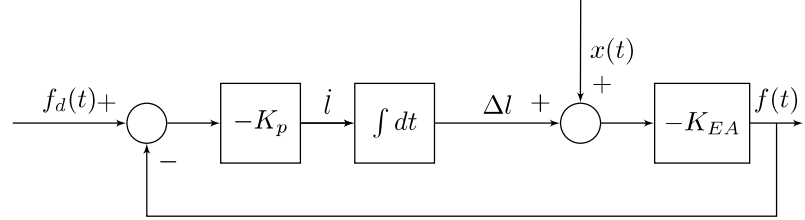


Figure 4.8: Tension control block diagram

If there is no motion, x , of the platform, then the closed-loop response in the Laplace domain is

$$\frac{F(s)}{F_d(s)} = \frac{1}{\frac{s}{K_p K_{EA}} + 1}, \quad (4.19)$$

where $F(s)$ is the Laplace transform of $f(t)$. This is equivalent to a first-order response with cutoff frequency or bandwidth of $\omega_c = K_p K_{EA}$.

The proportional controller is limited in its ability to reject disturbances in the form of platform motion. Figure 4.9 shows the block diagram rearranged to a disturbance rejection perspective.

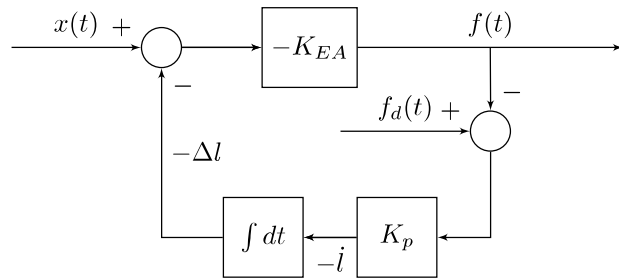


Figure 4.9: Tension control disturbance rejection block diagram

The transfer function of tension response to disturbances in the form of platform displacement, $X(s)$, is

$$\frac{F(s)}{X(s)} = \frac{K_{EA}}{1 + \frac{K_{EA} K_p}{s}} = \frac{K_{EA} s}{s + K_{EA} K_p} = \frac{1}{K_p} \frac{s}{\frac{s}{K_p K_{EA}} + 1}, \quad (4.20)$$

which is a first-order high-pass response with the same cutoff frequency as the tension response: $\omega_c = K_p K_{EA}$. The passband gain, however, is K_{EA} .

In terms of a velocity disturbance, the rejection can be seen to have a similar response as (4.19), except that it is also scaled by $1/K_p$:

$$\frac{F(s)}{\dot{X}(s)} = \frac{K_{EA}}{s + K_{EA}K_p} = \frac{1}{K_p} \frac{1}{\frac{s}{K_p K_{EA}} + 1} \quad (4.21)$$

This reveals an important point. Equation 4.19 shows that in terms of controlling tension, cable stiffness and controller gain play the same role and their product determines the overall gain, and bandwidth, of the system. As well, the response to velocity disturbances is the same as the tension-control response except that its passband gain is $1/K_p$ rather than unity. All together, this indicates that disturbance rejection can be improved while maintaining the same tension-control bandwidth by simultaneously increasing K_p and reducing K_{EA} . In theory, reducing cable stiffness while increasing feedback-control gain can make the tension controller more robust to platform motions without any compromise in response time. As such, cable stiffness is an important property that can aid the control problem and will be discussed more in later sections. Inserting a spring of known stiffness at the cable attachment point on the platform allows for easy adjustment of the overall cable stiffness.

In practice, the gain of the controller is limited by load cell measurement noise and the delay associated with measurement filtering. I found low-pass filtering to be helpful given the noise present, which is discussed further in Section 5.2.4. Adding a derivative term to the controller could improve stability but was not practical with the noise levels present in the available equipment. Fortunately, limitations in the proportional controller's performance can be compensated for by using motion

accommodation and feedforward control techniques. These are described in the following sections.

4.3.2.2 Motion Accommodation

To eliminate the effect of platform motion on the cable tensions, rather than relying on corrective action from the feedback controller, I added a disturbance accommodating control component that adjusts the cable lengths in response to observed platform motions.

If the platform position and velocity are known, the instantaneous cable velocities needed to maintain cable tension can be calculated from inverse kinematics as

$$\dot{\mathbf{i}}_x = \mathbf{A}\dot{\mathbf{x}}, \quad (4.22)$$

where it should be remembered that the Jacobian, \mathbf{A} , is a function of platform position, \mathbf{x} .

Adding these cable length rates, $\dot{\mathbf{i}}_x$, to those calculated by the tension controller, $\dot{\mathbf{i}}_f$, should allow the controller to accommodate disturbances in the form of platform motion. Elasticity in the cables would make equation (4.22) an approximation but such errors would be small and could be compensated for by the tension feedback controller.

The challenge in this disturbance accommodation approach is obtaining an accurate instantaneous observation of platform position and velocity. Some simple cases can be considered to understand the first-order effect of errors in platform motion observation. Figure 4.10 shows a block diagram for the same simplified one-directional case as in Figure 4.8, representing the tension feedback controller complemented with disturbance accommodation, where “Obs.” denotes the

observer that estimates platform velocity from platform position measurements according to transfer function H_{obs} .

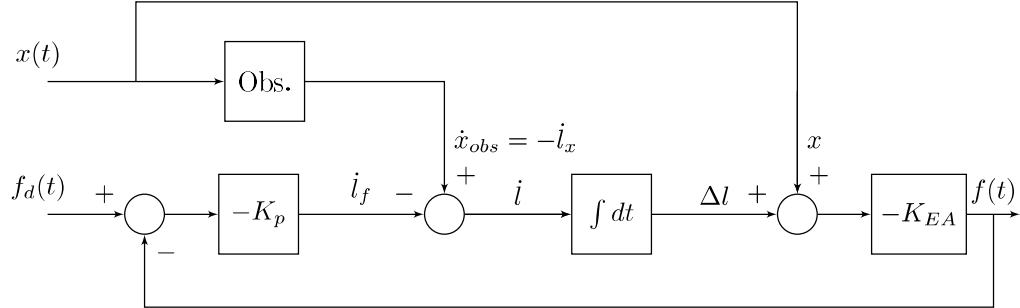


Figure 4.10: Disturbance accommodation and tension control block diagram

After some rearrangement, this block diagram can be made equivalent to that of Figure 4.8 except that the disturbance becomes $X(s)(1 - H_{obs}/s)$ rather than $X(s)$. In other words, in this linear approximation, the motion accommodation acts to reduce the input disturbance that the tension controller needs to reject. With a perfect observer ($H_{obs}(s) = s$) and the perfect motor response assumed in these diagrams, the velocity disturbance would be completely rejected. More realistically, the disturbance will consist of the error in velocity observation.

Subject to the bandwidth limits of the control system, errors in tension output could arise from several sources, including (1) nonlinearities in the motor response, (2) gain errors in observation or actuation, and (3) delay in the motion measurement, control, or actuation. Of these, the first two can be minimized by careful equipment selection and proper calibration and tuning. The third error source, delay, is the one for which a solution within the controller is most urgently needed.

The effect of delay can be considered in terms of harmonic response. Given a platform motion of $x = \sin \omega t$, a delay δt will cause a phase lag of $\omega \delta t$. The

position error that would appear as the disturbance in Figure 4.9 is:

$$\delta x = \sin(\omega t - \omega\delta t) - \sin(\omega t) = \sin(\omega t) [\cos(\omega\delta t) - 1] - \cos(\omega t) \sin(\omega\delta t). \quad (4.23)$$

Its magnitude is $\sqrt{2 - 2 \cos(\omega\delta t)} \approx \omega\delta t$, making the magnitude of the disturbance response (4.20) become

$$\left| \frac{F(s)}{X(s)} \right| = \omega\delta t \left| \frac{\frac{s}{K_p}}{\frac{s}{K_p K_{EA}} + 1} \right|, \quad (4.24)$$

for motions at frequency ω .

Considering an example of 10 m motions at 40 s period (full scale), in 1:50-scale model tests with a delay of 20 ms and $K_{EA} = 120$ N/m, the tension error magnitude would be 0.5 N. This is almost 10% of the turbine maximum thrust force at this scale. Clearly, a motion observer that includes delay compensation is important.

4.3.2.3 Motion Observer, Delay Compensation, and Stability

The goals of the motion observer are to filter out position measurement noise, compensate for delays, and provide estimates of platform velocity and acceleration. These are important not only for the quality of the motion accommodation, discussed in the previous section, but also the motion inputs given to the numerical sub-model. Filtering and delay compensation go hand-in-hand, because filtering adds delay while delay compensation is sensitive to noise. Except in the case of clean and delay-free measurements, a compromise of both is needed.

There are many advanced motion observer designs in existence, one of the most popular of which is the Kalman filter, which provides an optimal estimate of states if certain conditions are satisfied. I explored using Kalman filter techniques [101], including data fusion Kalman filters to combine measurements from inertial and

optical sensors (e.g. [102, 103, 104, 105, 106]), but found that they introduced an impractical level of complexity. Because the gains in a Kalman filter change dynamically in response to the assessed prediction quality, the control system bandwidths and phase lags are not constant. This poses a challenge for a hybrid coupling system, where delay compensation is crucial. Accordingly, I concluded that simple filtering methods, where delays are constant, are more practical for the project scope. Exploring the delay compensation issue was warranted before proceeding further on filter selection.

The literature on hybrid modeling in seismic engineering applications provides possible delay compensation approaches. These include techniques like delay estimators, polynomial extrapolation, phase lead filters, and feedforward control [10]. A straightforward approach already cast in terms of digital control is given by Horiuchi et al. [107]. They detail an extrapolation technique using a polynomial of the same order as the number of past measurement samples used.

Unfortunately, the presence of noise makes this approach difficult for my application. Filtering induces delay, which would in turn require greater compensation. As such, ensuring a linear phase response (i.e. uniform delay across frequencies) would be important. This would require digital filters with finite impulse response, which are more computationally expensive than infinite-impulse-response filters. Priorities of computational efficiency and simplicity led me away from this path. This exemplifies the challenge in floating wind turbine hybrid modeling, where the basin environment and multiple degrees of freedom create practical problems such as measurement noise which can interfere with direct transference of approaches used in other fields.

To deal with the noise problem without exacerbating the delay compensation challenge, I implemented a polynomial extrapolation technique where a cubic

polynomial is fit to a larger number of data points (the 20 points over the last 0.2 s in the final version). This low-order fit over a large number of samples provides a filtering effect (sometimes called polynomial regression filtering [108]) without increasing the delay-compensation demands the way a separate digital filter would. Experience has shown this approach to provide good delay compensation and noise rejection performance when extrapolating up to 0.05 s forward on position measurements used during testing.

Aside from the simplicity and performance, another reason I chose the above motion observer approach is that a least-squares fit of the cubic polynomial can be accomplished without excessive computational effort. The standard fitting process calculates the least-squares fit coefficients, β , using

$$\beta = (\mathbf{B}^\top \mathbf{B})^{-1} \mathbf{B}^\top \mathbf{y}, \quad (4.25)$$

where \mathbf{y} is the vector of measurements and

$$\mathbf{B} = \begin{bmatrix} 1 & t_1 & t_1^2 & t_1^3 \\ 1 & t_2 & t_2^2 & t_2^3 \\ \vdots & \vdots & \vdots & \vdots \\ 1 & t_{20} & t_{20}^2 & t_{20}^3 \end{bmatrix} \quad (4.26)$$

is a matrix of the exponents of the time at each measurement. If we assume time coordinates relative to the present and a constant sample rate, \mathbf{B} is constant. By precalculating the matrix $(\mathbf{B}^\top \mathbf{B})^{-1} \mathbf{B}^\top$, only $20 \times 3 = 60$ multiplications are necessary to perform the cubic fit at each time step. This efficiency is important since the calculation needs to be done for six DOFs every control cycle.

Once the polynomial coefficients are calculated, it is straightforward to extrapolate the future position, velocity, and acceleration for a given degree of freedom:

$$\begin{aligned}x_p &= \beta_3\delta t^3 + \beta_2\delta t^2 + \beta_1\delta t + \beta_0 \\ \dot{x}_p &= \beta_3\delta t^2 + \beta_2\delta t + \beta_1 \\ \ddot{x}_p &= \beta_3\delta t + \beta_2,\end{aligned}$$

where δt is the amount of delay compensation.

Delay compensation is valuable for motion accommodation, but it can be *crucial* for hybrid coupling. Coupling with a numerical dynamics model inevitably adds further delay. Whereas the numerical models used in haptic robotics applications are often computationally simple and consequently impose a negligible delay to the coupling, the wind turbine simulations for the hybrid model have a computation rate in the same order of magnitude as the Froude-scaled time in a basin test.

This entails a delay in the coupling of at least one control loop period.

The biggest issue with delay in the coupling is the stability of the system. Stability in other parts of the system could be studied; examples exist in the literature proving the stability of certain cable robot control schemes (e.g. [90]). However, the dominant concern about stability here concerns the interaction of physically- and numerically-modeled dynamics across the hybrid coupling. As mentioned in Section 4.3.1.2, the coupling of physically- and numerically-modeled inertias is one area of potential problem, especially for admittance coupling control. In an impedance coupling approach there is less risk, provided that care is taken in the division of the physical and numerical model components such that realistic damping is present on each side. In the issue of tower bending excitation identified in Figure 3.19, limiting the coupling bandwidth was one possible solution for avoiding resonances. However, the problem should be less severe in practice due to

the inevitable presence of some damping. The larger issue with stability in a hybrid modeling comes from coupling delay.

Even delay from the finite period of a digital control loop can cause problems with a scenario as simple as a numerical spring model coupled to a physical mass. In free decay, the numerical spring should apply a restoring force proportional to the mass's displacement. For pure stiffness, the reaction force should be in phase with and opposing the displacement. For damping, the reaction force has a phase lead. Conversely, any delay in the modeled spring force will constitute a phase lag, which is equivalent to negative damping. If this addition of energy to the system exceeds the energy dissipated by other damping sources, it will cause instability.

It is for this reason that delay compensation is so important in the hybrid coupling, especially if there are any stiffness terms at play in the numerical model, (or inertial terms in the numerical model and stiffness terms in the physical model). A possible alternative could be to characterize the delay in the system, model the negative damping caused by the delay interacting with the numerical dynamics model, and then apply corrective damping in the numerical model to compensate and ensure stability. This is an example of the potential for more advanced solutions which fall outside the scope of this thesis.

Horiuchi et al. analyzed the effect of delays and delay compensation and showed that third-order polynomial extrapolation is effective at avoiding negative damping until the delay exceeds one quarter the period of the highest frequency component in the motion [107]. The approach I used, of fitting over a large number of samples as described in Section 3.4.2.1, handles measurement noise with relatively little computational expense. In practice, I saw this apply an effect of low-pass filtering that clearly achieved the criterion of attenuating the higher frequencies that would make the extrapolation become unstable. It seems that this satisfies the criterion

of filtering the motion measurements to eliminate any frequencies greater than $1/4\delta t$ to avoid negative damping. However, this approach does not lend itself to easy stability analysis, so I have no rigorous theoretical statement of stability. Nevertheless, the analytical work about stability in references like [107] was useful in providing insight on the stability problem. Despite the different implementation, I found experimentally that third-order polynomials did in fact provide much better stability than first- and second-order extrapolations.

4.3.2.4 Feedforward Control and Tension Observer

While the motion observer provides a way to accommodate disturbances and the tension feedback controller provides a slower-responding correction on whatever error is left over, the ability to apply forces is thus far constrained to the bandwidth of the feedback controller. The bandwidth of this controller is limited by the presence of tension measurement noise. However, if the stiffness of the cables is known, any desired change in tension that is not based on feedback can be applied at a much faster response.

This is applicable for the wrench force, which is calculated by simulation. Because measurement noise is not present in this, the bandwidth of the controller can be much higher. Using the known cable elasticity, K_{EA} , the desired change in wrench force can be converted into a required change in cable lengths. Taking the time derivative of (4.8), assuming the desired mean tension is constant, and neglecting any change in the structure matrix gives

$$\dot{\mathbf{f}}_d = \frac{\partial}{\partial t} (-\mathbf{A}^{+\top} \mathbf{w} + \mathbf{f}_m - \mathbf{A}^{+T} \mathbf{A}^\top \mathbf{f}_m) \approx \mathbf{A}^{+\top} \dot{\mathbf{w}}. \quad (4.27)$$

Assuming constant stiffness K_{EA} , the feedforward cable speed command is then

$$\dot{\mathbf{i}}_{\text{ff}} = \frac{1}{K_{EA}} \mathbf{A}^{+\top} \dot{\mathbf{w}}. \quad (4.28)$$

Subject to the accuracy of the assumptions and actuator capabilities, this feedforward speed command will instantaneously apply the desired wrench forces on the platform. The tension feedback controller is then reserved for the role of mean cable tension management and correcting any tension errors remaining after the action of the feedforward tension controller and motion accommodation.

One final adjustment is required in order for these three control components to work in harmony. The tension feedback controller, which has a comparatively low bandwidth, needs to be shielded from any rapid tension changes enabled by the feedforward controller. Because the feedback controller filters tension measurements, it would perceive a delay between any rapid tension setpoint changes and the resulting change in tension driven by the feedforward controller. This delay would appear as a large tension error, which the feedback controller would then compensate for. In combination with the feedforward controller's action, this would lead to tension overshoots.

A solution suggested by Valentin Chabaud is to implement a model-based tension observer in the feedback controller. This observer creates an estimate of the cable tension based on platform position and cable lengths, including the action of the feedforward controller. This estimated tension is subtracted from the measured tension, and only the difference is filtered. After filtering, the estimated tension is added back in and the sum is sent to the comparator as the tension feedback. This technique, illustrated in the bottom-right of Figure 4.11, provides filtering of the tension measurement noise without filtering rapid tension changes that were commanded by the feedforward controller.

4.3.2.5 Integrated Controller

To provide an integrated view of the different control components, Figure 4.11 shows a diagram of the full actuator control system as described in the preceding sections. The diagram does not show the coupling with the numerical portion of the hybrid model nor the calculation of the desired cable tension, f_d . The two inputs on the left-hand side are the true platform position (\mathbf{x}) and the desired cable tension. The diagram describes action on a single cable, with f being the cable's true tension. “Meas.” represents the load cell tension measurement. “Obs.” represents the platform motion observer comprised of optical tracking and the cubic-fit smoothing and delay compensation approach to estimate positions, velocities, and accelerations. “I.K.” represents inverse kinematics calculations that convert from platform position or velocity to the component of platform displacement or velocity in the cable tangent direction. The three-way summation in the center of the diagram is where commands from the disturbance-accommodating controller (top), feedforward controller (middle), and feedback controller (bottom) are combined into the total cable length rate of change setpoint, l_d . The tension observer is on the bottom-right and “L.P.” represents the low-pass filter that is part of it.

The label “Servo” denotes the response of the servo motors. In practice, any controller setting motor velocity would rely on two additional nested inner control loops acting on the servo motor providing speed control and current control. These controllers are typically contained in the motor drive and, aside from basic automated tuning, can in most cases be excluded from the coupling control design and analysis because they have a much faster response than the cable robot control loops.

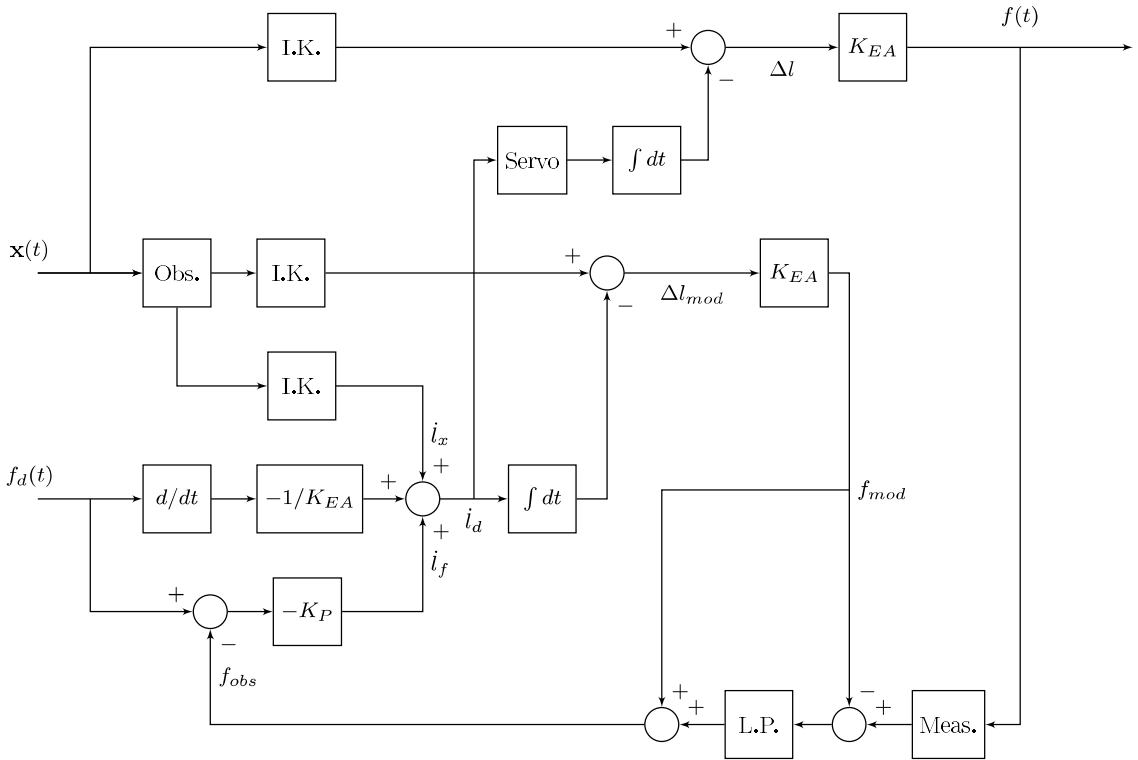


Figure 4.11: Final actuator control system including feedback, feedforward, and motion accommodation elements

Although the function of the different control elements are interrelated, the rationale for each of them can be summarized sequentially as follows:

1. For the tension control problem, proportional control is the simplest and cleanest approach. However, load cell noise and stability limits from the control loop rate limit the gain, constraining performance.
2. Platform motions can be better accommodated if they are measured separately, since motion tracking provides greater accuracy and bandwidth than force measurements.
3. Force actuation can be much more responsive (exceeding the tension-control bandwidth) if feedforward control is used.

4. Force actuation exceeding tension-control bandwidth will cause feedback errors due to sensor lag and abrupt setpoint changes, unless a special tension observer is used to isolate the tension feedback from the feedforward command.

I developed the controller through consideration of the factors discussed in this chapter and simultaneous experimentation with different approaches in isolation and combination. The next chapter describes the bench testing that I conducted to develop and characterize the control system and then presents a demonstration of the full system in a basin testing environment.

Chapter 5

HYBRID MODEL REALIZATION AND TESTING

This chapter describes the development and testing of a prototype hybrid coupling system following from the preparatory steps described in the preceding chapters. This includes mechanical design and construction of a cable-based actuator of the type described in Chapter 4 and approaching the specifications described in the case study of Chapter 3. I designed the system for coupling with the DeepCwind semisubmersible support structure, though it could suit other designs as well. For wind turbine aerodynamics, I used the modified FAST numerical model discussed in Section 2.1. Section 5.1 describes the coupling system I created.

To reduce the project complexity while still providing the basic and most valuable capability of interest to a wave-basin testing facility, I focused on the aero-elastic coupling case in a single degree of freedom, similar to what the pendulum bench tests represented. Applying aerodynamic forces in only the x direction (wind direction) provides the majority of the effect of the wind turbine in a basin test [26] and only requires two winch units. Having no inertia on the numerical side reduces demands on the coupling system, as touched on in the two previous chapters.

The majority of experimentation and tuning of the coupling system occurred through bench tests at reduced scale using a pendulum apparatus. Section 5.2 describes these tests. Then, I applied the system to a basin test with a floating wind turbine at 1:50 scale. These tests are discussed in Section 5.3.

5.1 Hybrid Coupling System Setup

The mechatronic system created to provide the hybrid coupling consists of instrumented winch units (I built two for testing) and central data acquisition and control hardware and software.

5.1.1 Winch Units

Winch units serve as the mechanical coupling between the physical and numerical sub-models. Design of the winch units affects the quality of hybrid coupling and the range of hybrid coupling arrangements that can be achieved. The winch units incorporate brushless servomotors to provide responsive motor control and load cells to measure cable tension.

The array of existing examples of winch designs for cable robots is diverse. The majority of designs use rotary motors (either DC or brushless) and many include a gearbox. A few designs (e.g. [109]) use linear actuators to avoid possible complications from spooling cable on a drum. Other designs meant for thick cables use moving guides or drums that slide as they rotate to facilitate proper spooling (e.g. [110]). Winches incorporating direct tension measurements typically integrate a load cell with a series of pulleys to measure the forces in a constant direction although the direction of the cable extending from the winch may vary. In order to not constrain the direction of the cable, some winch designs use a low-friction eye at the exit (e.g. [111]). Others use a pulley on a pivot, with the pivot axis collinear with the cable within the winch unit so that the pivoting does not alter the cable length. Some winch designs place an encoder on this pivot to measure the cable direction (e.g. [112]). Almost all designs feature an encoder on the motor for position or speed feedback.

The design I created incorporates a rotary servomotor, a spool of up to 6 cm length and diameter, a pivoting pulley for a wide exit angle range, and a load cell with a second pulley for built-in tension measurement. Figure 5.1 shows the design. The use of pulleys ensures that cable tension measurements are consistent and only impacted by friction a small degree. It also doubles the force felt by the load cell, improving sensitivity for the low tensions used in the system.

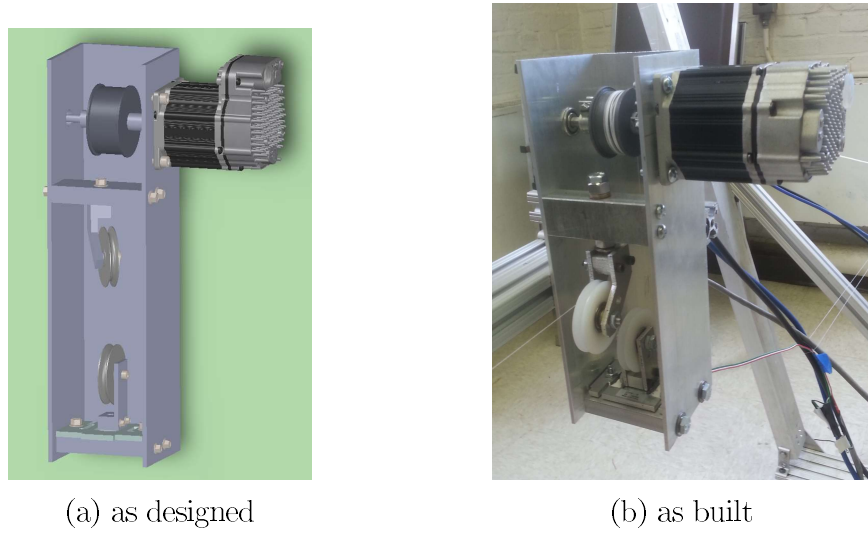


Figure 5.1: Winch unit design

By applying (4.5), the wrench forces on the platform can be calculated from the cable tensions, avoiding the need for a six-axis load cell at the coupling point for force feedback.

5.1.1.1 Sizing

I sized the winch units – servomotor, load cell, pulleys, and supporting structure – to be suitable for applying thrust loads at 1:50-scale in an opposing fore-aft cable arrangement. This means each winch must be able to provide the tension of half the maximum thrust force plus the mean tension level desired in the cable system. This is conservative since the applied loads would be shared more widely in a

system with more cables, and a single-cable system would also never need larger tensions than an opposing two-cable system. A mean cable tension equal to the expected maximum thrust force gives good results in terms of balancing spring linearity limits with tension signal-to-noise ratio, so I used this in sizing.

Motor selection needs to account for not only the tension but also the speed and power required. This can be simplified by making the approximations of perfect motor control, no elasticity in the cable, and coupling point motion only along the cable direction. With these assumptions, quantities calculated in Chapter 3 for the aero-elastic coupling case can be applied to identify the motor requirements. From Table 3.5 after 1:50 Froude scaling, the required surge velocity is 0.83 m/s and the maximum thrust force is 7.9 N. From Figure 3.9b, a motion bandwidth of 0.2 Hz full scale, or 1.4 Hz model scale, is sufficient for most cases. Assuming the maximum velocity occurs at this frequency gives a maximum linear acceleration of 7.3 m/s^2 (in terms of cable spooling), which the motor should also be able to provide.

I checked these requirements by modeling the motor dynamics as

$$(J_M + \tau^2 J_D) \ddot{\theta} = T - f \tau r_D, \quad (5.1)$$

where T is motor torque, J_M and J_D are motor and drum moment of inertia, respectively, $\dot{\theta}$ is motor speed, τ is the gear ratio, r_D is drum radius, and f is cable tension. The gear ratio and drum radius also relate the motor speed to the cable speed, and therefore also the coupling point motion, through

$$\dot{\theta} = \frac{\dot{x}_{nac}}{\tau r_D}. \quad (5.2)$$

Through these relations, I compared the requirements with published specifications for a variety of servomotors from different manufacturers. The motor

torque-to-inertia ratio can be important since it effects the bandwidth or accelerations possible. Another variable that matters for thick cables is the number of winds on the drum, in order to avoid overlap. Drum radius and gear ratio affect this and also shift the torque loading between cable tension and motor inertia. These are just some of the considerations that can go into the choice of motor characteristics, gearing, and drum radius. For impedance control with tension feedback from load cells, little compromise is needed as long as the motor meets speed, power, torque, and bandwidth requirements. In my case, the performance of appropriately-sized brushless servomotors exceeded the requirements by a large margin without the need for a gearbox, making selection straightforward.

The servomotors I chose are Teknic ClearPath model CPM-MCVC-2311S-RQN. They are brushless motors with integrated 1280 count encoders and tunable controllers for speed and torque. This integrated option offered low cost, ease of setup, and good performance. The motors have rated speed of 4000 rpm and torque of 0.41 N-m. According to motion tests discussed later in Section 5.2.2, the motor response time to commanded changes in speed or direction is less than 12 ms.

The inertia in the winch unit consists of the motor rotor inertia, the shaft-drum-fastener inertia, and the inertia of the two pulleys that guide the cable. The motor rotor inertia according to specifications is $0.077 \text{ kg}\cdot\text{cm}^2$. I estimated the additional inertia from the drive shaft, drum, fasteners, and pulleys to be $0.1 \text{ kg}\cdot\text{cm}^2$. Choosing a drum size with final radius of 18.25 mm made for a winch system that exceeded required speed, torque, and acceleration by more than a factor of two. From the maximum displacement indicated in Table 3.5, the amount of cable wound around the drum would never deviate from neutral by more than 6 winds, which is a manageable number that would not require special spooling

guides. Before operation, I tuned the motor controller automatically using the manufacturer’s software with the drum attached to correctly set the internal speed- and current-control gains for the inertial load on the motor.

I selected planar-beam load cells, Omega model LPCW-7.5, to provide an inexpensive and compact tension measurement capability. At 7.5 kg rated load, accounting for the doubling of force due to the pulley arrangement, the load cells support a maximum tension of just over 35 N. This is more than double the anticipated maximum tensions during testing at 1:50 scale.

Having a calibrated stiffness in the cable connection to the platform is an important part of the control system described in Section 4.3.2. I achieved this by using springs at the connection of the cables and the platform. The springs can be easily changed to accommodate different tension levels for different scales of testing. The tests presented in this chapter used high-strength upholstery thread. I estimated its stiffness over the range of forces expected at $EA = 266$ N based on calibration tests similar to those done for springs (discussed in Section 5.2.3).

5.1.2 Data Acquisition and Control

The complete data acquisition and control system, illustrated in Figure 5.2, uses two or three networked computers depending on the application. The *real-time target* runs the Pharlalp ETS real-time operating system and commands a National Instruments PXI chassis that houses modules for various inputs and outputs. This computer runs a deterministic (not prone to processing delay) control loop for commanding the winch units, filtering tension measurements, modeling cable tensions for feedforward control, and calculations to apply the simulation-provided loads onto the floating structure. It also runs a second loop in parallel that houses the FAST simulation, and a third loop that handles user interface interaction and

data logging. Figure 5.3 shows a chart of the control loops and functions that I implemented on the real-time target.

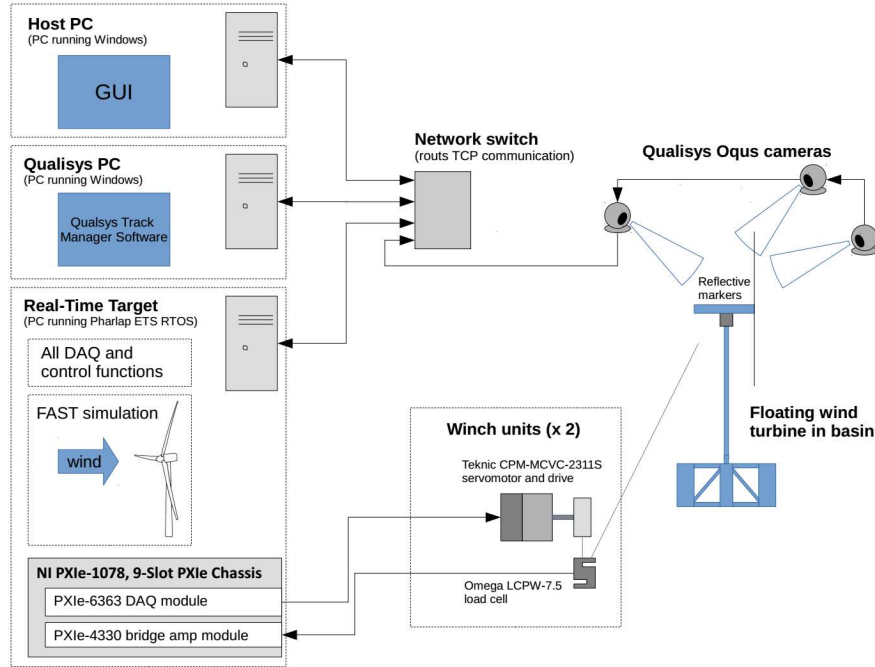


Figure 5.2: System electronics arrangement as used in basin testing

The *host PC* provides all the graphical user interface (GUI) functionality for developing and operating the real-time control system. Both of these computers run LabWindows/CVI programs. I developed the control and interfacing programs in this C-based language because it facilitates a finer degree of control than LabVIEW.

If Qualisys optical motion tracking is used, a third computer runs the motion tracking software, providing the processed motions to the real-time target over the network and also saving a separate log file. In bench testing without the Qualisys motion tracking, a third computer was not needed.

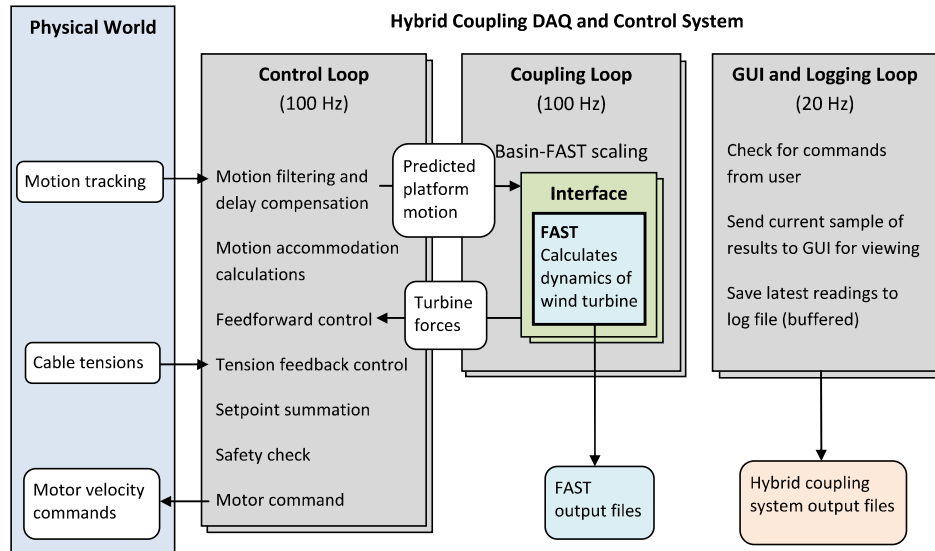


Figure 5.3: Overview of hybrid coupling data acquisition and control process

5.1.2.1 Load Cell Measurements

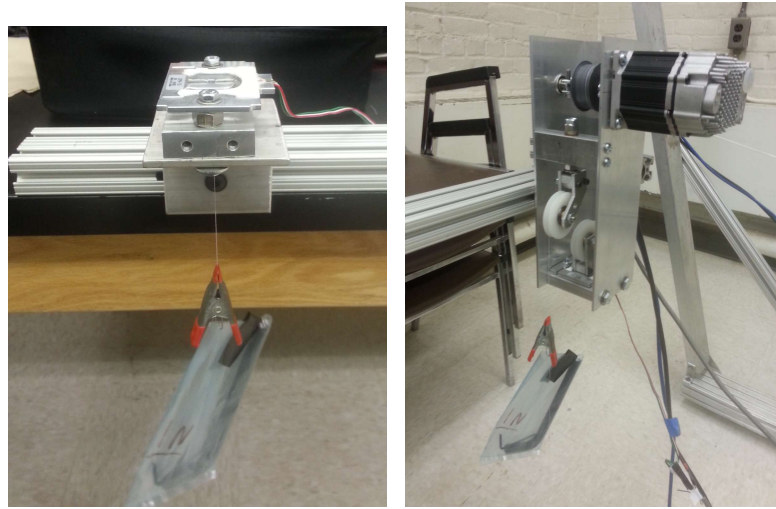
A National Instruments PXIe-4330 bridge amplifier module handled input from the load cells. The excitation level across each load cell was 10 V and a remote sensing configuration provided compensation for the voltage loss over the long cable runs used in basin testing. I created a streamlined two-point calibration process for the load cells when installed in the winch units to expedite setup of the system in new configurations.

The PXIe-4330 module needed some non-trivial settings adjustments to provide low-latency measurements for use in the control loop. The hardware low-pass filters, essential for minimizing measurement noise, required the continuous sampling mode. A little-known characteristic of the module results in a 32-26 sample delay in available data. To avoid this causing a large latency, I used a high sample rate of 10 kHz. With a control loop rate of 100 Hz, approximately 100 samples¹ are available to the controller at each step and the delay should be

¹Because of the way the buffer is read, this number in practice alternates between 96 and 128.

around 3 ms. After considering the signal-to-noise ratio in the resulting data at each time step, it was apparent that taking the average of each 100 readings was the most reasonable approach, given the computational constraint of a 100 Hz control loop. The act of averaging 10 ms worth of data adds an additional 5 ms of delay to the measurement, resulting in a total force measurement delay of approximately 8 ms.

Early tension control tests (the final ones are presented in Section 5.2.4) had a second load cell at the end attachment point of the cable. Figure 5.4 shows the setup for these tests. The tensions measured by this load cell during tests matched those measured from the load cell in the winch unit, verifying that the winch unit tension measurement was not impacted by friction or inertia of the pulleys.



(a) end with load cell, rotated down for gain calibration
(b) winch unit being calibrated

Figure 5.4: Experimental setup for tension tests with fixed endpoint

5.2 Bench Testing

Testing the constructed coupling system in simplified situations provided a means of comparing the efficacy of different control approaches, tuning the controllers,

and characterizing performance of the real system. Ultimately, experimenting with the real hardware is the easiest way to study the full problem, including the important factors of sensor noise, delays, and limited sample rates, which are not always straightforward to model numerically.

Testing the performance of the actuator and experimenting with different configurations and controllers is much more easily done in controlled ‘lab-bench’ scenarios than in the wave basin. The advantage of this is that the real physical dynamics of the system can be tested, and a lab-bench approach can aid in isolating certain aspects of the dynamics for closer study. Since the focus in bench testing is on dealing with the physical hardware, all values in this section are presented at model scale. The following subsections describe the final tests that I performed to tune and characterize the performance of the hybrid coupling system. Numerous tests took place beforehand while I considered different approaches and resolved programming bugs, but these results are of little general relevance.

Any bench tests involving coupling point motions used a pendulum test rig as a proxy for the floating platform at a scale of 1:100. This is smaller than most floating wind turbine basin tests but provides for more manageable and safer forces while the system is developed. It also serves as a conservative situation compared to 1:50-scale testing in a wave basin because the relative noise magnitudes are larger at small scales.

5.2.1 Pendulum Test Rig

I selected a pendulum as the simplest way to mimic floating wind turbine motions in a controlled and dry setting. Pitch is the most important degree of freedom for the DeepCwind semisubmersible design with respect to hybrid coupling.

Accordingly, I constructed a pendulum system to match that pitch response at 1:100 scale. Characteristics of the pendulum are given at model scale.

The pendulum weight approximates that of the scaled DeepCwind semisubmersible, at 13 kg. Adjusting the center of mass relative to the pivot point to match the design's metacentric height gave a measured pitch stiffness of 25 N-m/rad. To adjust the moment of inertia, I changed the spread of the masses on the pendulum, while preserving the center of mass and hence the stiffness, to achieve a natural period near 2 s, a value falling between the theoretical natural frequency of the DeepCwind model without hydrodynamic added mass, and the experimentally measured natural frequency (which would include the added mass) [63]. The final measured natural frequency was $\omega_n = 3.17$ rad/s. This indicates a pitch inertia (about the pivot point, which I set at the platform's theoretical metacenter) of 2.48 kg-m². I set the coupling point, where the cables attach to the pendulum, at 0.82 m above the pivot point, matching the hub elevation of the NREL 5-MW offshore reference turbine above the platform metacenter.

These properties provide for pitching behavior that is similar to that of a 1:100-scale DeepCwind semisubmersible model. Inevitable differences exist because the effect of added mass and mooring line stiffness are not explicitly included and the dominant source of damping is friction rather than hydrodynamic drag. However, this level of representation is sufficient for developing a coupling system that may well be applied to other designs aside from the DeepCwind semisubmersible.

I positioned the winch units such that the cable exit point was level with the height of the coupling point when the pendulum was vertical. The distance from each winch to the coupling point was 1.2 m. Figure 5.5 shows the arrangement.



Figure 5.5: Test rig with opposing winch units and 1:100-scale pendulum

A string potentiometer was the primary source of motion measurement during most of the tests. It was connected to the pendulum a distance of 103 mm below the pivot point. I made a linear calibration based on independent rotation measurements from an inertial measurement unit and a webcam-based optical tracking system. Over the $+/-10$ degree range of interest, the relation between voltage and angle was nearly linear.

5.2.2 Motor Motion Verification

Because the control scheme relies on the internal speed control in each servomotor, it was important to check that this black-box controller is reliable. This can be done experimentally. I tested the motor's steady-state speed tracking by running a constant speed command for a precise time duration. The number of revolutions matched the expected value.

Once this steady-state capability was confirmed at moderate speeds, I checked the transient performance and the limits at low speeds by running a speed command sequence developed for that purpose. The top two plots of Figure 5.6 show the motion sequence that I used to test this in terms of commanded velocities and the integrated change in position. This sequence includes a range of step changes in speed, on-off pulses of different lengths, and steady slow speeds. Importantly, it is designed so that the integrated speed setpoint always lines up with the same minimum and maximum position. By adding a spring to the system and looking at the resulting tension extremes from this test, the physical repeatability and position-change equivalence of these different motion commands can be seen.

The bottom two plots of Figure 5.6 show the results of this motion test with a spring of stiffness 62 N/m. It can be seen from the time series after 80 s that the motor accuracy at steady speeds is good above 0.01 m/s cable rate. There is a small amount of drifting in the ratio of integrated speed setpoint and measured tension at the lower speed ramp and also in the intermittent stepping tests. However, this slow drift would be easily corrected by feedback control in the final system. In general, the repeatability of the step-change type tests is good. Also, by looking at the lag between when a speed command is initiated and when a change in tension is measured, the response delay can be seen to be very small. The change in tension consistently appears two time steps after the speed command begins, indicating a lag of between 10 and 20 ms. The known tension measurement latency of 8 ms (discussed in Section 5.1.2.1) should be subtracted from this value, leaving a motor speed-control latency of between 2 and 12 ms. This informs the delay compensation setting used in the hybrid coupling controller.

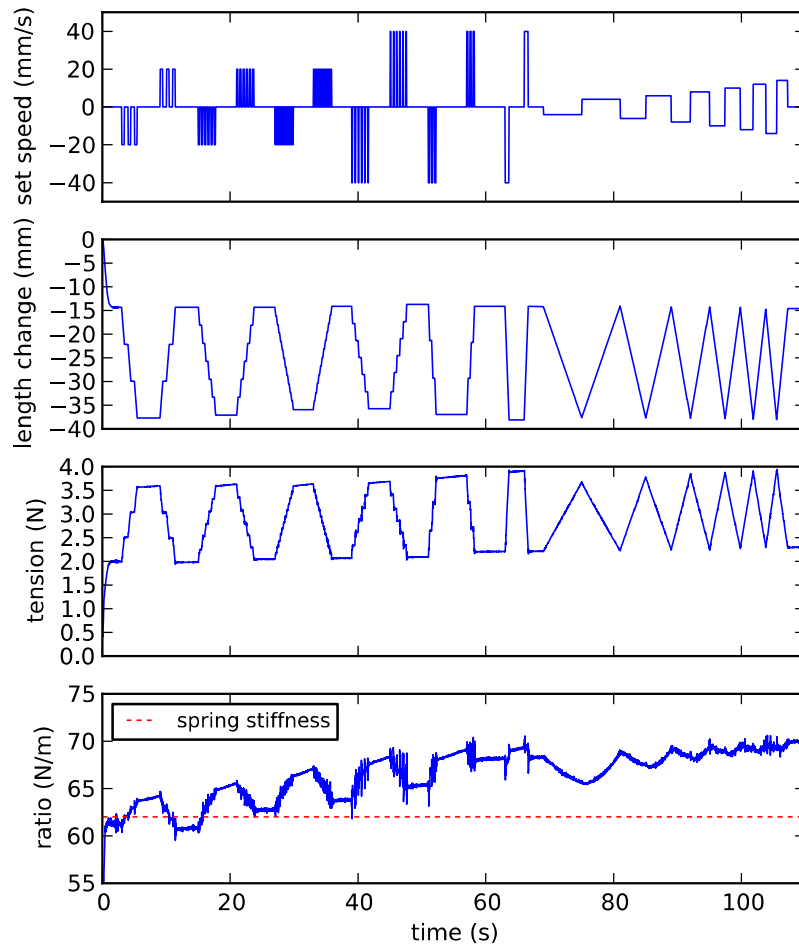


Figure 5.6: Motion repeatability test

5.2.3 Spring Calibration

Being able to set the compliance in the cables is an important capability for realizing a good control system. Springs in series with the cables is the most straightforward way of providing that compliance. A way of identifying the spring properties is therefore needed.

The most convenient approach is to measure the spring properties using the winch units themselves. This avoids additional equipment and also allows measuring of

the full system compliance, including not only the spring but also the elasticity of the cable (at a given length) and any other appreciable deflections in the actuator setup. I approached this by running a winch unit with a spring attached to a fixed endpoint through a program of constant-speed motions. Tensions were measured by the winch unit's load cell and displacements were estimated by integrating the velocity command. The approximately-constant stiffness and the tension bounds of the linear range could then be identified in postprocessing.

Figure 5.7 provides the setpoint velocity, displacement (calculated by integration) and measured tension for one of the springs. Figure 5.8 shows the force-displacement relationship from which a representative stiffness coefficient can be taken. For each spring, I visually identified the bottom of the range of tensions for which the relationship is approximately linear. Measurements above this tension then go into a linear fit that indicates the stiffness coefficient. There is evidence of hysteresis and slack in the spooled cable that is taken up during the first tensioning of the test. To handle the latter, I excluded the first tensioning sweep from the curve fit. The portion of the data included in the linear fit is plotted in dark blue in Figure 5.8. I estimated the maximum practical tension for each spring by visual observation of the spring's deflection at different tensions. Table 5.1 gives the properties found for the three different spring types that were most used in testing.

Table 5.1: Stiffness and linear range of springs used in testing

Spring name	Stiffness (N/m)	Min. tension (N)	Max. tension (N)
small	28	0.6	1.8
medium	71	1.6	6
large	116	3	15

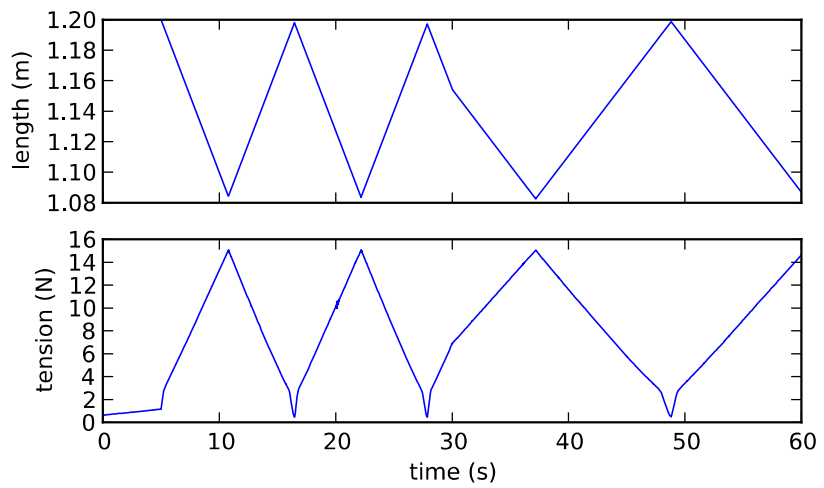


Figure 5.7: Cable length and tension in spring calibration test

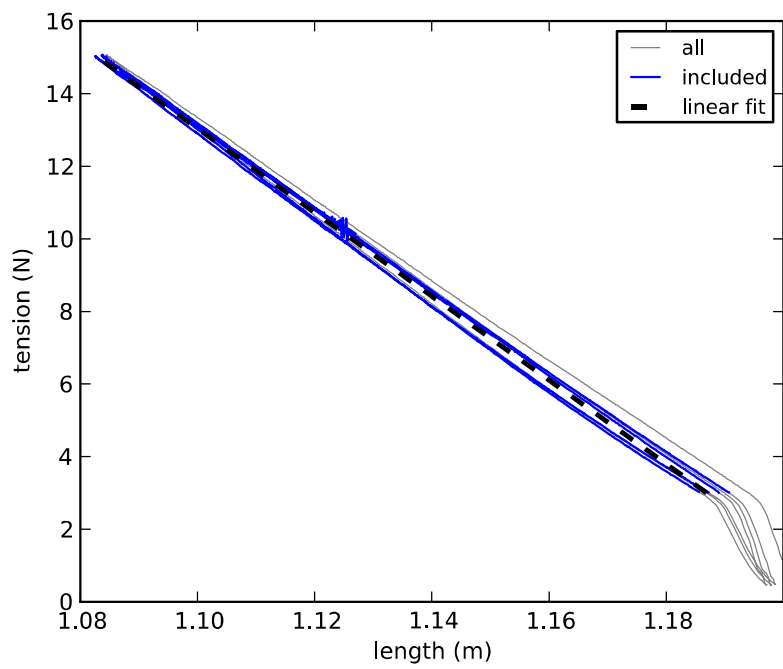


Figure 5.8: Force-displacement relationship in spring calibration test

5.2.4 Tension Control Testing

Most of the hybrid coupling control system, excluding the parts that accommodate platform motion and handle coupling with the numerical model, can be tested in isolated, single-cable conditions with a fixed endpoint and a prescribed sequence of tension commands. This section presents results of the final round of tension-control tests using this fixed-endpoint arrangement. The tension sequence used for all the tests presented here is shown in Figure 5.9. This sequence includes a series of step changes of different magnitudes and then a section of harmonic tension fluctuations with frequencies ranging from 0.5 Hz to 8 Hz in multiples of two and with each frequency applied at two different amplitudes.

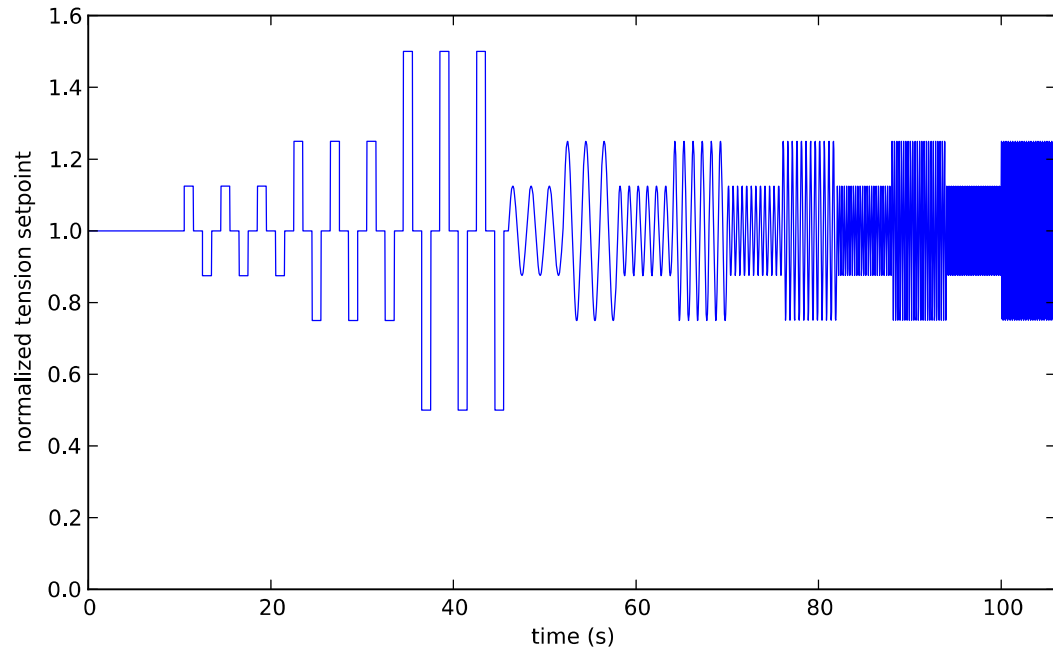


Figure 5.9: Tension setpoint sequence for tension-control tests

Certain metrics can be extracted from each test. The step response can be used to identify the time constant of the system. After the tension has settled from a step change, the standard deviation of the tension error after that point can provide a

measure of the noise or drift under a steady tensions setpoint. From the harmonic response at each frequency, the magnitude response and phase lag can be calculated, from which the useful bandwidth of tension actuation can be determined.

I created a script in Python to process the test results and identify these metrics, providing a consistent evaluation across all the tests. Figure 5.10 shows an example of the points identified from the step-response portion of a test. Figure 5.11 shows how curve-fitting is used to identify the magnitude and phase response of the system in the harmonic portion of a test. The algorithms that extract these values proved to be robust in terms of all the test cases analyzed.

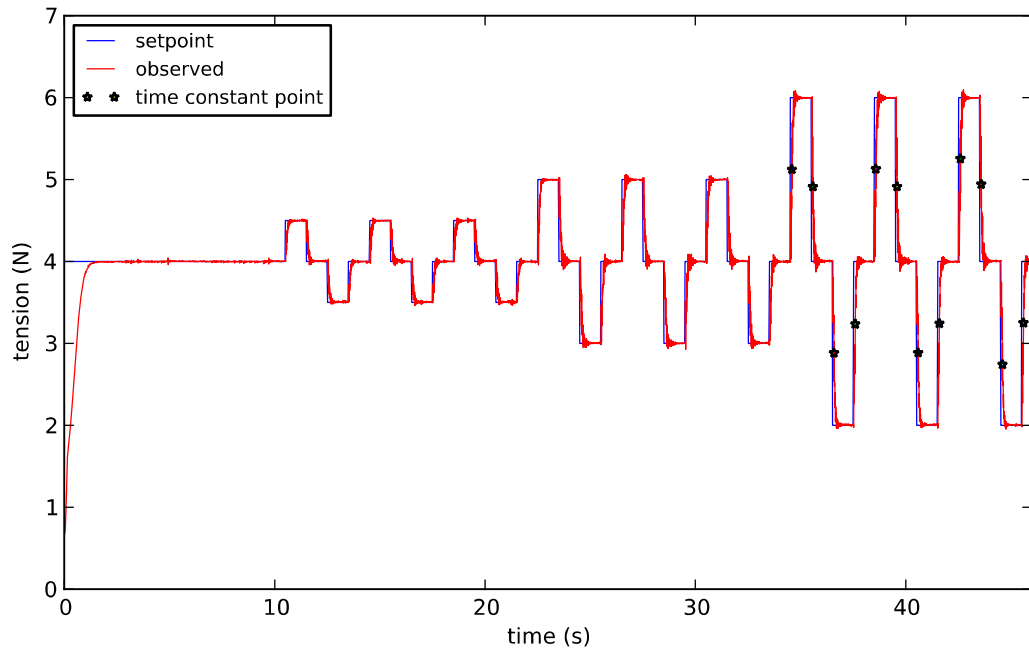


Figure 5.10: Sample of processed tension step response data

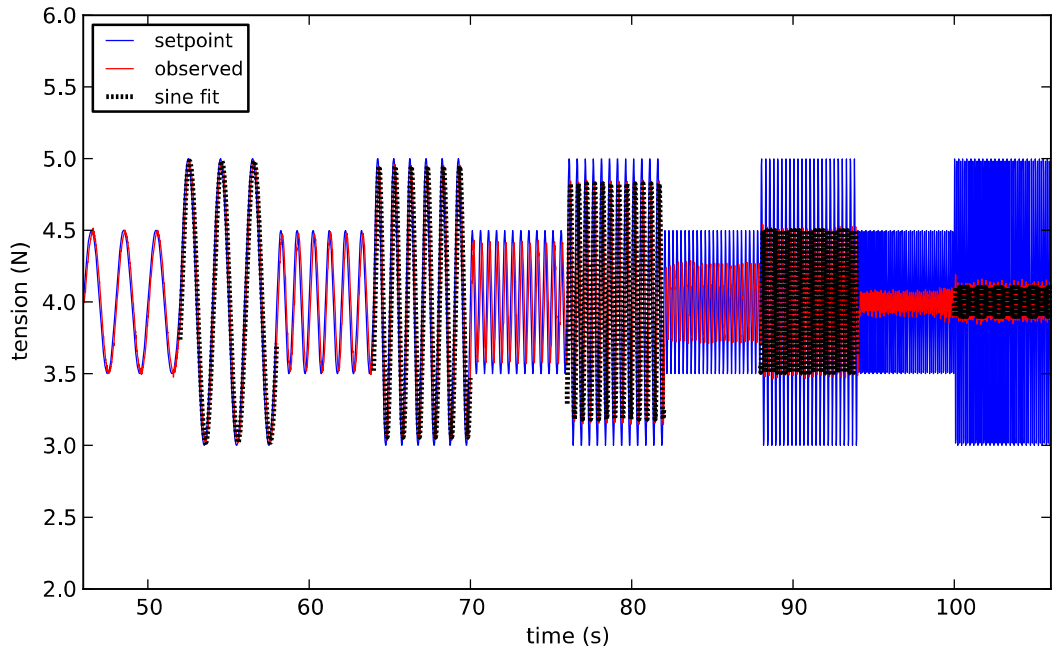


Figure 5.11: Sample of processed tension harmonic response data

5.2.4.1 Tension Filtering

The first set of tension-control tests is concerned with identifying the best filter settings for the tension measurements. For practicality of implementation and computational efficiency, I limited the filtering to the four-pole Butterworth low pass type. The parameter under investigation here is the cutoff frequency.

The cutoff period is roughly proportional to the delay introduced by the filter (though there is some frequency-dependence because it is an infinite-impulse-response filter) and also to the amount of noise rejected by the filter. Choosing the best value is therefore an issue of compromise. It is also an issue that cannot be solved by simple modeling since there are other uncharacterized delays and nonlinearities in the real closed-loop system. Because the tension measurements are used as feedback, there is a coupling between filtering of the tension measurements and the actual tensions in the system;

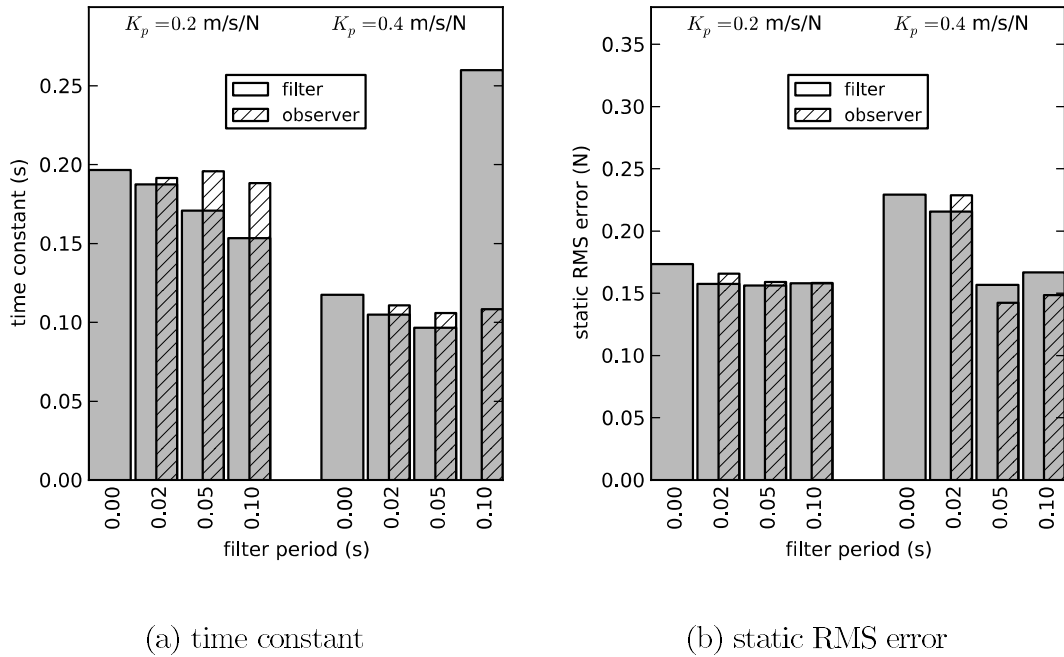


Figure 5.12: Tension step response metrics for different gains and filter types

filtering tension measurements results not only in smoother measurements, but also smoother tensions. This complexity motivated the choice of experimental rather than numerical filter tuning.

The data given here are for tests with the smallest spring (28 N/m stiffness) with two different controller gains: 0.2 m/s/N and 0.4 m/s/N. I tried four filter settings in each case: no filter, and filters with cutoff periods of 0.02 s, 0.05 s, and 0.1 s. Figure 5.12 shows the time constant and steady RMS error found in the step-response in each of these cases. Figure 5.13 shows the magnitude response to harmonic motion in these tests, and Figure 5.14 shows the accompanying phase lag. The solid bars in these plots correspond to simple filtering of the tension signal. The overlaid diagonal-hatched bars correspond to tests using the tension observer design discussed in Section 4.3.2.4 in which filtering is only applied to the portion of the measurement deviating from the model-predicted value.

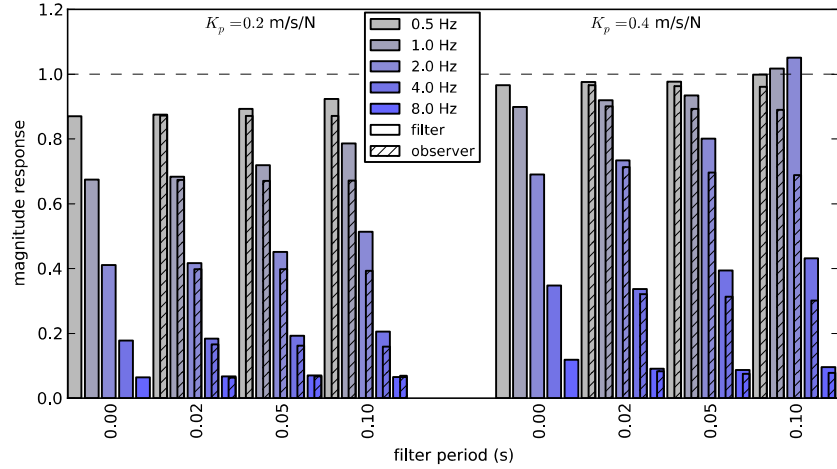


Figure 5.13: Tension magnitude response for different controller gains and filter types

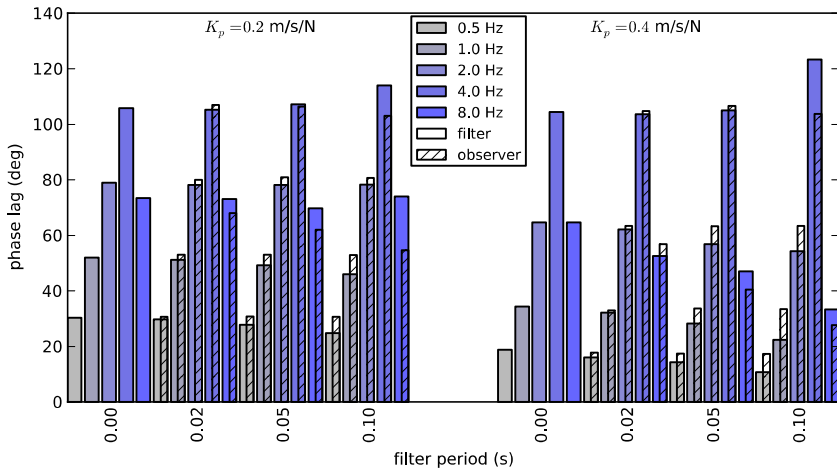


Figure 5.14: Tension phase lag for different controller gains and filter types

The results show that the higher controller gain gives better performance in general and that increasing the filter cutoff period up to 0.05 s also improves performance. However, at the higher gain the longest cutoff period of 0.1 s reduces performance. It seems that the large delay introduced by this filter causes some overshoot that is responsible for the longer time constants and larger RMS errors in Figure 5.12 and the greater-than-unity response in Figure 5.13.

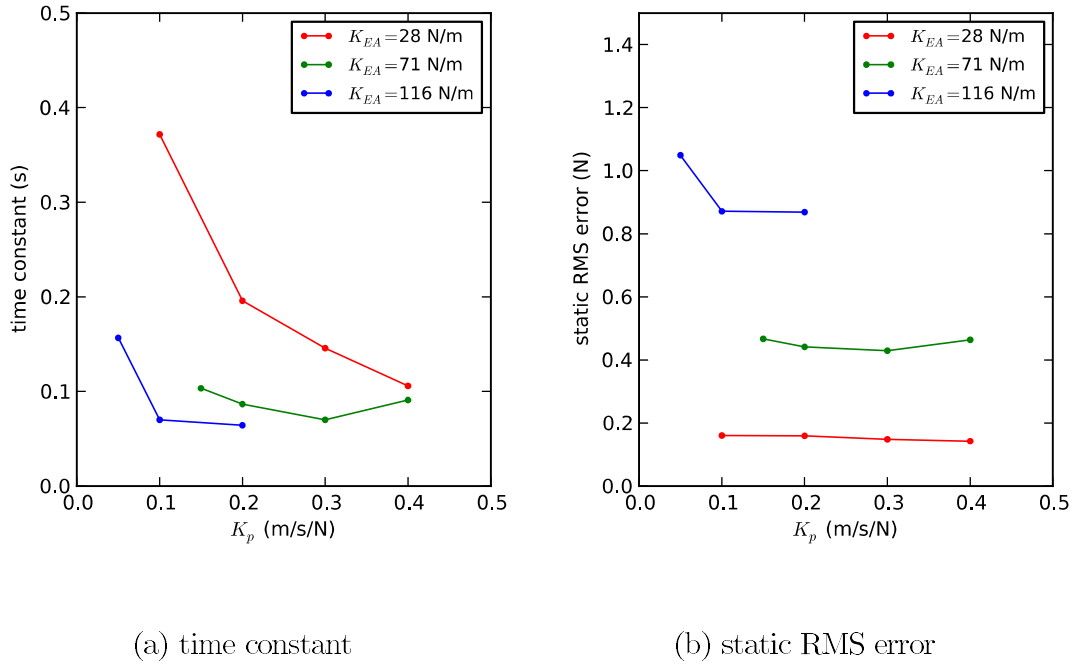


Figure 5.15: Tension step response metrics versus controller gain for feedback control

5.2.4.2 Effect of Gain and Stiffness on Response

As discussed in Section 4.3.2.1, the product of the feedback controller gain, K_p , and the cable or spring stiffness, K_{EA} , should in theory determine the tension-control response. This section gives tension-control test results from across a range of gains and using the three springs with stiffnesses listed in Table 5.1. These tests used the tension observer approach described in Section 4.3.2.4.

Figure 5.15 shows the time constants and static RMS errors measured from the step response of these different cases. The time constants decrease with spring stiffness and controller gain, except at high gains where instability compromises the response (as in the right-most point of the 71 N/m spring). The RMS error appears to depend primarily on spring stiffness.

Figure 5.16 shows the magnitude response as a function of tension oscillation frequency for the different spring stiffnesses and controller gains. The continuous

curves show the theoretically-expected response as predicted by (4.19) for comparison.

The agreement with predicted values is very good for the lowest spring stiffness, but the test data shows larger response magnitudes than expected for the stiffer springs, especially as controller gain is increased. This is likely a result of delay in the control loop which can lead to some degree of resonance at higher gains and higher frequencies (as mentioned in Section 4.3.2.2).

Figure 5.17 shows the phase response of the test results compared with the expected values in a similar format as Figure 5.16. The measured phase lags agree well with expectations at lower frequencies but increase well beyond the theoretical 90 degree asymptote at higher frequencies, another indication of delay in the control loop. The anomalous phase lags of the 28 N/m spring at the highest frequency can be disregarded since the response magnitude in this situation is very small.

Looking at the differences across spring stiffness and controller gain, a number of observations can be made. As expected, cable stiffness and controller gain both have a similar effect, with larger values providing faster response, or higher bandwidth. There is a limit, however, beyond which oscillations emerge at greater amplitude than commanded in the tension setpoint – these are particularly noticeable at 4 Hz.

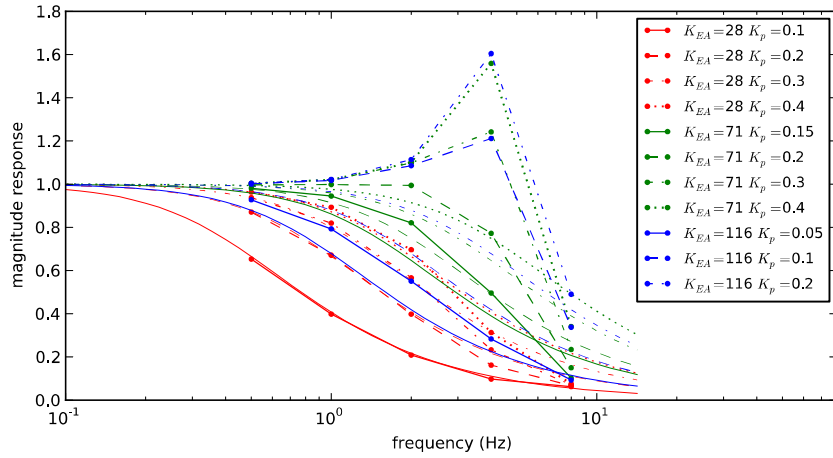


Figure 5.16: Tension magnitude frequency response with feedback control

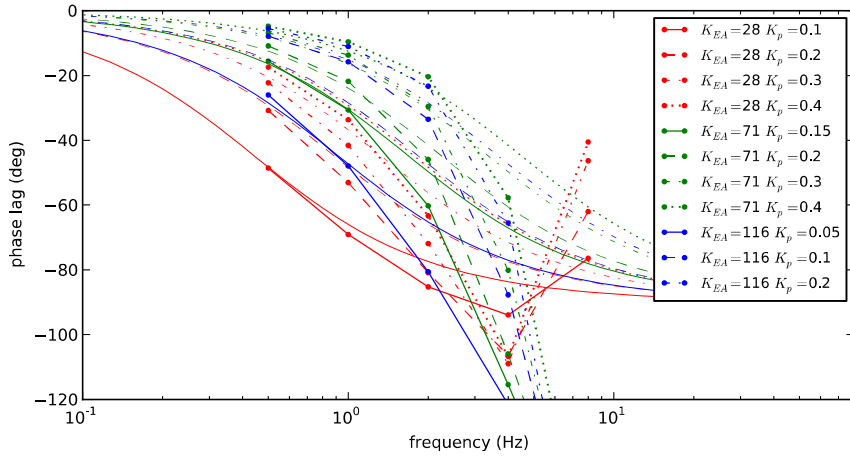


Figure 5.17: Tension phase frequency response with feedback control

5.2.4.3 Use of Feedforward Control

Use of a feedforward term in the tension controller, as was described in Section 4.3.2.4, gives a dramatic improvement in the response. Since it proactively actuates the cables according to changes in the tension setpoint rather than leaving all adjustments to the proportional controller reacting to the setpoint errors, the response is no longer limited by controller gain, K_p . This can be seen in the time constant and RMS error plots of Figure 5.18, which are almost constant

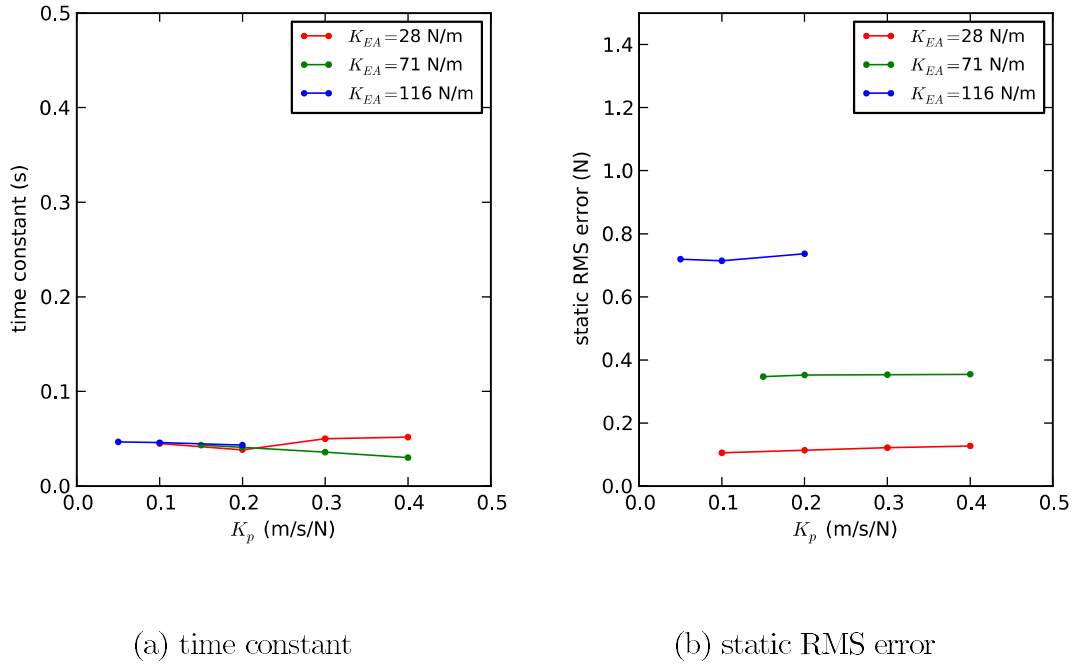


Figure 5.18: Tension step response metrics versus controller gain for feedforward control

with respect to K_p . Similarly, the magnitude and phase responses of Figures 5.19 and 5.20 show little sensitivity to K_p . They also show marked improvement in comparison to the results plotted without feedforward control (Figures 5.16 and 5.17) and the theoretical feedback-control response curves shown.

The decoupling of response and controller gain means that high gain levels are no longer required. This alleviates some of the instability concerns encountered when only feedback control was used. The feedback control now fills a less demanding “adjustment” role, complementing the rapid action of the feedforward controller with small adjustments to account for dynamic errors such as may be caused by the linear elasticity approximation and to ensure the mean cable tensions stay on target. In the complete system, the errors compensated for would also include those incurred in motion tracking and inverse kinematics calculations.

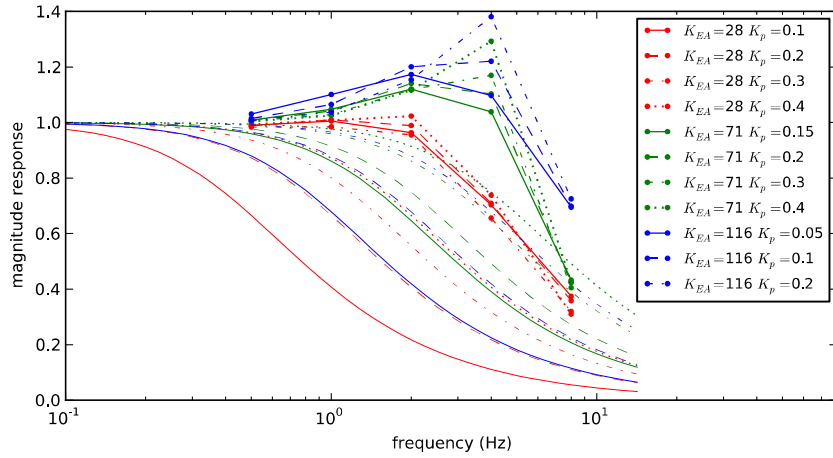


Figure 5.19: Tension magnitude frequency response with feedforward control

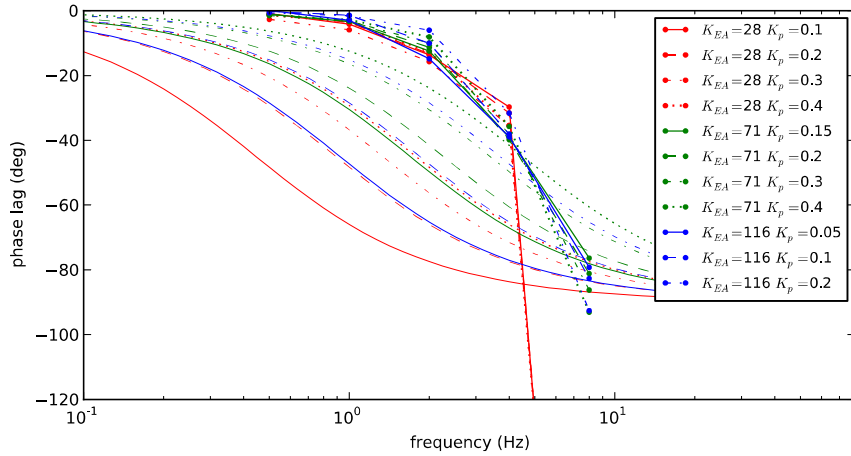


Figure 5.20: Tension phase frequency response with feedforward control

5.2.5 Motion Accommodation Testing

Experience showed that the cubic-fit smoothing and delay compensation technique described in Section 4.3.2.2 applied to position measurements was more practical in this case than using inertial measurement units and sophisticated observers such as a Kalman filter. None of the many tests with these other techniques approached the quality of results obtained using the cubic fitting technique. Free-decay tests

with the pendulum described in Section 5.2.1 and the tension control gain set very low provide a way to measure the effectiveness of the motion accommodation approach. These used the 116 N/m springs and a mean tension of 8 N.

Figure 5.21 shows pitch angles and net actuated force recorded from three free-decay tests. The net force is filtered for plotting clarity. The first test used the motion accommodation approach without any delay compensation applied. Forces of up to 0.5 N applied by the actuator indicate an error in the motion accommodation. These errors are nearly opposite in phase with the pitch accelerations and of a relatively small magnitude overall such that their effect on the pendulum response is only a small increase in natural period and little noticeable damping effect.

The second test features the motion accommodation commands sent to the winches reduced to 90% of their original value. This has a dramatic effect on the response, causing a complete motion decay in less than 4 seconds. Clearly, the magnitude of the motion accommodation commands is important.

To demonstrate the value of tension control on top of motion accommodation, the third test features the normal motion accommodation as well as the tension control gain turned back up to a normal value of 0.2 m/s/N. The tension control significantly reduces the unwanted applied force levels, eliminating the apparent “added mass” effect seen in the first test.

Figure 5.22 shows the effect of adding delay compensation to the motion accommodation approach. It compares results of the normal test shown in the previous plot with tests having 10 ms and 20 ms of delay compensation. This compensation, which seems to be much greater than any delay in this particular system setup, has the effect of shifting the phase of the motion tracking errors

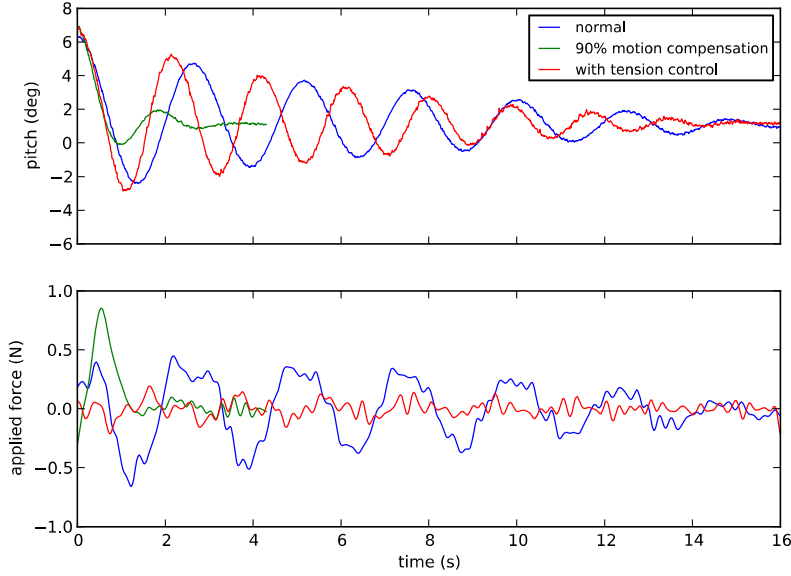


Figure 5.21: Free decay tests with motion accommodation

forward. The result is a slight reduction in the added mass effect and the introduction of a small amount of negative damping. It seems that this negative damping partially cancels with the physical damping in the system (such as from the string potentiometer) and, interacting with unknown nonlinearities in the system, causes the pitch amplitude to stabilize at a certain level for each test.

This sort of motion compensation becomes important when working with optical motion tracking systems that have more significant latency. The above results showed that the latency of the motion compensation part of the controller was closer to 0 ms than 10 ms when using position measurements from a string potentiometer. Brief experimentation with the Qualisys system that would later be used in basin testing and comparing simultaneous measurements from Qualisys and the string potentiometer showed that a delay compensation of 10 ms was appropriate when using the Qualisys measurements.

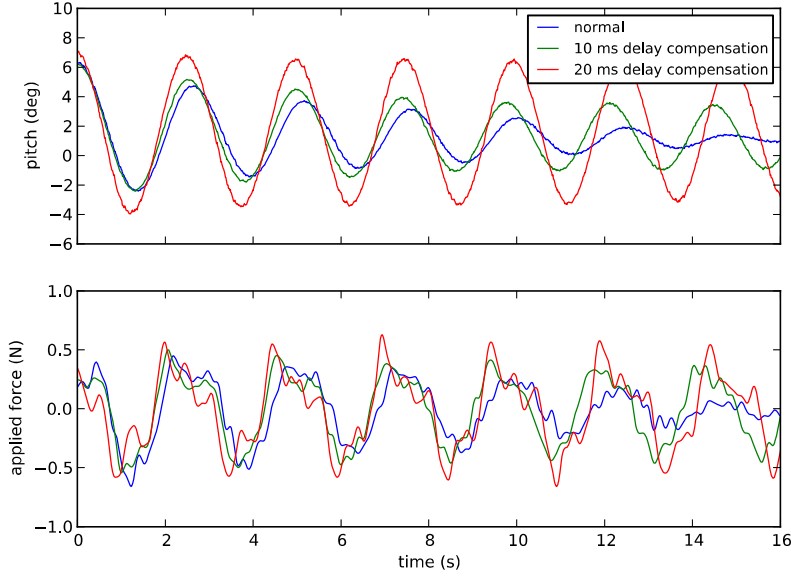


Figure 5.22: Effect of delay compensation in free decay tests

5.2.6 Hybrid Coupling Testing

The capability of the hybrid coupling approach can be tested by using the pendulum and applying simple stiffness, damping, and mass contributions on the numerical model to see their result on the pendulum motion. To make the pendulum more sensitive to the effects of the hybrid coupling, I removed mass to reduce its inertia and stiffness while maintaining a similar natural period. Making a linear approximation for the translation of the coupling point, the effect of the numerical sub-model on the free decay can be easily estimated. Table 5.2 gives the measured and linearized pendulum properties. Table 5.3 shows the expected and measured frequencies, T , and damping ratios, ζ , from free decay tests with the pendulum coupled with a numerical model incorporating mass m , damping c , and stiffness k .

The experimental results in comparison with the theoretical values show that the system accomplished the effect of adding simulated mass, damping, or stiffness

Table 5.2: Pendulum properties used in hybrid coupling tests including hub-height linearized values

natural frequency (rad/s)	2.8
pitch stiffness (N-m/rad)	5.35
moment of inertia (kg-m ²)	0.68
linearized stiffness (N/m)	7.96
linearized mass (kg)	1.01
linearized damping (N-s/m)	0.29

Table 5.3: Results of free decay tests with hybrid model

k (N/m)	c (N-s/m)	m (kg)	Expected decay		Measured decay	
			T (s)	ζ	T (s)	ζ
2			2.24	0.0506	2.24	0.0506
4			2.00	0.0452	1.845	0.0584
8			1.83	0.0413	1.769	0.0574
16			1.58	0.0357	1.724	0.0438
	0.5		1.29	0.0292	1.155	0.0344
	1.0		2.24	0.1387	1.98	0.0986
	0.2		2.24	0.2269	2.33	0.1298
	0.4		2.45	0.0462	2.32	0.0692
			2.65	0.0428	2.35	0.0664

across the hybrid coupling. Equally apparent are the limitations in this ability arising from the string potentiometer-based position measurement, which has a poor signal-to-noise ratio and adds difficult-to-quantify friction to the pendulum motion. The best performance of the hybrid model occurs when the numerical model adds stiffness, since this does not rely on differentiation of the position measurements. Stiffnesses of up to 16 N/m were added, double the physical stiffness of the pendulum. The effect on the natural frequency matches the predicted value to within 10%. Larger disagreement in observed damping ratio could be attributed to friction of the string potentiometer not fully accounted for. Angular changes could also have an effect at larger pendulum amplitudes. The addition of damping and inertia in the numerical half of the model did not have as much effect as expected and lead to instability at values larger than those shown in

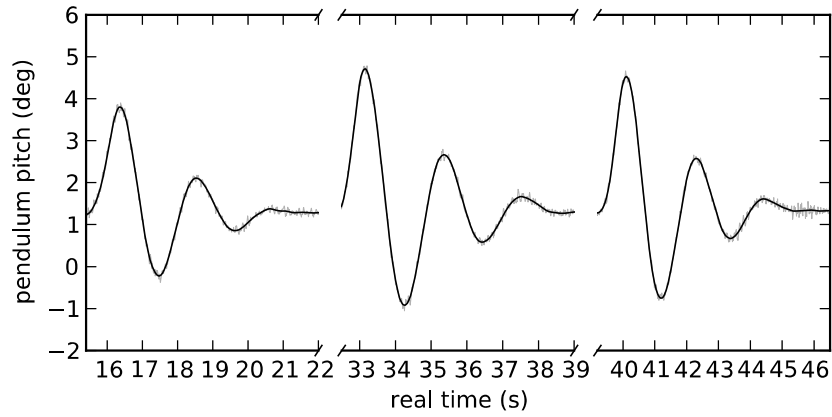
Table 5.3. The amplification of noise in differentiation of position measurements was the limiting factor in these tests.

Experience with the Qualisys optical tracking system that would be used in basin testing indicated that these limitations would be significantly reduced using that system. Because access to the equipment was limited, all bench testing with the Qualisys system was focused on integration with the control system and implementing safety control procedures rather than any methodical testing suitable for quantitative analysis.

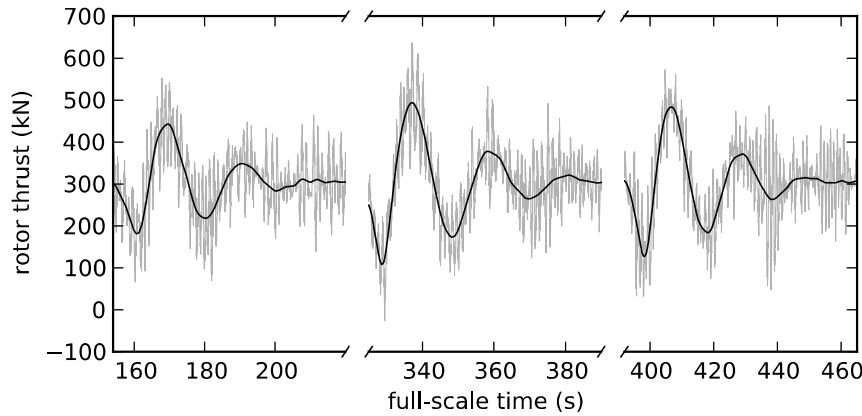
5.2.7 Pendulum-FAST Coupling Testing

As mentioned in Section 4.3.2.3, using a more advanced time-domain numerical model can make the hybrid coupling more challenging, particularly because of the greater need for delay compensation. I conducted a number of tests with the pendulum coupled to FAST in the course of developing the coupling system. Figure 5.23 gives sample time series from the most recent of these tests, showing the pendulum pitch angle, FAST-calculated rotor thrust, and actuator-applied force for decay tests in which the pendulum was rotated to 4 degrees and then released. The pendulum pitch and applied force are shown in model scale, while the calculated rotor thrust is given at full scale, to illustrate how the coupling connects models of different scale. Since the pendulum is considered a 1:100-scale model, the conversion is easy to see: time is scaled by a factor of 10 and forces are scaled by a factor of 10^6 .

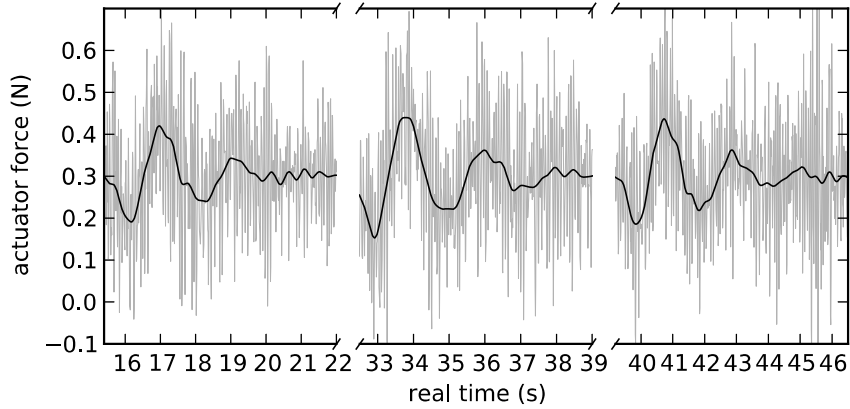
The pendulum in these tests is the same as that of the previous section to give greater sensitivity. To avoid this causing an overly large mean pitch angle, I reduced the thrust forces in the FAST model by setting the blade pitch to 8.6



(a) pendulum rotation



(b) calculated full-scale rotor thrust



(c) applied force by actuator

Figure 5.23: Raw (gray) and filtered (black) time series of free decay tests with pendulum-FAST hybrid model

degrees rather than 0 degrees. The simulated turbine is the NREL 5 MW design at a fixed rotor speed of 12 rpm operating in steady 12 m/s winds.

The time series show that the simulated aerodynamic forces damp out the physical pendulum motion rapidly. Agreement between the thrust force calculated by FAST and the force applied by the actuator is visible in the filtered results but far from perfect.² A large amount of noise in the calculated and applied forces degraded the force-actuation accuracy compared to the tension-control tests presented in Section 5.2.4. This noise is a result of the noise in position measurements from the string potentiometer, which is amplified in computing the velocities that are the main determinant of aerodynamic loading. As mentioned in the last section, use of an optical tracking system in basin testing would greatly reduce this noise. As well, the larger scale used in basin testing would significantly reduce the importance of error amplitudes observed in these 1:100-scale bench tests.

5.2.8 Conclusions on Bench Testing

Bench testing allowed for developing the hybrid coupling implementation in the presence of the real equipment constraints that have a large impact on control effectiveness. In combination with theoretical considerations described in the last chapter, this provided a balanced approach to achieving a successful system.

Tests revealed trends and practical limits in controller performance, such as how the product of controller gain and spring stiffness is limited by the presence of latency in the control loop and noise in the tension measurements. Comparing different tension-control strategies, I was able to show clear benefits to a control system combining feedback control with a tension observer, feedforward control,

²Filtered plots used a 6th-order Butterworth filter with 2.5 Hz (0.25 Hz full-scale) cutoff frequency.

and accommodation of platform motions using a polynomial-fit approach that includes delay compensation.

With this established, I evaluated the hybrid coupling system on the pendulum testbed with numerically-modeled stiffness, damping, and mass. Finally, I tested the complete coupling through free decay tests coupled with FAST. These tests showed the successful operation of the technique, but also the limitations in performance arising from a low-quality motion sensing approach compared to what would be used in basin testing.

The bench test results suggested what controller parameters were suitable for the large 116 N/m springs that would be used in the basin. The 0.05 s cutoff frequency on the tension observer filter provides a good compromise between noise and latency (Section 5.2.4.1). A delay compensation value of 20 ms improves the motion accommodation when using Qualisys motion tracking (Section 5.2.5). A proportional gain of 0.2 m/s/N provides the best gain characteristics at the important frequencies of 2 Hz and below (Section 5.2.4.3). Higher gains risk instability while lower gains provide less correction for errors in motion accommodation. These are the tunings that I used in basin testing.

5.3 Basin Testing

Following extensive bench testing, I tested the hybrid coupling system with a complete 1:50-scale floating wind turbine experiment in the UMaine W² wind-wave facility with assistance from several colleagues. This testing used the well-studied DeepCwind semisubmersible floating wind turbine prototype and followed the hybrid coupling approach that was bench tested by using two opposing winches to apply aerodynamic loads on the physical structure at hub height in the x (downwind) direction. The hybrid model tests were done in between conventional wind-wave tests of the same prototype. The resulting consistency of conditions between conventional and hybrid model results presents a unique opportunity for validating the hybrid model behavior and also exploring the effect of the capabilities only possible with the hybrid approach.

All tests with waves used a JONSWAP sea state with full-scale significant wave height of 7.1 m and peak spectral period of 12.1 s. This is the same “operational 2” sea state as was used in the DeepCwind tests at MARIN, and is near what could be expected in the Gulf of Maine in one-year storm conditions. As such, it is representative of conditions that could be design driving for a floating wind turbine in which the turbine would still be expected to be operational. Several wind conditions and turbine models were used, which will be described more in later sections. Table 5.4 summarizes the tests that were run in the basin, consisting of two conventional physical tests without the hybrid coupling system and five hybrid model tests. All tests with an operating turbine used a rotor speed of 12.1 rpm. Simulations of the true-to-scale NREL 5 MW turbine used a blade pitch angle of 0 degrees and a wind speed of 12 m/s, approximating the maximum-thrust operating conditions of the turbine. Tests or simulations with the Froude-scaled turbine used a blade pitch angle of 6.4 degrees and a wind speed of

21 m/s, set to match the maximum thrust force of the NREL 5 MW turbine given the performance reductions of Froude scaling.

Table 5.4: Summary of test cases used in wind-wave basin

Test name	Wind	Turbine	Aerodynamics model
physical, no wind	0 m/s	DeepCwind	physical (no cables)
physical turbine	21 m/s	DeepCwind	physical (no cables)
zero thrust	-	-	no net force
steady thrust	-	-	800 kN force
model turbine	21 m/s	DeepCwind	FAST/AeroDyn
NREL 5 MW	12 m/s	NREL 5 MW	FAST/AeroDyn
NREL turbulent	12 m/s trb.	NREL 5 MW	FAST/AeroDyn

In keeping with the bench testing section, the experimental setup is described in model-scale units. However, since the testing is of a scale-model floating wind turbine system, all results are reported in full-scale units.

5.3.1 Experimental Setup

The 1:50-scale DeepCwind semisubmersible model turbine tested is the same design as was tested at MARIN in 2011 with some adjustments. The platform has the same properties as presented earlier in Table 2.3. Load cells measure the mooring line tension next to the fairlead. Quantities in this section are at model scale to reflect the true size of the setup.

Figure 5.24 shows the overall arrangement of basin testing. The University of Maine W² wind-wave facility features a wave basin of 30 m length, 9 m width, and 4.5 m maximum depth. A movable floor allows the depth to be adjusted. Poly-chromatic and multi-directional waves can be produced by a 16-paddle wave maker at one end of the basin. At the other end, an elliptical beach minimizes wave reflection. A wind generator of 4.4 m width and 3.2 m height is positioned above the basin. With four rows of eight fans, a series of screens, and a

constriction, it produces winds of up to 7 m/s to allow full wind-wave testing of floating structures.

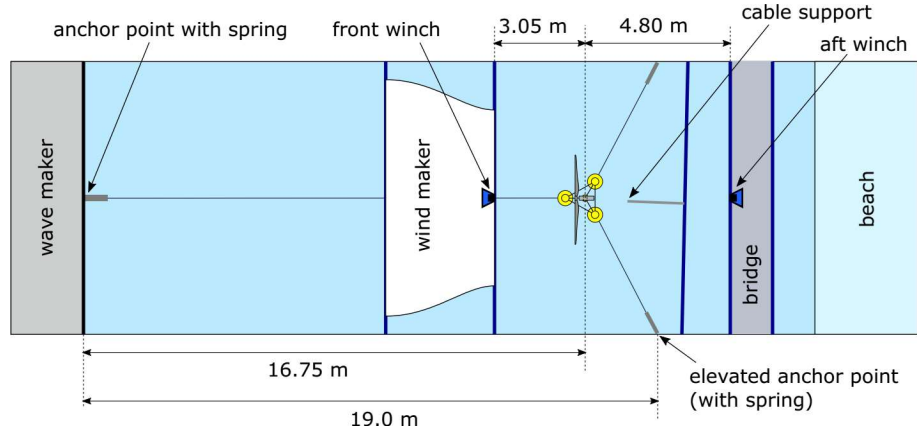


Figure 5.24: Layout of basin testing

The mooring system is not the same as the one used at MARIN because of the smaller dimensions of the facility. The moorings are truncated to fit within the 30 m by 9 m area of the W² basin. The water depth is 4 m. A spring at the anchor connection of the upwind mooring chain compensates for the stiffness increase from Froude scaling. The two lateral mooring lines, which are truncated by a large factor, are anchored at points 1.6 m above the bottom through compliant springs to approximate the force-displacement characteristics of the untruncated mooring system. The chain is of the same type as used previously (Table 2.5). This approach was designed and implemented by Matthew Fowler [113].

The wind turbine is the same as that described in Table 2.2 except that the nacelle mass is slightly reduced at 2.58 kg. It features the same instruments as used in previous tests [17], including rotor speed and torque measurements, a 3-axis accelerometer, and a 6-axes load cell at the tower top.

An important difference is the cable bundle connecting the instruments on the turbine and platform to the data acquisition and control system. As shown in

Figure 5.25, these cables were suspended from a point approximately 0.7 m above the water line and 0.5 m behind the tower centerline when the platform is in its neutral position. The turbine motor cable was relatively large and the weight and stiffness of the cables had an effect on the turbine motions greater than in tests at MARIN.

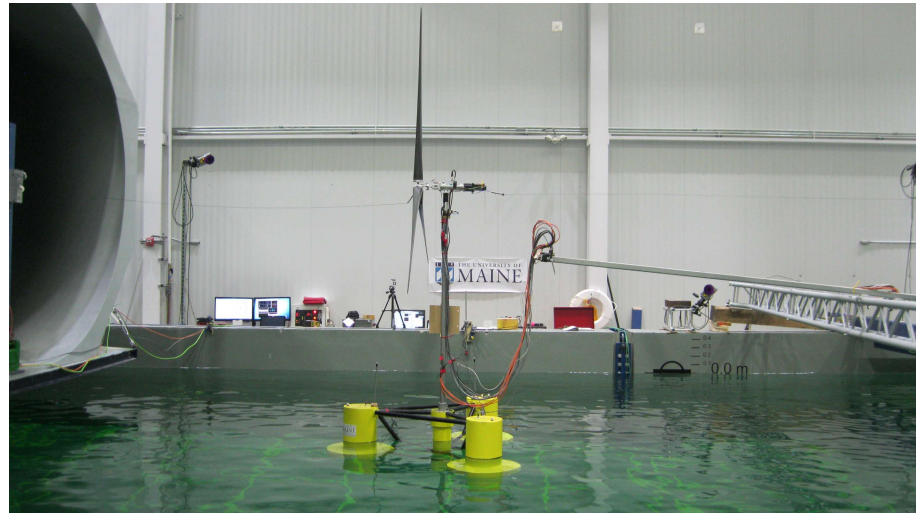


Figure 5.25: 1:50-scale DeepCwind semisubmersible in basin with hybrid coupling attached

Optical motion tracking is provided by a Qualisys system of three Oqus cameras. Five reflective markers on top of the platform and three on the nacelle enable 6-DOF position measurements of these bodies.

5.3.1.1 Hybrid Coupling Setup

The hybrid coupling system was set up over top of the existing basin setup without having to remove anything. We positioned the two winch units at hub height along the center of the tank 3.05 m ahead and 4.80 m behind the undisplaced platform center position. The mounting of the winch units can be seen in Figure 5.26.

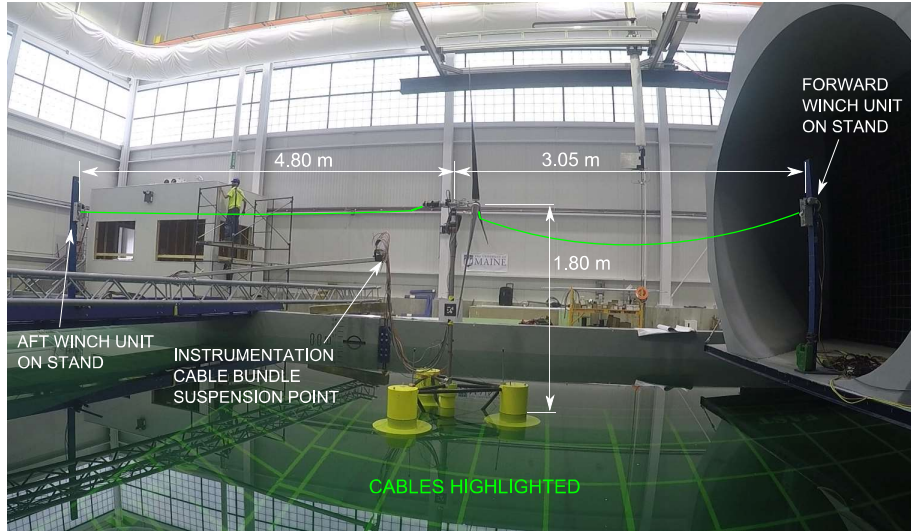


Figure 5.26: Arrangement of cable system in basin

Carefully secured thread and cable ties connected the springs to the turbine. The forward spring was connected to the center point of the hub, a distance of 212 mm ahead of the tower centerline. The aft spring was connected to encoder at the aft end of the nacelle, a distance of 272 mm behind the tower centerline. The nacelle with the springs connected is shown in Figure 5.27.

Given the maximum expected thrust force of 7.9 N at model scale (982 kN full scale), as described in the performance specifications in Table 3.5, I selected the 116 N/m springs and a mean tension of 8 N. This selection allows a maximum applied force of 10 N while staying within the spring's linear range (Table 5.1). The hybrid coupling control system is the same as described in Section 4.3.2.5. The tension filter cutoff period is 0.05 s, the controller gain is 0.2 m/s/N, and the motion observer delay compensation level is 20 ms for motion accommodation and 30 ms for input to FAST.

The same thread used in bench testing was used in the basin to run between the winch units and the springs on the nacelle. To prevent the long length from significantly reducing the cable stiffness, four strands of thread were run in parallel

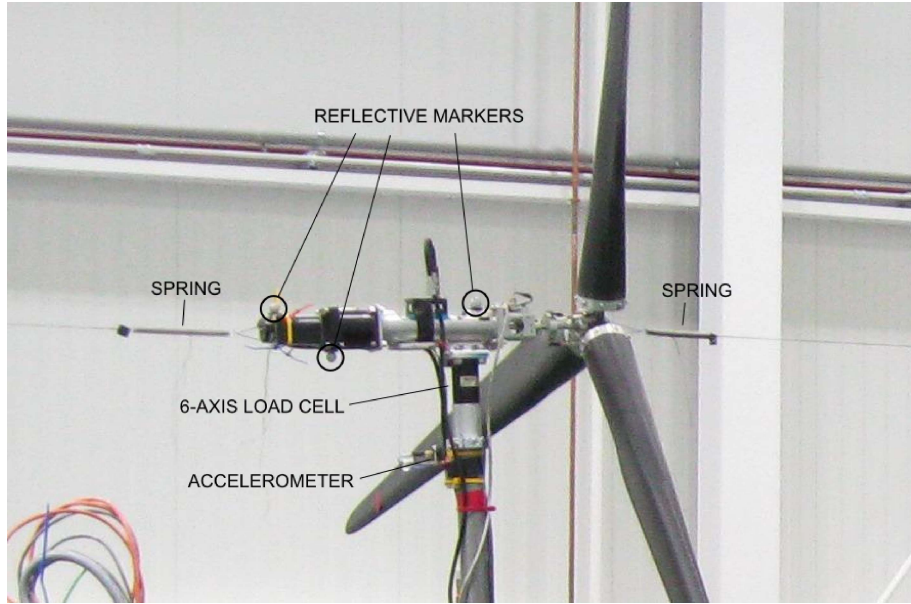


Figure 5.27: Turbine nacelle with cable system attached for hybrid model basin testing

over most of the length. I estimated the total stiffness of the thread running between each winch and spring at 380 N/m. Considering the 116 N/m spring stiffness in series with this, I used a total stiffness of $k_{EA} = 90$ N/m in the controller settings.

The Qualisys optical tracking setup already in place for testing the DeepCwind semisubmersible was not altered for use with the hybrid coupling system. The only change was using a different computer that was networked with the coupling system. Since the coupling point in the hybrid model was at the center of the nacelle, the 6-DOF motions of the nacelle were passed from the Qualisys software to the real-time control system during testing.

The sole problem in the Qualisys setup was that noise in the roll DOF was quite high. This was likely a result of the use of only three markers on the nacelle, and their arrangement almost in line with the x axis (the wind and wave propagation direction). Rather than solving the problem by adding another marker, I chose to

leave the setup intact and simply zero the roll DOF in the motions passed to the simulation. This seemed a reasonable simplification in this case since the roll amplitudes were very small during tests and the hybrid coupling only provides forces in the x direction.

5.3.2 Validation of Hybrid Approach

Two conditions that had the cable actuation system running match conditions tested conventionally in the basin. The first is the “zero-force” test, which aims for the actuation system to apply no net force on the floating structure. This case matches with the wave-only test run in the wave basin before the hybrid coupling system was attached. A time series excerpt and a PSD plot of the net force applied by the actuation system during this test are given in Figures 5.28 and 5.29, respectively, in full-scale units.

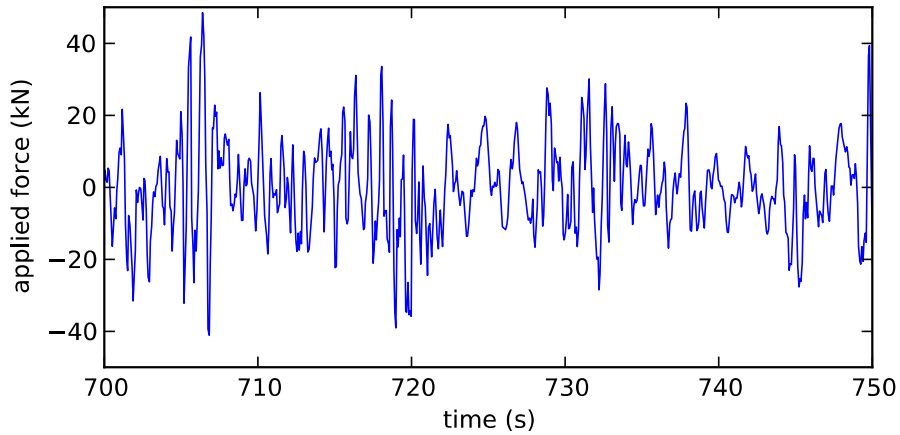


Figure 5.28: Applied force time series in zero-thrust test

This no-wind condition provides a good baseline of comparison between the response with the actuation system and the response of the conventional system, before the additional complexities of the wind turbine aerodynamics are introduced. In the zero-force test, the RMS amplitude of the force errors applied

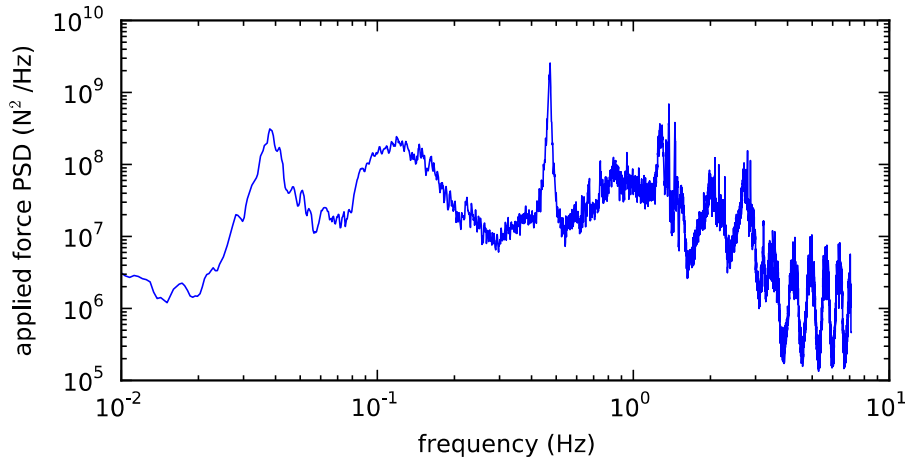


Figure 5.29: Applied force PSD in zero-thrust test

by the actuation system is 0.10 N model scale, or 12.5 kN full scale, which is just over 1.5% of the maximum steady thrust force of the wind turbine. Looking at the noise in this zero-force test allows characterization of the noise applied by the hybrid coupling system in general in any situation. As seen in Figure 5.29, the noise includes a wide range of frequencies from 0.03 Hz to 3 Hz, though the most energy is near 0.48 Hz. This coincides with the natural frequency of the first tower bending mode and confirms the potential for exciting tower bending that was found in Chapter 3.

I identified the tower bending natural frequency from the nacelle acceleration signal during a wave-only test. This measured natural frequency of 0.48 Hz is 41% greater than that found when testing the DeepCwind semisubmersible at MARIN in 2011 (Table 3.3). This difference may be due to the omission of a six-axis load cell at the tower base, which was present in the 2011 tests and would have reduced the stiffness of the tower-base connection.

The second condition that matches conventional test data is the test of the hybrid model featuring the DeepCwind turbine. I set the turbine and wind conditions in the simulation to match the conditions used in the conventional wind-wave test:

the blade pitch was approximately 6.4 degrees, the turbine speed was 12.1 rpm, and the free-stream output speed of the wind tunnel was 21 m/s (full scale). Since the wind turbine being simulated was tuned to match tests with the same physical floating wind turbine model, this case provides a thorough check of the adequacy of the hybrid modeling approach in producing the correct response in the physical subsystem.

Figure 5.30 shows time series excerpts of platform surge, platform pitch, and the upwind mooring line tension from the no wind and 21 m/s wind test cases just discussed. Results from the hybrid model tests are shown with dashed lines and results from conventional purely-physical model tests are shown in solid. The relative agreement between conventional and hybrid model approaches in each of these two cases reflects the successful performance of the hybrid coupling system. Differences between the wind and no-wind test cases are noticeable, with the wind giving higher mean values of surge, pitch, and mooring tension as expected.

Table 5.5 compares the means and standard deviations measured from these three channels for the different tests. As can be seen, the agreement between hybrid and purely-physical cases is quite good, in both means and standard deviations. The largest difference in the no-wind case is that the hybrid coupling system caused a 9% reduction in the pitch standard deviation. (The relative difference in mean surge in this case is insignificant because the mean surge is almost zero.) The most noticeable differences in the wind-turbine-operating case are that the hybrid approach yielded a 14% lower mean surge and 7% greater pitch motions (though a lower mean pitch) than the conventional test. The lower mean surge and pitch in the hybrid case can be attributed to a difference in mean thrust force between the physical turbine and the numerical model. This could be a result of difficulty in precisely setting and measuring the blade pitch angles on the prototype turbine, or

inaccuracy in setting the laboratory wind speed due to limited experience with the new wind generation equipment. The increased pitch standard deviation when using the hybrid approach may be an indication that the numerical aerodynamics model does not perfectly capture the dynamic response of wind loads to turbine motions.

Table 5.5: Comparison of hybrid and conventional approaches with and without wind

	Surge (m)		Pitch (deg)		Line 1 Ten. (kN)	
	mean	std.	mean	std.	mean	std.
no wind - hybrid	0.920	1.118	0.08	0.66	1185	134
no wind - conventional	0.789	1.118	0.08	0.72	1140	127
% difference	17%	0%	-1%	-9%	4%	6%
steady wind - hybrid	5.734	1.099	2.76	0.64	1476	191
steady wind - conventional	6.703	1.117	2.96	0.59	1539	202
% difference	-14%	-2%	-7%	7%	-4%	-5%

To provide a look at the frequency content of the measurements being compared, Figure 5.31 shows PSDs of the same three channels. Regardless of the presence of wind, the hybrid model test and physical test PSDs are in good agreement over most of the spectrum.

The agreement in surge is especially good at the 0.01 Hz peak, corresponding to surge natural frequency, and at 0.08 Hz, corresponding to the peak wave frequency. Surge disagreement is most noticeable around 0.035 Hz, which is the pitch natural frequency, suggesting that differences in pitch response are appearing in surge as a result of surge-pitch coupling.

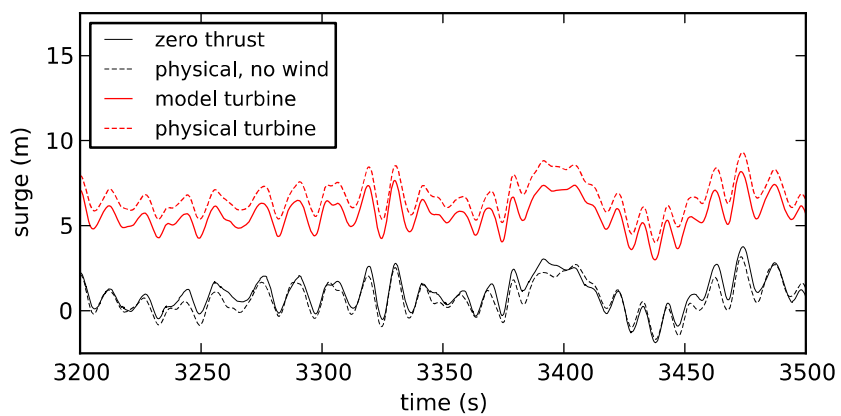
Looking at pitch in Figure 5.31, the height of the peak at 0.08 Hz, which lines up with the peak wave excitation, is very similar across cases. The cases with wind have slightly less excitation at the 0.035 Hz pitch natural frequency and around the 0.01 Hz surge natural frequency. This supports the general understanding that

having the turbine operating (without blade pitch control) adds aerodynamic damping on the fore-aft motions at hub height.

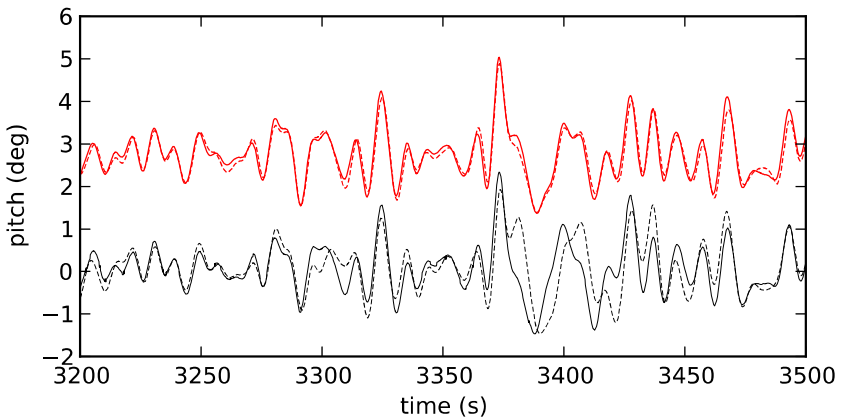
When the turbine is operating, the apparent aerodynamic damping of pitch is slightly greater in conventional tests than in hybrid tests. This difference is clearly observable only at the pitch natural frequency since this is the most resonant mode of the global response. This may be evidence of effects from the hybrid coupling system or differences between the physically- and numerically-modeled aerodynamics. One possible effect of the hybrid coupling system is the single directionality of the force applied by the cables, which excludes the vertical components and pitching moments that exist when operating the physical turbine. Not accounting for the aerodynamic pitching moment (about hub height) would contribute to the reduced aerodynamic pitch damping apparent in the hybrid model results. Another effect of the coupling system is added pitch stiffness because the cable connection points on the nacelle are spaced 0.48 m apart. This adds a moment whenever the platform is pitched, and it varies depending on the applied thrust force and cable pretensions. Stated another way, the moment arm of the thrust force acting on the platform changes when the platform pitches. Differences between the numerical and physical wind turbine models could also play a role, since the numerical wind turbine model was tuned for steady-state rather than dynamic characteristics [63]. Between these three factors, small differences in pitch response between hybrid and conventional tests are not surprising. Investigating and eliminating these differences is an important area for future work.

The mooring tension PSD is higher across-the-board in the wind-wave case than the wave-only case. This corroborates an observation in work with MoorDyn: that, for a given sea state, the nonlinear stiffness of the mooring system causes

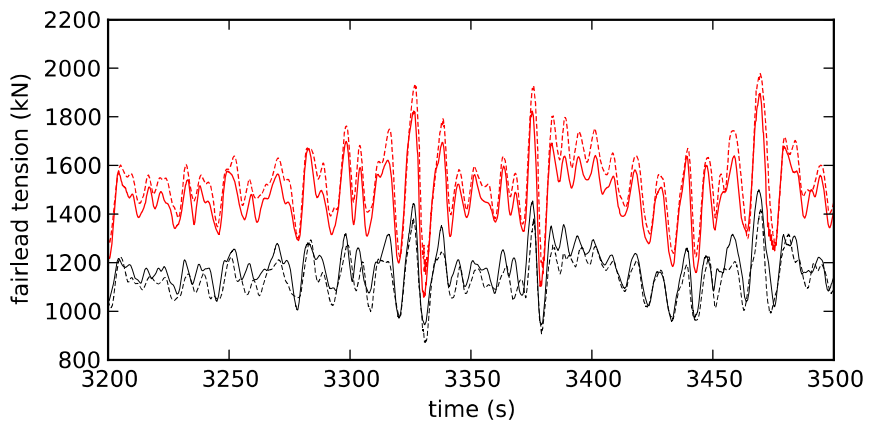
increased tension fluctuations in the up-wind line when the mean surge is increased. The consistent difference seen in Figure 5.31c indicates that this difference applies across a wide frequency range. This phenomena can be understood from a quasi-static point of view by considering the nonlinear force-displacement relationship of a single mooring line.



(a) platform surge

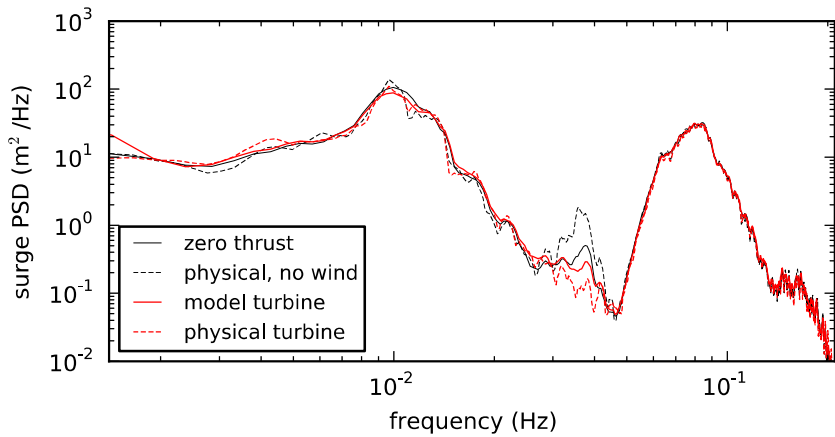


(b) platform pitch

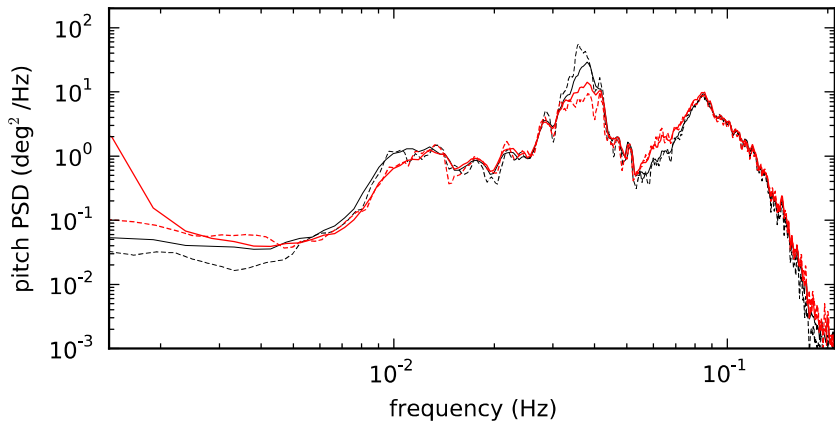


(c) mooring line 1 tension

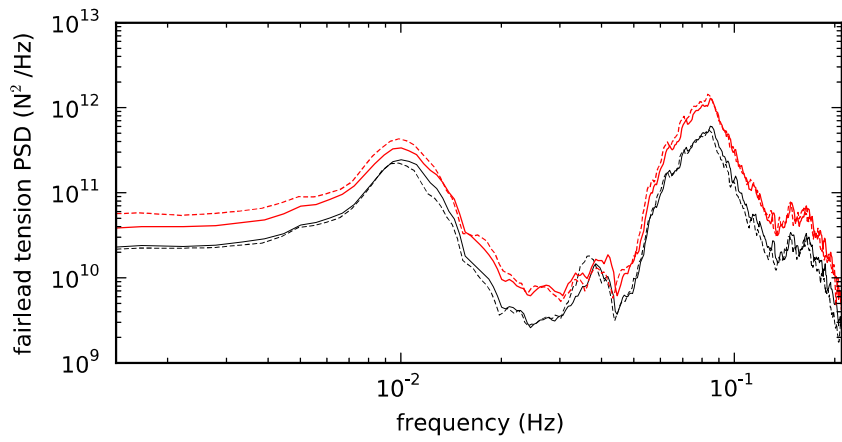
Figure 5.30: Comparison of hybrid (solid line) and conventional (dashed line) wave-only and wind-wave tests



(a) platform surge



(b) platform pitch



(c) mooring line 1 tension

Figure 5.31: PSD comparison of hybrid (solid line) and conventional (dashed line) wave-only and wind-wave tests

5.3.3 Results with New Hybrid Model Features

After the hybrid model approach is verified by comparing against a conventional physical wind-wave approach, new capabilities enabled by the hybrid approach can be explored. The first of these is using true-to-scale turbine characteristics of the NREL 5 MW turbine, since scalability is the most fundamental limitation of the conventional testing approach. Then, additional features that are more easily done in the hybrid approach can also be considered, such as blade-pitch control and wind turbulence.

We tested two cases with a numerical model of the full-scale NREL 5 MW reference turbine with the hybrid coupling system in the basin. The first test features fixed rotor speed and blade pitch with steady 12 m/s wind. The second test adds a stochastic wind field with 12 m/s mean speed and class B turbulence (as defined by IEC 61400-1 [85]) calculated by TurbSim [86]. All tests featured the same JONSWAP sea state with 7.1 m significant wave height and 12.1 peak period.

Figure 5.32 shows time series excerpts of platform surge, platform pitch, and upwind mooring line fairlead tension from the three different hybrid model test cases. The similar fluctuations across the three test cases in these plots indicates that wave excitation is the dominant driver of these responses. The greatest deviations are found in the case with wind turbulence, an indication of wind excitation having an important effect. The mean offset between the different cases reflects the different mean thrust forces in the three simulated conditions.

Figure 5.33 shows PSDs of the same three channels. The peaks at 0.08 Hz correspond to the peak wave excitation and have very close agreement across the test cases, corroborating the synchronization visible in Figure 5.32. The peak in

pitch response at the 0.035 Hz pitch natural frequency reveals interesting differences between the simulated conditions.

The Froude-scaled model turbine case has the greatest pitch motion, indicating that it has the least aerodynamic damping. This can be understood by considering that the Froude-scaled wind turbine uses a wind speed of 21 m/s, almost double the 12 m/s wind speed used by the true-to-scale NREL 5 MW turbine. As such, the fluctuations in relative wind velocity induced by a given amount of pitch motion will be smaller in a relative sense for the Froude-scaled turbine. This translates into smaller thrust force fluctuations and hence less aerodynamic damping than cases with the true-to-scale turbine.

That using true-to-scale wind turbine characteristics causes a significant reduction in pitch response at the pitch natural frequency compared to the Froude-scaled turbine characteristics is an expected and important difference made possible with the hybrid modeling approach.

When wind turbulence is added to the true-to-scale turbine scenario, the pitch excitation is increased at all frequencies up to and including the pitch natural frequency. As well, wind turbulence increases excitation in surge and mooring tension at the surge natural frequency and below. As evident in Figure 5.33, wind turbulence at Class B levels has a significant effect on the floating wind turbine response. This speaks to the value of including wind turbulence in basin tests.

Tables 5.6 and 5.7 show the standard deviations of important parameters measured from the basin and recorded from the simulation, respectively, in the hybrid model test cases. These are given to show the differences in excitation between the different conditions imposed on the simulation side: whether model-scale or full-scale turbine and inclusion of turbulence. Differences also exist

in the mean values of these channels, however they are of little relevance to showing the capabilities offered by a hybrid coupling since mean forces and displacements can be easily adjusted (whether physically or numerically) by changing wind speed and rotor RPM. In Table 5.6, fairlead tensions of the upwind line (line 1) and one of the downwind lines (line 2) are shown.

Table 5.6: Standard deviations of measured quantities in hybrid model testing

Turbine sim.	Surge (m)	Pitch (deg)	Line 1 ten. (kN)	Line 2 ten. (kN)
steady thrust	1.11	0.69	196.5	40.1
model turbine	1.10	0.64	191.4	41.2
NREL 5 MW	1.08	0.57	177.0	41.7
NREL turbulent	1.44	0.72	190.1	57.9

Table 5.7: Standard deviations of simulated quantities in hybrid model testing

Turbine sim.	Tower-top mom. (kN-m)	Rotor thrust (kN)	Nacelle acc. (m/s ²)	Blade-root mom. (kN-m)
model turbine	223	20.9	1.90	351
NREL 5 MW	380	46.3	1.91	627
NREL turbulent	1482	118.9	2.04	1819

Table 5.6 shows that simulating true-to-scale conditions with the NREL reference turbine rather than the Froude-scaled basin conditions gave a small reduction in pitch motions and tension fluctuations in the windward mooring. This table also shows the steady-thrust hybrid test case; the absence of aerodynamic damping is apparent in the larger pitch motions compared to cases with simulated aerodynamics. More significant differences appear when looking at the addition of turbulence; all four standard deviations increase, with the increase in platform surge and the aft line tensions being particularly large.

Table 5.7 reveals changes in the variances of forces and acceleration in the simulated turbine across the three different simulation conditions. The variances of all three loads increase significantly when using the true-to-scale turbine rather

than the Froude-scaled basin model. This is likely a result of the much larger wind speed used by the basin model, which as previously mentioned makes the relative wind speed changes caused by platform motion to be less significant to the overall loads. The addition of wind turbulence causes a more than doubling of the rotor thrust and blade-root bending moment standard deviations.

Dividing the standard deviation of the forces applied in the zero-thrust case with the standard deviation in modeled rotor thrust allows estimation of the discrepancy metric that I used throughout Chapter 3, albeit for rotor thrust rather than tower-base bending moment. The relative RMS discrepancy calculated this way is 60% for the Froude-scaled model turbine case, 27% for the true-to-scale case with steady wind, and 11% for the true-to-scale case with wind turbulence. Keeping in mind that much of the discrepancy is at high frequencies that have little effect on the physical support structure model and that, as discussed in Chapter 3, 10% discrepancy is actually very good agreement, these values are not unsatisfactory for a first trial of the hybrid coupling technique.

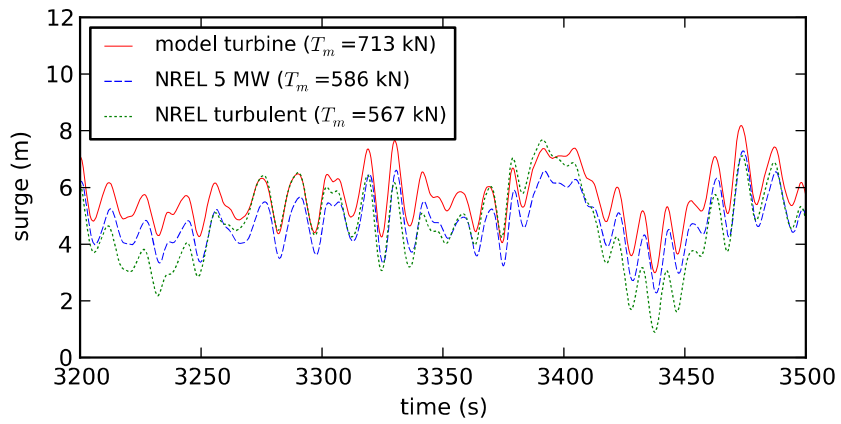
Figure 5.34 shows time series excerpts of rotor thrust, blade-root bending moment, and tower-top bending moment calculated by FAST in the three hybrid model tests. These channels contain a noticeable amount of excitation in the higher frequencies that are relevant for the wind turbine. To uncover the lower-frequency signals which have more influence on the response of the platform, I smoothed the time series with a 6th-order Butterworth filter with 0.5 Hz cutoff frequency. These are overlaid in a darker shade over the original readings.

The rotor thrust fluctuations are visibly larger for the true-to-scale turbine than the Froude-scaled turbine. This difference exists over a wide range of frequencies and is evidence of the greater aerodynamic damping in the true-to-scale turbine, which gives the reduced pitch excitation seen earlier. Naturally, the larger

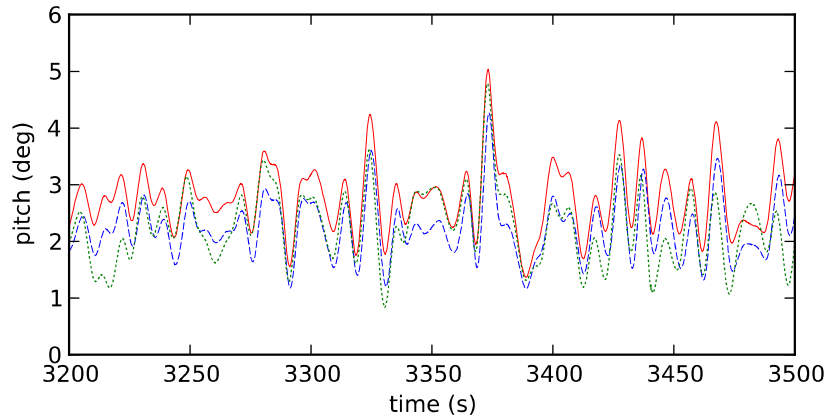
aerodynamic forces also have implications for turbine structural loading and are visible in the yaw-bearing bending moment and the blade-root bending moment. In the presence of turbulent wind, much larger low-frequency variations in the loads appear. These are the source of the low-frequency excitation seen in the platform response in this test.

Figure 5.35 shows PSDs of the same three channels. The excitation in the vicinity of 1 Hz reflects the high-frequency content seen in the time series. As was visible in the time series plots, the true-to-scale turbine has generally larger load amplitudes than the Froude-scaled turbine due to its relatively larger changes in relative wind speed with wave-induced motion. This emphasizes the importance of the thrust versus wind speed curve's slope in affecting the global response of a floating wind turbine. The fact that physical approaches to better-performing Froude scaled turbines still have difficulty matching this slope in some operating conditions ([19]) leaves a useful role for hybrid modeling approaches even at facilities with above-basin wind generation and state-of-the-art turbine rotors for Froude-scaled conditions.

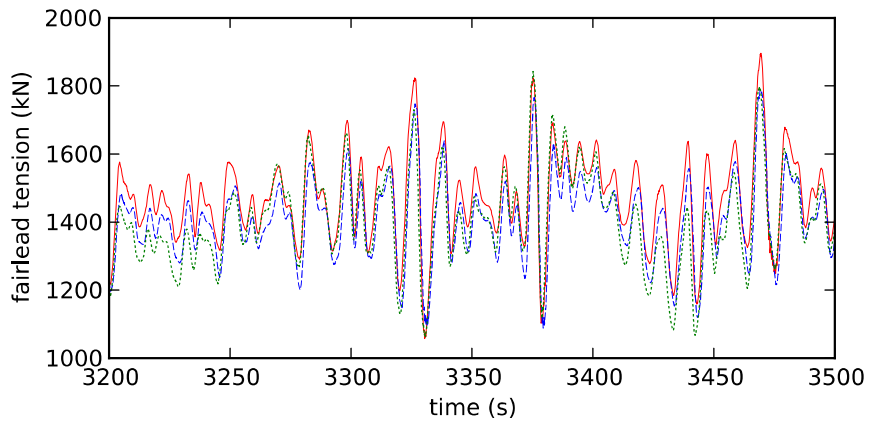
The presence of wind turbulence adds significant further excitation at frequencies below the wave excitation but also at some higher frequencies, such as the 1P and 3P frequencies of rotor rotation and their harmonics. A peak in the blade-root bending moment PSD appears at 0.2 Hz, the 1P frequency, indicating the effect of the spatial variation in wind speed present in the turbulent wind field, which each blade sweeps through at this frequency. The large difference made by wind turbulence, which can be easily introduced and controlled in a hybrid model, demonstrates another advantage of the approach.



(a) platform surge (mean thrust given in legend)



(b) platform pitch



(c) mooring line 1 fairlead tension

Figure 5.32: Sample time series of different hybrid model test cases

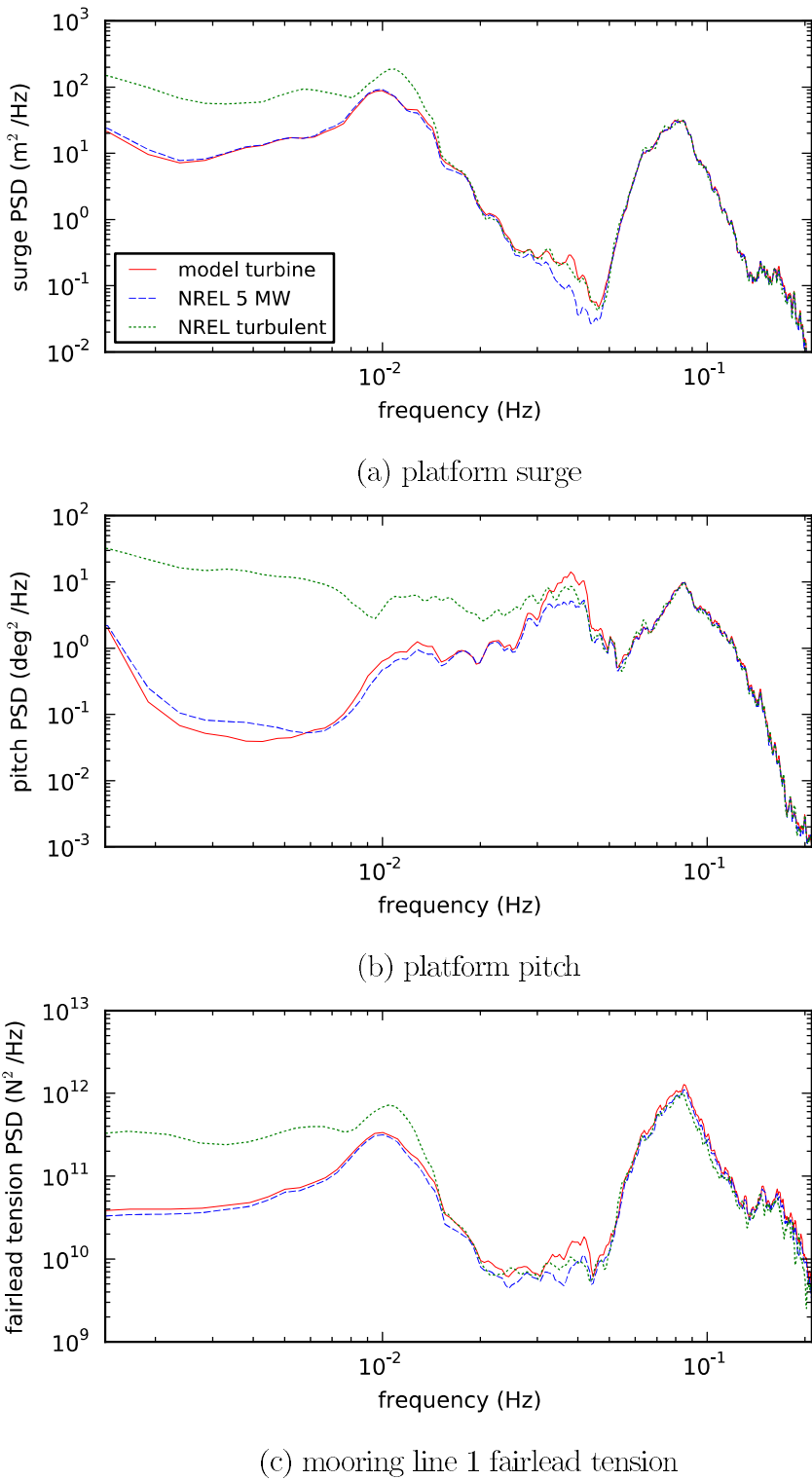


Figure 5.33: PSD comparison of different hybrid model test cases

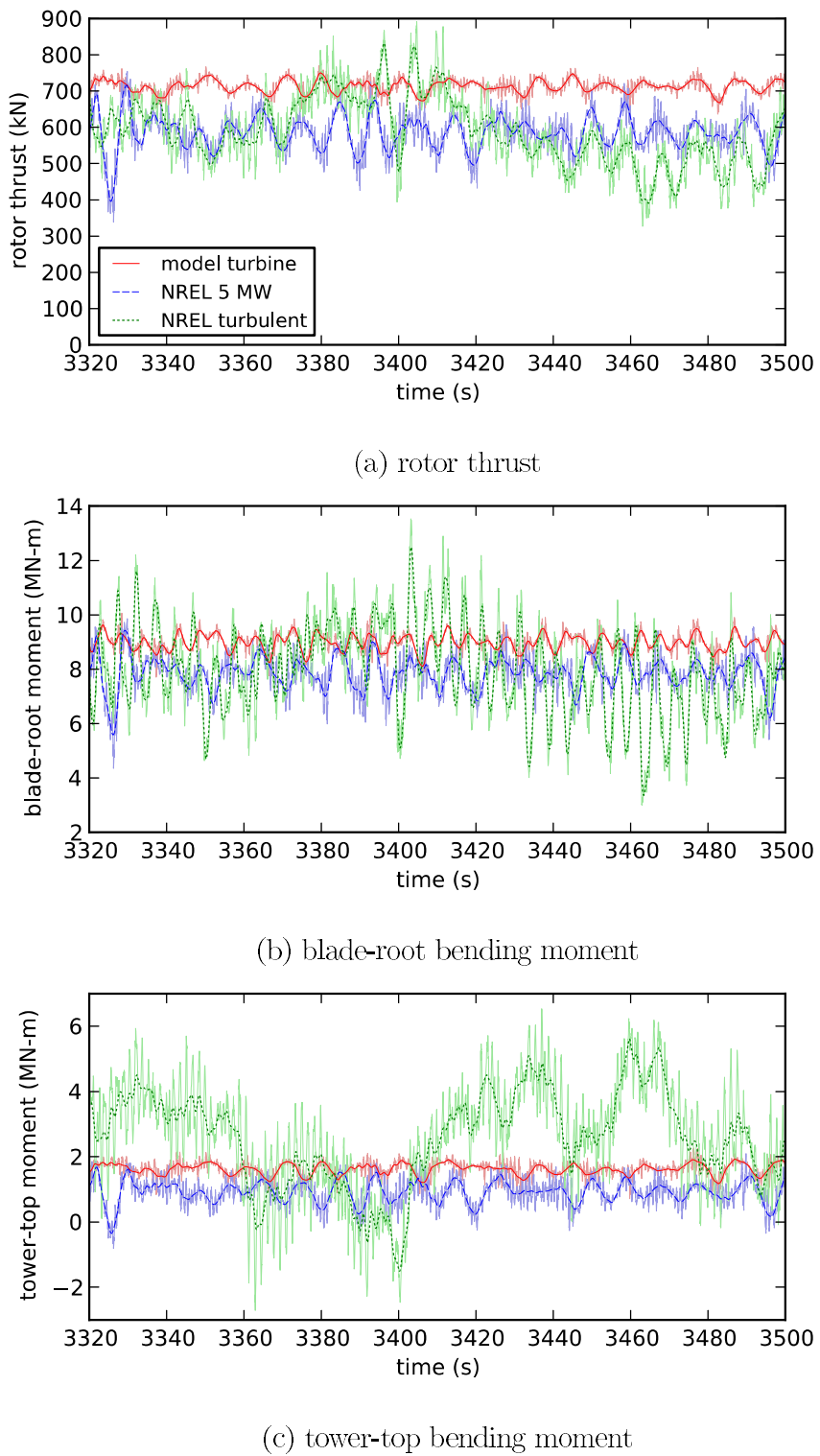
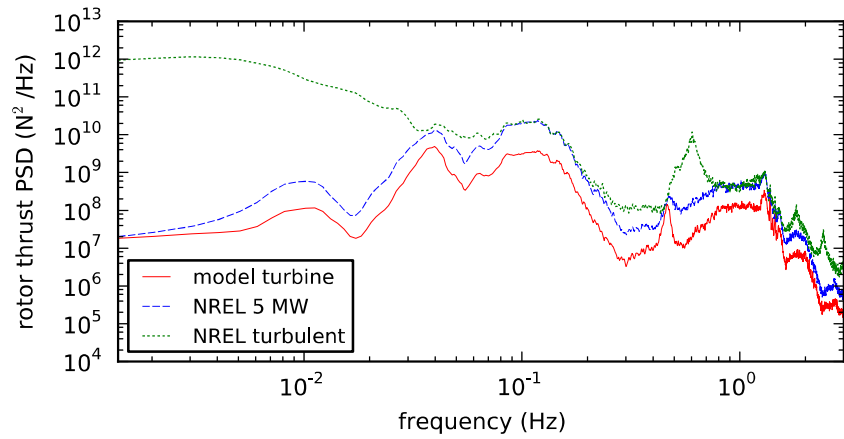
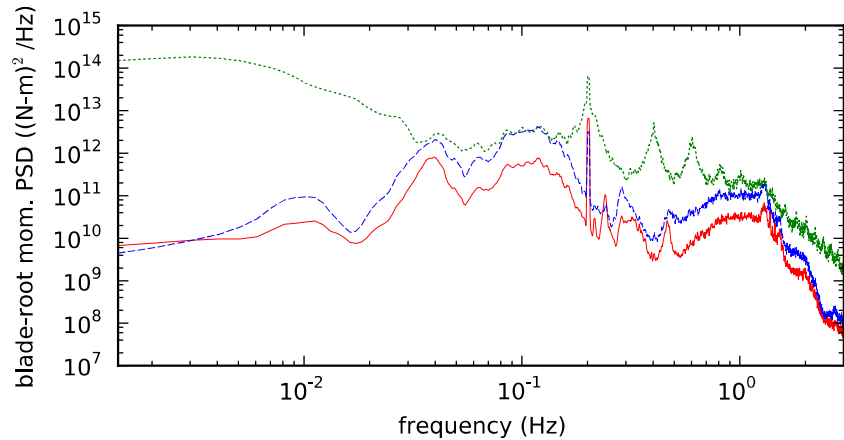


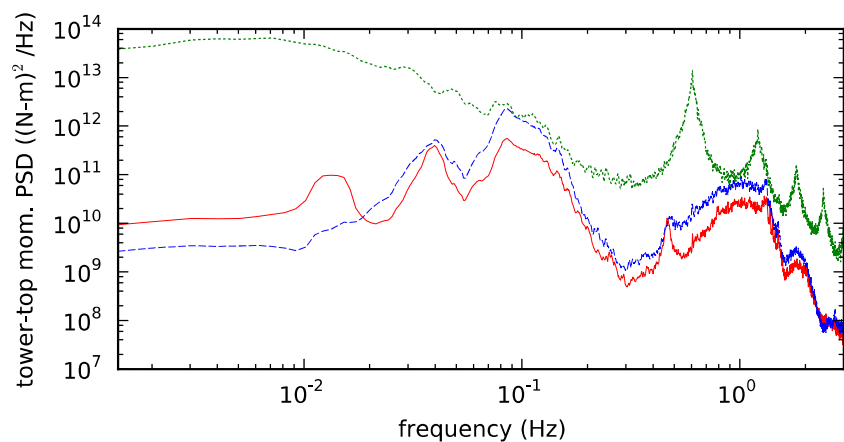
Figure 5.34: Sample FAST time series of different hybrid model test cases



(a) rotor thrust



(b) blade-root bending moment



(c) tower-top bending moment

Figure 5.35: FAST PSD comparison of different hybrid model test cases

5.3.4 Conclusions on Basin Testing

Tests in the UMaine W² wind-wave facility with a 1:50-scale model of the DeepCwind semisubmersible floating wind turbine served to validate and demonstrate the developed hybrid modeling approach. The lack of need for controller tuning demonstrated the efficacy of the extensive bench testing approach in which the entire system was developed in simplified, dry laboratory conditions. This is encouraging for the versatility of the system across different setups.

We also conducted tests of the DeepCwind semisubmersible with the physical model turbine operating in response to the facility's wind generation capability to provide a benchmark dataset representing the conventional testing approach. Comparison of conventional tests with and without wind and the matching tests using the hybrid model showed very good agreement, validating the hybrid modeling approach.

Several additional hybrid model test cases incorporating a true-to-scale wind turbine numerical model allowed exploration of the benefits of the hybrid approach. Using the true-to-scale wind turbine and also including wind turbulence in the simulation caused changes in the coupled system response in line with expectations. This demonstrates the value of a hybrid model approach for wave-basin testing in providing true-to-scale dynamic thrust loads while accounting for the important effects of wind turbulence, which has not yet been achieved in purely-physical wind-wave basin tests. The important difference in aerodynamic damping between Froude-scaled and true-to-scale wind turbine performance was clear in the results.

Although the presented results did not include the effect of blade-pitch control, they demonstrate a level of fidelity that is more than sufficient for including that

effect. Blade-pitch control could be applied in future tests without any change to the system beyond changing a single variable in the FAST input files. This would open a whole range of new possibilities for study.

The goal of the results shown is to demonstrate that true-to-scale wind turbine performance can be accomplished with the hybrid model approach, and that the true-to-scale characteristics have an important effect on the basin-test results. The presence of turbulence was also demonstrated and seen to have an important effect. The intention is not to claim these are important findings from a design point of view, since they are easily accessible from numerical modeling studies and in a real situation an active turbine controller would play a large role in reducing some of the observed differences. Rather, the point is to show that these potential differences do exist, and that a hybrid model testing approach which is capable of capturing them can therefore offer a meaningful improvement to the value of basin testing.

Chapter 6

CONCLUSIONS

The work of this thesis brought together diverse elements including numerical modeling, actuation and control, and physical testing into an integrated approach for hybrid modeling of floating wind turbines.

As described in Chapter 2, I prepared numerical modeling capabilities to handle three types of hybrid coupling: tower-base, aero-elastic, and mooring-platform coupling. Modifications to the floating wind turbine simulator FAST allow its use to study different aspects of hybrid modeling and also its real-time hybrid use.

Towards numerical mooring dynamics sub-models, I created a computationally-efficient lumped-mass mooring dynamics model and validated it against experimental data. This tool benefited the coupled floating wind turbine simulations performed in this thesis and can be used as-is in any future work exploring mooring-platform hybrid modeling.

To inform the development of a hybrid coupling system, I performed a study of what its requirements might be, as described in Chapter 3. I conducted simulations across three support structure designs and seven load cases to identify the performance envelope requirements of the actuation system in terms of motion and force capabilities. Then, I explored the quality requirements of a coupling system using a sensitivity study in which coupling errors in the form of noise and latency were simulated. The results include conclusions for hybrid coupling at the aero-elastic interface and at the tower base. Ultimately, the findings confirm the general feasibility of the hybrid model approach, provide guidelines towards

coupling system design, and shed light on the sources of error which could impact hybrid model accuracy.

After selecting an actuation approach based in part on the work of the previous chapter, Chapter 4 presents the theoretical groundwork and integration of control elements from various sources to end up with a complete strategy for controlling a hybrid coupling system. I reviewed existing approaches to the mechanics of controlling a cable-based robot and then developed a modified approach to meet the requirements of the hybrid coupling application. This impedance-control coupling approach incorporates tension feedback control, accommodation of platform motions using a carefully designed motion observer, and feedforward control for responsive actuation of forces transmitted from the numerical sub-model.

In parallel with the theoretical groundwork described in Chapter 4, I designed and built a prototype hybrid coupling system based on speed-controlled winch units with tension feedback. As described in Chapter 5, I conducted extensive bench tests with the prototype to explore different control strategies and then characterize and tune the final coupling system. Tests with a single winch unit acting on a fixed endpoint allowed parametric study of tension-control performance in order to inform selection of spring stiffnesses, controller gains, and tension filtering. A pendulum test rig provided a way to test all aspects of the coupling system performance in a controlled environment. Results with this system using simplified mass-spring-damper models as well as a wind turbine aerodynamics model had the expected effect in the pendulum's overall response, verifying the legitimacy of the numerical-physical dynamic coupling.

To prove the concept, I applied the hybrid coupling system prototype to a 1:50-scale wave basin testing scenario with the DeepCwind semisubmersible. Tests

of the hybrid approach took place in between tests with the conventional wind-wave approach, providing a unique opportunity for comparison. The platform motions and mooring tensions in conventional tests were matched very well by those produced using the hybrid model corresponding to the same Froude-scaled conditions, validating the hybrid modeling approach. Additional tests featuring a true-to-scale wind turbine model and also simulated wind turbulence showed the capability of the hybrid approach for providing features that are difficult to achieve with conventional methods. The differences between these and Froude-scaled results indicate the improvement that can be realized in basin test results by using a hybrid coupling system.

Ultimately, the basin tests brought the project to a successful completion, demonstrating what I set out to do and, thanks to comparison with conventional wind-wave tests, validating the approach. No significant problems emerged with the hybrid coupling system, and the results do not seem inferior to the conventional test results. As such, the stage is set for use of cable-based hybrid model techniques in basin testing of floating wind turbines.

6.1 Limitations of a Hybrid Approach

Because a hybrid modeling approach adds significant numerical modeling to a basin test, the result is no longer strictly a physical experiment and the attendant disadvantages should be recognized. Aside from limitations in the hybrid coupling system, some of which this thesis considered in detail, a very important factor is limitations in the numerical wind turbine model. The blade element momentum theory approach to wind turbine simulation, as was used in the numerical sub-model in this work, is a medium fidelity approach relying on a number of assumptions. In particular, it is known to lose accuracy when turbine motions are

very large. Quantitative study of this effect was outside the scope of my work, but the issue has been studied in detail by others [114]. Clearly, when deciding whether to use a conventional or hybrid approach for basin testing a floating wind turbine, scaling problems from Froude-scaled aerodynamics should be weighed against the simplifications inherent in numerical wind turbine models. The best choice depends on the performance of the available Froude-scaled wind turbine prototype, the accuracy of the available numerical wind turbine model, and the objectives of the basin testing campaign. Table 6.1 presents a summary comparing the suitability of conventional and hybrid approaches for meeting various basin testing objectives.

Table 6.1: Limitations of conventional and hybrid approaches for basin testing

Basin test objective	Conventional test	Hybrid model test
global response and mooring loads:		
- for design validation	affected by turbine scaling limitations including control	as good as the numerical model
- for model validation	suitable	suitable
turbine loads:		
- for design validation	affected by turbine scaling limitations including control	as good as the numerical model, sensitive to coupling quality
- for model validation	suitable for Froude-scaled numerical models	unsuitable
identification of coupled modes, resonances, etc.	affected by scaling limitations	sensitive to coupling quality
physical proof of concept	affected by scaling limitations	as good as the numerical model, but no longer 100% experimental

Although expanding on all the entries in the table is outside the scope of this work, some preliminary comments can be made based on findings in this thesis and other published work. Some of the entries are obvious: validating a numerical wind turbine model does not make sense with a hybrid approach where the turbine is already simulated. Conversely, if the only concern is numerical model validation, irrespective of scale, then there is no need for a hybrid approach. The technical benefit of a hybrid approach comes into play when true-to-scale coupled response of the system is desired.

Scaling limitations are the most difficult hurdle for conventional testing approaches to be used in validation of full-scale designs. Studies of special rotors designed for Froude-scaled testing give an indication of how large the deviations in rotor torque and thrust are from true-to-scale values [6, 60]. Understanding the effect of these deviations on the global response and turbine loads could be achieved through simulation-based comparison studies.

The numerical model limitations mentioned as a potential weakness for hybrid model approaches have been discussed by Sebastian and Lackner [114, 4] and are associated most with high-velocity platform motions. As higher fidelity aerodynamics models such as free vortex methods and even computational fluid dynamics approaches continue to evolve, broader comparisons with more conventional BEM modeling approaches will provide insight into how important a factor the BEM limitations are to coupled floating wind turbine response. A computationally-efficient free-vortex wind turbine model combined with high-end real-time control hardware could make hybrid model basin tests with improved aerodynamic response possible.

The other limiting factor in a hybrid model is the quality of the coupling system. An exploration of the effects of actuating in reduced DOFs comes from Bachynski

et al. [26], and similar studies could be done to draw conclusions for specific testing scenarios. The findings in Chapter 3 suggest that the required coupling system response for giving good platform motion and mooring tensions is easily achievable. In contrast, modeling turbine loads or structural response acting *across* the hybrid coupling is much more demanding. The experience described in Sections 4.3.1 and 5.2.6 demonstrates the difficulty in achieving a hybrid coupling through a structural member, where inertia exists in both physical and numerical sub-models. The greatest limiting factors are actuator response and measurement noise; improvements in instrumentation, actuation, and control are necessary for hybrid coupling of inertia to be effective.

In summary, the hybrid modeling approach as developed brings some advantages to basin testing in avoiding the scaling limitations of conventional testing. At the same time, some limitations to hybrid approaches make conventional testing more suitable for other situations. The degree of error or discrepancy introduced by conventional or hybrid approaches is an area for further study. When all options are on the table, the choice of hybrid or conventional approaches depends on the objectives of the basin testing. Consideration should also be given to the newness of hybrid approaches; there is likely potential for rapid performance improvement with continued development.

6.2 The Advantage of Accessibility

Aside from its performance potential relative to conventional testing, the hybrid approach offers an important advantage in terms of accessibility. Using a numerical sub-model for the aerodynamics means that floating wind turbine basin testing can be done in facilities without above-basin wind generation capabilities. Excluding the motion tracking system and mounting equipment, which should

already be present at a testing basin, the hybrid coupling system can be fit entirely on a cart, as shown in Figure 6.1. This makes it easy to set up and portable between different facilities. In terms of expense, the cost of the equipment shown on the cart is significantly less than that of a typical high-quality motion tracking system found at a wave basin.



Figure 6.1: Hybrid coupling system used at basin

Given the differences between Froude-scaled and true-to-scale wind turbine performance, designers may find benefit in terms of more trustworthy results by using a hybrid approach in basin testing. Given the non-prohibitive equipment requirements and portability of the system, this technique could be useful even to smaller basin facilities engaged in floating wind turbine research. Given the expense and difficulty of above-basin wind generation capability, the cable-based hybrid approach could be an enabling technology for increased floating wind turbine wave basin research.

6.3 Future Work

There are many possible future steps from the work presented here, some incremental improvements and some new applications.

- A small amount of consistent jitter in the cables was visible during basin testing. Not seen in the bench testing, it may have been due to the longer cable lengths which gave a less-accurate estimate of overall cable stiffness and also could have shifted the optimal controller gain values. Controller tuning at the basin or in larger lab environments could help smooth out minor issues such as this to reduce noise levels.
- Incremental improvements could be made to the control system. For example, motion accommodation and feedforward controllers could be adjusted to account for cable elasticity, and the delay compensation could be improved with more advanced techniques (e.g. [108]).
- Work could be done toward the more challenging situation of hybrid coupling with inertia in both sub-models. This could require additional instrumentation and control improvements, such as adding accelerometer and gyroscope measurements to provide a more accurate and instantaneous observation of velocities and accelerations.
- The tests in the basin did not include blade-pitch control simulation due to limited time. This is a topic of strong research interest, and it could be explored with great flexibility with a hybrid model since the control parameters can be changed on-the-fly in the simulation setup. This raises a variety of opportunities for floating wind turbine controls research that includes physically-modeled hydrodynamics. In the language of controls

design, this approach would be an especially colorful example of hardware-in-the-loop testing.

- Since the coupling system controller was designed for multi-DOF coupling, it would be relatively easy to expand the existing single-DOF, two-cable prototype into a full six-DOF prototype with seven or eight cables. The control algorithms are already in place, and examples exist in the cable robot literature of cable layouts that would be suitable for above-basin actuation (e.g. [90]). This would allow for much more sophisticated hybrid modeling cases such as multi-directional winds, squall, independent blade pitch control, tower-base hybrid coupling and mooring-platform hybrid coupling (e.g. with MoorDyn) – few of which have yet been explored in basin testing.

REFERENCES

- [1] S. Breton and G. Moe, “Status, plans and technologies for offshore wind turbines in europe and north america,” *Renewable Energy*, vol. 34, no. 3, pp. 646–654, Mar. 2009.
- [2] A. R. Henderson, R. Leutz, and T. Fujii, “Potential for floating offshore wind energy in japanese waters,” in *Proceedings of The Twelfth International Offshore and Polar Engineering Conference*, Kitakyushu, Japan, May 2002, p. 26–31.
- [3] A. Cordle and J. Jonkman, “State-of-the-art in floating wind turbine design tools,” in *Proceedings of ISOPE 2011*, Maui, Hawaii, USA, 2011.
- [4] T. Sebastian and M. Lackner, “Characterization of the unsteady aerodynamics of offshore floating wind turbines,” *Wind Energy*, vol. 16, no. 3, pp. 339–352, Apr. 2013.
- [5] R. W. Kimball, A. J. Goupee, M. Fowler, E. de Ridder, and J. Helder, “Wind/Wave basin verification of a Performance-Matched Scale-Model wind turbine on a floating offshore wind turbine platform,” in *Proceedings of the 33rd International Conference on Ocean, Offshore and Arctic Engineering*, San Francisco, California, Jun. 2014.
- [6] E. de Ridder, W. Otto, G. Zondervan, F. Huijs, and G. Vaz, “Development of a scaled down wind turbine for model testing floating wind turbines,” in *Proceedings of the 33rd International Conference on Ocean, Offshore and Arctic Engineering*, San Francisco, California, Jun. 2014.
- [7] S. Mahin and P. Shing, “Pseudodynamic method for seismic testing,” *Journal of Structural Engineering*, vol. 111, no. 7, pp. 1482–1503, 1985.
- [8] J. E. Carrion and B. F. Spencer, “Model-based strategies for real-time hybrid testing,” NSEL, Tech. Rep. NSEL-006, Dec. 2007.
- [9] J. Carrion, B. Spencer, Jr., and B. Phillips, “Real-time hybrid testing of a semi-actively controlled structure with an MR damper,” in *American Control Conference*, St. Louis, MO, USA, Jun. 2009, pp. 5234–5240.
- [10] T. Tidwell, X. Gao, H. Huang, C. Lu, S. Dyke, and C. Gill, “Towards configurable real-time hybrid structural testing: a cyber-physical system approach,” in *IEEE International Symposium on Object/Component/Service-Oriented Real-Time Distributed Computing*, Tokyo, Japan, Mar. 2009, p. 37–44.

- [11] R. Isermann, J. Schaffnit, and S. Sinsel, “Hardware-in-the-loop simulation for the design and testing of engine-control systems,” *Control Engineering Practice*, vol. 7, no. 5, pp. 643–653, May 1999.
- [12] C. Villegas and H. van der Schaaf, “Implementation of a pitch stability control for a wave energy converter,” *Wavebob Ltd*, 2011.
- [13] S. J. Beatty, M. Hall, B. J. Buckingham, P. Wild, and B. Bocking, “Experimental and numerical comparisons of self-reacting point absorber wave energy converters in regular waves,” *Ocean Engineering*, vol. 104, pp. 370–386, Aug. 2015.
- [14] G. Bracco, E. Giorcelli, G. Mattiazzo, V. Orlando, and M. Raffero, “Hardware-In-the-Loop test rig for the ISWEC wave energy system,” *Mechatronics*, vol. 25, pp. 11–17, Feb. 2015.
- [15] S. Chakrabarti, “Physical model testing of floating offshore structures,” in *Proceedings of MTS Dynamic Positioning Conference*, Houston, Texas, 1998, pp. 1–33.
- [16] Y. Cao and G. Tahchiev, “A study on an active hybrid decomposed mooring system for model testing in ocean basin for offshore platforms,” in *Proceedings of the 32nd International Conference on Ocean, Offshore and Arctic Engineering*, Nantes, France, Jun. 2013.
- [17] H. Martin, “Development of a scale model wind turbine for testing of offshore floating wind turbine systems,” MS Thesis, University of Maine, Orono, Maine, 2011.
- [18] K. Müller, F. Sandner, H. Bredmose, J. Azcona, A. Manjock, and R. Pereira, “Improved tank test procedures for scaled floating offshore wind turbines,” in *Proceedings of International Wind Engineering Conference - Support Structures & Electrical Systems*, Hannover, Germany, Sep. 2014.
- [19] H. R. Martin, A. M. Viselli, R. W. Kimball, and A. J. Goupee, “Methodology for Wind/Wave basin testing of floating offshore wind turbines,” in *Proceedings of the 31st International Conference on Ocean, Offshore and Arctic Engineering*, Rio de Janeiro, Brazil, Jun. 2012.
- [20] M. Fowler, R. W. Kimball, D. A. Thomas, and A. J. Goupee, “Design and testing of scale model wind turbines for use in wind/wave basin model tests of floating offshore wind turbines,” in *Proceedings of the 32nd International Conference on Ocean, Offshore and Arctic Engineering*, Nantes, France, Jun. 2013.
- [21] I. Bayati, M. Belloli, A. Facchinetti, and S. Giappino, “Wind tunnel tests on floating offshore wind turbines: A proposal for Hardware-in-the-Loop approach to validate numerical codes,” *Wind Engineering*, vol. 37, no. 6, pp. 557–568, Dec. 2013.

- [22] I. Bayati, M. Belloli, D. Ferrari, F. Fossati, and H. Giberti, “Design of a 6-DoF robotic platform for wind tunnel tests of floating wind turbines,” *Energy Procedia*, vol. 53, pp. 313–323, 2014.
- [23] J. Azcona, F. Bouchotrouch, M. González, J. Garciandía, X. Munduate, F. Kelberlau, and T. A. Nygaard, “Aerodynamic thrust modelling in wave tank tests of offshore floating wind turbines using a ducted fan,” *Journal of Physics: Conference Series*, vol. 524, no. 1, Jun. 2014.
- [24] V. Chabaud, S. Steen, and R. Skjetne, “Real time hybrid testing of marine structures: Challenges and strategies,” in *Proceedings of the ASME 2013 32nd International Conference on Ocean, Offshore, and Arctic Engineering*, Nantes, France, 2013.
- [25] M. Hall, J. Moreno, and K. Thiagarajan, “Performance specifications for real-time hybrid testing of 1:50 scale floating wind turbine models,” in *Proceedings of the ASME 2014 33rd International Conference on Ocean, Offshore and Arctic Engineering*, San Francisco, California, Jun. 2014.
- [26] E. E. Bachynski, V. Chabaud, and T. Sauder, “Real-time hybrid model testing of floating wind turbines: sensitivity to limited actuation,” in *12th Deep Sea Offshore Wind R&D Conference*, Trondheim, Norway, Feb. 2015.
- [27] T. Sauder, V. Chabaud, M. Thys, E. Bachynski, and L. Saether, “Real-time hybrid model testing of a braceless semi-submersible wind turbine: Part i: The hybrid approach,” in *Proceedings of the 35th International Conference on Ocean, Offshore and Arctic Engineering*, Busan, South Korea, Jun. 2016.
- [28] E. Bachynski, M. Thys, T. Sauder, V. Chabaud, and L. Saether, “Real-time hybrid model testing of a braceless semi-submersible wind turbine: Part II: experimental results,” in *Proceedings of the 35th International Conference on Ocean, Offshore and Arctic Engineering*, Busan, South Korea, Jun. 2016.
- [29] M. Hall and A. Goupee, “Validation of a lumped-mass mooring line model with DeepCwind semisubmersible model test data,” *Ocean Engineering*, vol. 104, pp. 590–603, Aug. 2015.
- [30] J. M. Jonkman and M. L. Buhl Jr., “FAST user’s guide,” National Renewable Energy Laboratory, Golden, Colorado, Tech. Rep. NREL/EL-500-29798, 2005.
- [31] J. M. Jonkman, “Dynamics modeling and loads analysis of an offshore floating wind turbine,” PhD Thesis, University of Colorado at Boulder, Nov. 2007.
- [32] M. Hall, B. Buckham, and C. Crawford, “Evaluating the importance of mooring line model fidelity in floating offshore wind turbine simulations,” *Wind Energy*, vol. 17, no. 12, pp. 1835–1853, Dec. 2014.

- [33] P. J. Moriarty and A. C. Hansen, “AeroDyn theory manual,” NREL, Tech. Rep., Dec. 2004.
- [34] J. G. Leishman and T. S. Beddoes, “A Semi-Empirical model for dynamic stall,” *Journal of the American Helicopter Society*, vol. 34, no. 3, pp. 3–17, Jul. 1989.
- [35] W. E. Cummins, “The impulse response function and ship motions,” in *Symposium on Ship Theory at Institut fur Schiffbau der Universitat Hamburg*, vol. 9, Hamburg, Germany, Jan. 1962, pp. 101–109.
- [36] F. Sandner, D. Schlipf, D. Matha, R. Seifried, and P. W. Cheng, “Reduced nonlinear model of a spar-mounted floating wind turbine,” in *Proceedings of DEWEK 2012*, Bremen, Germany, 2012.
- [37] C. Kwan and F. Bruen, “Mooring line dynamics: Comparison of time domain, frequency domain, and Quasi-Static analyses,” in *Offshore Technology Conference*, Houston, Texas, 1991.
- [38] M. Masciola, J. Jonkman, and A. Robertson, “Implementation of a multisegmented, Quasi-Static cable mode,” in *Proceedings of the Twenty-third (2013) International Offshore and Polar Engineering Conference*, Anchorage, Alaska, USA, Jul. 2013.
- [39] T. S. Walton and H. Polacheck, “Calculation of nonlinear transient motion of cables,” David Taylor Model Basin, Washington, D.C., Tech. Rep., 1959.
- [40] N. U. Khan and K. A. Ansari, “On the dynamics of a multicomponent mooring line,” *Computers & Structures*, vol. 22, no. 3, pp. 311–334, 1986.
- [41] S. Huang, “Dynamic analysis of three-dimensional marine cables,” *Ocean Engineering*, vol. 21, no. 6, pp. 587–605, Aug. 1994.
- [42] J. Palm, G. Moura Paredes, C. Eskilsson, F. Taveira Pinto, and L. Bergdahl, “Simulation of mooring cable dynamics using a discontinuous galerkin method,” in *Proceedings of V International Conference on Computational Methods in Marine Engineering*, Hamburg, Germany, May 2013.
- [43] D. L. Garrett, “Dynamic analysis of slender rods,” *Journal of Energy Resources Technology*, vol. 104, no. 4, pp. 302–306, Dec. 1982.
- [44] R. C. Malahy, “A nonlinear finite element method for the analysis of the offshore pipelaying problem,” PhD Thesis, Rice University, Houston, Texas, 1985.
- [45] J. F. McNamara, P. J. O’Brien, and S. G. Gilroy, “Nonlinear analysis of flexible risers using hybrid finite elements,” *Journal of Offshore Mechanics and Arctic Engineering*, vol. 110, no. 3, pp. 197–204, Aug. 1988.

- [46] B. J. Buckham, “Dynamics modelling of low-tension tethers for submerged remotely operated vehicles,” PhD Thesis, University of Victoria, Victoria, Canada, 2003.
- [47] M. Hall, B. Buckham, and C. Crawford, “Evolving offshore wind: Genetic Algorithm-Based optimization of floating wind turbine platforms,” in *OCEANS’13 MTS/IEEE Bergen*, Bergen, Norway, Jun. 2013.
- [48] B. S. Kallesoe and A. M. Hansen, “Dynamic mooring line modeling in Hydro-Aero-Servo-Elastic wind turbine simulations,” in *Proceedings of the Twenty-first International Offshore and Polar Engineering Conference*, Maui, Hawaii, USA, Jun. 2011.
- [49] D. Matha, O. Bischoff, U. Fechter, and M. Kuhn, “Non-Linear Multi-Body mooring system model for floating offshore wind turbines,” in *EWEA Offshore 2011*, Amsterdam, The Netherlands, 2011.
- [50] M. Masciola, A. Robertson, J. Jonkman, A. Coulling, and A. Goupee, “Assessment of the importance of mooring dynamics on the global response of the DeepCWind floating semisubmersible offshore wind turbine,” in *Proceedings of the Twenty-third (2013) International Offshore and Polar Engineering Conference*, Anchorage, Alaska, USA, Jul. 2013.
- [51] J. Azcona, T. A. Nygaard, X. Munduate, and D. Merino, “Development of a code for dynamic simulation of mooring lines in contact with seabed,” in *EWEA Offshore 2011*, Amsterdam, The Netherlands, 2011.
- [52] Y. Bae, M. Kim, S. Im, and I. Chang, “Aero-Elastic-Control-Floater-Mooring coupled dynamic analysis of floating offshore wind turbines,” in *Proceedings of the Twenty-first (2011) International Offshore and Polar Engineering Conference*, Maui, Hawaii, USA, Jun. 2011.
- [53] B. Koo, A. J. Goupee, K. Lambrakos, and H. Lim, “Model test data correlations with fully coupled Hull/Mooring analysis for a floating wind turbine on a Semi-Submersible platform,” in *Proceedings of the 33rd International Conference on Ocean, Offshore and Arctic Engineering*. San Francisco, California: ASME, Jun. 2014.
- [54] J. R. Morison, M. P. O’Brien, J. W. Johnson, and S. A. Schaaf, “The forces exerted by surface waves on piles,” *Petroleum Transactions, A.I.M.E.*, vol. 189, 1950.
- [55] J. M. Jonkman, “The new modularization framework for the FAST wind turbine CAE tool,” in *Proceedings of the 51st AIAA Aerospace Sciences Meeting and 31st ASME Wind Energy Symposium*, Grapevine, Texas, USA, 2013.

- [56] S. Sirnivas, Y. Yu, M. Hall, and B. Bosma, “Coupled mooring analysis for the WEC-Sim wave energy converter design tool,” in *Proceedings of the 35th International Conference on Ocean, Offshore and Arctic Engineering*, Busan, South Korea, Jun. 2016.
- [57] F. F. Wendt, M. T. Andersen, A. N. Robertson, and J. M. Jonkman, “Verification and validation of the new dynamic mooring modules available in FAST v8,” in *Proceedings of the Twenty-sixth International Offshore and Polar Engineering Conference*, Rhodes, Greece, Jun. 2016.
- [58] M. T. Andersen, F. T. Wendt, A. N. Robertson, J. M. Jonkman, and M. Hall, “Verification and validation of multisegmented mooring capabilities in FAST v8,” in *Proceedings of the Twenty-sixth International Offshore and Polar Engineering Conference*, Rhodes, Greece, Jun. 2016.
- [59] A. Goupee, B. Koo, K. Lambrakos, and R. Kimball, “Model tests for three floating wind turbine concepts,” in *Proceedings of Offshore Technology Conference (OTC 2012)*, Houston, Texas, May 2012.
- [60] A. Goupee, M. Fowler, R. Kimball, J. Helder, and E. de Ridder, “Additional Wind/Wave basin testing of the DeepCwind Semi-Submersible with a Performance-Matched wind turbine,” in *Proceedings of the 33rd International Conference on Ocean, Offshore and Arctic Engineering*, San Francisco, California, Jun. 2014.
- [61] A. Robertson, J. Jonkman, M. Masciola, H. Song, A. Goupee, A. Coulling, and C. Luan, “Definition of the semisubmersible floating system for phase II of OC4,” National Renewable Energy Laboratory, Golden, Colorado, USA, NREL Technical Report TP-5000-60601, Sep. 2014.
- [62] A. Robertson, J. Jonkman, F. Vorpahl, W. Popko, J. Qvist, L. Froyd, X. Chen, J. Azcona, E. Uzunoglu, C. Guedes Soares, C. Luan, H. Yutong, F. Pengcheng, A. Yde, T. Larsen, J. Nichols, R. Buils, L. Lei, T. A. Nygaard, D. Manolas, A. Heege, S. R. Vatne, H. Ormberg, T. Duarte, C. Godreau, H. F. Hansen, A. W. Nielsen, H. Riber, C. Le Cunff, F. Beyer, A. Yamaguchi, K. J. Jung, H. Shin, W. Shi, H. Park, M. Alves, and M. Guérinel, “Offshore code comparison collaboration continuation within IEA wind task 30: Phase II results regarding a floating semisubmersible wind system,” in *Proceedings of the 33rd International Conference on Ocean, Offshore and Arctic Engineering*. San Francisco, California, USA: ASME, Jun. 2014, p. V09BT09A012.
- [63] A. J. Coulling, A. J. Goupee, A. N. Robertson, J. M. Jonkman, and H. J. Dagher, “Validation of a FAST semi-submersible floating wind turbine numerical model with DeepCwind test data,” *Journal of Renewable and Sustainable Energy*, vol. 5, no. 2, pp. 023116:1–29, Mar. 2013.

- [64] J. M. Jonkman, S. Butterfield, W. Musial, and G. Scott, ‘‘Definition of a 5-MW reference wind turbine for offshore system development,’’ National Renewable Energy Laboratory, Golden, Colorado, Tech. Rep. 38060, Feb. 2009.
- [65] A. J. Coulling, A. J. Goupee, A. N. Robertson, and J. M. Jonkman, ‘‘Importance of second-order difference-frequency wave diffraction forces in the validation of a fast semi-submersible floating wind turbine model,’’ in *Proceedings of the ASME 2013 32nd International Conference on Ocean, Offshore, and Arctic Engineering*, Nantes, France, Jun. 2013.
- [66] S. Gueydon, T. Duarte, and J. Jonkman, ‘‘Comparison of Second-Order loads on a semisubmersible floating wind turbine,’’ in *Proceedings of the 33rd International Conference on Ocean, Offshore and Arctic Engineering*. San Francisco, California, USA: ASME, Jun. 2014.
- [67] DNV, ‘‘DNV-RP-C205: environmental conditions and environmental loads,’’ Det Norske Veritas, Hovik, Norway, Tech. Rep., 2007.
- [68] ——, ‘‘DNV-RP-F205: global performance analysis of deepwater floating structures,’’ Det Norske Veritas, Hovik, Norway, Tech. Rep., 2004.
- [69] ——, ‘‘DNV-OS-E301: position moorings,’’ Det Norske Veritas, Hovik, Norway, Tech. Rep., Oct. 2013.
- [70] API, ‘‘API RP 2A-WSD: recommended practice for planning, designing and constructing fixed offshore platforms - working stress design,’’ American Petroleum Institute, Tech. Rep., 2007.
- [71] G. Hayman and M. L. Buhl, ‘‘MLife user’s guide for version 1.00,’’ National Renewable Energy Laboratory, Golden, Colorado, Tech. Rep., Oct. 2012.
- [72] D. Matha, ‘‘Model development and loads analysis of an offshore wind turbine on a tension leg platform, with a comparison to other floating turbine concepts,’’ PhD Thesis, University of Colorado - Boulder, USA, Apr. 2009.
- [73] G. Vissio, B. Passione, M. Hall, and M. Raffero, ‘‘Expanding ISWEC modelling with a Lumped-Mass mooring line model,’’ in *Proceedings of the 11th European Wave and Tidal Energy Conference*, Nantes, France, Sep. 2015.
- [74] G. E. P. Box and M. E. Muller, ‘‘A note on the generation of random normal deviates,’’ *The Annals of Mathematical Statistics*, vol. 29, no. 2, pp. 610–611, Jun. 1958.
- [75] A. J. Goupee, B. Koo, R. W. Kimball, K. F. Lambrakos, and H. J. Dagher, ‘‘Experimental comparison of three floating wind turbine concepts,’’ *Journal of Offshore Mechanics and Arctic Engineering*, vol. 136, no. 2, 2014.

- [76] J. M. Jonkman, “Definition of the floating system for phase IV of OC3,” National Renewable Energy Laboratory, Golden, Colorado, Technical Report 47535, May 2010.
- [77] W. L. Moon III and C. J. Nordstrom, “Tension leg platform turbine: A unique integration of mature technologies,” in *Proceedings of the 16th Offshore Symposium, Houston, Texas Section of the Society of Naval Architects and Marine Engineers*, Feb. 2010.
- [78] G. Stewart, M. Lackner, A. Robertson, J. Jonkman, and A. J. Goupee, “Calibration and validation of a FAST floating wind turbine model of the DeepCwind scaled tension-leg platform,” in *Proceedings of the 22nd International Offshore and Polar Engineering Conference*, Rhodes, Greece, Jun. 2012.
- [79] I. Prowell, A. Robertson, J. Jonkman, G. M. Stewart, and A. J. Goupee, “Numerical prediction of experimentally observed behavior of a scale model of an offshore wind turbine supported by a Tension-Leg platform,” in *Offshore Technology Conference*, Houston, Texas, May 2013.
- [80] B. Koo, A. J. Goupee, R. W. Kimball, and K. F. Lambrakos, “Model tests for a floating wind turbine on three different floaters,” *Journal of Offshore Mechanics and Arctic Engineering*, vol. 136, no. 2, 2014.
- [81] L. Roald, J. Jonkman, A. Robertson, and N. Chokani, “The effect of second-order hydrodynamics on floating offshore wind turbines,” *Energy Procedia*, vol. 35, pp. 253–264, 2013.
- [82] S. Gueydon, P. Wuillaume, J. Jonkman, A. Robertson, and A. Platt, “Comparison of Second-Order loads on a Tension-Leg platform for wind turbines,” in *Proceedings of the Twenty-Fifth International Offshore and Polar Engineering Conference*, Kona, Hawaii, Jun. 2015.
- [83] A. M. Viselli, G. Z. Forristall, B. R. Pearce, and H. J. Dagher, “Estimation of extreme wave and wind design parameters for offshore wind turbines in the gulf of maine using a POT method,” *Ocean Engineering*, vol. 104, pp. 649–658, Aug. 2015.
- [84] “ABS guide for building and classifying floating offshore wind turbine installations,” American Bureau of Shipping, Houston, Texas, Tech. Rep., Jan. 2013.
- [85] “Wind turbines - part 1: Design requirements,” International Electrotechnical Commission, International Standard IEC 61400-1:2005(E), Aug. 2005.
- [86] B. J. Jonkman and L. Kilcher, “TurbSim user’s guide: Version 1.06.00,” National Renewable Energy Laboratory, Golden, Colorado, Tech. Rep., Sep. 2012.

- [87] A. J. Goupee, K. F. Lambrakos, R. W. Kimball, B. Koo, and H. J. Dagher, “Experimental comparison of three floating wind turbine concepts,” in *Proceedings of the 31st International Conference on Ocean, Offshore and Arctic Engineering*, Rio de Janeiro, Brazil, Jul. 2012.
- [88] S. Kawamura, W. Choe, S. Tanaka, and S. R. Pandian, “Development of an ultrahigh speed robot FALCON using wire drive system,” in *Robotics and Automation, 1995. Proceedings., 1995 IEEE International Conference on (Volume:1)*, Nagoya, May 1995.
- [89] D. Surdilovic and R. Bernhardt, “STRING-MAN: a new wire robot for gait rehabilitation,” in *Robotics and Automation, 2004. Proceedings. ICRA '04. 2004 IEEE International Conference on*, New Orleans, LA, May 2004.
- [90] S. Kawamura, H. Kino, and C. Won, “High-speed manipulation by using parallel wire-driven robots,” *Robotica*, vol. 18, no. 01, pp. 13–21, Jan. 2000.
- [91] R. Verhoeven, “Analysis of the workspace of tendon-based stewart platforms,” PhD Thesis, Universität Duisburg-Essen, Jul. 2004.
- [92] W. Y. Ho, W. Kraus, A. Mangold, and A. Pott, “Haptic interaction with a Cable-Driven parallel robot using admittance control,” in *Cable-Driven Parallel Robots*, ser. Mechanisms and Machine Science, A. Pott and T. Bruckmann, Eds. Springer International Publishing, Jan. 2015, no. 32, pp. 201–212.
- [93] A. Fortin-Cote, P. Cardou, and C. Gosselin, “An admittance control scheme for haptic interfaces based on cable-driven parallel mechanisms,” in *2014 IEEE International Conference on Robotics and Automation (ICRA)*, May 2014, pp. 819–825.
- [94] D. Wagner and D. Schmalstieg, “ARToolKitPlus for pose tracking on mobile devices,” in *Proceedings of 12th Computer Vision Winter Workshop (CVWW'07)*, Feb. 2007.
- [95] A. Alp and S. Agrawal, “Cable suspended robots: design, planning and control,” in *IEEE International Conference on Robotics and Automation, 2002. Proceedings. ICRA '02*, vol. 4, 2002, pp. 4275–4280 vol.4.
- [96] R. Roberts, T. Graham, and J. Trumpower, “On the inverse kinematics and statics of cable-suspended robots,” in *, 1997 IEEE International Conference on Systems, Man, and Cybernetics, 1997. Computational Cybernetics and Simulation*, vol. 5, Oct. 1997, pp. 4291–4296 vol.5.
- [97] A. Pott, T. Bruckmann, and L. Mikelsons, “Closed-form force distribution for parallel wire robots,” in *Proceedings of the 5th International Workshop on Computational Kinematics*, Jan. 2009, pp. 25–34.

- [98] G. Zeng and A. Hemami, "An overview of robot force control," *Robotica*, vol. 15, no. 05, p. 473–482, Sep. 1997.
- [99] A. Witkin, M. Gleicher, and W. Welch, "Interactive dynamics," *Computer Graphics*, vol. 24, no. 2, pp. 11–21, Mar. 1990.
- [100] C. Reichert, K. Muller, and T. Bruckmann, "Haptic interaction with a Cable-Driven parallel robot using admittance control," in *Cable-Driven Parallel Robots*, ser. Mechanisms and Machine Science, A. Pott and T. Bruckmann, Eds. Springer International Publishing, Jan. 2015, no. 32, pp. 131–144.
- [101] R. E. Kalman, "A new approach to linear filtering and prediction problems," *Journal of Basic Engineering*, vol. 82, no. 1, pp. 35–45, Mar. 1960.
- [102] S. You and U. Neumann, "Fusion of vision and gyro tracking for robust augmented reality registration," in *IEEE Virtual Reality, 2001. Proceedings*, Mar. 2001, pp. 71–78.
- [103] F. Caron, E. Duflos, D. Pomorski, and P. Vanheeghe, "GPS/IMU data fusion using multisensor kalman filtering: introduction of contextual aspects," *Information Fusion*, vol. 7, no. 2, pp. 221–230, Jun. 2006.
- [104] A. Tobergte, M. Pomarlan, and G. Hirzinger, "Robust multi sensor pose estimation for medical applications," in *IEEE/RSJ International Conference on Intelligent Robots and Systems, 2009. IROS 2009*, Oct. 2009, pp. 492–497.
- [105] A. Angrisano, "GNSS/INS integration methods," PhD Thesis, Universita degli Studi di Napoli "Parthenope", Napoli, Italy, 2010.
- [106] N. Enayati, "Quaternion-Based unscented kalman filter for robust motion tracking in neurosurgery," MSc Thesis, Politecnico di Milano, Milano, Italy, 2013.
- [107] T. Horiuchi, M. Inoue, T. Konno, and Y. Namita, "Real-time hybrid experimental system with actuator delay compensation and its application to a piping system with energy absorber," *Earthquake Engineering & Structural Dynamics*, vol. 28, no. 10, pp. 1121–1141, Oct. 1999.
- [108] T. Proietti and A. Luati, "Real time estimation in local polynomial regression, with application to Trend-Cycle analysis," *The Annals of Applied Statistics*, vol. 2, no. 4, pp. 1523–1553, 2008.
- [109] J. Merlet, "Kinematics of the wire-driven parallel robot MARIONET using linear actuators," in *Proceedings of IEEE Conference on Robotics and Automation*, Pasadena, California, May 2008.

- [110] A. Pott, H. Mütherich, W. Kraus, V. Schmidt, P. Miermeister, and A. Verl, “IPAnema: a family of Cable-Driven parallel robots for industrial applications,” in *Cable-Driven Parallel Robots*, ser. Mechanisms and Machine Science, T. Bruckmann and A. Pott, Eds. Springer Berlin Heidelberg, 2013, no. 12, pp. 119–134.
- [111] S. Fang, D. Franitz, M. Torlo, F. Bekes, and M. Hiller, “Motion control of a tendon-based parallel manipulator using optimal tension distribution,” *IEEE/ASME Transactions on Mechatronics*, vol. 9, no. 3, pp. 561–568, Sep. 2004.
- [112] T. Heyden and C. Woernle, “Dynamics and flatness-based control of a kinematically undetermined cable suspension manipulator,” *Multibody System Dynamics*, vol. 16, no. 2, pp. 155–177, Aug. 2006.
- [113] M. J. Fowler, A. J. Goupee, and A. M. Viselli, “Advances in model scale testing of floating offshore wind turbines utilizing the w2 Wind/Wave basin,” in *Offshore Technology Conference*, Houston, Texas, May 2016.
- [114] T. Sebastian and M. A. Lackner, “A comparison of First-Order aerodynamic analysis methods for floating wind turbines,” in *Proceedings of the 48th AIAA Aerospace Sciences Meeting*, Orlando, Florida, Jan. 2010.

APPENDIX

PERFORMANCE SPECIFICATIONS FOR MOORING-PLATFORM HYBRID COUPLING

Although the primary focus of my work has been hybrid modeling solutions to basin testing challenges associated with the wind turbine, there is also potential for using hybrid modeling to avoid mooring challenges in basin testing. This application was one of the secondary motivations for creating MoorDyn. By applying numerically-modeled mooring system loads onto the floating wind turbine in the basin, potentially using an actuation approach similar to that for the tower-base hybrid coupling, the challenge of mooring system truncation in small basins could be avoided.

Figure A.1 provides an illustration of this idea. If actuation is applied at the same point as the tower-base coupling case described in Chapter 3, then the motions required of the actuator are the same as those presented in Table 3.4 and the sensitivity to actuation force noise is the same as was presented in Figures 3.15a and 3.16a. What remains to be seen are the forces that the actuator would be required to provide, as well as the sensitivity of the results to noise and latency in the motion tracking inputted to the mooring simulation.

For this purpose, I consider the same output channels as in the previous two hybrid coupling cases. The choice of not considering mooring line tensions or net mooring forces is deliberate. In results of other couplings, looking at mooring tensions specifically is unnecessary since platform motions, which are measured, are the means by which coupling errors are transmitted to the mooring lines. In

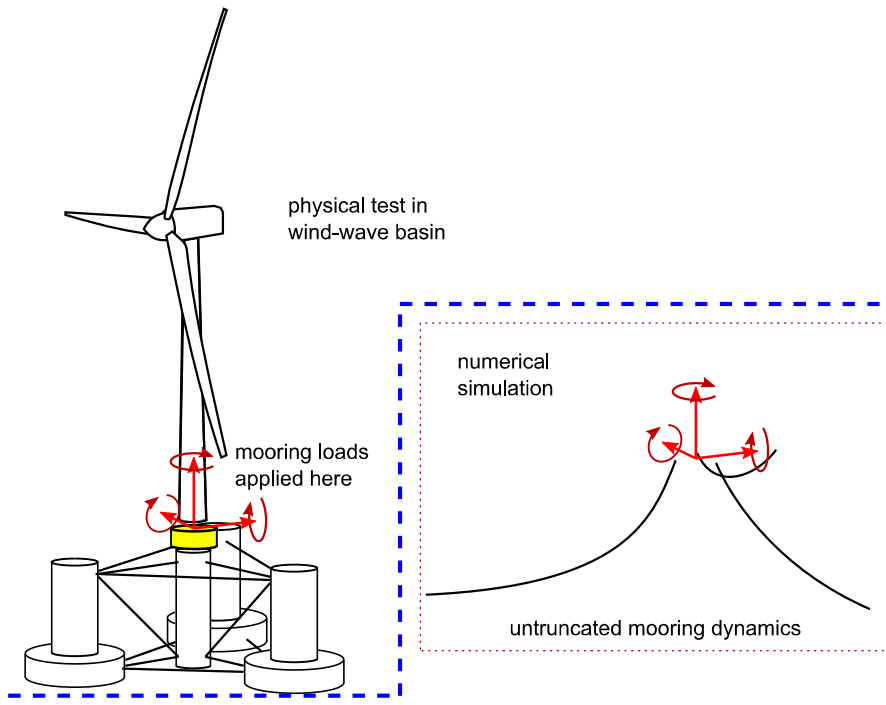


Figure A.1: Mooring-platform hybrid coupling

mooring-platform coupling, what matters is the coupled response of the platform and turbine, since these are being tested experimentally. If these are satisfactory, then any problems arising from the coupling specific to the mooring lines alone could be corrected after the test in uncoupled simulations driven by the measured platform motion.

Figures A.2-A.4 show the maximum surge, heave, and pitch loads required from the actuator in each of the seven wind and wave cases used previously. Since six simulations were run for each case, the bar heights indicate the mean of these identified extreme loads, while the error bands indicate the standard deviation. Results shown are at full-scale. The stiffness of the TLP mooring vertically is apparent in the large heave forces and pitch moments. Clearly, the viability of

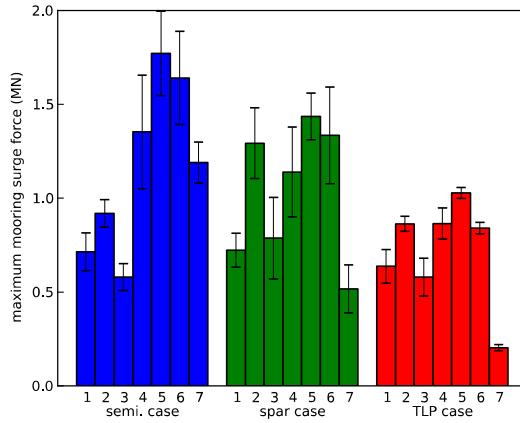


Figure A.2: Maximum surge forces in mooring coupling

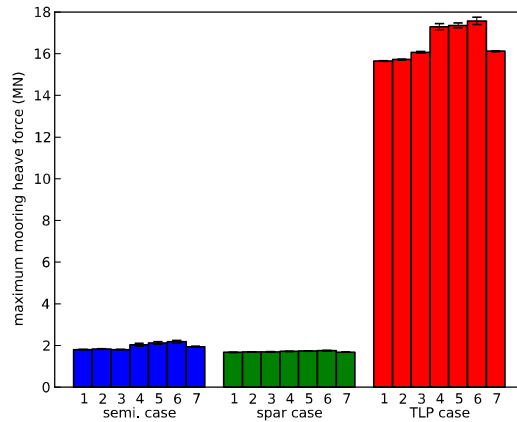


Figure A.3: Maximum heave forces in mooring coupling

mooring-platform hybrid coupling may be more case-specific than that of aero-elastic or tower-base hybrid coupling.

Table A.1 shows the maximum forces and moments expected in each direction for each design.

Figure A.5 shows the sensitivity to errors in translational motion measurements passed to the mooring model. The low sensitivity of the spar may be a result of its moorings being both light and elastic, making for little sensitivity of line tension to small fairlead motion fluctuations. In contrast, the weight of the semisubmersible mooring chains would cause large inertial loads in response to fairlead

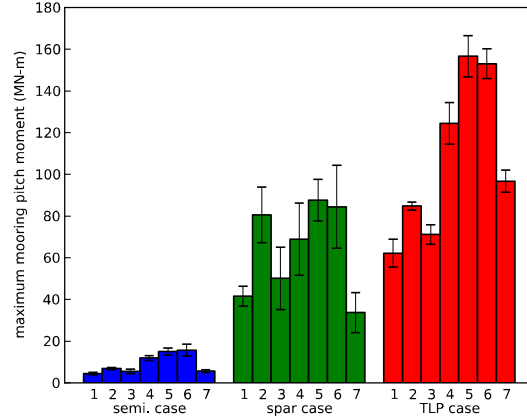


Figure A.4: Maximum pitch moments in mooring coupling

Table A.1: Maximum forces and motions in mooring-platform coupling for each design

Design	Surge (MN)	Sway (MN)	Heave (MN)	Roll (MN-m)	Pitch (MN-m)	Yaw (MN-m)
semi.	2.4	0.1	2.4	2.3	24.1	13.2
spar	2.1	0.2	1.8	12.8	144.2	4.9
TLP	1.1	0.1	18.1	21.1	186.3	6.0

accelerations, and the stiffness of the TLP tendons would cause large tension changes in response to fairlead displacements.

Figure A.5 shows the sensitivity to rotational motion tracking errors. Here, the high sensitivity of the TLP reflects the high stiffness provided in pitch by its taut mooring lines.

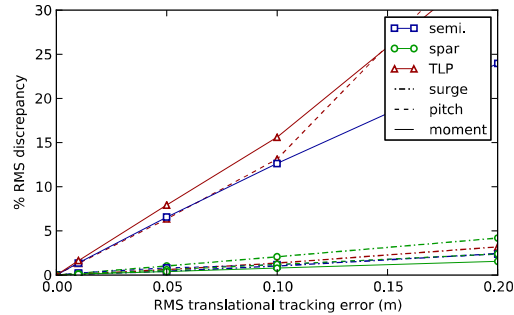


Figure A.5: Sensitivity to translational tracking errors in mooring coupling

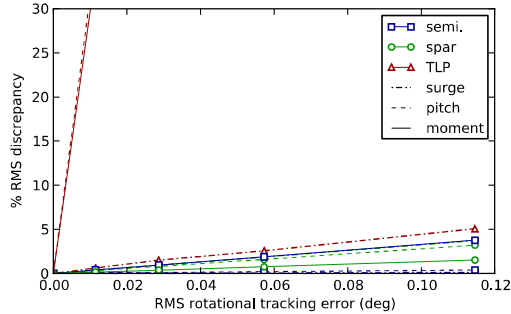


Figure A.6: Sensitivity to rotational tracking errors in mooring coupling

Figure A.7 shows the sensitivity to latency in the numerical mooring model coupling. The high sensitivity of the TLP and low sensitivity of the other designs reflects the very different natural frequencies of the stiff TLP mooring versus the catenary semisubmersible mooring and the taut-but-compliant spar mooring. As alluded to in Section 2.2.6, hybrid modeling a taut mooring system like that of the TLP could require a mooring model that runs efficiently with sub-ms time step lengths.

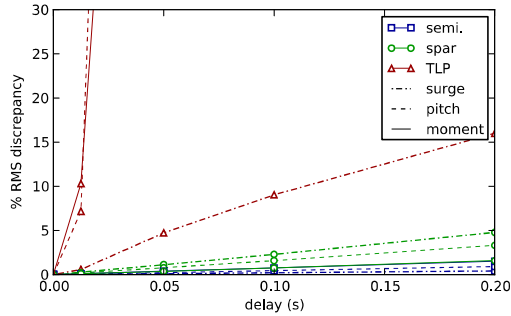


Figure A.7: Sensitivity to latency in mooring coupling

Compared to the two aerodynamics-focused hybrid coupling scenarios considered in Chapter 3, requirements for a mooring-focused hybrid coupling seem to be somewhat larger and much more dependent on the specifics of the mooring system. While the actuator motion requirements would be similar to tower-base coupling, the force actuation requirements may be two-to-three times larger in most

directions. Furthermore, the forces for the TLP mooring are dramatically larger in heave, making mooring-platform hybrid modeling of TLP designs considerably more demanding.

BIOGRAPHY OF THE AUTHOR

Matthew Hall was born in Ontario, Canada. He graduate from Charlottetown Rural High School in Prince Edward Island in 2005 and received a Diploma in Engineering from the University of Prince Edward Island in 2008. He completed his Bachelor of Science in mechanical engineering at University of New Brunswick in Fredericton in 2010, and then returned to the west coast to pursue graduate studies in renewable energy at the University of Victoria, British Columbia. Following two-and-a-half years of research on floating wind turbines, Matt completed his Masters of Applied Science in 2013 under the supervision of professors Brad Buckham and Curran Crawford. From there, Matt moved to Orono, Maine to continue graduate work in connection with the floating wind turbine research activities at the University of Maine. He is a candidate for the Doctor of Philosophy degree in Mechanical Engineering from the University of Maine in August 2016.